

RIKAGAKU KENKYUSHO

the Institute of Physical and Chemical Research

Yamato-machi, Saitama Pref., JAPAN

'68

IPCR cyclotron
Progress Report 1968

Vol. 2

Edited by Administration Committee of the IPCR Cyclotron

IPCR Cyclotron Progress Report 1968

Vol. 2

The Institute of Physical and Chemical Research
"RIKAGAKU KENKYUSHO" Yamato-machi, Saitama, 351 JAPAN
December, 1968

This volume contains recent information of the IPCR cyclotron, informal reports and abstracts of papers which will be published at scientific meetings or in publications by staff members, guests, and visitors.

All rights reserved. This report or any part thereof may not be reproduced in any form (including photostatic or microfilm form) without written permission from the publisher.

CONTENTS

	Page
1. INTRODUCTION	1
2. MACHINE OPERATION	2
3. MACHINE DEVELOPMENT	
3-1. Machine Improvement	7
3-2. Multicharged Heavy Ion Source	11
3-3. The Focusing Magnetic Channel	16
4. ACCELERATOR PHYSICS	
4-1. Initial Motion of Ions	19
4-2. Heavy Ion Acceleration	23
4-3. Investigation of Electromagnet	29
On the Energy Reproducibility in Magnetic Analyzers	
4-4. Energy of Cyclotron Beam Estimated by Radio Frequency	33
5. NUCLEAR PHYSICS	
Scattering and Reaction	
5-1. Elastic Scattering of ^3He from Nuclei and Optical Model Analysis	36
5-2. Elastic and Inelastic Scattering of Heavy Ions	48
5-3. ($^3\text{He}, \alpha$) Reactions of Al and Si at 22.34 MeV	54
5-4. The (d,d), (d,d') and (d,t) Reactions of ^{27}Al and ^{28}Si	63
5-5. Inelastic Scattering of Protons from ^{91}Zr	67
5-6. The $^{12}\text{C}(^3\text{He},\text{p})^{14}\text{N}$ and $^{27}\text{Al}(^3\text{He},\text{p})^{29}\text{Si}$ Reactions	74
5-7. Double Scattering of ^3He from Carbon	77
5-8. Two-Nucleon Transfer Reaction Code	83
5-9. The Automatic Search Code of the Optical Model	87

6.	NUCLEAR PHYSICS	
	Nuclear Spectroscopy and its Applications	
6-1.	The Excited States in Xe Isotopes Studied by (H.I., xn γ) and (α , xn γ) Reactions	98
6-2.	Decay of ^{171}Lu	101
6-3.	Study of Internal Conversion Electrons from ^{151}Eu	105
6-4.	Decay of ^{87}Zr	109
6-5.	Nuclide Analysis Using Nuclear Reactions	110
7.	NUCLEAR INSTRUMENTATION AND TECHNIQUES	
7-1.	The Polarized Ion Source	112
7-2.	The Electrically Detecting and Recording System Used for Broad-Range Magnetic Spectrometer	116
7-3.	A Charge Spectrometer	120
8.	RADIOCHEMISTRY	
8-1.	Charged Particle Activation Analysis for Carbon, Nitrogen and Oxygen in Semiconductor Silicon	121
8-2.	Recoil Chemistry of Halates	126
8-3.	Preparation of a ^{61}Cu -Copper Source for the Measurement of the Mössbauer Effect in ^{61}Ni	129
8-4.	^{14}C -labeling Reaction with Proton Beam from Cyclotron	131
9.	RADIATION CHEMISTRY AND RADIATION BIOLOGY	
9-1.	Radiation-Chemical Studies of Fricke Dosimeter with Cyclotron Beams	134
9-2.	α - Radiolysis of Methanol and Tetrahydrofuran. LET Effect	138
9-3.	The LET Effects on Biological Cells	141

10.	SOLID STATE PHYSICS	
10-1.	Behavior of Helium Bubbles in Stainless Steel	145
10-2.	Mössbauer Effect of ^{61}Ni in Magnetic Materials	148
10-3.	γ -Ray Goniometer for Positron Annihilation Experiment	150
10-4.	Preparation of Positron Sources for Positron Annihilation Experiment	154
11.	RI PRODUCTION AND ITS APPLICATIONS	
11-1.	Preparation of ^{18}F -labelled Compounds by the Bombardment of an Oxygen Stream	156
11-2.	Preparation of ^{52}Fe	159
11-3.	Separation of Carrier-free ^{206}Bi from ^{206}Pb	161
12.	RADIATION MONITORING	
12-1.	Neutron Monitoring with a Large Neutron Counter	163
12-2.	Health Physics	166
13.	LIST OF PUBLICATIONS	170
14.	LIST OF PERSONNEL	171

1. INTRODUCTION

The energy of accelerated ions in our cyclotron was increased in this year; especially it was succeeded in accelerating heavy ions, C^{4+} , N^{4+} , N^{5+} , O^{4+} etc., up to the scheduled energy values.

Accelerated ions were used by the research groups for nuclear physics, isotope production, radiochemistry, radiation chemistry, radiation biology, and solid state physics in our institute. Some research groups included members from outside, who participated in the research program as part-time members. Machine time of two days a month were preserved for isotope production for non-members. Examples of use of ions were as follows. Protons up to 16 MeV were used for inelastic scattering by Zr-Mo region nuclei, linear energy transfer in chemical and biological substances, activation analysis, chemical effect, and isotope production. Deuterons up to 25 MeV were used for (d, t) and (d, ^3He) reactions in (s-d) shell region nuclei and chemical effects in substances. Alpha-particles up to 45 MeV were used for isotope production, Coulomb excitation and in beam spectroscopy of nuclei, linear energy transfer in chemical and biological substances, and in solid state physics. ^3He ions up to 45 MeV were used for studies of optical model by elastic scattering by nuclei, polarization by scattering, ($^3\text{He}, \alpha$) reactions by (s-d) shell region nuclei, isotope production, linear energy transfer in substances, and activation analysis. C^{4+} , N^{4+} ions up to 95 MeV were used for elastic and inelastic scatterings by nuclei and in beam spectroscopy.

Hiroo Kumagai

Hiroo Kumagai, Chairman
Administration Committee of
the IPCR Cyclotron

2. MACHINE OPERATION

After the first period of the machine time as reported in the first volume of this Progress Report, there have been two main periods, intervened by a long term for the machine improvement. The second period ranged from July 13 to Oct. 18, 1967, including a half-a-month summer vacation. Then the machine was improved and repaired in many ways which will be described in Section 3 of this report. The main purposes of this machine stop were to obtain higher dee-voltages and to accelerate heavy ions steadily. These purposes and the realization of the magnetic channel were achieved successfully during this period as will be described later. The third period of the machine time was from May 23 to Oct. 22, 1968, including a half-a-month summer vacation and a half-a-month small-scale overhaul.

During these two periods, the machine was operated by a 2 shift 24 h/day system to perform many scientific works. Some results will be described in this Progress Report. The scheduled machine time for each subject is shown in Table 1. The machine was stopped for unscheduled repair only for a few days as integrated over these 16 months. The beam time, i.e. the actual machine operating time was estimated from the indication of working time meters for the Oscillator input power and for the Ion Source input power. These are shown in Table 2. This shows that during 16 months (~ 480 days) including times for machine operation, machine improvement and vacation, about 5000 h were on-beam that is equivalent to net 43 % (3750 h/year). Sundays were omitted from the scheduled machine time, but nuclear reaction experiments were often continued on Sundays. Thus the total used time might be more than 250 days. Time meters showed that in these used days, the beam time was no less than 80 %. At first, the scheduled machine time was aimed at to be 200 days per year. However, the actual machine time was a little shorter than this limit, because a long time was for machine improvement during these periods.

Fig. 1 was obtained from the diary of machine operation. Many kinds of particles and energies were available with this machine for scientific research. The variation of deflected currents was found to be large. It was partly due to the user's demands, but partly because of the machine conditions. Why such a large variation occurs? It will be the next problem for the machine staff. Of course, the matching of the deflected beam and the beam transport system is one subject, but the accelerating conditions, especially the beam deflecting conditions, will be another subject.

Since the 3rd period, the beam irradiation for the radio isotope production has been commenced upon the request from other organizations in this country. In spite of the scarcity of staff members, the preliminary test was trially made with a great success.

Table 1. Scheduled machine times.

Period II. July 13th, 1967 – Oct. 18th, 1967

Subjects	Days
Nuclear reactions with ^3He	49.75
Coulomb excitations	5
RI production for nuclear spectroscopy	6
Radio chemistry and RI production	9.25
Radiation chemistry and radiation biology (LET Effects)	5
Solid state physics	5
Analysis of nucleid	0.5
Accelerator physics and machine improvement	6
Machine inspections and repairs	3.5
	91

Period III. May 23rd, 1968 – Oct. 22nd, 1968

Subjects	Days
Heavy ion reactions	10
Direct reactions	24
Polarization phenomena	18
In beam spectroscopy	20
RI production for nuclear spectroscopy	10
Radiochemistry and RI production	12
Radiation chemistry and radiation biology (LET Effects)	11.2
Solid state physics	5.8
Labelled compound	2.25
Analysis of nucleid	2.25
Accelerator physics and machine improvement	15.5
Machine inspections and repairs	5
RI productions for other organizations	8
	144

Table 2. Machine operating times.

Indications of working time meters

	Oscillator input power	Ion Source input power
Oct. 11, 1968	7228.2 (h)	7868.2 (h)
July 13, 1967	2242.1 (h)	2355.4 (h)
~11500 (h)	4986.1 (h)	5512.8 (h)

Schedule for these 16 months (~ 480 days)

Scheduled machine time	240 (days)
Scheduled machine improvement	110 (days)
Summer vacations, sundays, etc.	130 (days)
	~480 (days)

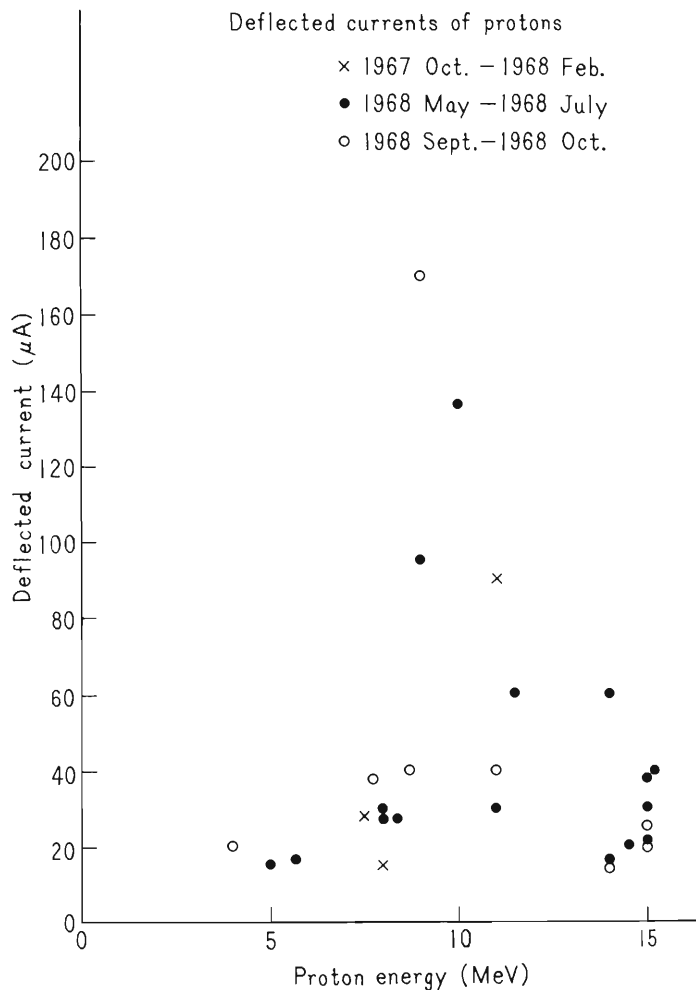


Fig. 1(a). Records of used beam energies and deflected currents for proton beams.

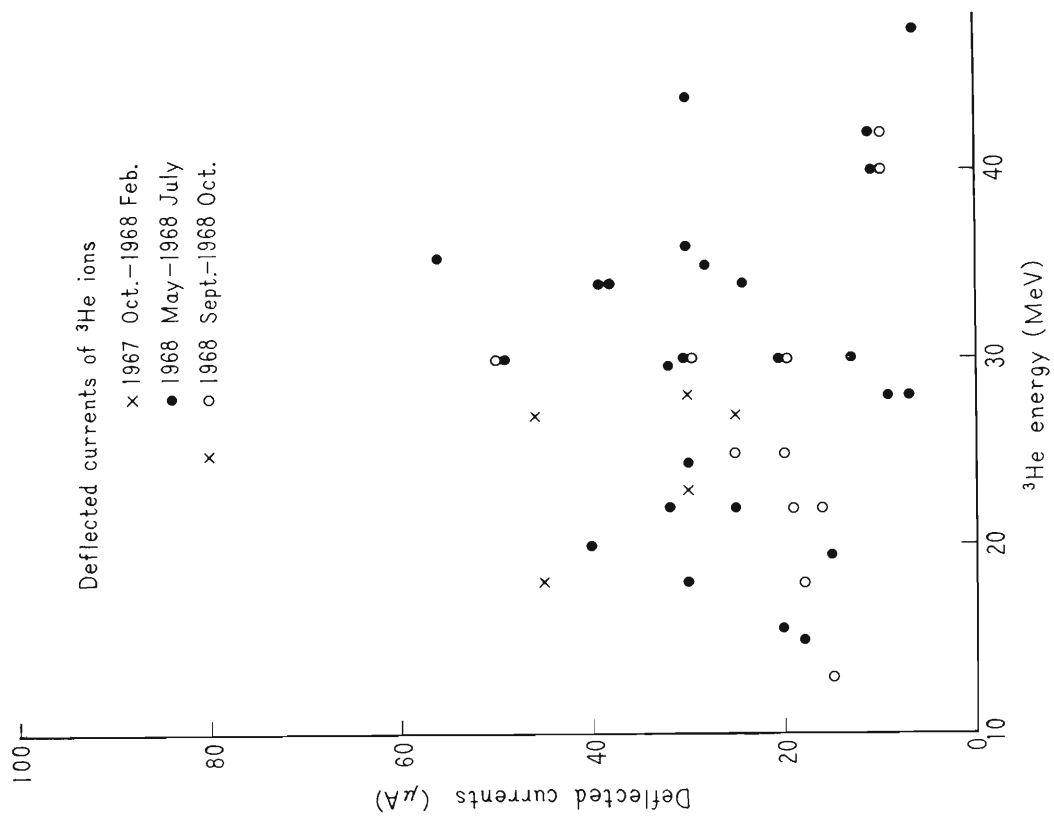


Fig. 1(c). Records of used beam energies and deflected currents for ^3He beams.

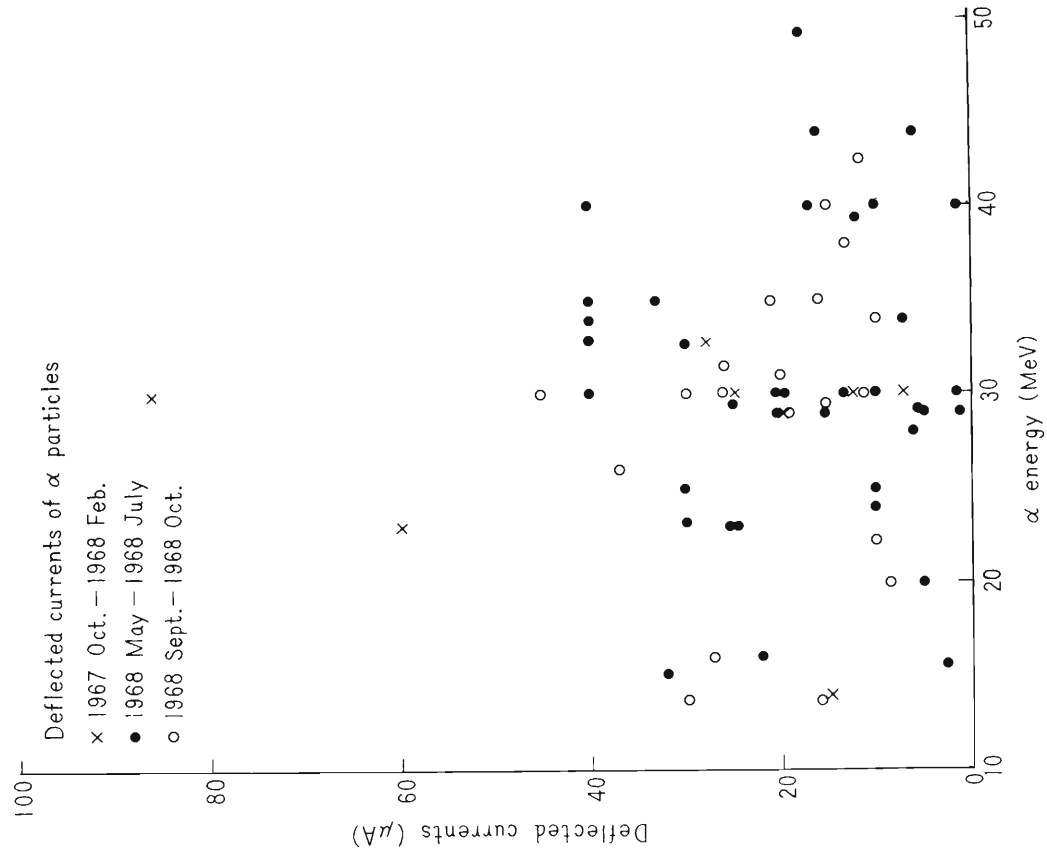


Fig. 1(b). Records of used beam energies and deflected currents for α particle beams.

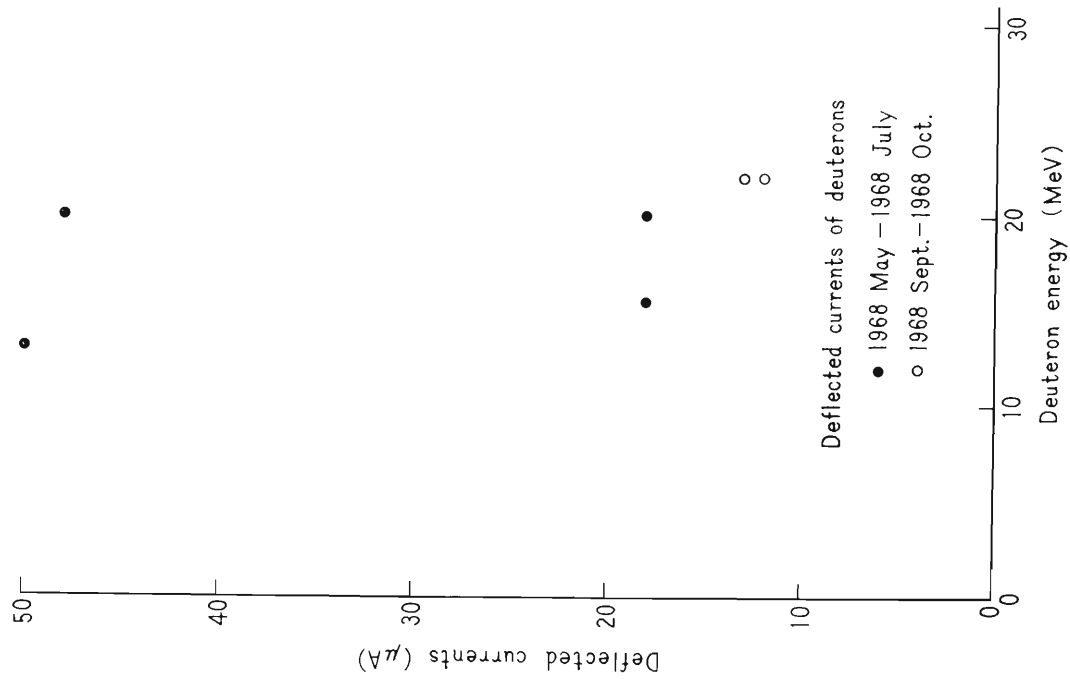
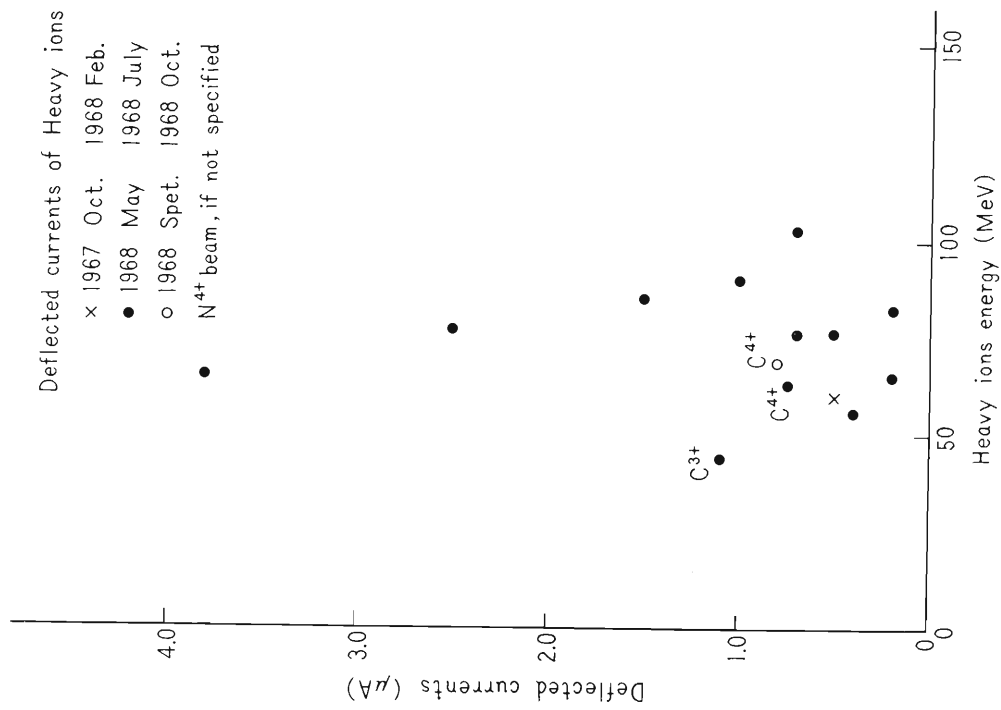


Fig. 1(d). Records of used beam energies and deflected currents for deuteron beams.



3. MACHINE DEVELOPMENT

3-1. Machine Improvement

T. Karasawa, Y. Miyazawa, T. Tonuma, T. Inoue, A. Shimamura,
O. Terajima, K. Yoshida, and M. Odera

(1) Increase of beam energy

When the magnetic field and the radio frequency satisfy the resonance condition in an ordinary type variable energy cyclotron, the dee voltage limits the maximum beam energy. Some improvements for the increase of dee voltage was made.

In autumn, 1967, glow discharges behind the shorting device caused cracks on the cooling tube and made the electric resistivity of insulators worse for the shorting device. In the overhaul period in January, 1968, the cooling tubes made of synthetic rubber for the shorting device were replaced by metallic flexible tubes and the insulators made of teflon were replaced by ceramic ones. New dee liners were installed. The cooling tubes were soft-soldered on the old liner and silver-soldered on the new one. The silicon rubber insulating electric leads for the circular trimming coils were removed and ceramic insulating leads were installed.

After these improvements, pressure of the vacuum chamber has been reduced. Operating pressures are collectively shown in Fig. 1 compared with those before improvements, which shows that the pressures are reduced to about a half by these improvements.

High dee voltages have been easily applied under the condition of good vacuum. The highest dee voltage applied without spark in the clearance gap between dees and movable dee liners is shown in Fig. 2. Extension of highest energy of d , α and ${}^3\text{He}^{++}$ was examined in March, 1968. The operating energies of these particles including heavy ions from the date of using the first beam to the present time, are shown in Fig. 3.

(2) Other improvements

A new vacuum condenser with variable large capacity was set in the oscillator house. For changing the frequency, the coupling parameters between the oscillator and the resonator were easily adjusted from the control desk. For obtaining better coupling in the operation of high frequency and high dee voltage, the plate loop was covered with a copper sheet, which reduced the area of loop to a half.

The second ${}^3\text{He}$ recirculating system was installed. The new system was simplified and made easy to handle, and consisted of complete two recirculation and purification systems for continuous operation for several days.

A new cone supporting tube for the ion source was installed. It supplies gases directly to the canal of the cone. Troubles of electric breakdown arised in the filament and its supporting tube. Several types of insulating parts were examined. This problem is under development.

After the overhaul period, the cyclotron was operated under good conditions with higher energy compared with the period of 1967. A failure was found on the dee liner

around the entrance of deflector. Because of high power dissipation on the entrance of septum and heavy discharge towards the dee liner, the dee liner was eroded. In five weeks after the erosion was found, one of the circulating trimming coils set behind the dee liner was destroyed. Then an electromagnet was used at below 1.8 Wb/cm^2 in June and July. For this reason, a small scale overhaul was done in summer, 1968. The movable dee liners were demounted from the accelerating chamber and removable tungsten pieces were attached at the eroded parts on the dee liner. The destroyed circular trimming coil was replaced with a new one.

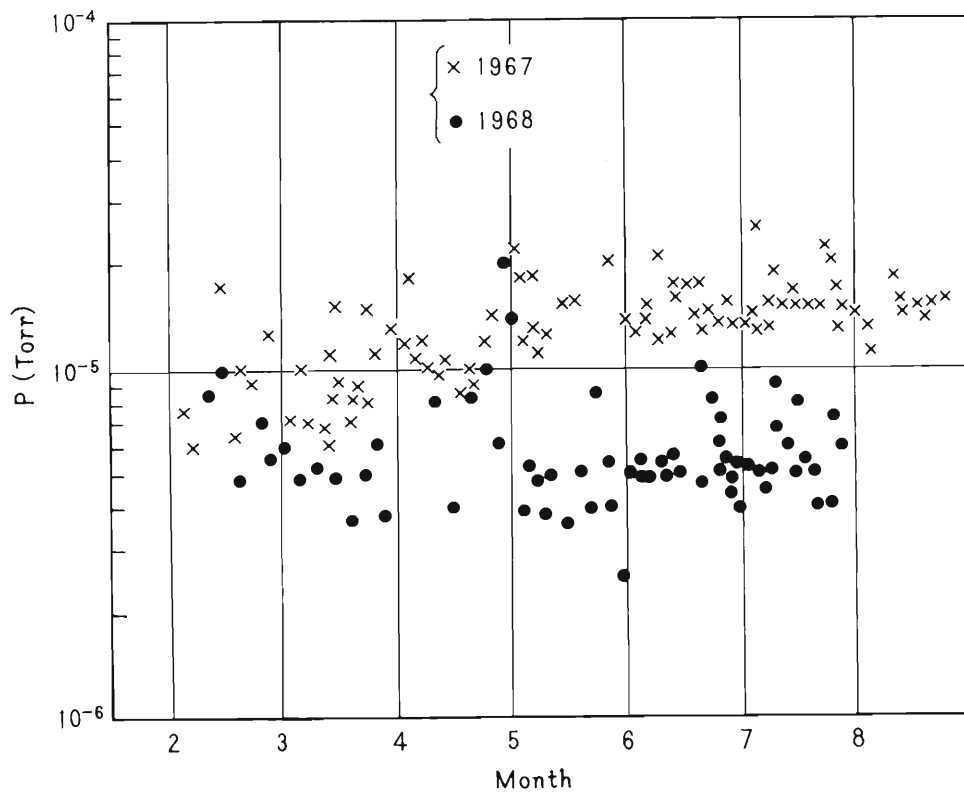


Fig. 1. Operating pressure of cyclotron.

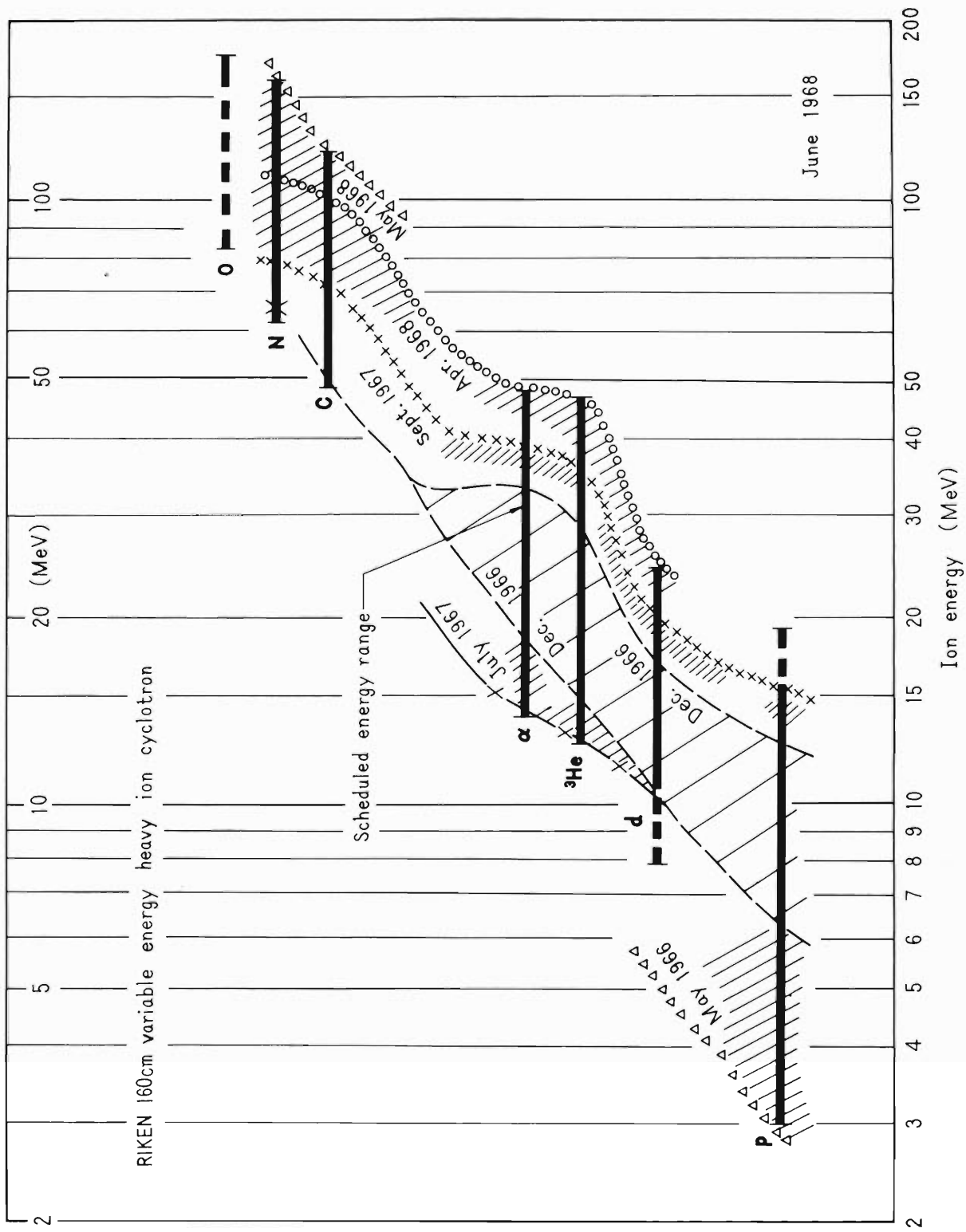


Fig. 2. Increase of beam energy.

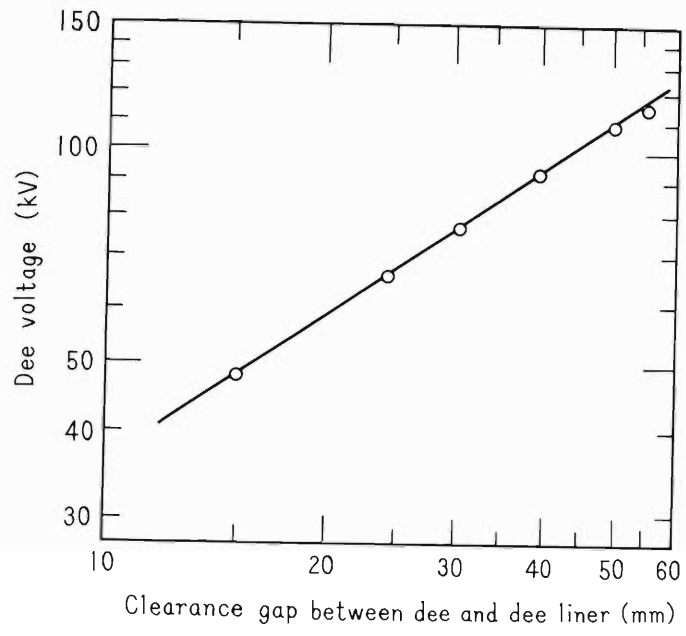


Fig. 3. Maximum dee voltage vs. clearance gap.

3-2. Multicharged Heavy Ion Source

T. Tonuma, I. Kohno, Y. Miyazawa, S. Nakajima, T. Inoue,
A. Shimamura, K. Yoshida, and T. Karasawa

A multicharged heavy ion source was constructed for the cyclotron according to the design based on the result of the bench test,¹⁾ at which we had obtained some multicharged ions, i.e. N^{3+} , N^{4+} , C^{3+} , and C^{4+} , using an electron bombarded type ion source similar to the Morosov one.²⁾

Fig. 1 is a schematic view of the multicharged heavy ion source and Fig. 2 is a photograph of this source which is arranged for the cyclotron. The upper cathode (C_1 , 10 mm dia. \times 8 mm) is heated by electron bombardment from the tungsten filament (F, 2 mm dia.) and an arc plasma is established between C_1 and the lower cathode (C_2 , 10 mm dia. \times 18 mm). The cathode mount (CM) is a water-cooled copper cylinder. The arc chamber (G) is made of a graphite cylinder 80 mm long with inner diameter of 6 mm and the gas is introduced into the arc chamber uniformly along the discharge axis from the distribution plenum (4 mm I.D.) which is arranged at the side of the arc chamber.

The electron bombarded cathode C_1 is the most important part for this type of ion source. As C_1 is heated by electron bombardment on the upper surface and emits many thermal electrons into the arc chamber from the lower surface, it is necessary to conduct heat effectively through C_1 block from the upper side to the lower. But by the radiation loss of heat from the surface in the face of the cathode mount (CM), temperature difference between the upper and the lower side is large. So, C_1 must be devised to operate as the thermal cathode without melting on the electron bombarded surface. In the present work, the cathode is made of tungsten, because of high melting point and large difference between the melting point and the temperature at which thermal electrons are emitted adequately, and because tungsten is sputtered poorly³⁾ by ion bombardment. A tungsten heat shield (HSH) is also put between C_1 and the cathode mount to reduce thermal radiation loss. To prevent undersired discharge between F and C_1 , the space around the cathodes is evacuated through two large holes of 30 mm in diameter, prepared into the stainless steel cases of upper and lower parts, respectively.

The ion source is supported by two stainless steel tubes with length of about 2 m and O.D. of 55 mm, and is inserted in the center of the cyclotron accelerating chamber. To prevent spark in the support tubes or in the end box of the support, the filament and cathode lead tubes are all covered with Steatite and Teflon in the support, and the end box is evacuated by the cyclotron vacuum system through the by-pass pipe. So, an arc voltage of 1 kV and an electron bombardment voltage of 2 kV can be applied at the same time without spark or glow discharge when the ion source is operated. The over-all height of source is 170 mm and the ion-extracting slit is rectangular, with an aperture of 12 mm \times 3 mm.

Heavy ions extracted from the ion source and accelerated in the cyclotron were N^{3+} , N^{4+} , N^{5+} , C^{3+} , N^{4+} , and O^{5+} , of which the yields were measured with a beam probe inserted from the side flange of accelerating chamber. For production of nitrogen ions, nitrogen gas and for carbon and oxygen ions, CO_2 gas were introduced to the ion source, respectively.

Figs. 3 (a) and 3 (b) show the variation of N^{4+} and N^{5+} yields with the gas flow rate at constant arc voltage and current. For obtaining a large quantity of multicharged ion yield it is very effective to reduce the amount of gas flow as small as possible to the

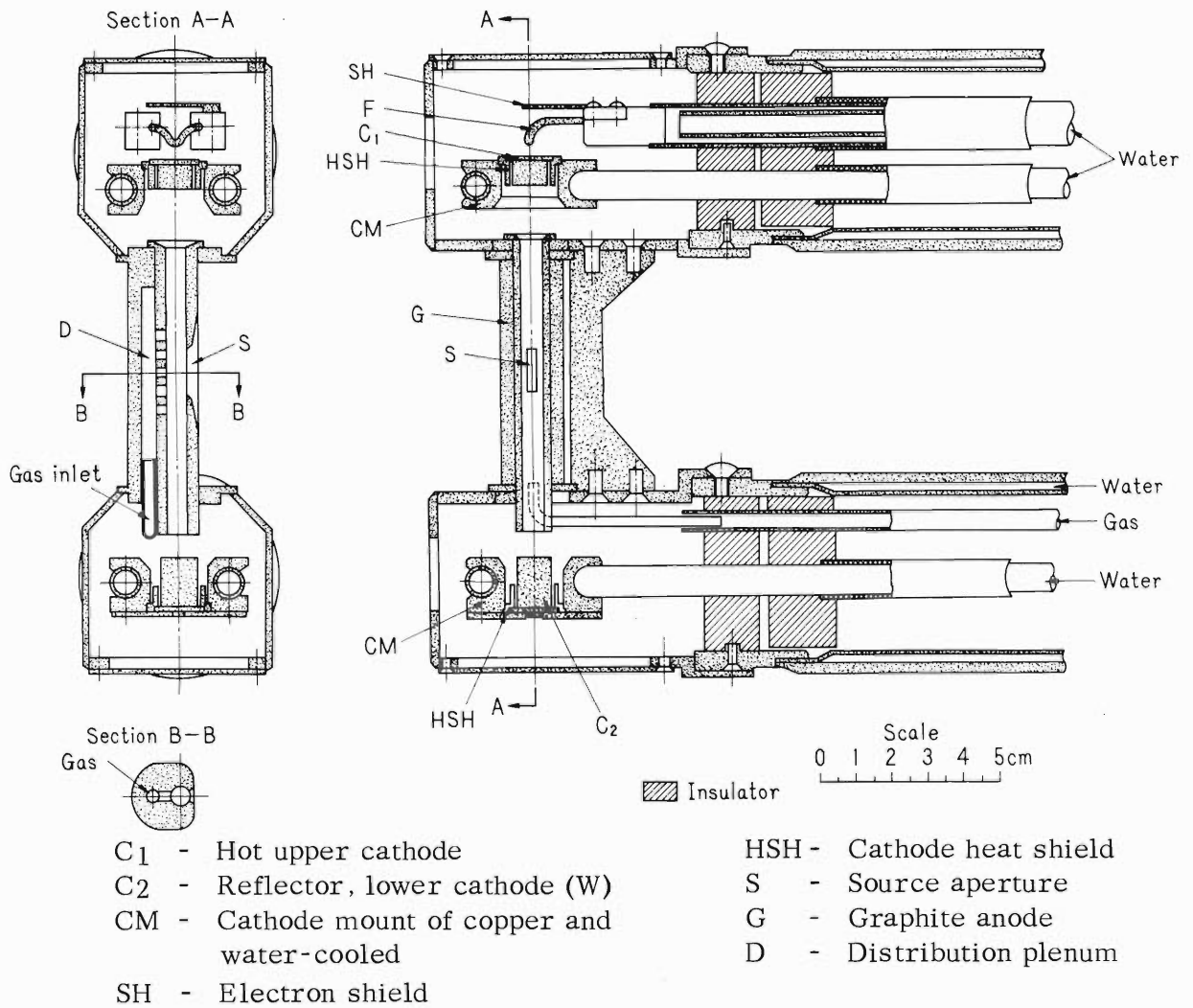


Fig. 1. Schematic view of the ion source.

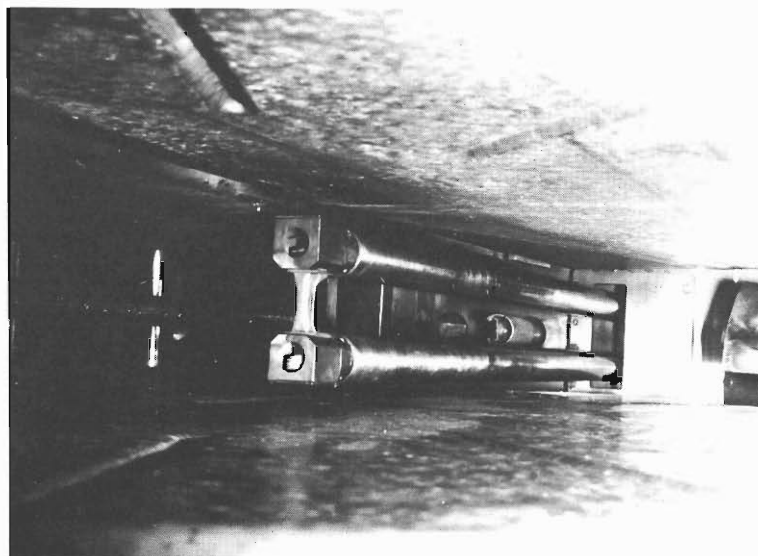
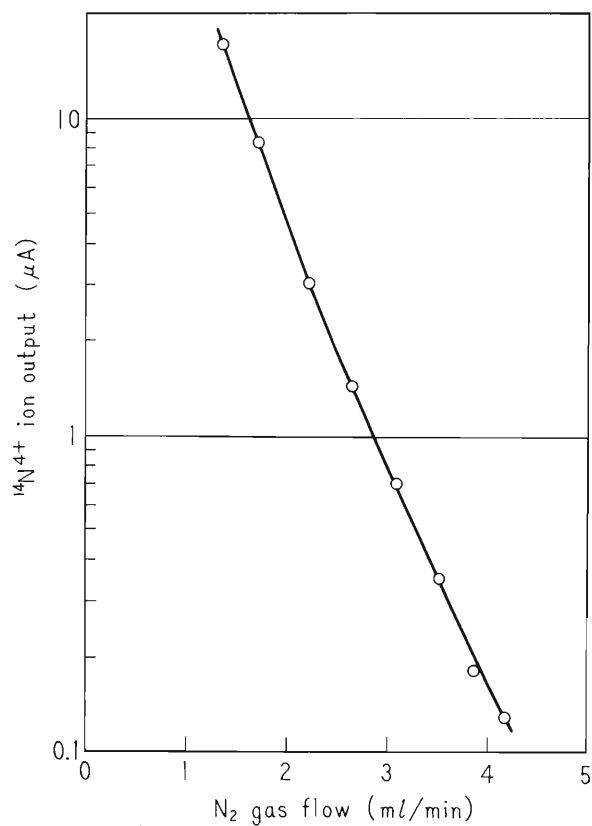
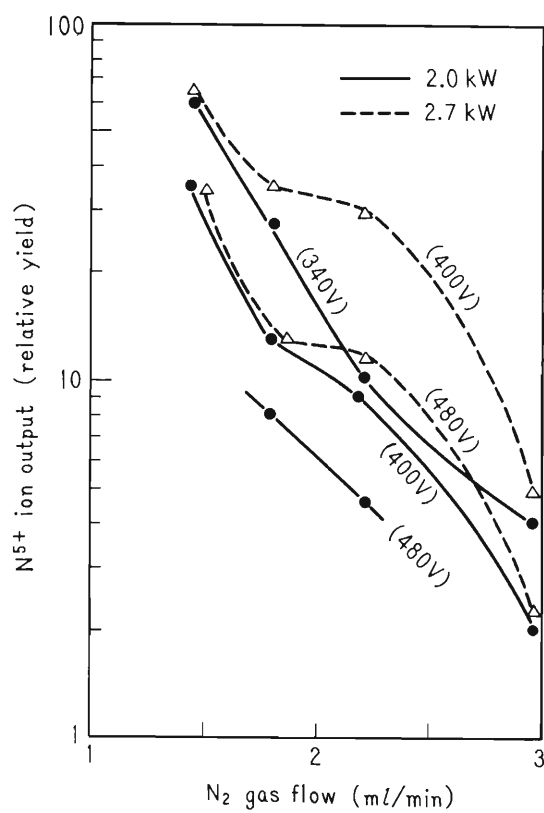


Fig. 2. Photograph of ion source inserted in the cyclotron accelerating chamber.



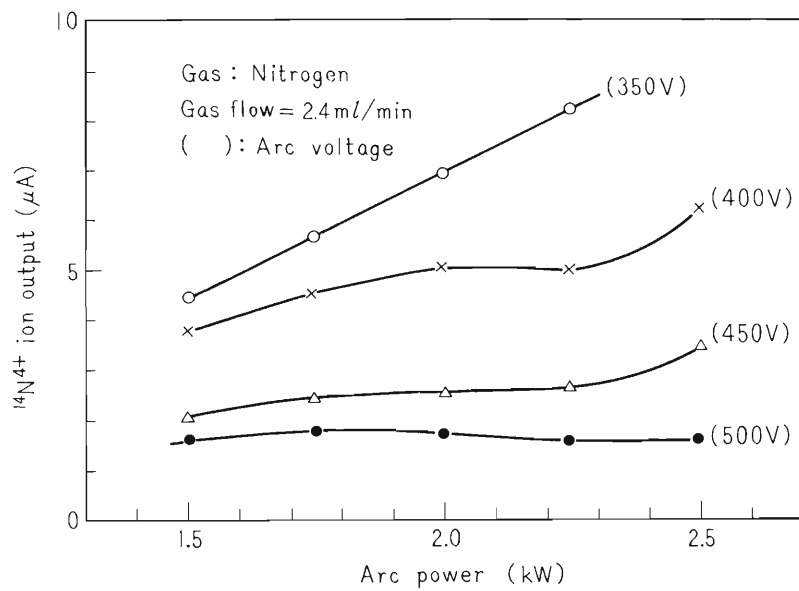
Arc voltage and current: 450 V and 4 A
 Dee voltages: 65 kV
 Radius of probe position: 65 cm
 Magnetic field strength: 16.1 kG
 Radio frequency: 6.99 Mc/sec

Fig. 3(a). N⁴⁺ ion yield vs. nitrogen gas flow rate.



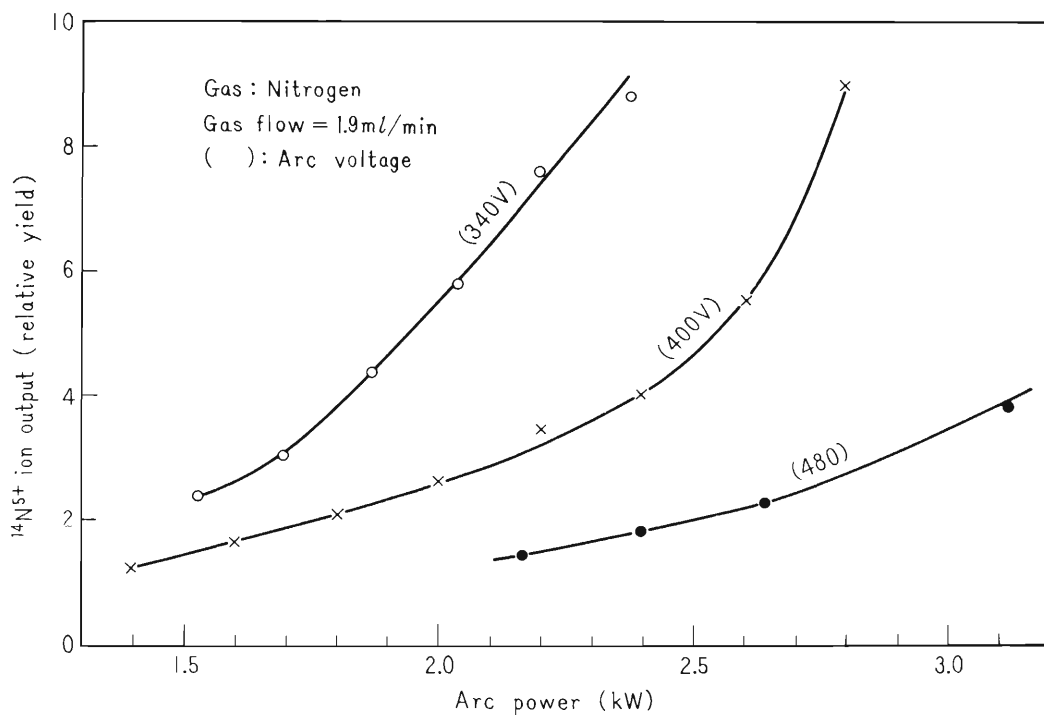
Arc power: 2.0 and 2.7 kW
 Dee voltages: 65 kV
 Radius of probe position: 85 cm
 Magnetic field strength: 12.7 kG
 Radio frequency: 6.93 Mc/sec

Fig. 3(b). N⁵⁺ ion yield vs. nitrogen gas flow rate.



Gas flow rate: 2.4 ml/min
Dee voltages: 65 kV
Radius of probe position: 65 cm
Magnetic field strength: 16.1 kG
Radio frequency: 6.99 Mc/sec

Fig. 4(a). N^{4+} ion yield vs. arc power.



Gas flow rate: 1.9 ml/min
Dee voltage: 65 kV
Radius of probe position: 85 cm
Magnetic field strength: 12.7 kG
Radio frequency: 6.93 Mc/sec

Fig. 4(b). N^{5+} ion yield vs. arc power.

degree that the discharge does not extinguish. As the larger gas flow rate is needed at the start of discharge, the gas flow is reduced after an arc was burned.

Fig. 4 shows the variation of N^{4+} and N^{5+} yields with the arc power and the arc voltage at a constant gas flow rate. Both N^{4+} and N^{5+} yields increased with the arc power, especially N^{5+} yield increased about five times for the arc voltage of 340 V when the arc power varied from 1.5 to 2.5 kW. When the arc power was kept constant, both yields increased with decreasing the arc voltage to about 350 V and increasing the arc current. The establishment of these arc conditions at the constant gas flow, was controlled by varying the electron bombardment power. In the case of C^{4+} , yield variations with the gas flow rate, the arc power and the arc voltage showed almost the same features as N^{4+} and N^{5+} . But the region of gas flow rate needed for discharge was narrower than in the case of N^{4+} or N^{5+} .

The life of the source was limited by the upper cathode erosion. When the source was operated at the arc power of 2.0 to 2.5 kW using nitrogen gas, the source life was 15 to 20 hours. But, the source was recovered after one hour by exchanging only the upper cathode C_1 . Cathode erosion depended remarkably on the alignment of the arc axis in the magnetic field.

References

- 1) I. Kohno et al.: J. Vacuum Soc. Japan, 10, 27 (1967);
IPCR Cyclotron Progress Report, Vol. 1 (1967).
- 2) P.M. Morosov et al.: At. Energ. (USSR), 2, 272 (1957).
- 3) O. Almen and G. Bruce: Nucl. Instr., 11, 257 (1961).

3-3. The Focusing Magnetic Channel

M. Odera, Y. Miyazawa, M. Hemmi, T. Tonuma, and O. Terajima

The aim and principle of the channel were described previously.¹⁾ The results of study of a scale model (1 : 3) and the practical design were also given there.

The channel was installed in the acceleration chamber in Nov. 1967. Its position can be adjusted from outside of the chamber through vacuum-tight O-ring seals. Fig. 1 is a photograph of the channel at its site.

The disturbance of the magnetic field induced by the channel in the gap of the main magnet was measured. Fig. 2 shows the result. It decreases faster than the inverse square of distance from the channel. The rate of decrease is somewhere between the values given by the inverse square law for an infinitely long bar and by the inverse cube law for a sphere. At $R = 60$ cm the azimuthal "bumps" cannot be distinguished already from that originally existing in the main magnetic field. The disturbance of field induced by the channel gives hardly bad effect in the main field where the acceleration of the ions are made. Any compensation measures were not taken and the beam came out in the expected trajectory.

The beam quality was measured at the exit of the acceleration chamber by several methods. The first was an array of graphite plates, permitting quick centering of the beam. Secondly, light sensitive di-azo papers used ordinarily for the duplication of documents were exposed to the beam and then developed. Their low sensitivity to room light, ease of development and direct representation of the beam intensity distribution helped us very much to judge the quality of the beam. Fig. 3 shows some of the profiles taken in this way: (a) is taken from H_2^+ without the channel. The beam spreads out in the full width of the window. The shadow near the center serves for the measurements of the beam direction. (b) is obtained by He^{++} with the channel of the initial length. The focusing effect is excessively strong. This was expected since the length of the iron bars were chosen somewhat longer under the condition of vague knowledge of the emergent beam from the deflector canal. The bars were simply cut off and the profiles were taken again. (c) is the image of the H^+ beam after the channel is shortened by 20 cm. This gives a slightly divergent beam which can be easily handled by the beam transport system. Thirdly we used several combinations of transversely travelling needle probes placed apart along the beam pipes.

After making these measurements and some adjustments of positions of the channel, the intensity of beam at the entrance of the beam transport system amounted to from 60 to 90% of that emerged from the deflector channel. Thus, over ten μA of proton, deuteron, α and 3He beams could be utilized at the outside of the acceleration chamber. Also the extraction of multiple-charged heavy ions became efficient. The course of beam was essentially the same over all the range of energies and particles used. Any readjustment was not required throughout.

Moreover, the activation of the acceleration chamber and beam pipes near the exit window is decreased. The channel itself hardly suffers activation, except the small graphite pieces which detect the beam current and protect the iron from beam hitting. Most halflives of activities induced in graphite are generally short except that of 7Be . By partially covering with a copper plate the channel requires no cooling in spite of its proximity to the dee.

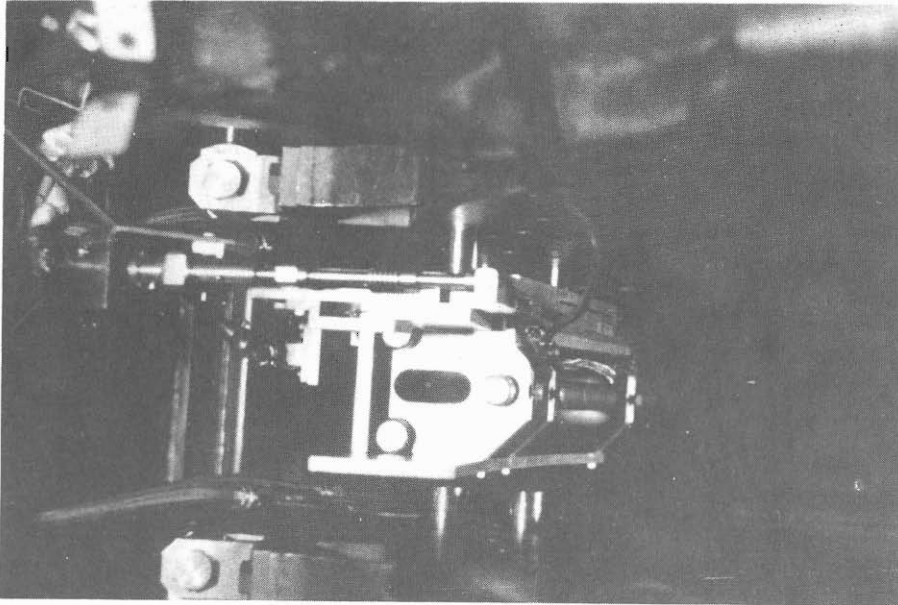


Fig. 1. Photograph of the channel placed in the acceleration chamber.

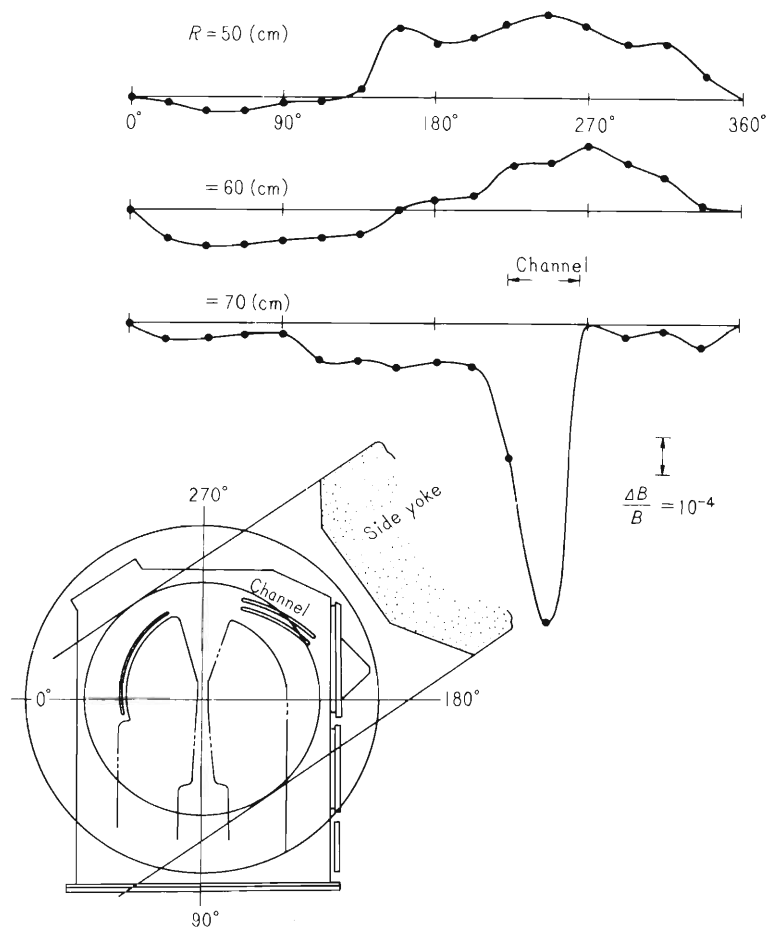
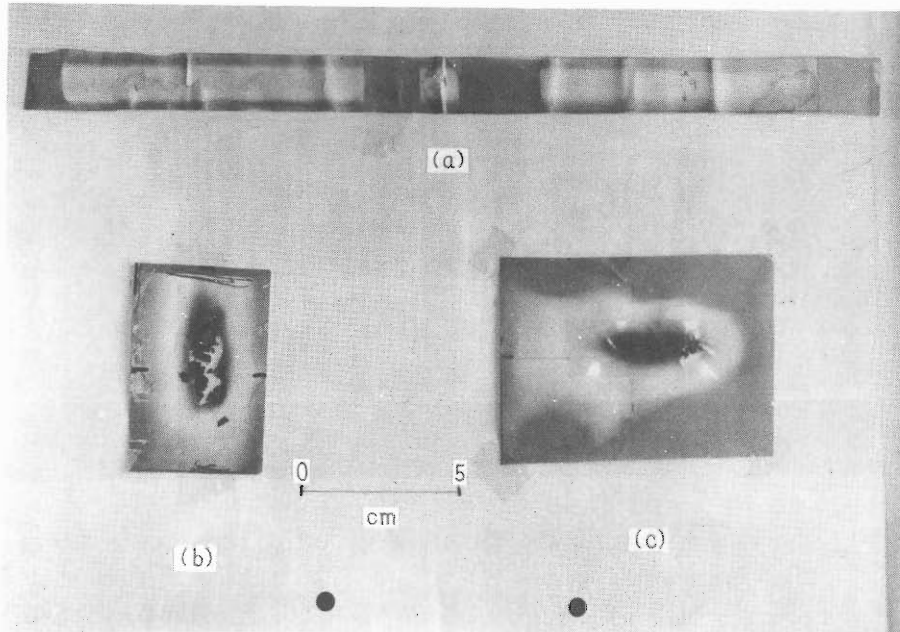


Fig. 2. The azimuthal non-uniformity in the field of the main magnet. Those of $R = 50 \text{ cm}$ and 60 cm are the same with that present before the channel is installed.



- (a) H_2^+ 18 MeV, without the channel. Beam spreads out in the full width of the port 24 cm.
 (b) He^{++} 28 MeV. With the channel of initial length of 80 cm.
 (c) H_2^+ 14 MeV shortened channel. Length : 60 cm.

Fig. 3. The profiles of the beam at the exit port of the acceleration chamber.

Reference

- 1) M. Odera, Y. Miyazawa, M. Hemmi, T. Tonuma, and O. Terajima: IPCR Cyclotron Progress Report, 1, 19 (1967). Also, by the same authors including the results described here; Nucl. Instr. Methods, 65, 247 (1968).

4. ACCELERATOR PHYSICS

4-1. Initial Motion of Ions

T. Karasawa, T. Tonuma, A. Shimamura,
T. Inoue, and Y. Miyazawa

In this year, accelerator physicists and engineers mainly devoted their efforts to acceleration of multicharged heavy ions. Study of initial motion was done during a few days of cyclotron machine time. In this paper, all experimental results are concerned with acceleration of proton with energy of 7.2 MeV at the maximum radius.

Comparison of beam behaviors between ions extracted from ion source by usual feelers and feelers with grid was made. The grid was attached at the center of west dee and the arrangement of the wire grid is shown in Fig. 1. Thick copper plate (10 mm) and tungsten wire of somewhat large diameter (2 mm) assured geometrical accuracy and withstood high beam currents. Arrangement of usual feeler is shown in the IPCR Cyclotron Progress Report 1967, page 26.

Beam attenuation curves for 7.2 MeV proton are shown in Fig. 2. The feelers with grid may reduce vertical beam spread and the attenuation of beams at the radii from 35 cm to 50 cm by the usual feelers does not appear for the ions extracted by the feelers with grid. Causes of the attenuation at the radii below 35 cm for ions extracted by the feeler with grid are not ascertained at present. The attenuation at the radii from 65 cm to 71 cm for the ions extracted by the usual feelers disappears by phase selection, at which the ions leave from the ion source. A screen made of copper plate is attached as shown in Fig. 3(a) and ions left at later phase are removed by the screen. Attenuation curves of beams with and without the screen are shown in Fig. 3(b). The attenuation at the radii from 65 cm to 71 cm on the main beam probe may be explained by beam precession, in which ions left at later phase have an instantaneous orbit center displaced largely from the magnetic center and reach the exit slit, disregarding that the ions have a radius larger than 65 cm on the main beam probe.

Resonance curves are shown in Fig. 4. In the figure, the beam intensities at lower frequencies are independent of the radii below 72 cm. These beams give a flat attenuation curve at these radii as shown in the curve of feelers with grid.

Shadow technique is applied using with a stem probe which is installed at about 180° clockwise to the main beam probe. According to the shadow technique, radial width for the deflected beam at maximum radius is about 5 mm.

The beam intensity and dee voltage with parameters of ion source conditions are shown in Fig. 5 and usual operation is done with dee voltage between 25 kV and 30 kV.

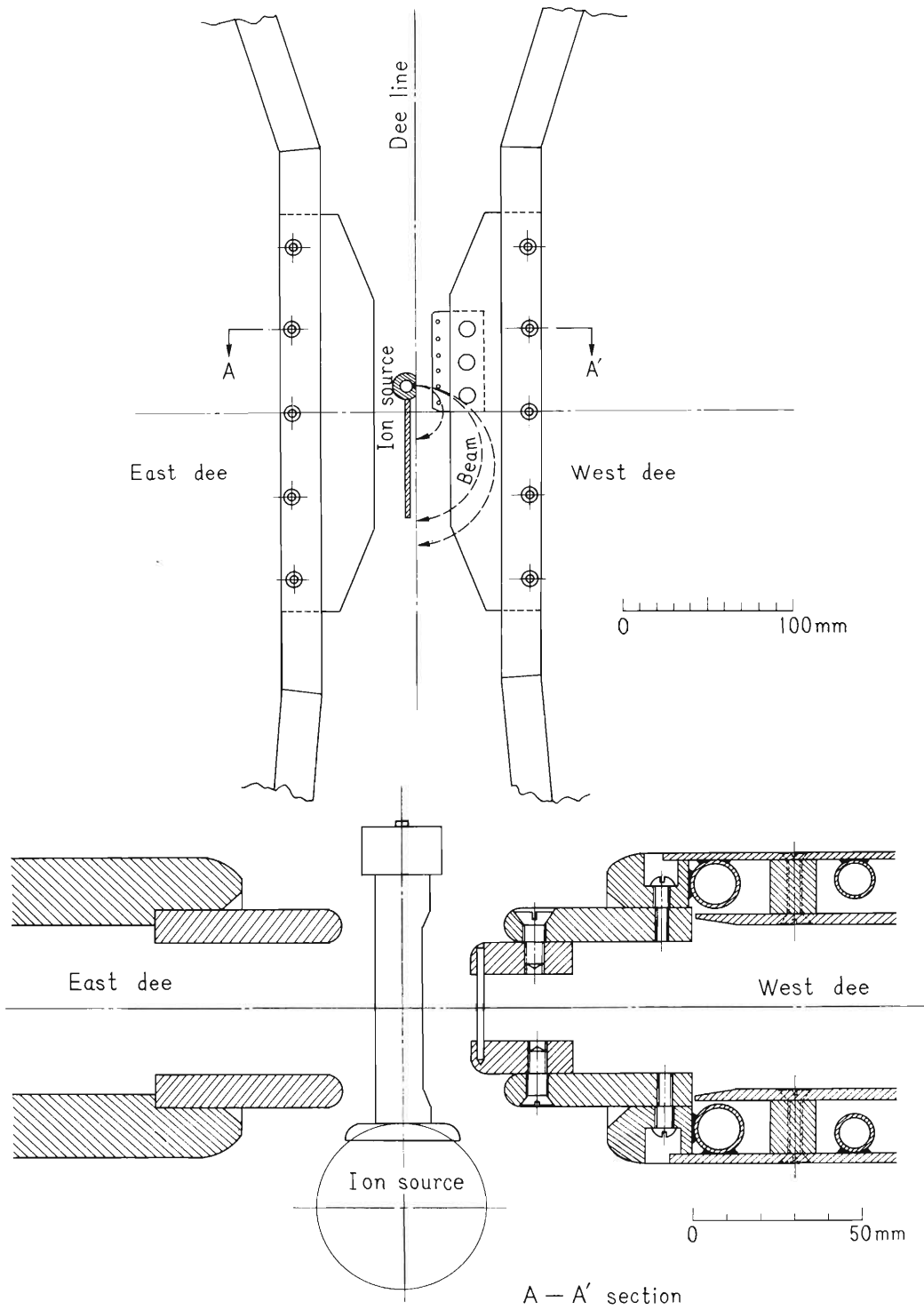


Fig. 1. Feeler with grids.

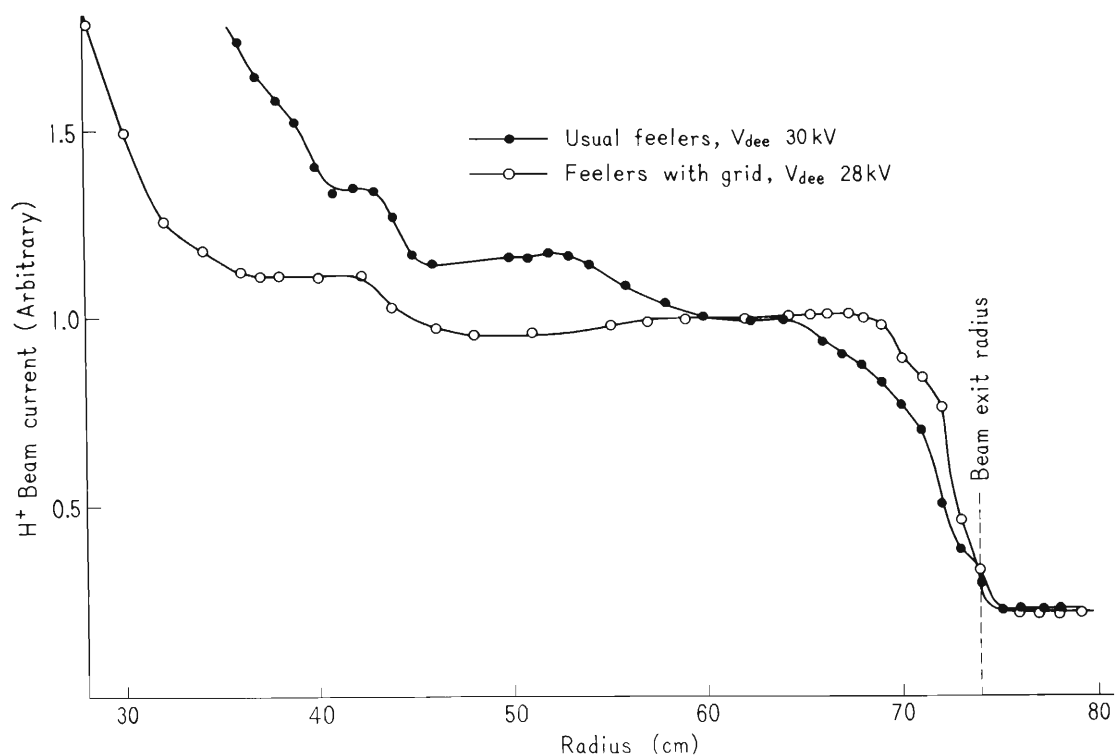


Fig. 2. Beam attenuation curve.

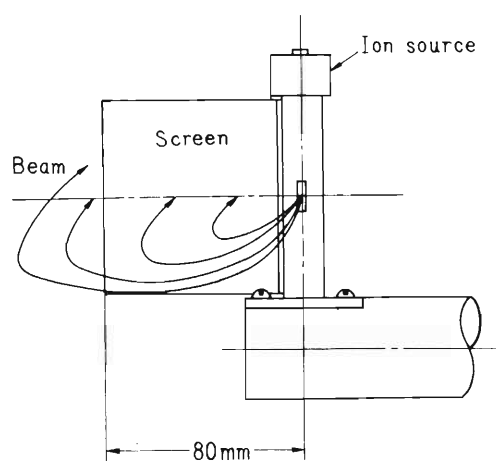


Fig. 3 (a).

Ion source attached with screen.

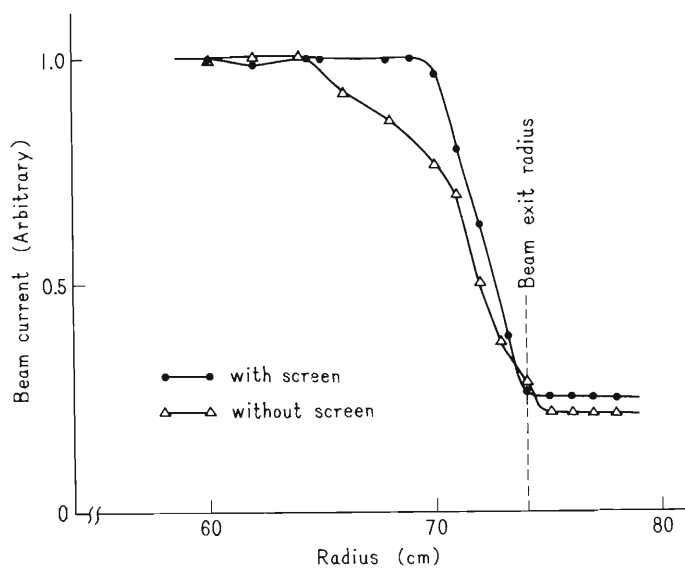


Fig. 3 (b).

Attenuation curve with usual feeler.

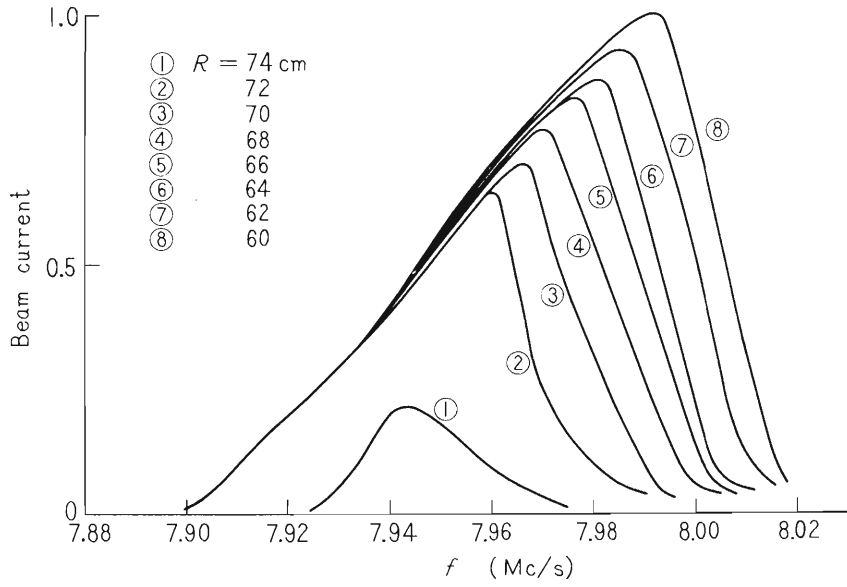


Fig. 4. Resonance curve.

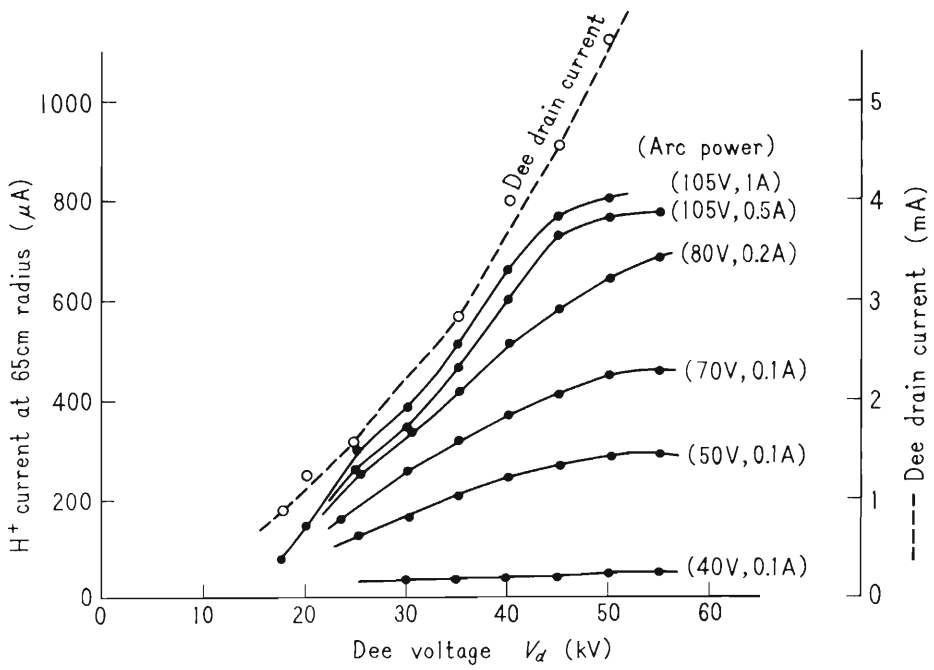


Fig. 5. Beam intensity vs. dee voltage.

4-2. Heavy Ion Acceleration

I. Kohno, Y. Miyazawa, T. Tonuma, S. Nakajima, T. Inoue,
A. Shimamura, K. Yoshida, T. Inamura, and T. Karasawa

Acceleration of multicharged heavy ions has been tried in the IPCR 160 cm cyclotron since fall, 1966. The energy region of various ions accelerated in the cyclotron at present is shown in Table 1 and Fig. 1.

Table 1.

	$^{12}\text{C}^{3+}$	$^{12}\text{C}^{4+}$	$^{14}\text{N}^{4+}$	$^{14}\text{N}^{5+}$	$^{16}\text{O}^{5+}$
T(MeV)	45 ~ 70	45 ~ 120	50 ~ 100	50 ~ 160	88
Current* (μA)	5	3	4	1	0.08

* Peak ion current measured by gate drop probe.

In Fig. 1, wide solid lines show the kind of ions which can be extracted from the cyclotron and their energy region, and the wide dotted line shows the ion which could be accelerated to the maximum radius but could not be extracted from the cyclotron. N^{3+} ion could not be extracted from the cyclotron because a high deflector voltage required could not be applied. N^{4+} , N^{5+} , and C^{4+} ions were accelerated successfully and used for experiments on nuclear reactions, but O^{5+} ion could not be accelerated stably. The beam current of ions that have the mass to charge ratio of more than 4 and are accelerated by the third harmonic was large enough, but these ions could not be extracted from the cyclotron because of the RF-deflector in which the dee voltage only is applied as the deflector voltage. The maximum energy of heavy ions is limited by electric field strength of a deflector channel between a deflector and a septum. It is well known that the electric field is typified by $V \cdot E$ numbers. The highest dee voltage without breakdown by discharge between a deflector and a septum, was often measured during operation. The maximum $V \cdot E$ number obtained is about $17000 \text{ (kV)}^2/\text{cm}$ at present. In the ordinary cyclotron, the minimum dee voltage is determined under conditions of maximum and minimum phases of the dee voltage when the ion crosses the dee gap. The calculated results are shown in Fig. 2 for maximum and minimum phases of $+60$ and -60 degree, respectively. In the region of low RF-frequencies, the dee voltage described in Fig. 1 could not be applied for discharge between the dee and the dee liner when some ions of large m/q were accelerated.

In the case of acceleration of multicharged heavy ions a higher dee voltage must be applied as compared with the acceleration of p, d, and α ion beams, and the charge exchange loss of ion beam must be reduced in the way of travelling in the cyclotron. For these reasons, the accelerating chamber must be kept at high vacuum as much as possible. Details of several machine improvements for applying the high dee voltage and obtaining the high vacuum are described in Section 3-1. At present, the vacuum pressure is about 5×10^{-6} Torr under the operating condition.

The ion source is designed in the electron bombarded hot cathode type similar to that described by Morosov et al. Its construction and operating conditions are reported in Section 3-2.

The m/q spectra were measured with a beam probe fixed at the radius of 65 cm by varying the magnetic field. The spectrum when N_2 gas was fed in the source is shown in Fig. 3(a), in which 3rd and 5th mean the numbers of harmonics. Large carbon (C) peaks are found as well as nitrogen (N) peaks and some oxygen (O) ions are detected. C peaks are supposed to come from a graphite cone of the ion source or oil vapor of the vacuum pump. The spectrum in Fig. 3(b) is that when CO_2 gas was fed in the source. Only C and O peaks are found in this case. Resonance curves of N^{3+} and N^{4+} ion beams measured at several radii are shown in Fig. 4 and Fig. 5 respectively. In Fig. 4 the broad resonance at the higher radio frequency is that of N^+ ion beam which has been accelerated by the 3rd harmonic. In Fig. 6 the N^{4+} ion beam intensity is reduced to about one-third in the way of passing from 40 to 70 cm. This feature was compared with the change of He^{++} beam intensity when both ion beams were passed in the same orbit, and in Fig. 7 both intensity changes are shown. The intensity decrease of N^{4+} ion beam is larger than that of He^{++} ion beam by about 3 times. The He^{++} is an all charge stripped ion and its charge state is not exchanged by the collision with the residual gas at high energy, but the charge state of the N^{4+} is exchanged from N^{4+} to N^{5+} , N^{6+} , and N^{7+} . So the intensity decrease is supposed to be due to the charge exchange loss. I.S. Dmitriev et al.¹⁾ measured the cross sections of some ions, such as nitrogen and carbon ions, for charge exchange with some gas molecules. But their data cannot be applied to our case as the incident energy is lower by one order. Therefore, we will measure the cross sections of the high energy N and C ions for charge exchange with air or some gases.

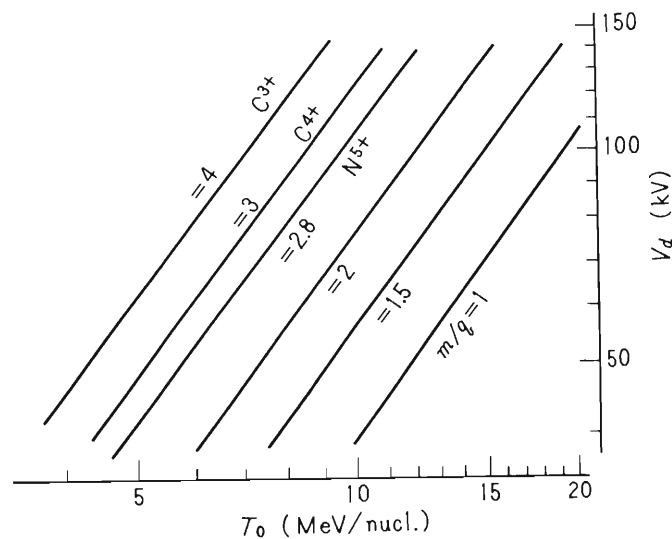


Fig. 2. Relation between dee voltage and energy for various ions.

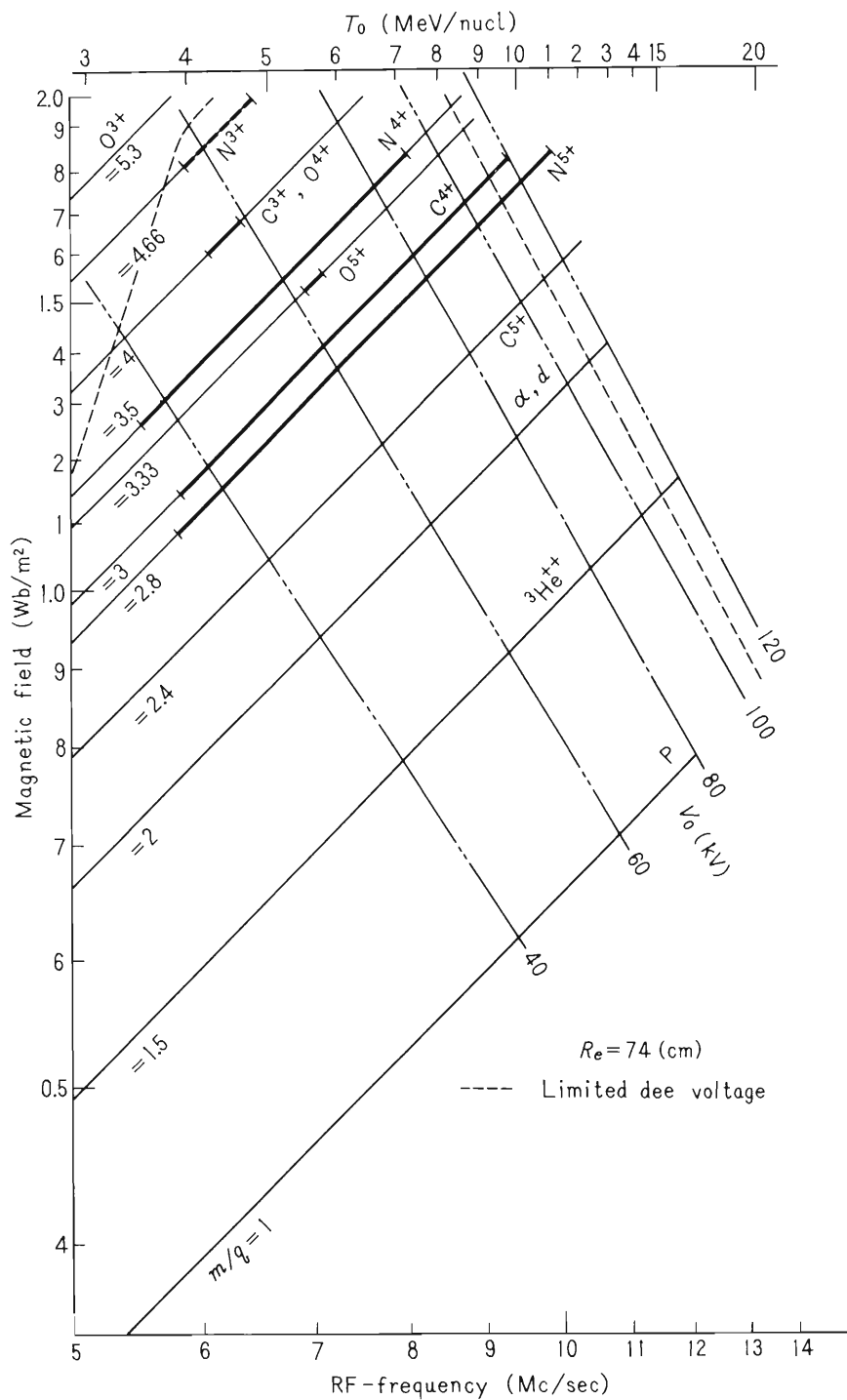


Fig. 1. Resonance condition for various ions in the IPCR 160 cm cyclotron.

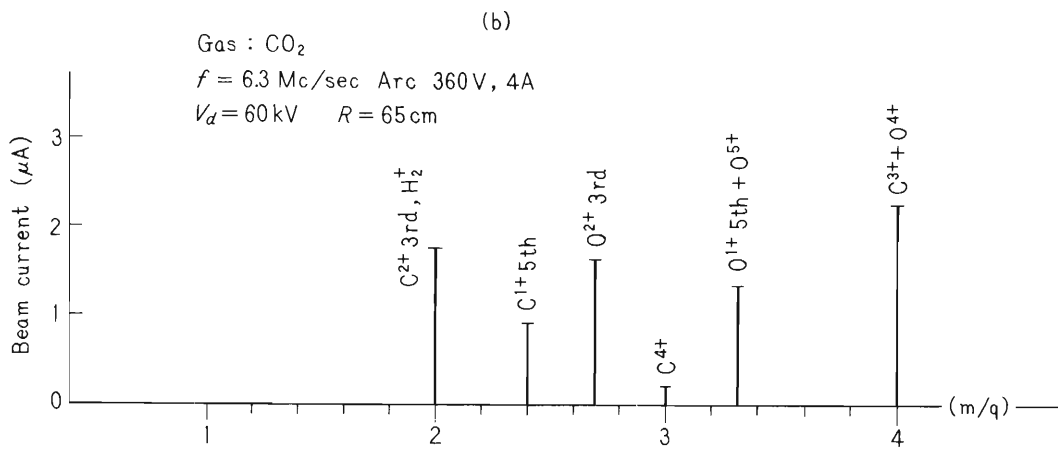
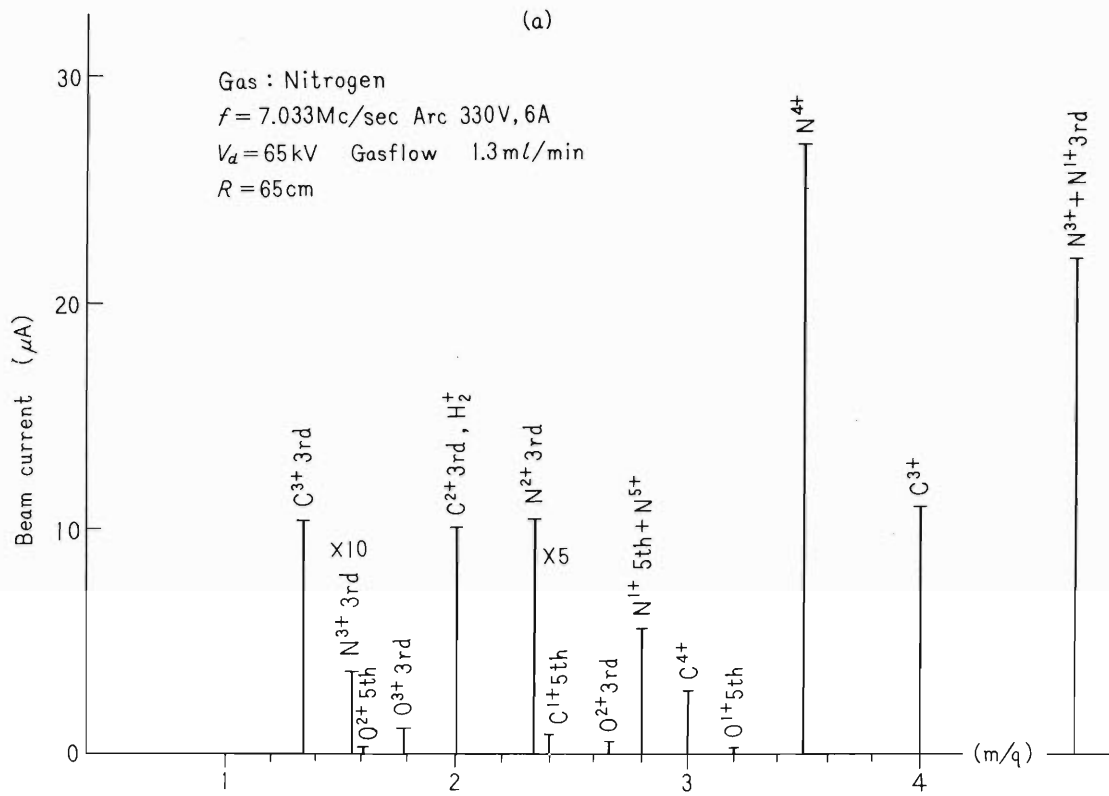


Fig. 3. Spectrum m/q of various ions.

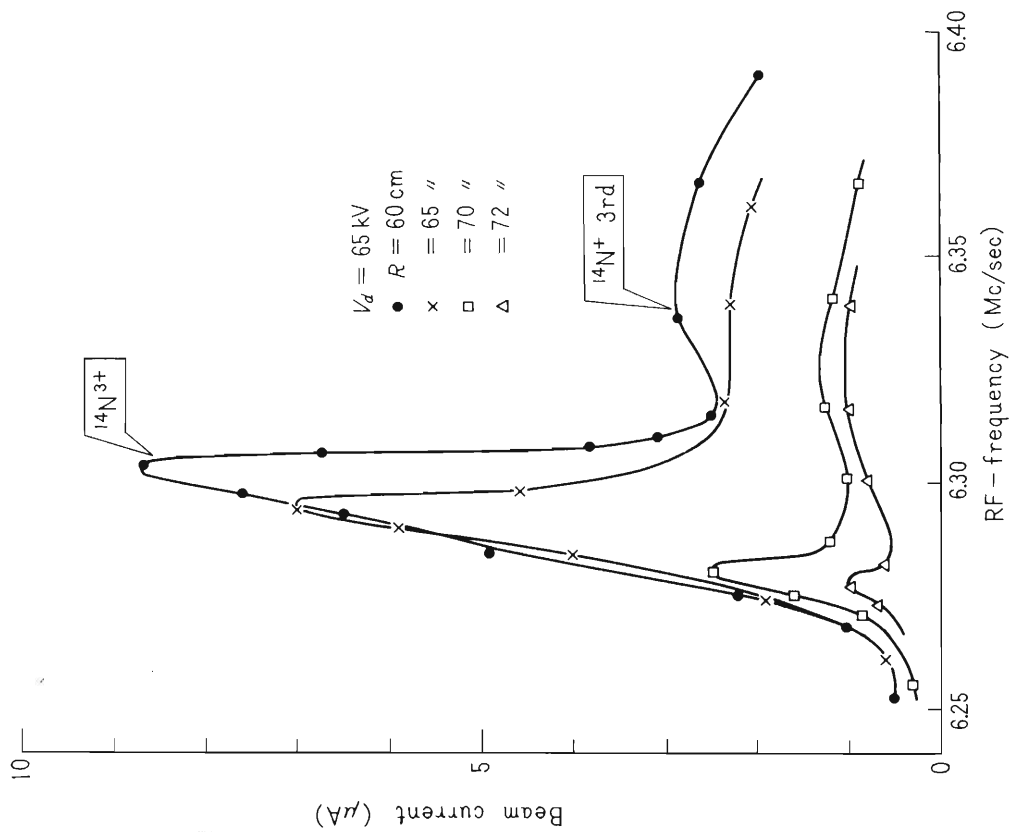
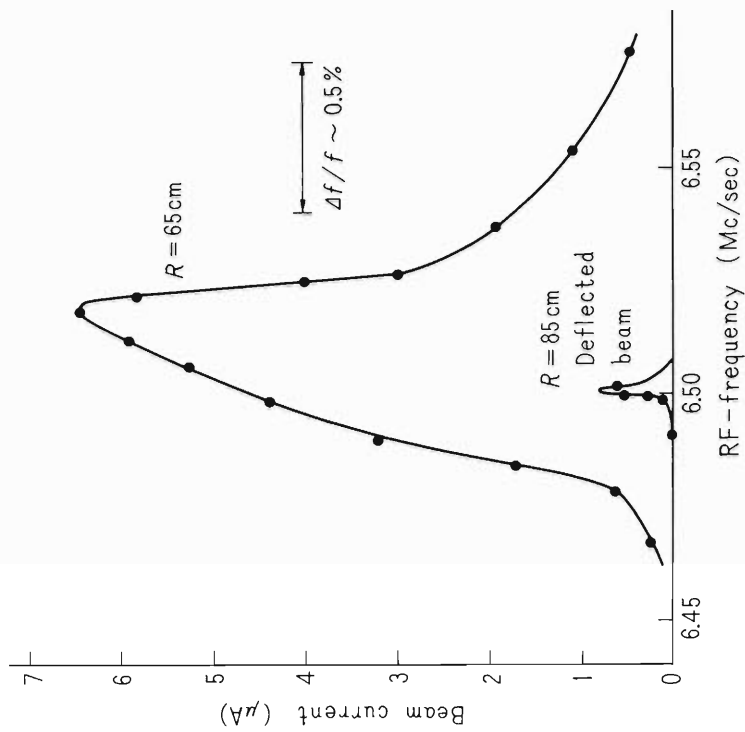
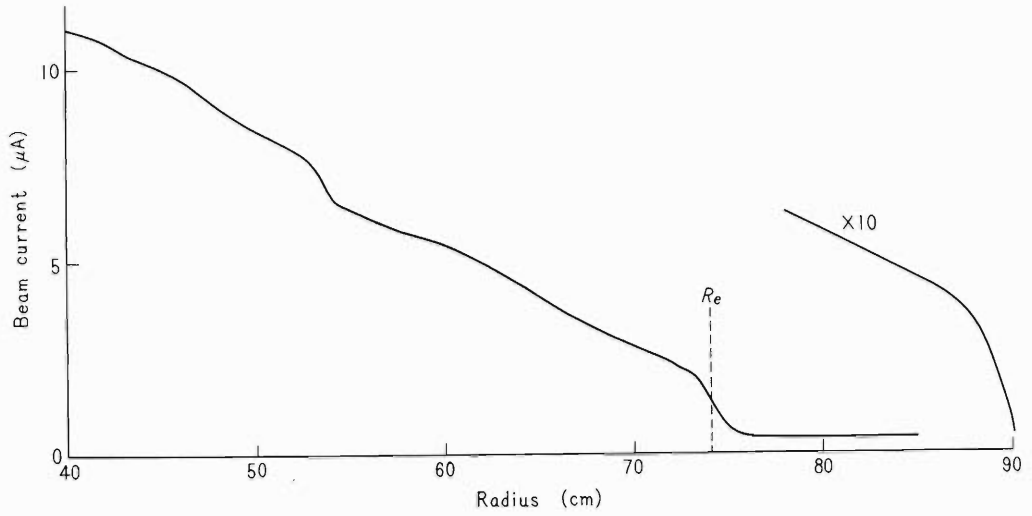


Fig. 4. Resonance curves of the N^{3+} ion beam and third harmonic accelerated N^+ ion beam.



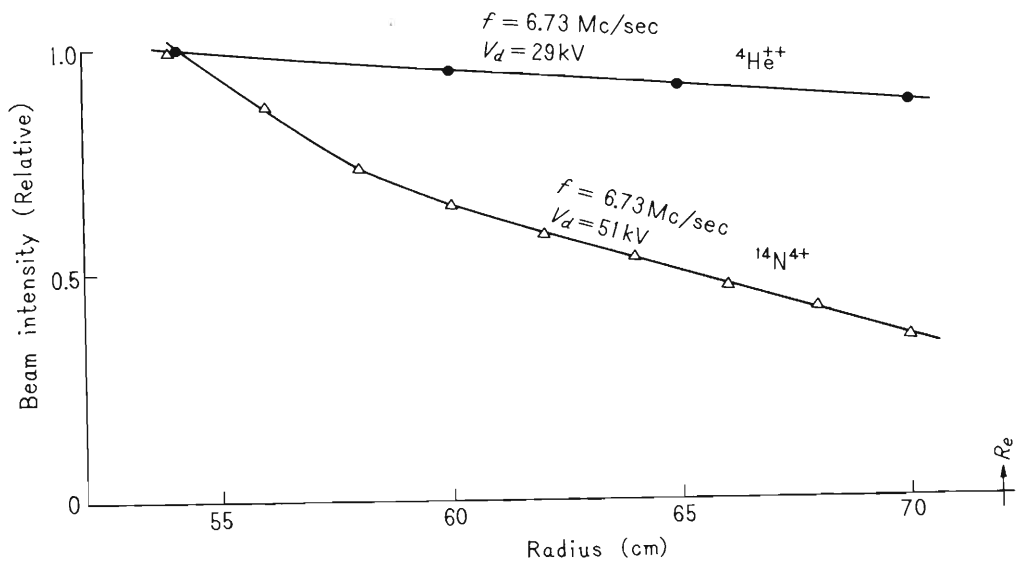
$V_d = 66 \text{ kV}$.

Fig. 5. Resonance curves of N^{4+} (66.5 MeV) ion beam vs. radius.



$V_d = 66 \text{ kV}$, $P = 8 \times 10^{-6} \text{ Torr}$, arc power = $440 \text{ V} \times 4 \text{ A}$,
gas flow = 2.8 ml/min .

Fig. 6. Typical plots of N^{4+} (66.5 MeV) ion beam vs. radius.



$P = 1.5 \times 10^{-5} \text{ Torr}$.

Fig. 7. Ion beam attenuation of N^{4+} and He^{++} ion beams.

Reference

- 1) I.S. Dmitriev et al.: JETP (Sov. Phys.), 15, 11 (1962).

4-3. Investigation of Electromagnet On the Energy Reproducibility in Magnetic Analyzers

S. Motonaga, N. Nakanishi, M. Hemmi, and K. Matsuda

In a beam analyzing magnet it is very important to reproduce the magnetic field distribution for a given beam energy.

Since

$$P \propto \int B ds$$

where P , B , and ds are linear momentum of analyzed beam, magnetic field strength of the analyzing magnet, and small increment along the beam path, respectively. It is inadequate to reproduce only the field strength accurately. The same turn-on procedure should be employed, as the field distributions along the beam path are different by the magnet turn-on procedure, that is, whether the current is raised from zero to a desired value or is lowered from a higher to the value.¹⁾ Snelgrove et al. reported the effect of the turn-on procedure was less than 1 part in 15000 using the 45° beam analyzing magnet with cylindrical poles of Michigan State University.²⁾

We have been tried the measurement of the radial distribution of magnetic fields and effects of the turn-on procedure using a edgeless-type magnet³⁾ with pole base dia. 720 mm and pole gap 87.95 mm. Fig. 1 shows the magnet layout.

Magnetic fields were monitored with a nuclear magnetic resonance probe which was positioned near the magnet center. Two Hall generators⁴⁾ were employed to measure the field distributions. One of them was positioned at the magnet center and the other was slid along the radial direction with a motor driven mechanism. The difference of their outputs was drawn on a X - Y plotter.

Fig. 2 shows the radial distributions of magnetic fields for the central field strength of 0.5, 1.0, and 1.5 Wb/m² by different setting procedures. Procedure I is to raise the field from zero to each of given values. Procedure II is to raise the field from zero to the maximum value, 2.1 Wb/m², to wait for 30 min and to lower the field to given values.

Fig. 3 shows the difference in the case of field strength at 0.5 Wb/m². The difference of outputs by the procedures I and II was negligibly small in the radial region less than 250 mm, but it appeared in the outer region. We estimated $\Delta P/P \approx 2.5 \times 10^{-3} \pm 6 \times 10^{-4}$ based on the results obtained. There may be some reasons, that is, (a) hysteresis effect due to local difference of flux density induced by the fact that the base region of the magnet pole piece used is substituted a cylindrical type for the edgeless one, (b) local difference of remanence due to various magnetic circuits.

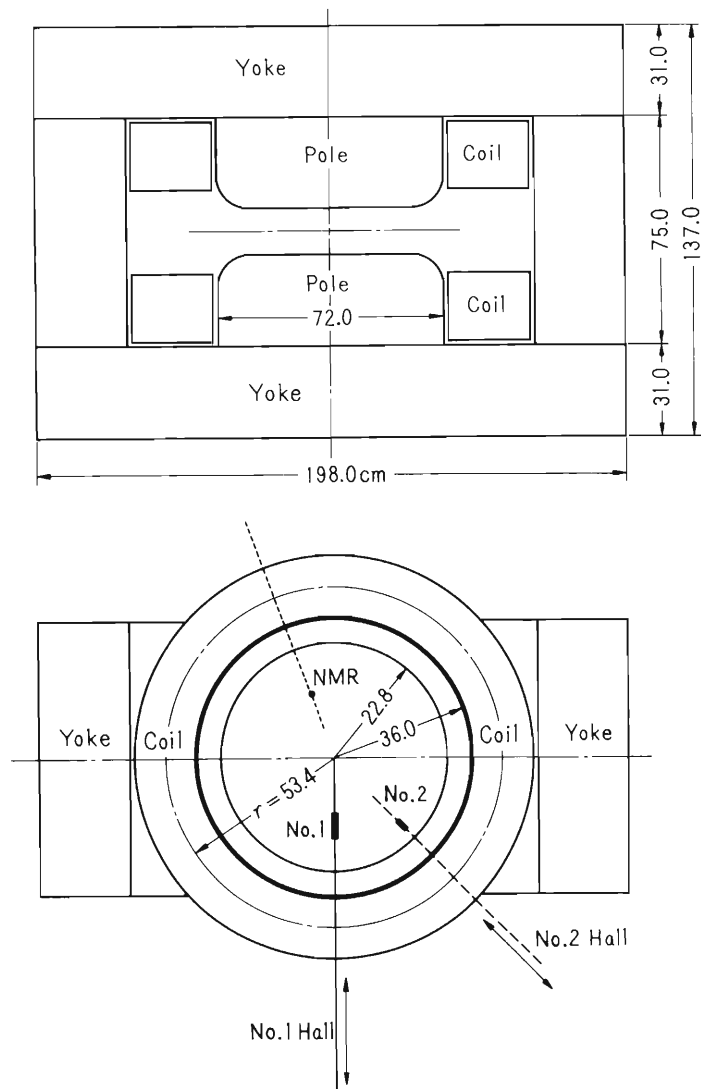


Fig. 1. Layout of 720 cm magnet used in the experiments.

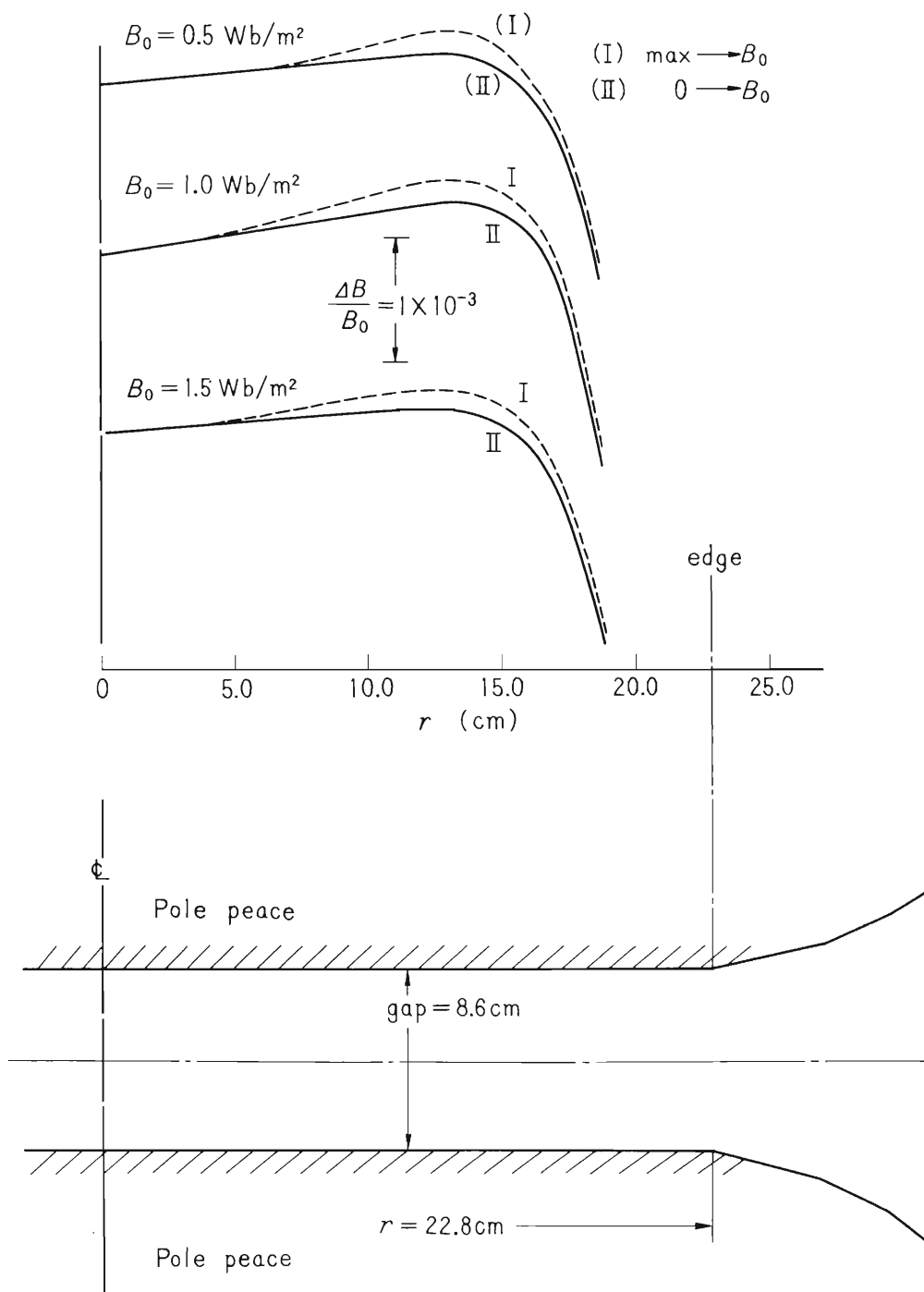


Fig. 2. Radial distributions of magnetic field. Solid and broken lines show those due to procedures I and II, respectively.

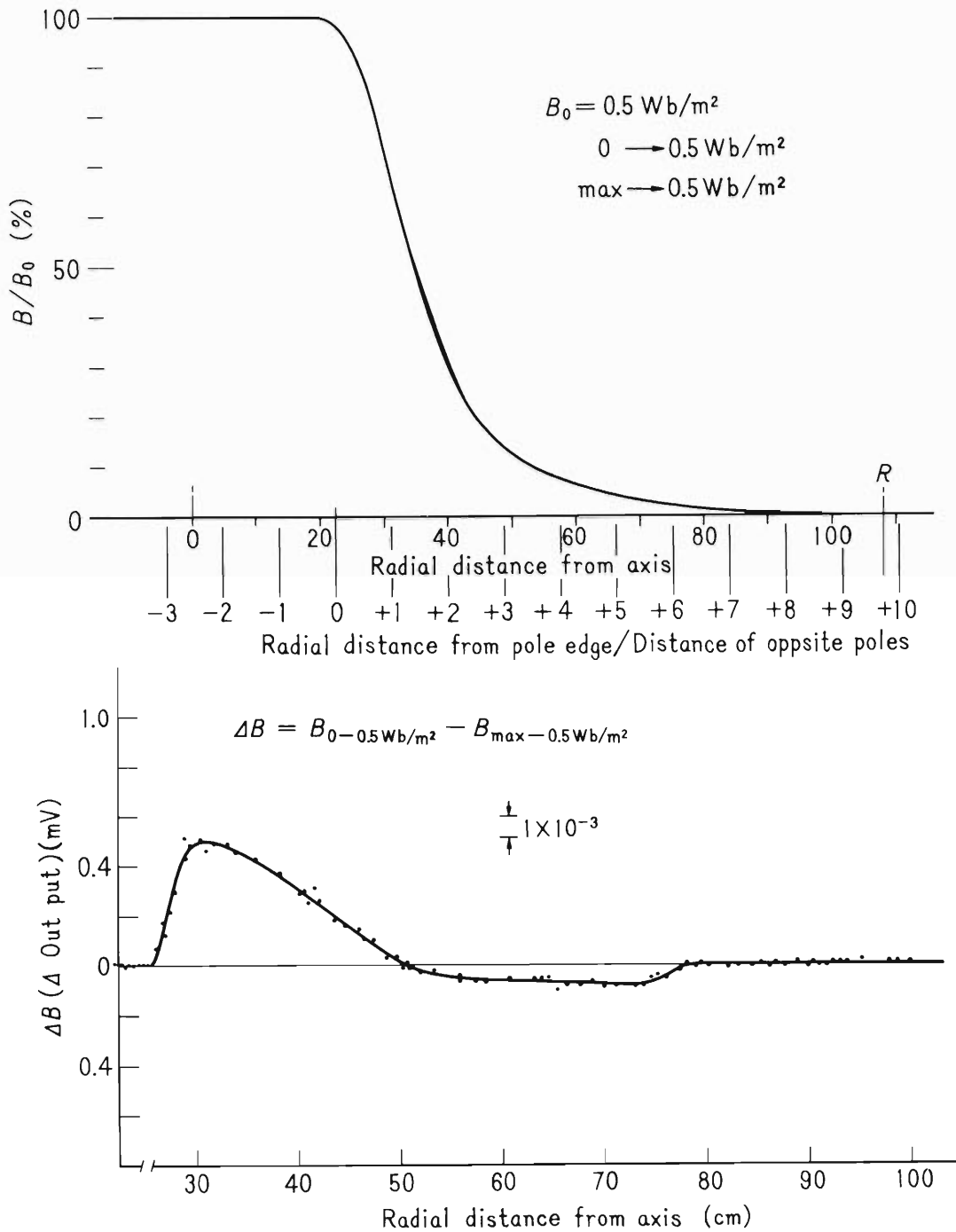


Fig. 3. The upper view shows the difference of field strength due to the procedure I and II, and the lower over all radial distribution of the magnetic field at field strength of 0.5 Wb/m^2 .

References

- 1) S. Motonaga, K. Matsuda, N. Nakanishi, M. Hemmi, and H. Kumagai: IPCR Cyclotron Progress Report, 1, 29 (1967).
- 2) J.L. Snelgrove and E. Kashy: Nucl. Instr. Methods, 52, 153 (1967).
- 3) T. Karasawa, S. Motonaga, Y. Miyazawa, N. Nakanishi, M. Hemmi, and H. Kumagai: Proc. Intern. Symp. Magnet Technol., p. 239 (1965).
- 4) M. Hemmi, T. Karasawa, and S. Motonaga: *ibid.*, p. 472.

4-4. Energy of Cyclotron Beam Estimated by Radio Frequency

T. Karasawa

Cyclotron operators are often demanded to estimate ion energy as precisely as possible. When the value of energy for some kind of particle is given, it is feasible to determine it from the radio frequency at dee.

During these two years of cyclotron operation, the ion energy used in nuclear reaction experiments was determined by beam analyzing magnet and radio frequency at dee as shown in Table 1 and energy spectra of alpha particles obtained by the beam analyzing magnet are shown in Figs. 1 (a), (b), (c), and (d).

The ion energy can be approximately expressed by the following equation:

$$E = K \cdot f_e^2,$$

where E is ion energy in MeV, f_e is radio frequency in MHz and K is a constant depending on the particle.

Now, we find out discrepancy between actual ion energy and the value given by the equation. In the cyclotron, the radio frequency is proportional to the velocity of ions at the maximum radius on the assumptions mentioned below:

(a) Relativistic mass increase is trivial, (b) dee voltage is proportional to energy for the same ratio of mass to charge, (c) it is proportional to the ratio of mass to charge for the same ion energy per nucleon. When the relativistic mass increase is not small, a phase shift of ions during acceleration in the ordinary cyclotron introduces some complicated problems, but a discrepancy in proportionality between radio frequency and ion velocity at the maximum radius is found to be below 0.5 % by theoretical consideration. The discrepancy between the calculated ion energy by the equation and the actual value is mainly due to change of the maximum radius of ions caused by beam precession. In Table 1 (a) we get the average value of K for ${}^3\text{He}^{++}$ as 0.323 ± 0.004 . This value of K corresponds to the ion energy at the maximum radius of 728 mm. Now, we could calculate the values of K for proton, deuteron, and alpha particle, obtaining 0.108, 0.215, and 0.428 respectively. In Table 1 (b), the experimental results for other particles are shown. In the cases of deuteron and alpha particle, the values of K are less than those obtained by calculation. These particles may be affected by precession more than normal ones.

Energy spread of deflected beam can be determined from the spectrum obtained by the beam analyzing magnet as shown in Fig. 1. It is below 1 % at FWHM for normal operation. The wide spread of ion energy may be caused by irregular acceleration, in which two beams accelerated on slightly different radii at the entrance of septum may be deflected.

It is thus concluded that ion energy estimated by radio frequency is accurate within an error of 2 % under normal operation.

Table 1 (a).

 $(^3\text{He}^{++})$

f_e (MHz)	B_a (Wb/m ²)	E (MeV)	K	Date*
10.84	0.4848	38.50	0.3248	70730
10.20	0.4574	34.29	0.3297	71021
10.19	"	"	0.3302	71003
9.607	0.4236	29.43	0.3190	81011
9.608	0.4228	29.34	0.3179	81011
9.510	"	"	0.3245	81022
9.170	0.4073	27.22	0.3239	81028
9.12	"	"	0.3274	71021
8.89	0.3934	25.28	0.3201	70930
8.693	0.3834	24.15	0.3198	81011
8.648	"	"	0.3227	81022
8.32	0.3690	22.38	0.3234	70919
8.26	0.3646	21.83	0.3193	70929
8.175	0.3624	21.57	0.3226	81019
7.88	0.3486	19.90	0.3204	70930

* The dates are given by figures to be read, for example,
70730: July 30, 1967,
81011: Oct. 11, 1968.

Table 1 (b).

Particle	f_e (MHz)	B_a (Wb/m ²)	E (MeV)	K	Date
α	9.673	0.5612	39.01	0.4170	81105
	8.130	0.4780	28.26	0.4276	81025
	8.093	0.4750	27.91	0.4260	81203
	7.080	0.4135	21.18	0.4208	81029
	7.075	0.4121	20.99	0.4190	81029
	5.967	0.3522	15.36	0.4314	81025
p	11.62	0.3444	14.53	0.1076	81029
	11.53	0.3413	14.28	0.1075	81002
d	9.991	0.5862	21.11	0.2112	81008

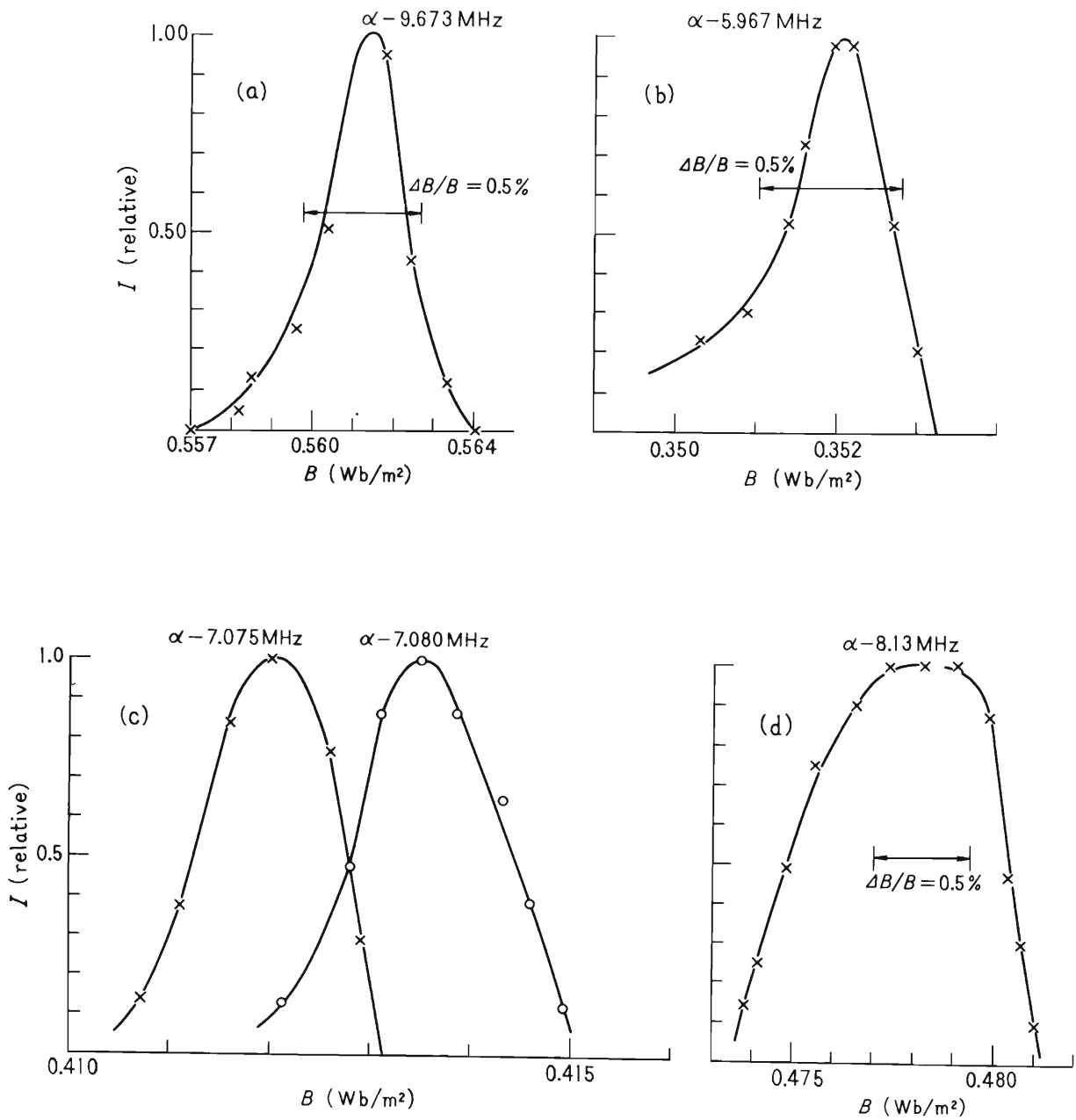


Fig. 1. Energy spectra of beams obtained with beam analyzing magnet.

5. NUCLEAR PHYSICS

Scattering and Reaction

5-1. Elastic Scattering of ^3He from Nuclei and Optical Model Analysis

K. Matsuda, M. Odera, I. Kohno, H. Kamitsubo,*
Y. Chiba, Y. Awaya, N. Nakanishi, T. Fujisawa,
S. Takeda, T. Wada, S. Nakajima, and M. Igarashi**

At the beginning of nuclear experiments with the cyclotron, a project of elastic scattering of ^3He from nuclei was adopted. During the investigation, several works were published on this subject from other organizations,¹⁾ for example, Birmingham,²⁾ Colorado-Oak Ridge³⁾, and Los Alamos.⁴⁾ The present work has features in wide ranges of angle and incident energy. Targets were ^{27}Al , Ca, ^{58}Ni , and carbon. The experiments and their analyses were made independently by four different groups in this institute and results will be published in the near future.⁵⁾ The analysis for the carbon target is now in progress and will be referred to later⁶⁾ and is omitted in this report. Here a general survey and some conclusions deduced from these independent works for the targets of ^{27}Al , Ca, and ^{58}Ni will be given. Throughout the analyses, an automatic search code of optical model named "SEARCH" put forward by one of the authors (T.W.) in a paper presented in this progress report⁷⁾ was used, where the notations used here will be given.

(1) Experiments and results

Standard techniques for study of angular distribution were undertaken. The incident energy was defined by a 85° analyzing magnet with a resolution and an accuracy of 0.2%. Because of an ordinary cyclotron beam, the emittance is not so good, obtaining a spot of $(2 \sim 3) \text{ mm} \times (5 \sim 8) \text{ mm}$ and a divergence of $(1 \sim 2)$ degrees. The average beam current attainable was $0.1 \sim 0.3 \mu\text{A}$ on the target. A 75 cm scattering chamber was used and its angular accuracy was about ± 0.2 degrees. Elastic ^3He particles were detected with solid state detectors. For the target of Ca and C, the discrimination of ^3He ions from alpha particles was essential and the method of a counter telescope and an identifier circuit was used.

Fig. 1 shows an example of the experimental results and calculated curves for ^{58}Ni . The angular distribution over a wider angular range in this work caused to modify the Bassel's parameters. Other results will be shown in the figures of following sub-sections.

* Now staying at Saclay.

** On leave from the Tokyo Institute of Technology.

(2) Potential ambiguities

It is well known that there are several ambiguities on the optical model parameters for composite projectiles. One is the so-called discrete ambiguity of the central real depth. An example for ^{58}Ni ($E_{\text{h}} = 34.14$ MeV) is presented in Fig. 2, where different sets of parameters, especially widely different depths of the central real potential give very similar angular distributions. Fig. 3 shows the typical sets of this kind of ambiguity for the case of 34.14 MeV ^3He scattering from ^{58}Ni , where a real depth is fixed at each value and other five parameters (in this case a volume imaginary type is used) are searched to make χ^2/N minimum. Thus three families which have the values of real depth around 90, 130, and 180 MeV give the minima of χ^2/N . It is noted that the three sets of the best-fit parameters have approximately the same value of the radius of central real potential as $1.10 F$. It is considered to be plausible that the central real depth for ^3He is about three times that for nucleons.⁹⁾ The potential family of 180 MeV, however, does not give the smallest values of minimum χ^2/N in Fig. 3. This trend of the discrete ambiguity was also found for the Ca target as shown in Table 1 where the best fit sets of parameters belonging to five families are shown for the case of 34.4 MeV ^3He scattering from Ca. In this case, the potential family of 240 MeV gives the smallest value of χ^2/N . The similar situation exists for the Al target. The results for ^{27}Al are shown in Figs. 4 and 5 and the optical parameters are given in Table 2. Clearly, the 100 MeV family (curves 1, 2, 3) gives the smallest χ^2/N among other families with deeper potentials in the case of the volume imaginary type as shown in Fig. 5. As will be discussed in Section 5 - 3 of this report, however, a deeper potential gives a better DWBA result for $^{27}\text{Al}(^3\text{He}, \alpha)^{26}\text{Al}$ reactions. It is noted that for these three nuclei, ^{27}Al , Ca, and ^{58}Ni , the best family of real depth may not be determined from the scattering cross section alone. On this point a comment on the analysis for Ca will be given later.

As for the continuous ambiguity, such as $V_{\text{r}}^{\text{n}} = \text{const.}$, Fig. 3 shows this tendency. In the present work, however, the best fit set can be obtained by the criterion on the minimum value of χ^2/N . The ambiguity of form factor is most serious and this point will be discussed in the following.

(3) Spin-orbit term

The strength of the spin-orbit potential for the ^3He scattering from nuclei is now a problem. There were several attempts to determine this value.^{10) 11) 12)} A simple consideration gives about one-third of the nucleon's V_{SO} . The present work extended the angular range to the backward hemisphere and the backward behavior may be sensitive to the spin-orbit term. Actually, the phase of backward diffraction can only be explained with a spin orbit term. Fig. 6 shows an example of 34.1 MeV ^3He scatterings from ^{58}Ni and the optical model parameters are given in Table 3.¹³⁾ The examples for the Ca target are given in Figs. 7 and 8, and some of the optical model parameters are given in Tables 1, 4, and 5. For the both targets, the backward behaviors at higher incident energies can be fitted fairly well to a potential using a V_{SO} of $3 \sim 4$ MeV. In the case of ^{27}Al , this kind of diffraction is not clear, but also the backward behavior is well fitted to with a spin-orbit potentials of $5 \sim 12$ MeV. The calculated curves are shown in Figs. 4 and 5 and the sets of parameter are given in Table 2. This large value of V_{SO} is not yet conclusive and the experiment of polarization and the analysis of scatterings for carbon under progress will be expected to give an answer to this problem. Throughout this investigation, r_{SO} is always set to be equal to r_0 only for simplicity.

(4) Surface imaginary term

Generally, in the optical potential for ^3He scattering a volume type imaginary part has been used. It is perhaps because its use in the alpha particle scattering has been followed. Recently, however, a surface type imaginary term was used,^{11), 12)} which would give a better fit for the case of carbon target if it is used with a spin-orbit potential. In the present work, a surface imaginary term was tested. The effects on the Ca target are seen in Figs. 7 and 8. In the case of including a (1-s) term, the surface imaginary type seems to be better. The value of χ^2/N , however, is not necessarily smaller with a surface imaginary term than with a volume one. The reason will be discussed later. For the ^{58}Ni target, a surface imaginary type gives a better fit if V_{SO} is set aside, however, no definite advantage of a surface imaginary term was found with V_{SO} . For the ^{27}Al target, the surface imaginary term was also tested for the family of $V = 100$ MeV and no advantage was found for a surface type. At any rate, the form factor of the imaginary potential is a question and there are some indications of the advantage of a surface type.

(5) Comments on individual targets

For the ^{58}Ni target, the agreement between the experimental and calculated curves seems to be best. It is plausible from the applicability of the optical model to a heavier target. The behavior at backward angles, however, is not yet explained completely.

For the Ca target, with V_{SO} of 3 ~ 4 MeV, a surface imaginary potential and a family of $V = 180$ MeV (see Tables 3 and 4), the behavior of angular distributions can be reproduced fairly well as shown in Figs. 7 (a) and (b). Especially, with these sets of parameters, the variation of potential parameters is small in spite of variation of $E_{\text{h}} = 18.8$ MeV to 39.3 MeV as seen in Fig. 4. This small variation with energy is considered to be important in the optical model. At higher incident energies (34.4 and 39.3 MeV), however, the absolute cross section around 120° cannot be fitted well especially in the case of finite V_{SO} . This effect makes the χ^2/N large.

For the ^{27}Al target, the fitting process is most difficult. This is, however, an example of the general fact that the optical model is less applicable to light nuclei. At this stage, it may be better to fix the central real depth to a family and search for better form factors and parameters.

The experiments and discussions were done by the three groups comprising M. Odera, I. Kohno, S. Takeda, and S. Nakajima (^{27}Al), N. Nakanishi, Y. Chiba, Y. Awaya, and K. Matsuda (Ca), and T. Fujisawa, T. Wada, M. Igarashi, and H. Kamitsubo (^{58}Ni) respectively. The optical model analyses were done mainly by M. Odera (^{27}Al), T. Fujisawa and T. Wada (^{58}Ni), and N. Nakanishi (Ca). The automatic search code was written by T. Wada.

Table 1. Discrete ambiguity in the ^3He scattering from Ca. $E_h = 34.4$ MeV with a volume imaginary part and without a (1-s) term.

E_h	V_o	r_o	a_o	$W_{\text{vol.}}$	r'	a'	V_{SO}	χ^2
34.4	80.44	1.149	0.8121	8.425	1.906	0.7164		30.9
34.4	125.78	1.150	0.7378	10.376	1.830	0.7779		22.3
34.4	179.29	1.145	0.6957	12.687	1.744	0.8259		18.6
34.4	242.84	1.135	0.6668	15.479	1.650	0.8694		17.8
34.4	317.52	1.120	0.6457	18.697	1.559	0.9085		18.7

Table 2. Optical parameters for the ^{27}Al target. The curves are shown in Figs. 4 and 5.

No. of curves	E_h	V	r_o	a_o	$W_{\text{vol.}}$	r'	a'	V_{SO}	χ^2/N
1	24.2	99.92	1.055	0.863	14.75	1.811	0.688	0	38.95
2	"	98.17	1.19	0.757	12.92	1.70	0.876	8.59	8.51
3	"	95.85	1.19	0.757	11.79	1.70	0.876	5.09	20.46
4	31.5	100.46	1.072	0.848	14.52	1.811	0.694	0	46.4
5	24.2	120.03	1.356	0.536	14.05	1.578	1.201	12.0	40.6
6	"	163.96	1.371	0.515	16.02	1.592	1.236	11.53	14.10
7	"	194.84	1.474	0.530	17.68	1.850	1.196	5.13	92.9

Table 3. Optical potential parameters for the elastic scattering from ^{58}Ni .
The angular distributions are shown in Fig. 6.

	V	r_R	a_R	$W_{\text{vol.}}$	r_I	a_I	V_{so}	r_c	χ^2/N
A	173.0	1.14	0.723	16.5	1.60	0.810	0	1.4	214.
B	180.0	1.10	0.772	20.3	1.62	0.757	0	1.4	13.6
C	192.6	1.05	0.797	17.4	1.66	0.750	3.68	1.4	8.6
D	174.1	1.14	0.723	19.2	1.60	0.810	4.75	1.4	18.2

Table 4. Optical potential parameters for the elastic scattering from Ca,
with a volume imaginary part.

E_h	V_0	r_0	a_0	$W_{\text{vol.}}$	r'	a'	χ^2
18.8	181.86	1.145	0.7086	15.05	1.644	0.7849	1.9
24.9	182.69	1.145	0.7004	16.774	1.633	0.6692	12.9
31.0	177.27	1.145	0.7355	13.919	16.92	0.7778	28.3
34.4	179.29	1.145	0.6957	12.687	1.744	0.8259	18.6
39.3	177.63	1.145	0.6981	13.367	1.714	0.9002	28.1
37.7	176.9	1.14	0.723	14.5	1.64	0.91	29.71
(Gibson et al.)*							

* E. F. Gibson, B. W. Ridley, J. J. Kraushaar, M. E. Rickey, and R. H. Bassel:
Phys. Rev., 155, 1194 (1967).

Table 5. Optical potential parameters for the elastic ${}^3\text{He}$ scattering from Ca, with a surface imaginary part and a real spin orbit* part.

E_{h}	V_0	r_0	a_0	W_{surf}	r'	a'	V_{SO}	χ^2
18.8	182.46	1.145	0.7047	19.407	1.207	0.8224	3.984	15.7
24.9	181.15	1.145	0.7054	18.669	1.235	0.7506	4.285	13.8
31.0								
34.4	180.82	1.145	0.6776	16.039	1.277	0.8830	3.483	21.2
39.3	177.46	1.145	0.7000	17.713	1.271	0.8636	3.843	44.6

* $r_{\text{SO}} = r_0$, $a_{\text{SO}} = a_0$.

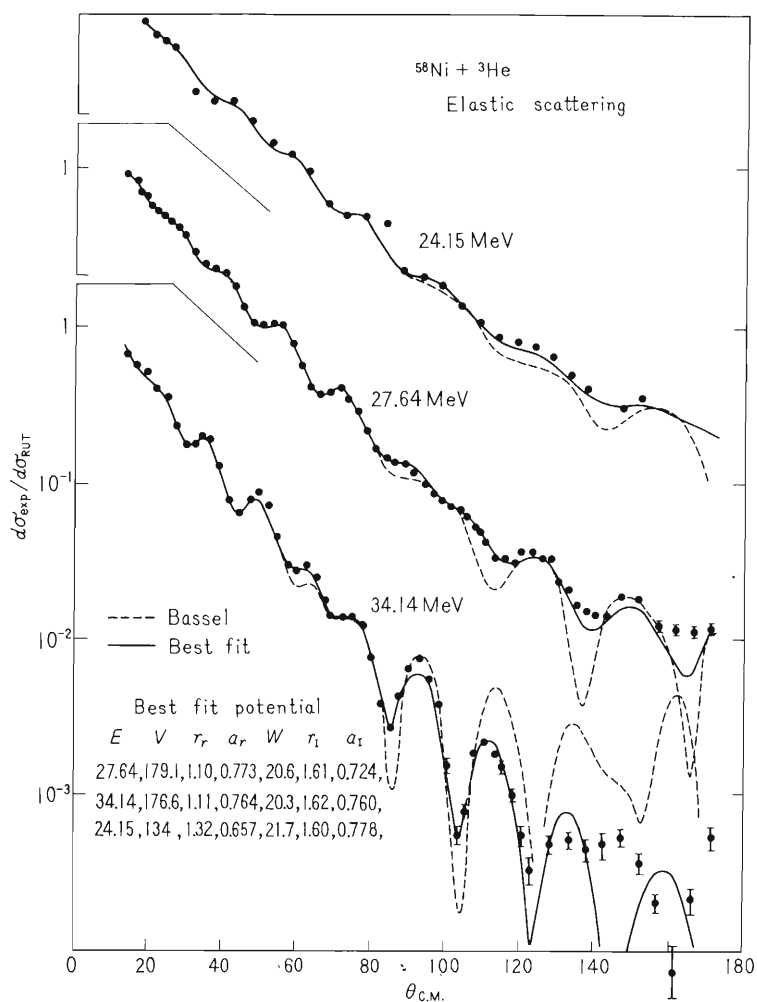


Fig. 1. Angular distributions for the target of ${}^{58}\text{Ni}$ and the best-fit calculated curves without a spin-orbit term and the corresponding potential parameters.

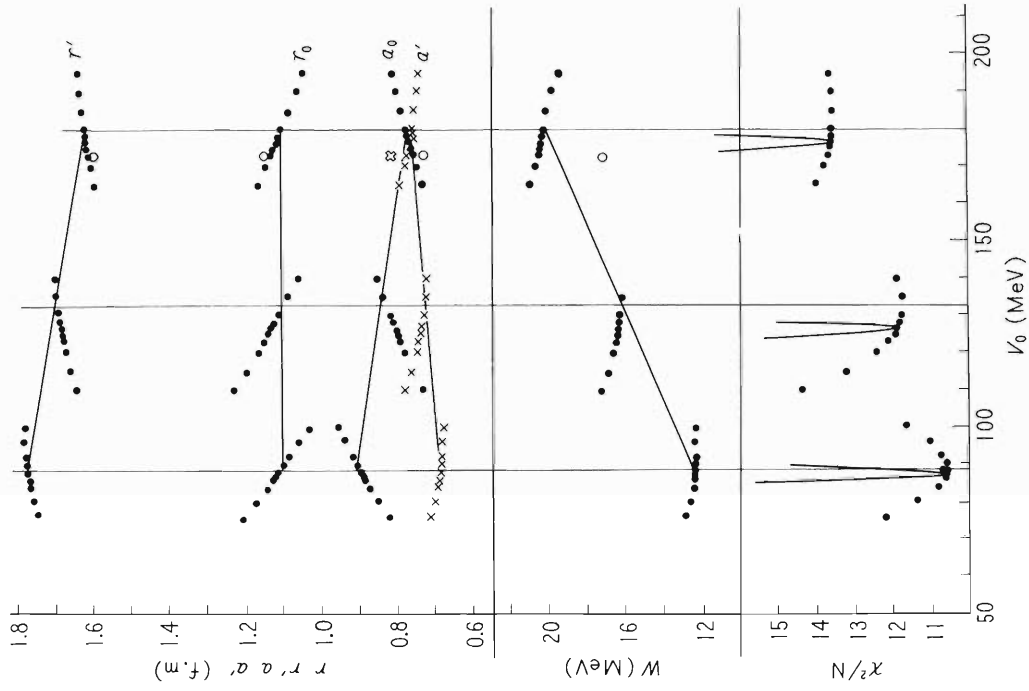


Fig. 3. An example of the best-fit parameter search. This figure shows three discrete families, continuous ambiguities, and constancy of r_0 .

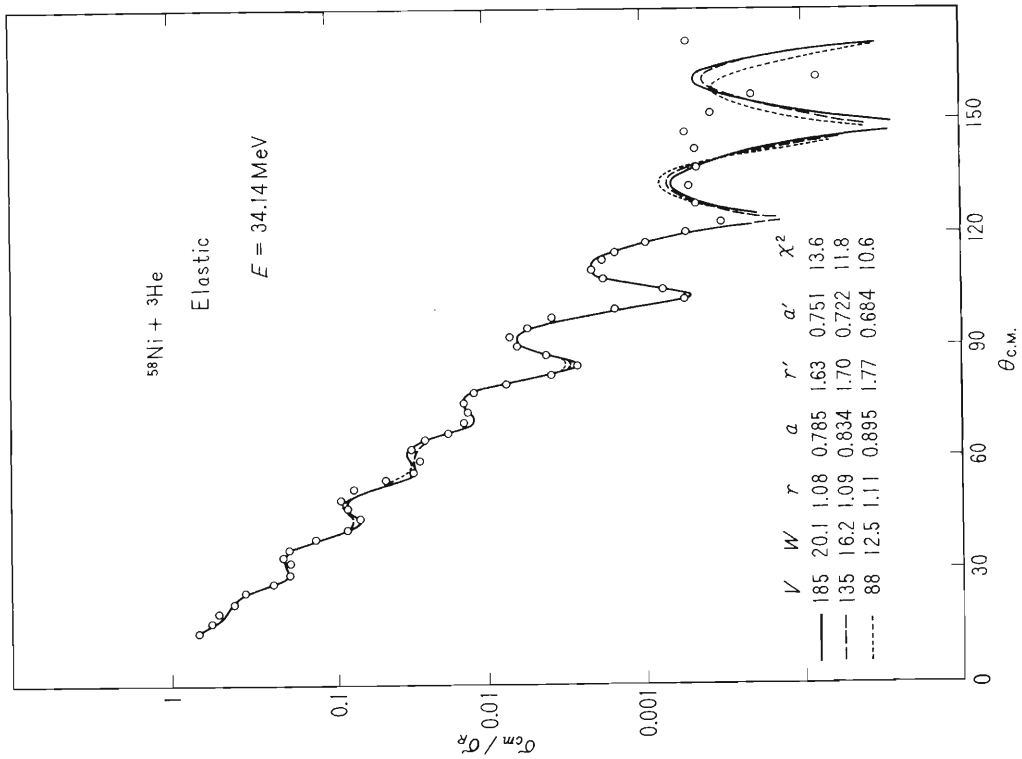


Fig. 2. Discrete ambiguities. Different sets give very similar angular distributions.

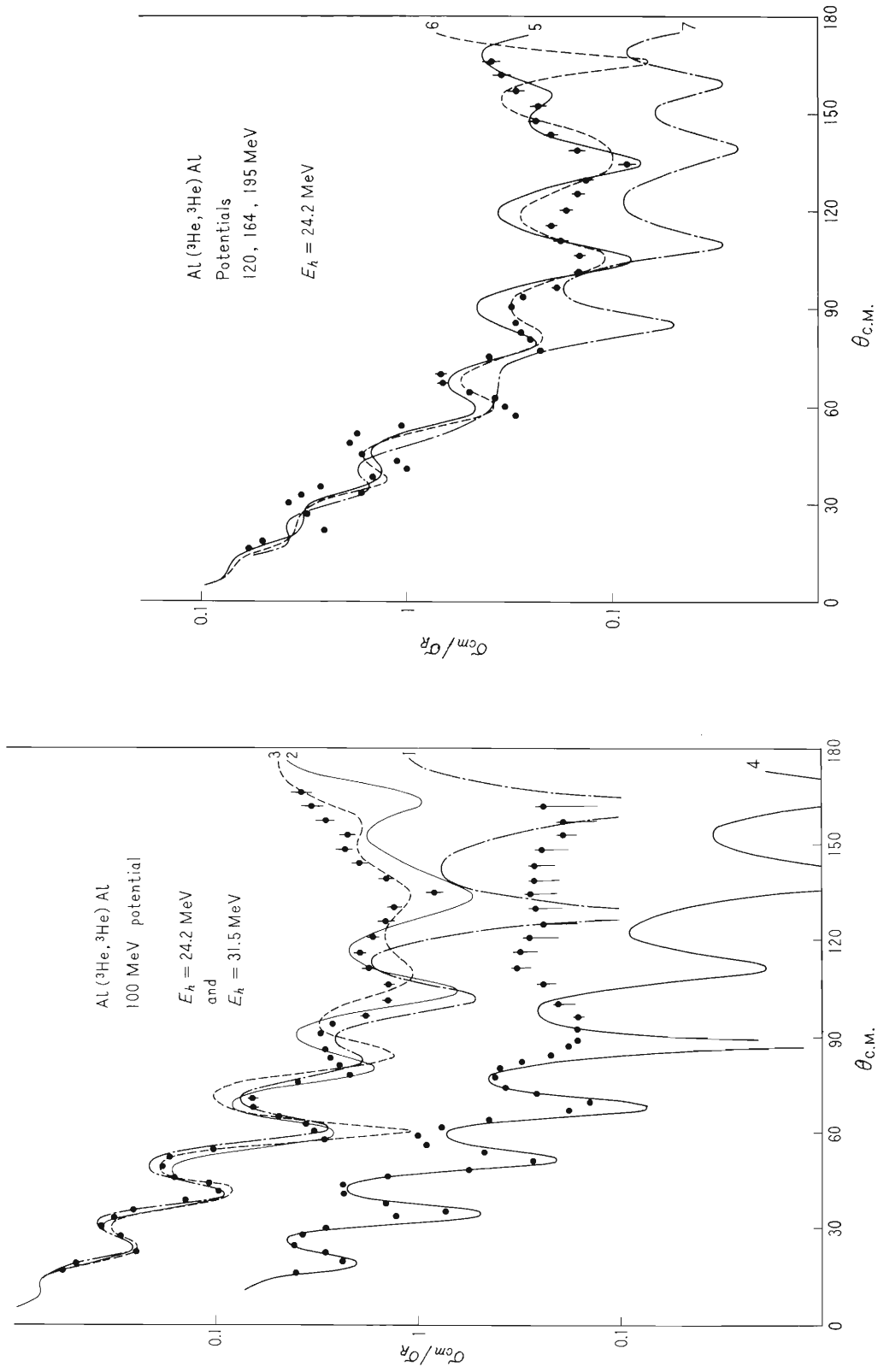


Fig. 5. Comparison of experimental angular distributions with other families of potential.

Fig. 4. Comparison of experimental angular distributions for ^{27}Al with optical model parameters of 100 MeV family.

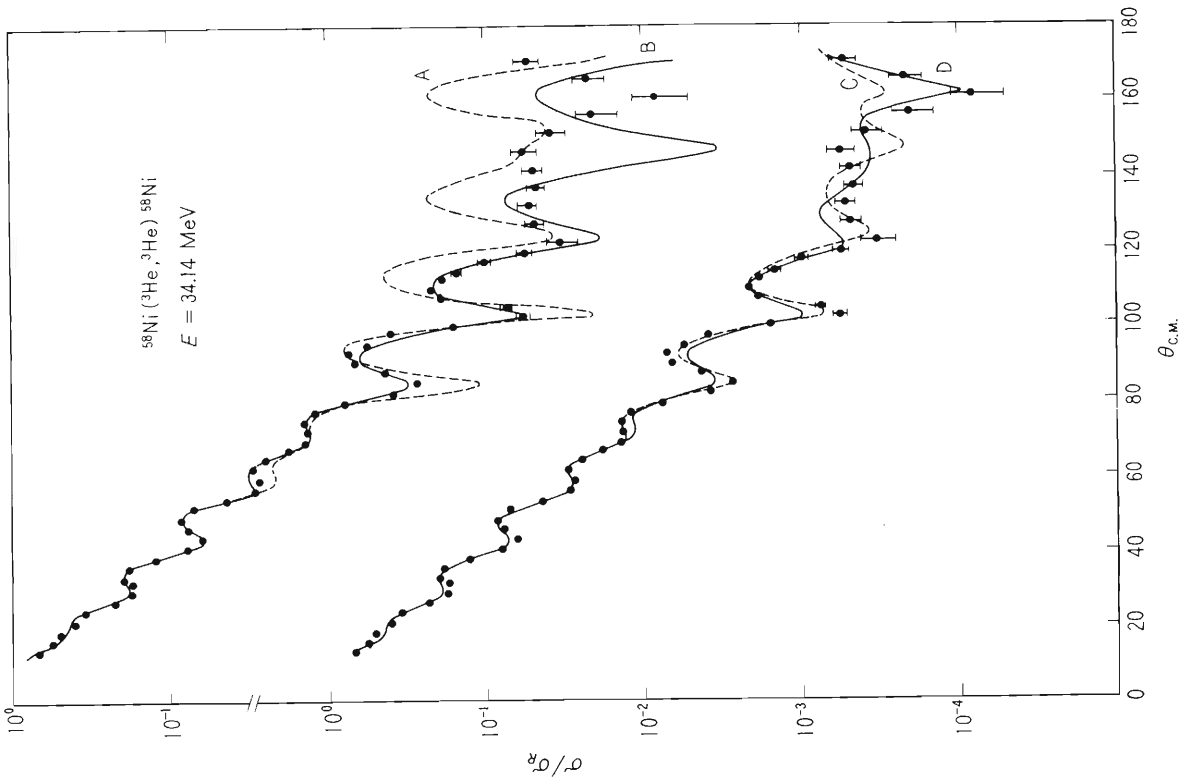


Fig. 6. Effect of a spin-orbit potential. Without a (l-s) term the phase relation cannot be reproduced.

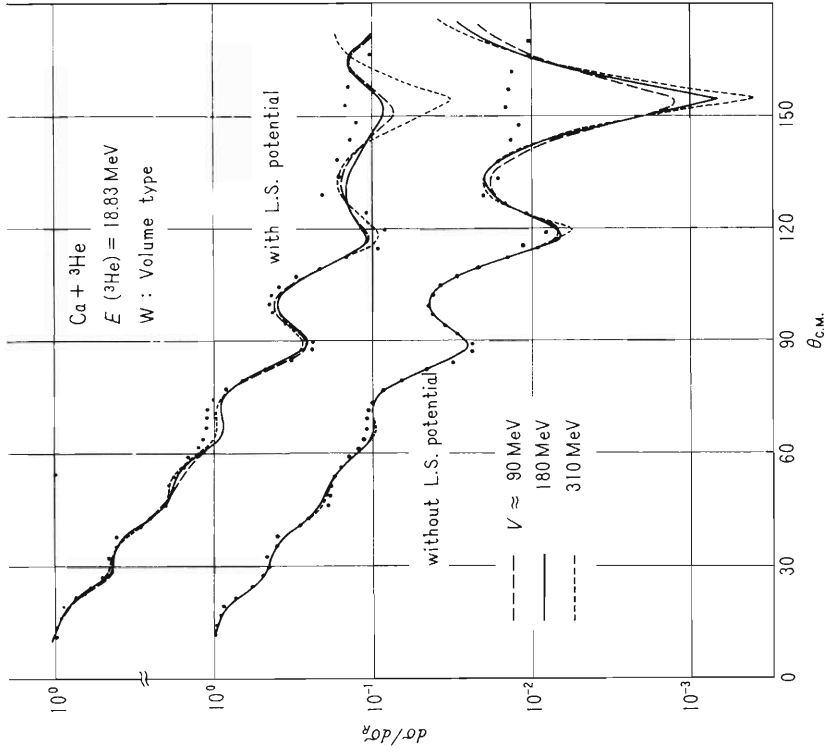


Fig. 7 (a). Optical model analysis of the ${}^3\text{He}$ scattering from Ca at 18.8 MeV with a volume imaginary term.

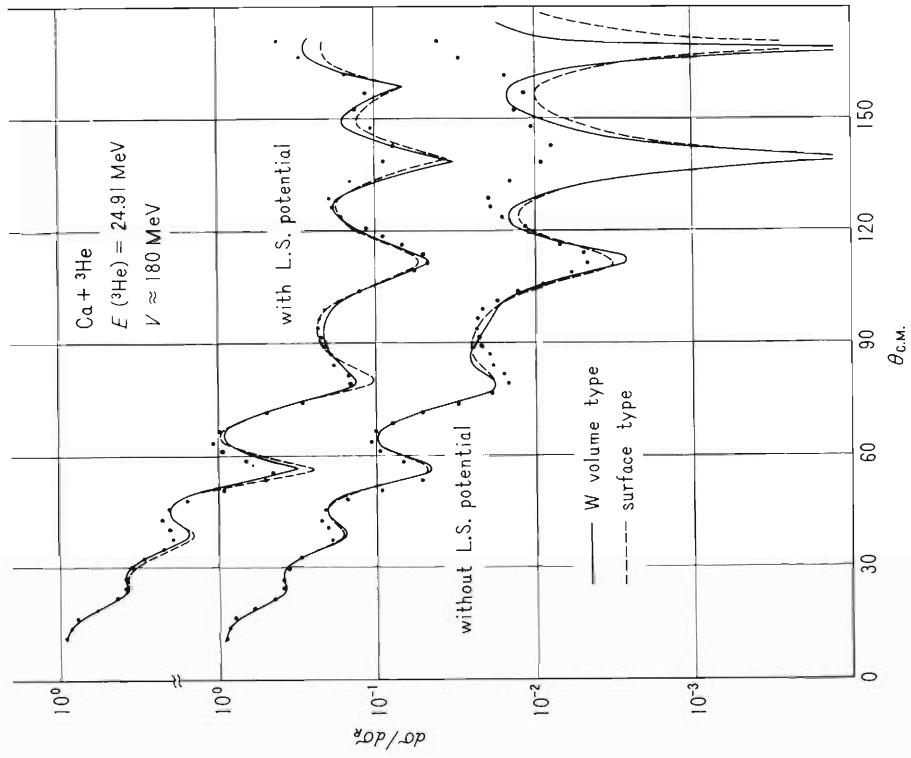


Fig. 8 (a). Optical model analysis of the ^3He scattering from Ca at 24.9 MeV with 180 MeV family.

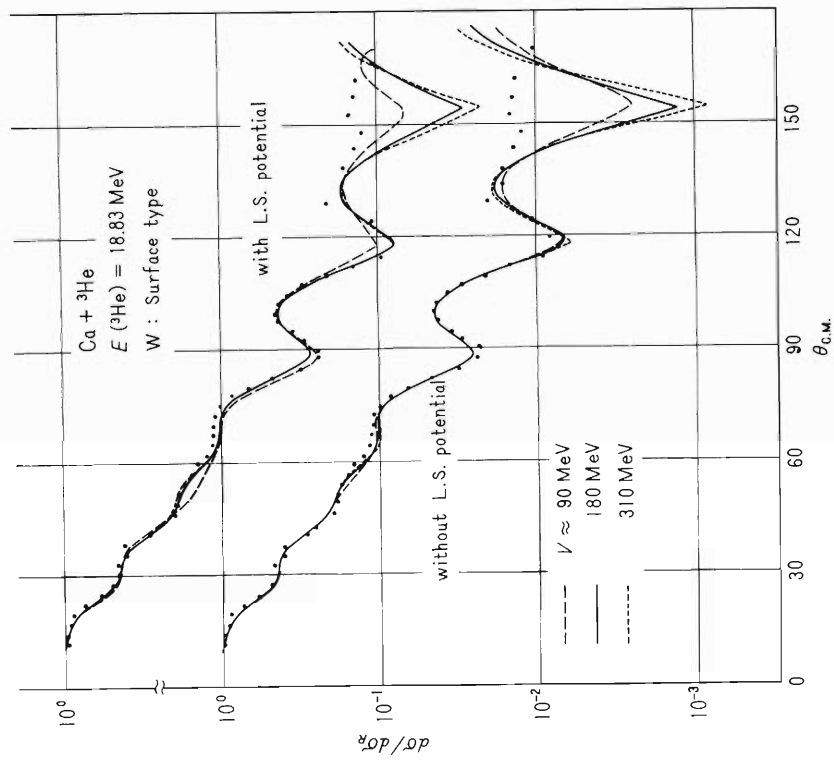


Fig. 7 (b). With a surface imaginary term.

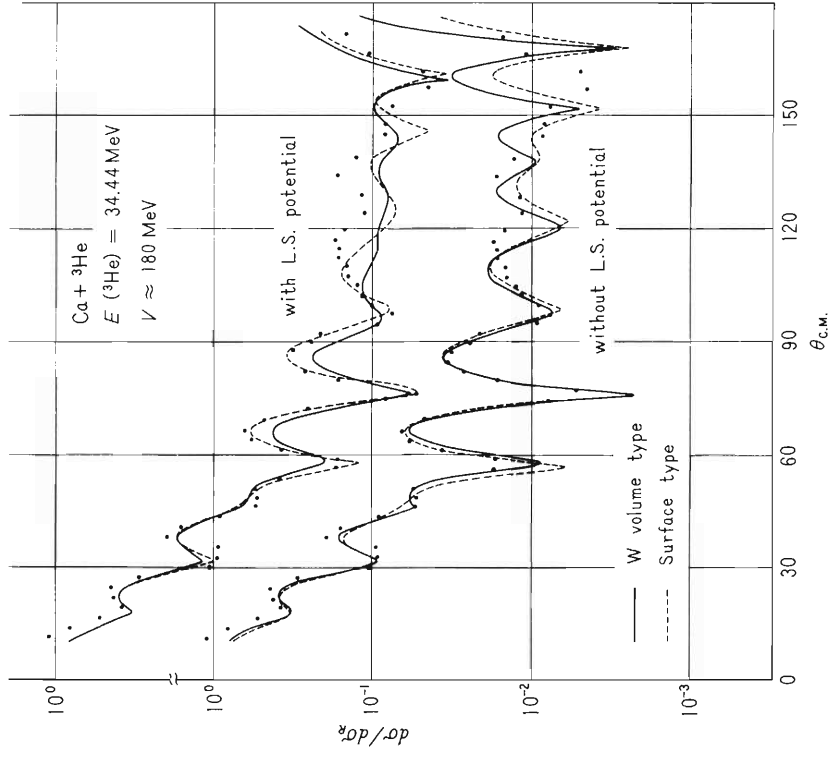


Fig. 8 (c). The same at 34.4 MeV.

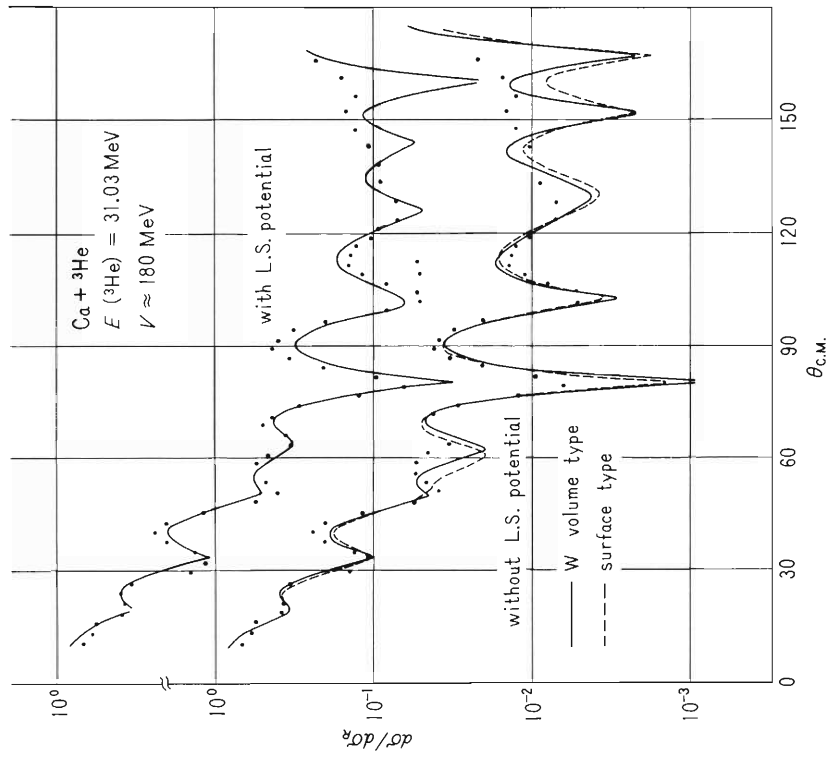


Fig. 8 (b). The same at 31.0 MeV.

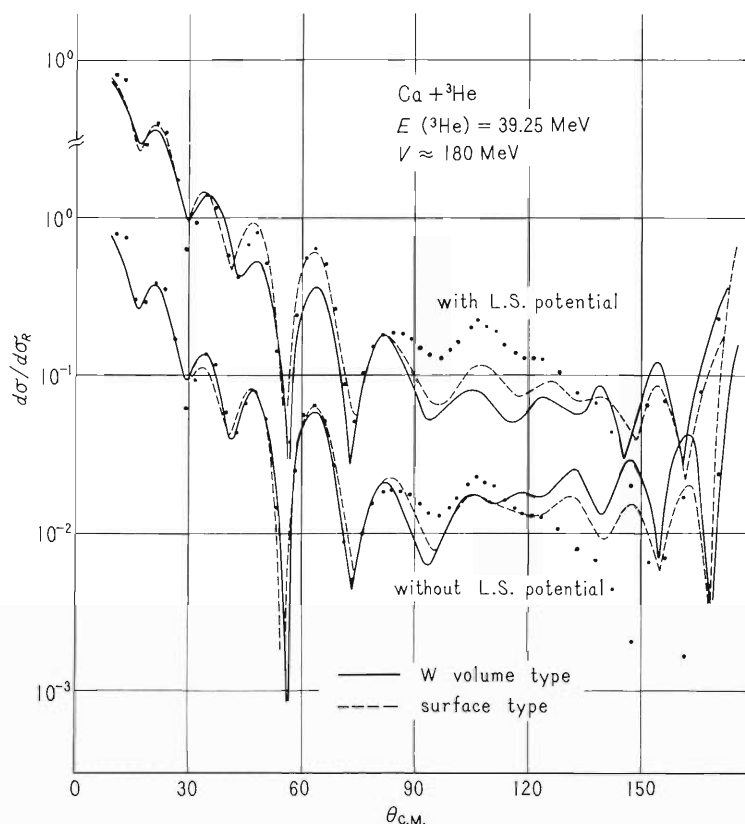


Fig. 8 (d). The same at 39.3 MeV.

References

- 1) P. E. Hodgson: "Proceedings of the Symposium on Direct Reactions with ^3He (Sept. 1967)", IPCR Cyclotron Progress Report, Supplement 1, p. 41 (1967).
- 2) D. J. Bangh, G. J. Pyle, G. J. Rolph, and S. M. Scarrott: Nucl. Phys., A 95, 115 (1967).
- 3) E. F. Gibson, B. W. Ridley, J. J. Kramshaar, M. E. Rickey, and R. H. Bassel: Phys. Rev., 155, 1194 (1967).
- 4) E. R. Flynn and L. Rosen: *ibid.*, 153, 1228 (1967).
- 5) These works were partly reported by H. Kamitsubo in "Proceedings of the Symposium on Direct Reactions with ^3He (Sept. 1967)", (IPCR Cyclotron Progress Report Supplement 1).
- 6) T. Fujisawa et al.: p.77 of this volume.
- 7) T. Wada: p.87 of this volume.
- 8) T. Fujisawa and Y. Awaya: IPCR Cyclotron Progress Report, p. 54 (1967).
- 9) R. H. Bassel and R. M. Drisko: "Proceedings of the Symposium on Direct Reactions with ^3He , (Sept. 1967)", IPCR Cyclotron Progress Report, Supplement 1, p. 13 (1967).
- 10) W. E. Burcham, J. B. A. England, J. E. Evans, A. Garcia, R. G. Harris, and C. Milne: Compt. Rend. Congr. Intern. Phys. Nucl. Paris, p. 877 (1964).
- 11) R. L. Hutson, S. Hayakawa, M. Chabre, J. J. Kraushaar, B. W. Ridley, and E. T. Boschitz: Phys. Letters, 27B, 153 (1968).
- 12) D. M. Patterson and J. G. Cramer: *ibid.*, p. 373 (1968).
- 13) H. Kamitsubo, T. Wada, T. Fujisawa, and M. Igarashi: *ibid.* (to be published).

5-2. Elastic and Inelastic Scattering of Heavy Ions

I. Kohno, S. Nakajima, T. Tonuma, and M. Odera

Differential cross sections of 84 MeV ^{14}N particles and 73 MeV ^{12}C particles elastically and inelastically scattered by ^{12}C , ^{27}Al , ^{28}Si , and ^{58}Ni have been measured in order to investigate the reaction mechanisms between complex nuclei at the energies above coulomb barrier.

The extracted ion beams of ^{14}N and ^{12}C from the 160 cm cyclotron were led into the 75 cm scattering chamber and focused in a size of $1.5\text{ mm} \times 7\text{ mm}$ on a target. The energy resolution of the beam was below 0.5 % and the intensity was about $0.05\ \mu\text{A}$. The C, Al, and Si targets were all natural and self-supporting ones, but the ^{58}Ni target was the self-supporting foil of the separated isotope. Thicknesses of the targets were $50\ \mu\text{g}/\text{cm}^2$ for ^{12}C , $350\ \mu\text{g}/\text{cm}^2$ for ^{27}Al , $750\ \mu\text{g}/\text{cm}^2$ for ^{28}Si , and $650\ \mu\text{g}/\text{cm}^2$ for ^{58}Ni . Scattered particles were detected by a silicon surface barrier detector with the depletion layer of $200\ \mu$.

Fig. 1(a) is a pulse height spectrum of ^{14}N particles scattered by the ^{12}C target, and Fig. 1(b) is a spectrum of ^{12}C particles scattered by the ^{28}Si target. Difference of energy resolution between the two spectra is explained by the difference of the target thickness. In Fig. 1(a) there are several peaks corresponding to the ground level (0^+), 4.43 (2^+), 9.6 (3^-), 14.1 MeV excited levels of ^{12}C and 5.7 MeV excited level of ^{14}N . In Fig. 1(b) the ground level (0^+), 1.78 (2^+), 6.88 MeV (3^-) excited levels of ^{28}Si and 4.43 MeV (2^+) of ^{12}C are found.

The angular distribution of the 4.43 MeV peak in Fig. 1(b) is in phase at all angles with that of the 1.78 MeV (2^+) peak. Then, this peak can be supposed to be a superposition of ^{12}C 4.43 MeV and ^{28}Si 4.6 MeV (4^+) states. On the other hand, in the case of $^{28}\text{Si} + ^{14}\text{N}$, there is no peak in the range of 4 to 6 MeV, so the 4.43 MeV peak may consist of ^{12}C 2^+ level only.

In Fig. 2 the angular distributions of the elastically scattered ^{14}N and ^{12}C particles are shown. As to the angular distributions of ^{14}N particles, a diffraction pattern is more distinct when the target mass is less. At present, fits of these experimental results with the optical model parameters are being tried by the automatic search code.

In Fig. 3 the angular distributions of ^{14}N peaks inelastically scattered by the ^{12}C target corresponding to $Q = -4.43\text{ MeV}$ (^{12}C 2^+), -5.69 MeV (^{14}N 1^-), and -9.69 MeV (^{12}C 3^-) are shown, and in Fig. 4 and Fig. 5 the angular distributions of ^{14}N and ^{12}C peaks inelastically scattered by the ^{28}Si target corresponding to $Q = -1.78\text{ MeV}$ (^{28}Si 2^+), -4.43 MeV (^{12}C 2^+), and -6.88 MeV (^{28}Si 3^-) are indicated. Each angular distribution shows the clear diffraction pattern and the regular phase relations between each cross sections are observed.

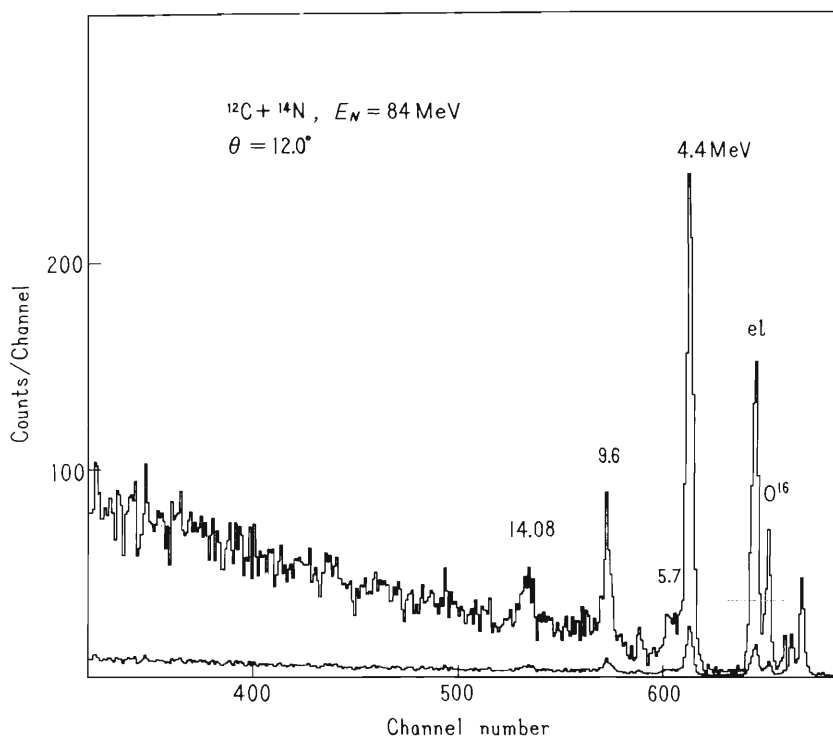


Fig. 1(a). Spectrum of $^{12}\text{C} + ^{14}\text{N}$ at energy of 84 MeV. ^{16}O means elastic scattering peak of ^{14}N by ^{16}O contaminated in ^{12}C target.

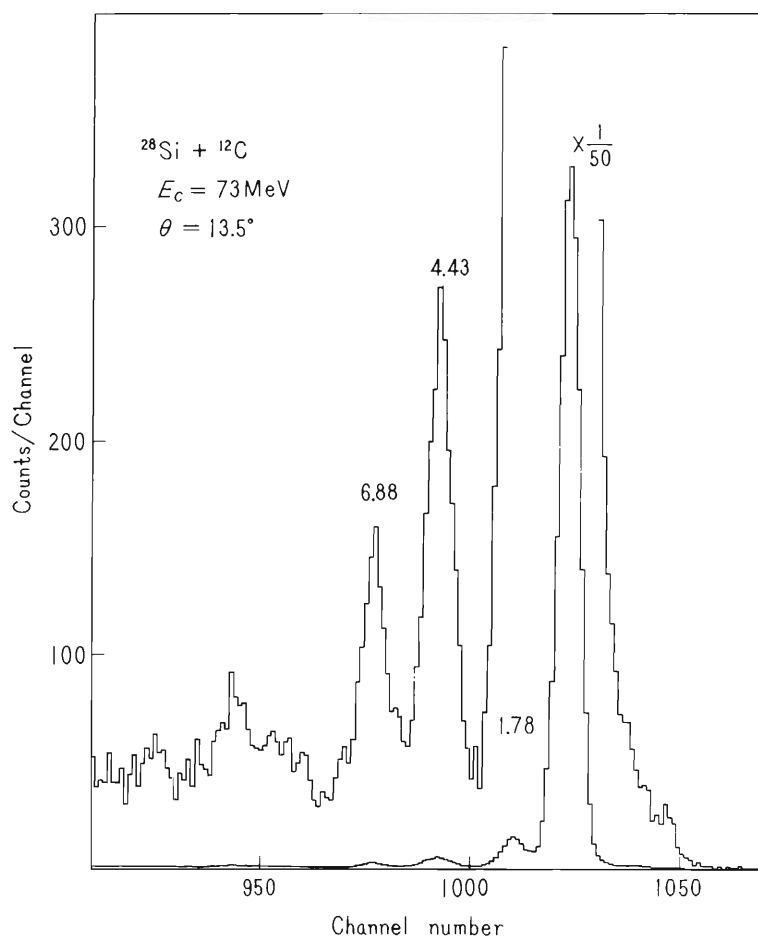


Fig. 1(b). Spectrum of $^{28}\text{Si} + ^{12}\text{C}$ at ^{12}C energy of 73 MeV.

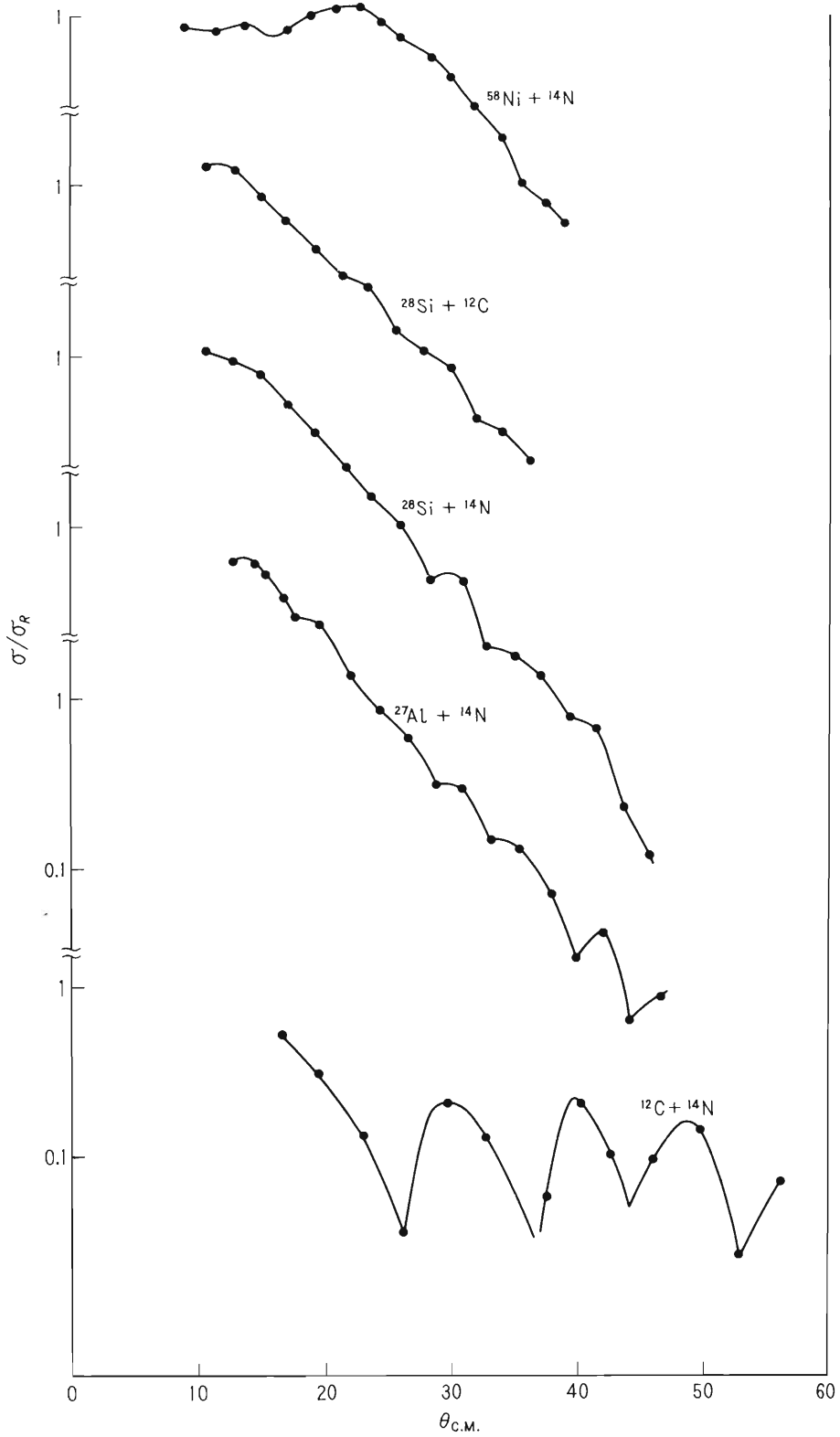


Fig. 2. Angular distributions of ^{14}N and ^{12}C elastically scattered by ^{12}C , ^{27}Al , ^{28}Si , and ^{58}Ni at the energy of 84 MeV with ^{14}N and 73 MeV with ^{12}C .

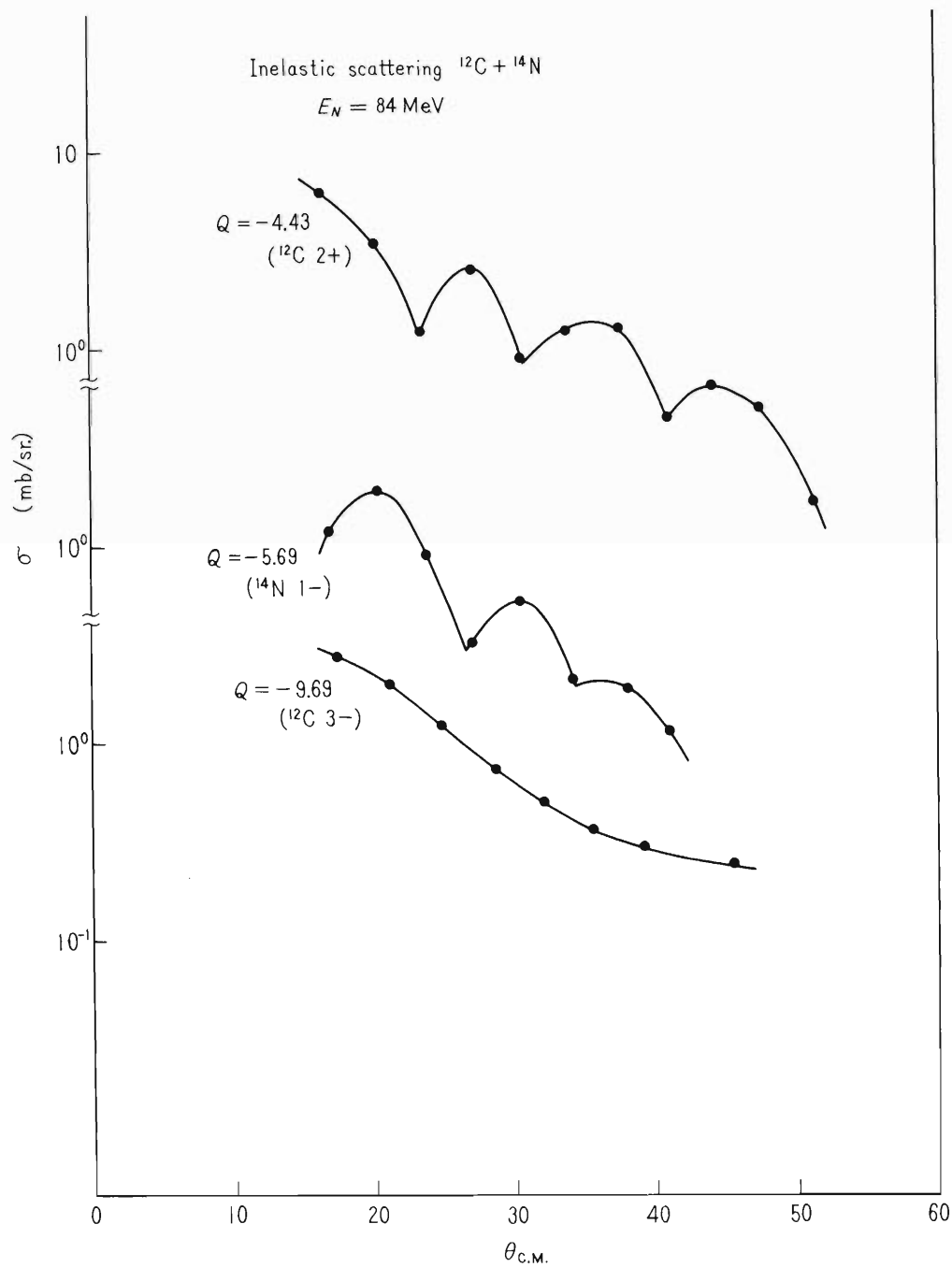


Fig. 3. Angular distributions of ^{14}N inelastically scattered by ^{12}C at energy of 84 MeV. (^{12}C) and (^{14}N) mean excited levels of ^{12}C and ^{14}N respectively.

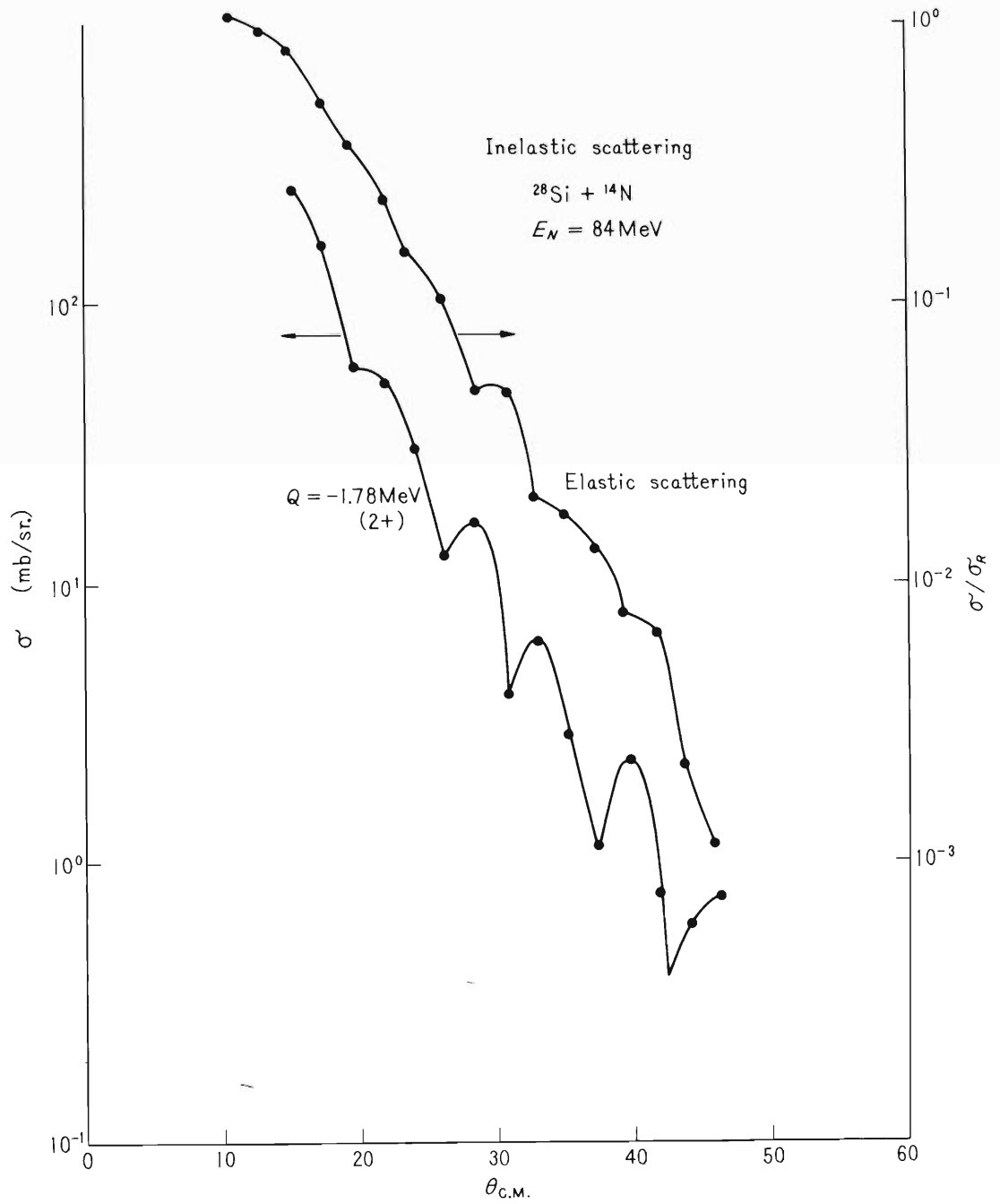


Fig. 4. Angular distributions of ^{14}N elastically and inelastically scattered by ^{28}Si at energy of 84 MeV.

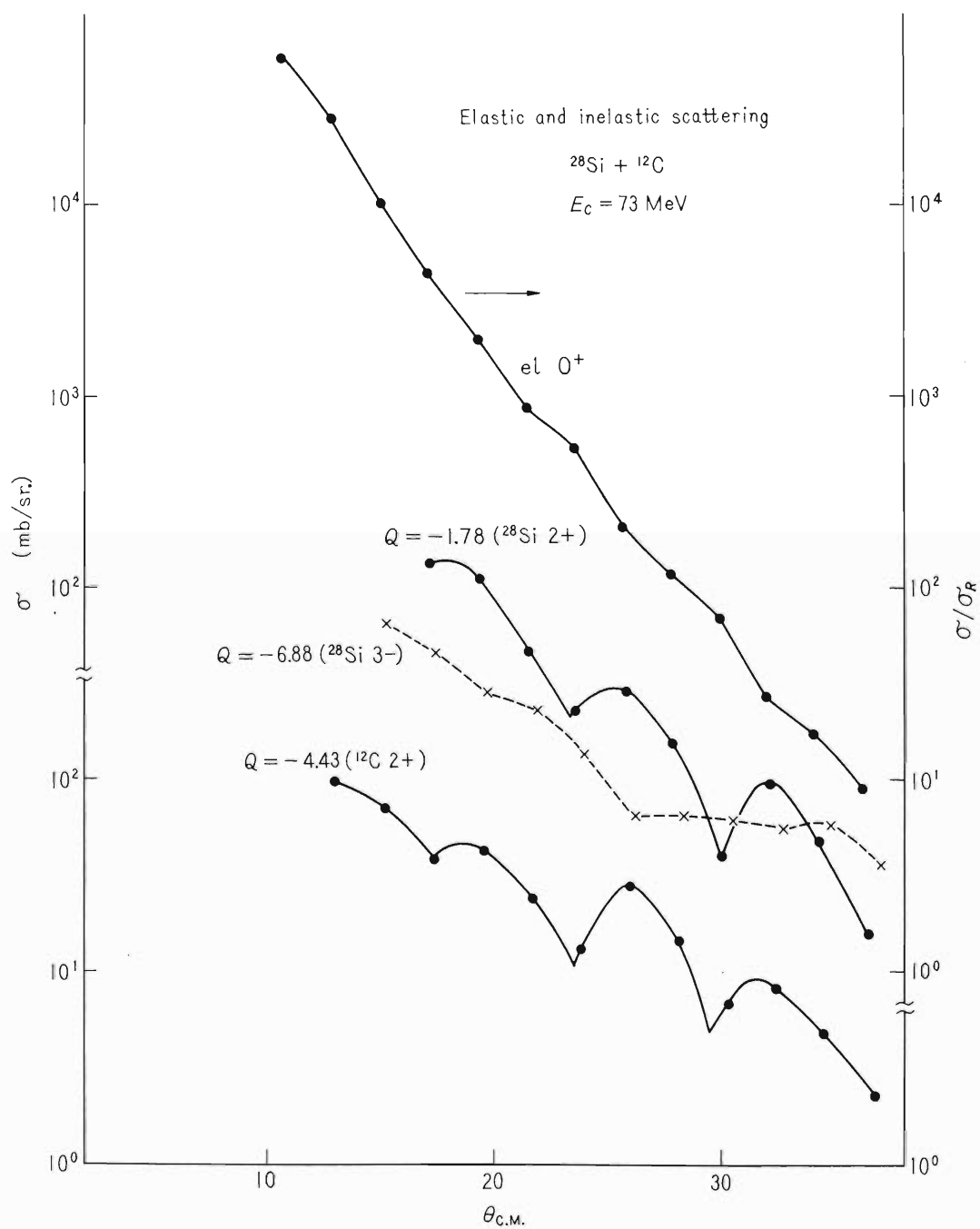


Fig. 5. Angular distributions of ^{12}C elastically and inelastically scattered by ^{28}Si at energy of 73 MeV. (^{28}Si) and (^{12}C) mean excited levels of ^{28}Si and ^{12}C respectively.

5-3. ($^3\text{He}, \alpha$) Reactions of Al and Si at 22.34 MeV

M. Odera, I. Kohno, S. Takeda, and S. Nakajima

An aluminum target was bombarded by the magnetically analyzed ^3He ions of 22.34 MeV. The thickness of the target was $351 \pm 17 \mu\text{g}/\text{cm}^2$.

Fig. 1 shows a spectrum. Numbers on the top of each peak correspond to the excitation of the residual nuclei. Letters represent particles which lead to each nucleus. Contaminant peaks are denoted by the names and excitation of the residual nuclei. The energy resolution of the detection was 70 keV.

There is a prominent peak labelled as 4.699. There is little contribution of the neighboring levels to this peak at least at angles smaller than 60° .

About 20 peaks are identified with the known levels of ^{26}Al . The angular distributions are obtained for 12 of them. They are shown in Fig. 2. DWBA analyses were applied using INS DWBA 2 code prepared by Kawai, Kubo, and Yamaura.¹⁾ Fig. 3 is the examples of the fits to the ground state transition with the various combinations of the optical model parameters in the incident and exit channels. Table 1 shows several parameter sets used in Fig. 3. The shape of distributions differs little in the forward angles but varies considerably at large angles. Overall feature of the distribution seems to be determined by the parameters of the exit channel as has been noted by R. Stock et al.²⁾ The exception is the set 5 where different parameters for the bound state wave function of transferred neutron are used. The best parameter set for this reaction is not the best fit parameter set for the elastic scattering in the input channel³⁾ and for the α channel⁴⁾ either. Solid lines of Fig. 2 were calculated by the set 3.

As seen in Fig. 2 most distributions can be fitted excellently by $\ell = 2$ transitions. Only the distribution of 0.418 level needs $\ell = 0$ component in disagreement with the result of Nurzyński et al.⁵⁾ They found that in the same reaction with ^3He of 10 MeV, only $\ell = 2$ component was necessary to reproduce the experimental distribution. Other single neutron processes as (d, t)⁶⁾ and (p, d)⁷⁾ show invariably an $\ell = 0$ pattern in this transition. Also there is large differences in the values of spectroscopic factors as will be seen later. The origin of the discrepancies is not clarified yet but seems to come partly from the large momentum mismatch, characteristic to the ($^3\text{He}, \alpha$) reaction.

As seen in Fig. 4, the distribution can be fitted by mixing of 50 % of 3S component as good as or even better than 50 % mixing of 2S component. Of course the existence of 3S neutron in the ground state of ^{27}Al is hardly probable. Perhaps the form of wave function generated by spherical 3S state showed a distribution similar to the nonspherical bound state wave function the nucleus might have.

Table 2 tabulates the relative spectroscopic factors obtained along with the previously reported values.^{5, 7)} Those values for the levels of known spin are plotted against $2J + 1$ in Fig. 5. Large deviation of 0.418 from the linear relationship is seen.

The level is excited by $^{25}\text{Mg} (^3\text{He}, \text{d})$ reaction rather strongly by $\ell = 0$ proton transfer. Its absolute spectroscopic factor is reported to be 0.55.⁸⁾ On the other hand, mixing of 2S 1/2 proton state in the ground state of ^{27}Al is estimated to be negligible.⁹⁾ Thus small overlap of the wave functions in this ($^3\text{He}, \alpha$) transition can be expected.

A preliminary result of the DWBA analysis of the $^{27}\text{Al} (\text{d}, \text{t}) ^{26}\text{Al}$ reaction at 21.6 MeV¹⁰⁾ shows that fits of almost all angular distributions with $\ell = 2$ transition can be obtained. Also, that of 0.418 MeV level needs an admixture of $\ell = 0$ of about 30 to 40 % in agreement with the ($^3\text{He}, \alpha$) case. But single $\ell = 0$ distribution cannot be compared

favorably with the experiment. The experimental result is at variance with that of Vlasov et al.⁶⁾ in this respect.

A natural silicon target of $570 \mu\text{g}/\text{cm}^2$ was bombarded by ^3He ions. The energy and other experimental conditions were the same with those of aluminum. Figs. 6 and 7 are the spectrum and the angular distributions obtained. The features of the latter are considerably different from the case of aluminum especially in the flat distributions of 0.953 and 2.165 transitions.

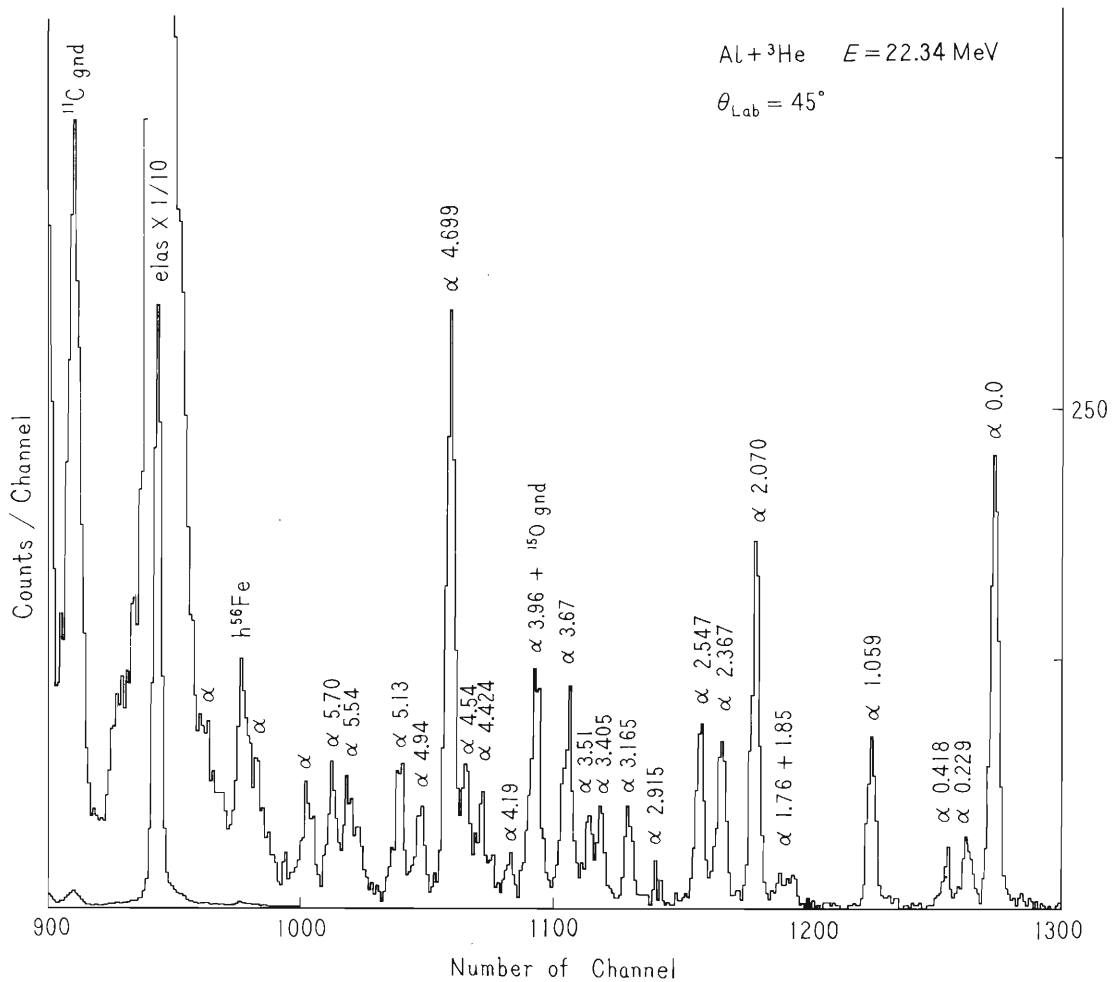


Fig. 1. Spectrum of $^{27}\text{Al} + ^3\text{He}$ at 22.34 MeV. α and h mean $^{27}\text{Al}(^3\text{He}, \alpha)^{26}\text{Al}$ and $^{27}\text{Al}(^3\text{He}, ^3\text{He})^{27}\text{Al}$ reactions respectively.

Table 1. Optical model parameters used in the analysis.

	No.	V	W	V_S	r_V	r_W	a_V	a_W
^3He channel	1	92.95	23.62	3.98	1.12	1.69	0.835	0.678
	2	121.90	15.38	1.70	1.19	1.70	0.757	0.876
	3	142.29	20.48	9.40	1.05	1.64	0.794	0.776
	4	179.85	24.68	3.98	1.04	1.61	0.742	0.732
α channel	1	127.80	12.80	0	1.53	1.53	0.543	0.543
	2	172.0	20.0	0	1.35	1.35	0.60	0.60
	3	197.1	17.0	0	1.35	1.35	0.59	0.59

Set No.	^3He channel	α channel
(1)	1	1
(2)	1	2
(3)	2	2
(4)	3	2
(5)	2	3
(6)	3	3
(7)	4	3

Table 2. Spectroscopic factors.

^{26}Al	J^π	T	Nurzyński et al. ⁵⁾		Present		Bevington et al. ⁷⁾		$\frac{2J+1}{2J+1g.s.}$
level			ℓ (s/sg.s.)		ℓ (s/sg.s.)		ℓ (s/sg.s.)		
0	5^+		2	1	2	1.0	2	1.0	1.0
0.229	0^+	1	2	0.23	2	0.14	2	0.15	0.09
0.418	3^+		2	0.61	2×0.5	0.12**	0	0.16	0.64
					$+0 \times 0.5$				
1.059	1^+		2	0.30	2	0.32	2	0.30	0.27
2.070*	2^+	1	2	0.59	2	0.59	0	0.20	0.46
2.367					2	0.35			
2.547					2	0.35			
3.156		1			2	0.25			
3.67					2	0.32			
3.96					2	0.24			
4.699					2	1.0			
5.126					2	0.26			

* Excitation of 2^+ T = 1 state is assumed among the triplet states at 2.070.

** Mixing of $1d\ 5/2$ and $2S\ 1/2$ is used.

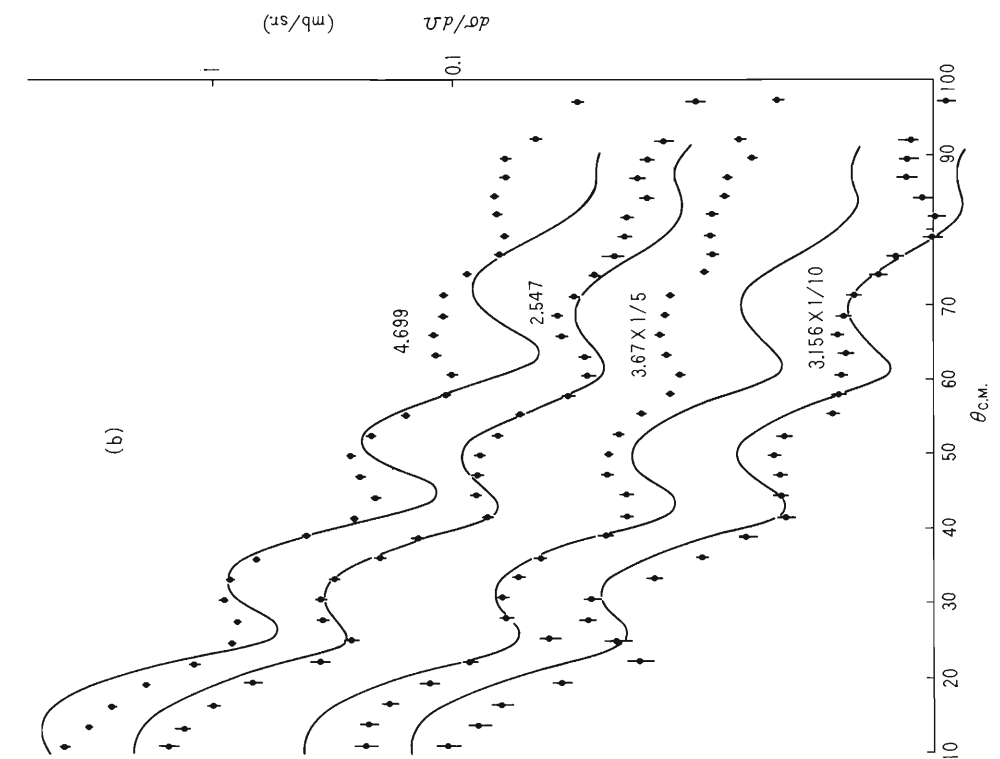


Fig. 2(a).

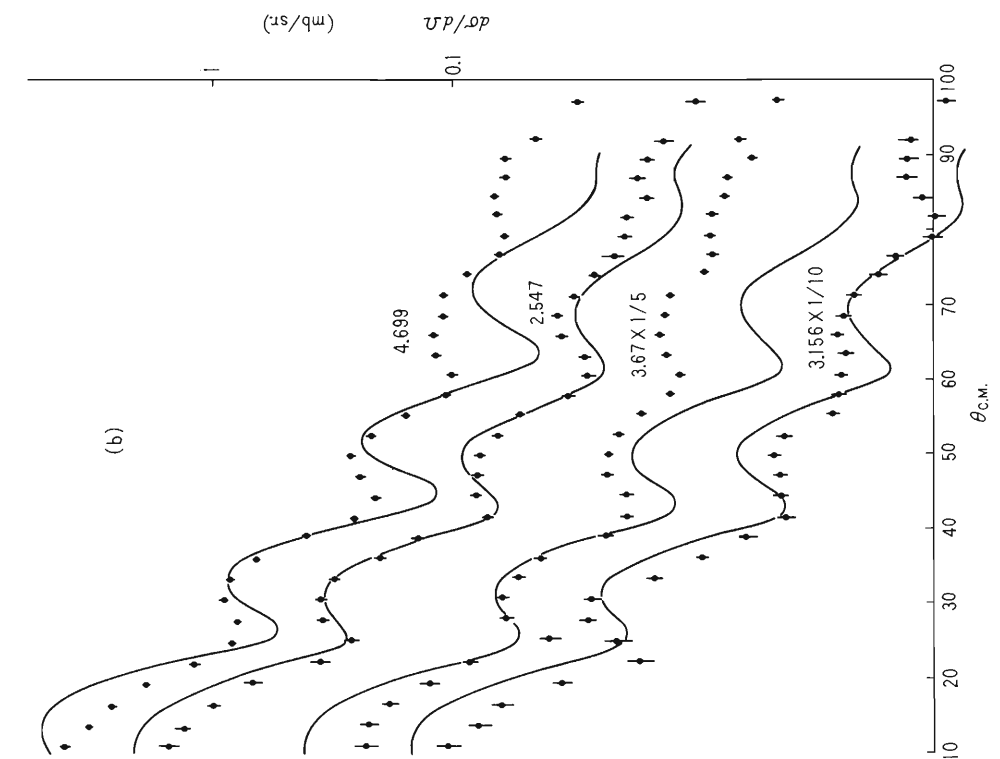


Fig. 2(b).

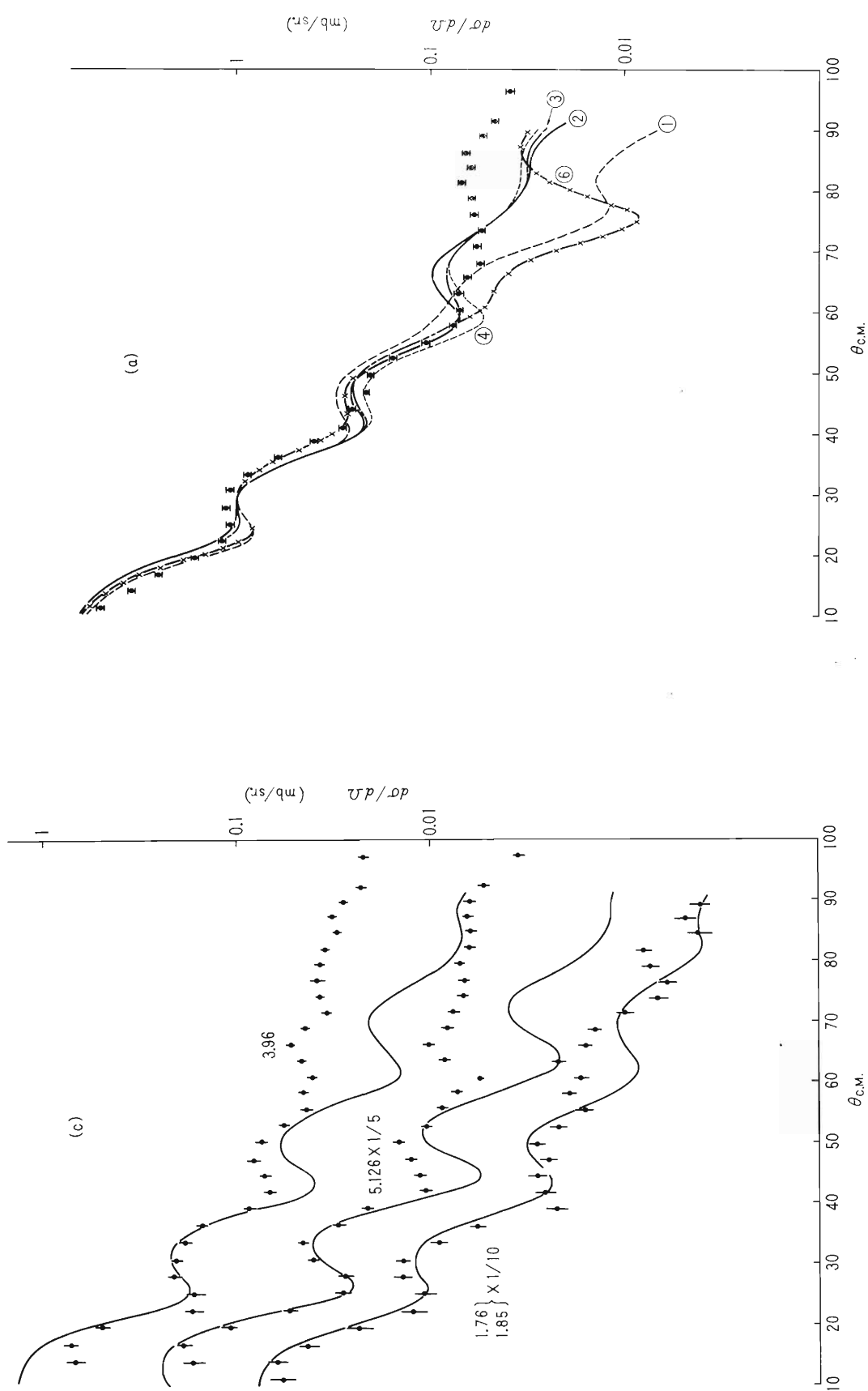


Fig. 2(c).

Fig. 2. The angular distribution of α particles which can be fitted by $l = 2$ neutron transfer. Values of excitation of the residual nucleus ^{26}Al are given to each curve. Solid lines are results of DWBA analyses.

Fig. 3(a).

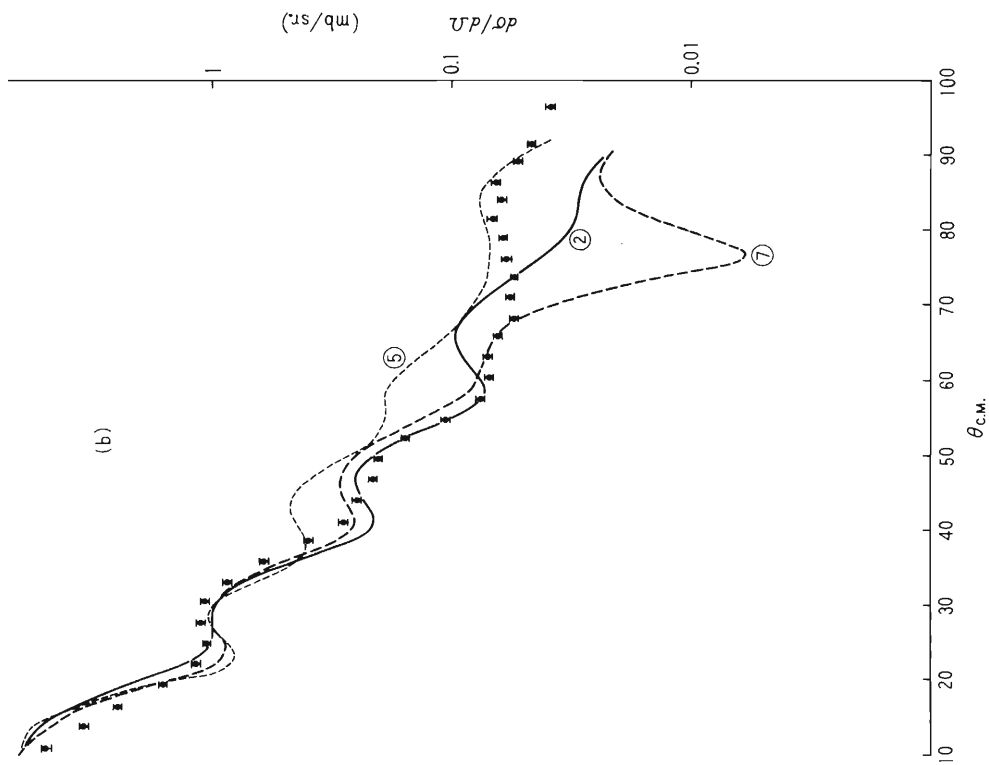


Fig. 3(b).

Fig. 3. Comparison of DWBA fits of various combination of input and exit channel optical parameters to the ground state transition. Numbers correspond to the set number of Table 1.

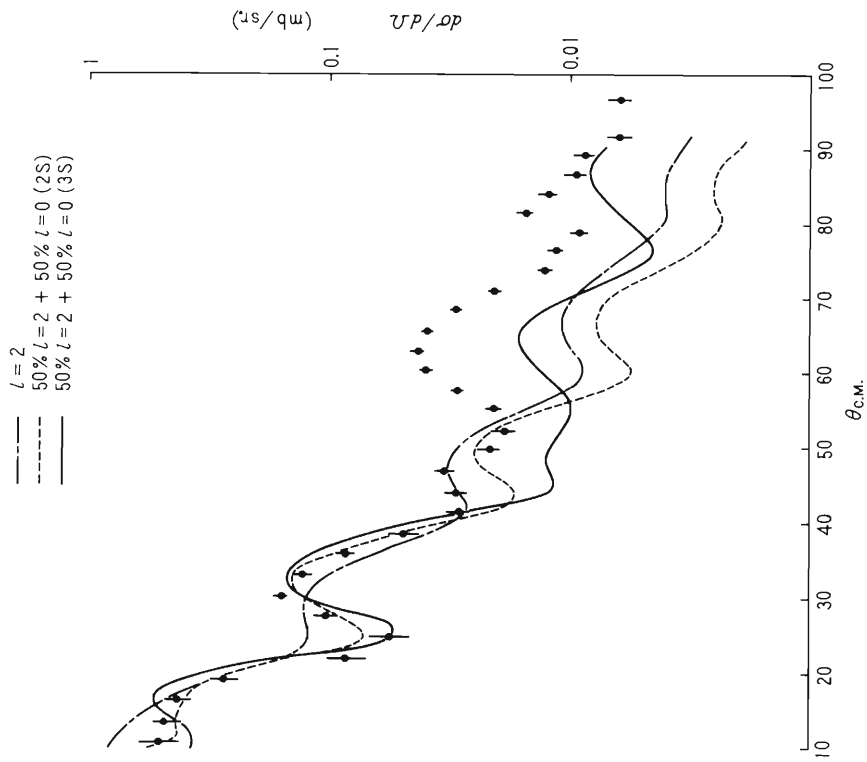


Fig. 4. Fits of DWBA calculations to the transition to the 0.418 state.

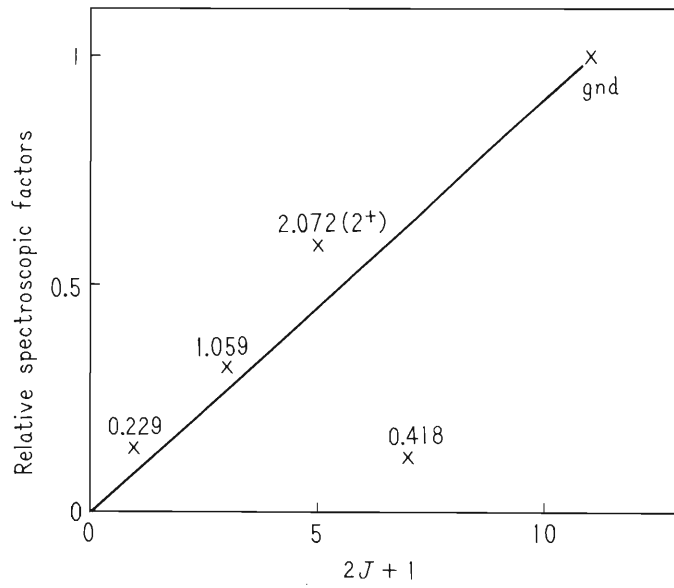


Fig. 5. Relative spectroscopic factors plotted against $2J + 1$.

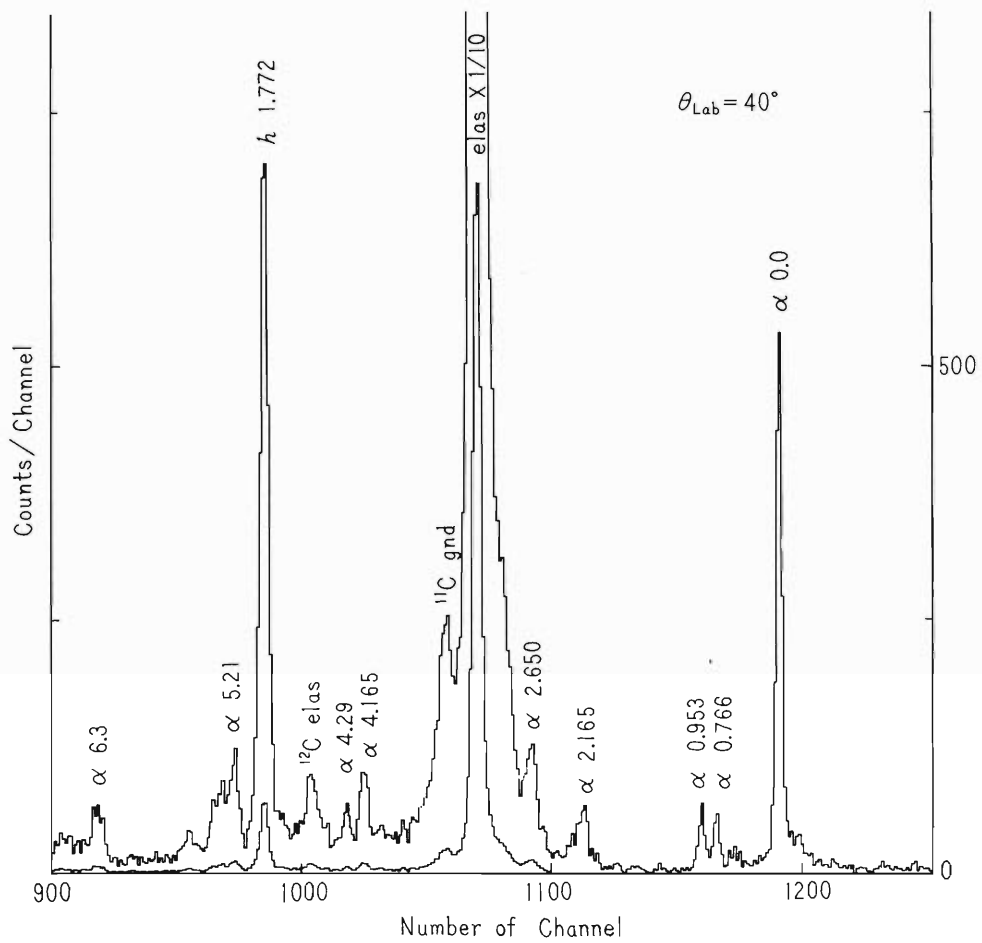
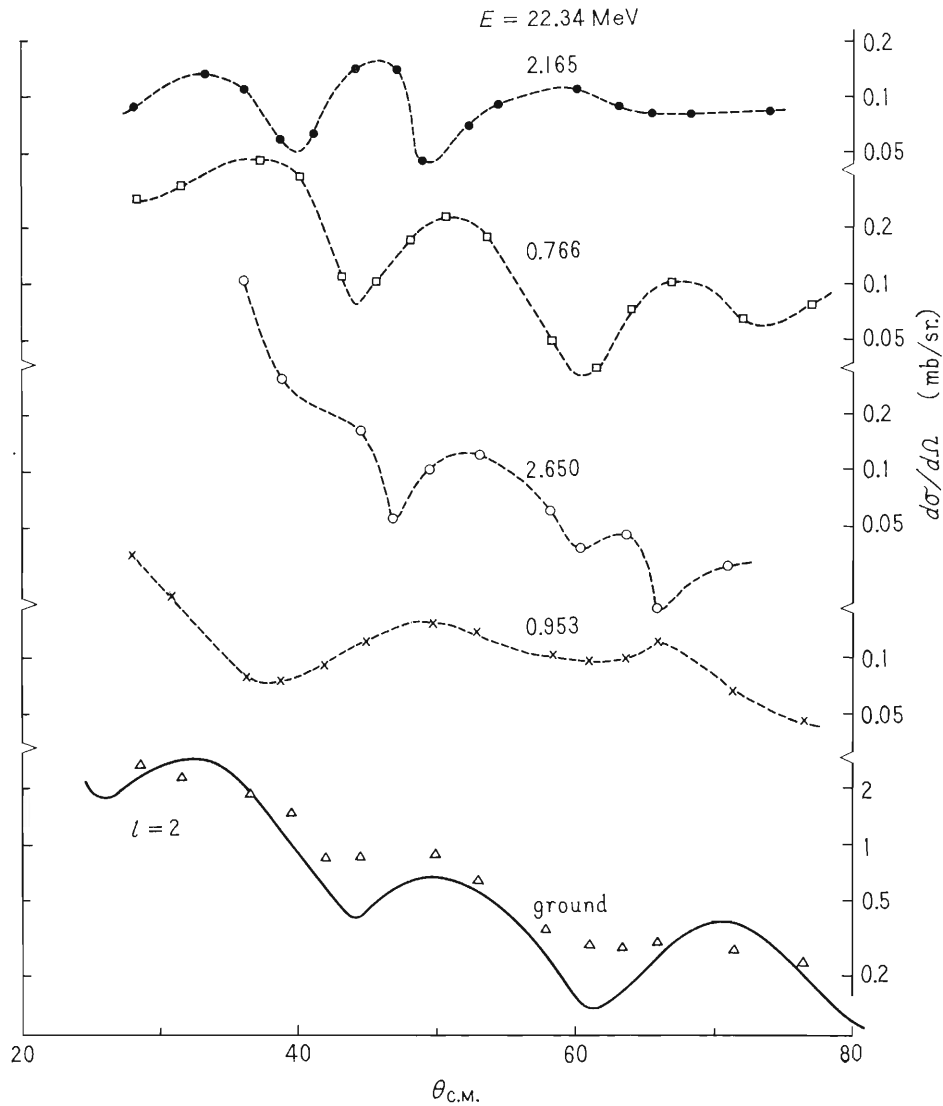


Fig. 6. $^{28}\text{Si} + ^3\text{He}$ spectrum at 22.34 MeV. Meanings of notation are the same with those of Fig. 1.



Optical parameters of the input channel are $V = 122.76$, $W = 15.57$, $r_V = 1.26$, $r_W = 1.74$, $a_V = 0.693$, $a_W = 0.788$. Those of α channel, is No. 2 of Table 1.

Fig. 7. Angular distributions of $^{28}\text{Si}(^3\text{He}, \alpha)^{27}\text{Si}$ reaction.

References

- 1) M. Kawai, K. Kubo, and H. Yamaura: INS DWBA 2 Code (unpublished).
- 2) R. Stock, R. Bock, P. David, H.H. Duhamel, and T. Tamura: Nucl. Phys., A104 136 (1967).
- 3) K. Matsuda et al.: This progress report, p.36.
- 4) L. McFadden and G.R. Satchler: Nucl. Phys., 84, 177 (1966).
- 5) J. Nurzynski, K.H. Bray, and B.A. Robson: *ibid.*, A107, 581 (1968).
- 6) V.A. Vlasov, S.P. Kalinin, A.A. Ogloblin, and V.I. Chuev: JETP (Sov. Phys.), 10, 844 (1960).
- 7) P.R. Bevington and A.S. Anderson: Bull. Am. Phys. Soc., 11, 908 (1966).
Progress Report Dept. Phys. Stanford Univ., p. 12 (1967).
- 8) A. Weidinger, R.H. Siemssen, G.C. Morrison, and B. Zeidman: Nucl. Phys., A108, 547 (1968).
- 9) R.W. Barnard and G.D. Jones: *ibid.*, p. 641.
- 10) S. Takeda et al.: This progress report, p. 63.

5-4. The (d, d), (d, d'), and (d, t) Reactions of ^{27}Al and ^{28}Si

S. Takeda, M. Odera, and I. Kohno

The (d, d), (d, d'), and (d, t) reactions have been investigated on the ^{27}Al and ^{28}Si targets at a bombarding energy of 21.6 MeV using a particle-identifier circuit.* The energy analyzed deuteron beam was passed through thin metallic targets of aluminum ($350 \mu\text{g}/\text{cm}^2$) or natural silicon ($600 \mu\text{g}/\text{cm}^2$), and collected in a Faraday cup at the rear of the 75 cm scattering chamber. The reaction products were observed with a dE/dx -E counter telescope consisting of two silicon surface barrier detectors (200μ or 50μ thick for ΔE detector and 2000μ thick for E detector). An over-all electronic noise width of 30 keV was obtained and the over-all deuteron and triton energy resolution for aluminum target was about 75 keV. A typical deuteron spectrum on the silicon target (Fig. 1) shows that several levels of ^{28}Si as high as 10 MeV excitation energy are considerably excited. Especially 9.314 MeV level ($J\pi = 3^+$, $T=1$) is observed distinguishably. Angular distribution for this ΔT forbidden reaction is shown in Fig. 2, and the other ones for several levels of ^{28}Si are shown in Fig. 3. The angular distributions of the 1.78 MeV 2^+ , 6.88 MeV 3^- , and 4.975 MeV 0^+ levels show clear diffraction patterns, while that of the 4.62 MeV 4^+ level shows no remarkable pattern. The 6.27 MeV 3^+ level is rather weakly excited, and the 6.68 MeV 0^+ level is not excited. Optical-model analysis for the elastic scattering and DWBA analyses for the inelastic scattering are in progress.

The reaction $^{28}\text{Si}(d, t)$ is expected to give a detailed information concerning the shape of ^{28}Si .¹⁾ The excitation of the 0.77 MeV $1/2^+$ level is the evidence for a $2S_{1/2}$ admixture in the ^{28}Si ground state. The $\ell_n = 0$ angular distribution for this level in the (h, α) reaction has been observed by L. W. Swenson et al.²⁾ On the other hand, the 0.952 MeV $3/2^+$ level indicates the same $\ell_n = 2$ neutron pickup as the ground state $5/2^+$.²⁾ According to the results of the present (d, t) reaction (Fig. 4), the angular distribution pattern of $3/2^+$ level is similar to that of $5/2^+$ level, but obviously another ℓ_n will be assigned for $1/2^+$ level. Although detailed discussions have to be made under DWBA analyses (now in progress), the fact that the lower levels of $5/2^+$, $3/2^+$, and $1/2^+$ were excited fairly well would suggest a difficulty to interpret the ground state of ^{28}Si in terms of a simple Nilsson model.

The results of $^{27}\text{Al}(d, d)$ and (d, d') reactions are shown in Fig. 5. Angular distributions of tritons on the $^{27}\text{Al}(d, t)$ ^{26}Al reactions are shown in Fig. 6. Some discussions on the results of (d, t) reaction in comparison with $(^3\text{He}, \alpha)$ are given by M. Odera et al.³⁾ Theoretical analyses are now under way.

* ORTEC Model 423.

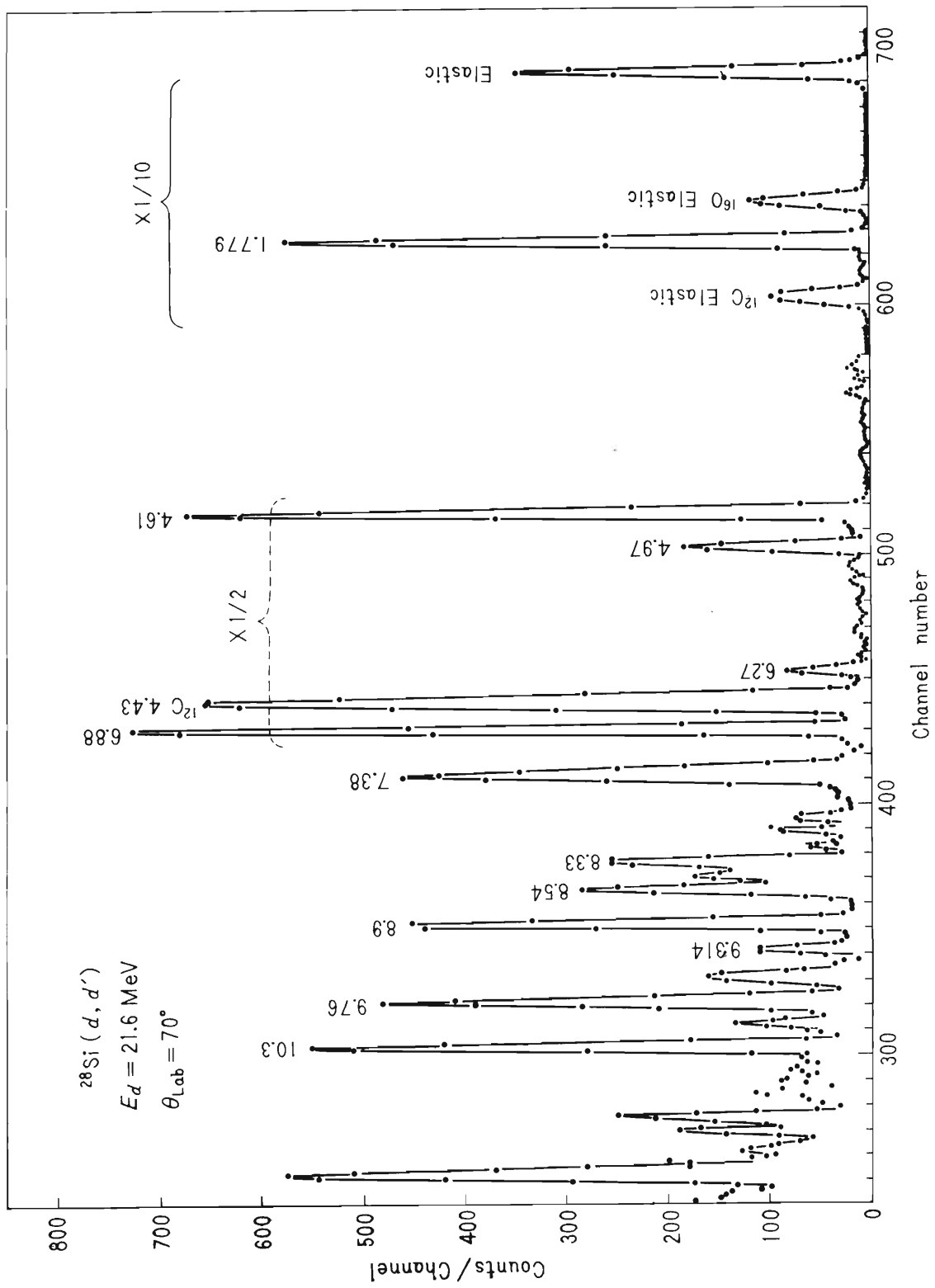


Fig. 1. Deuteron spectrum produced by 21.6 MeV deuterons at $\theta_{\text{Lab}} = 70^\circ$. The 9.314 MeV level was assigned by the kinematical method.

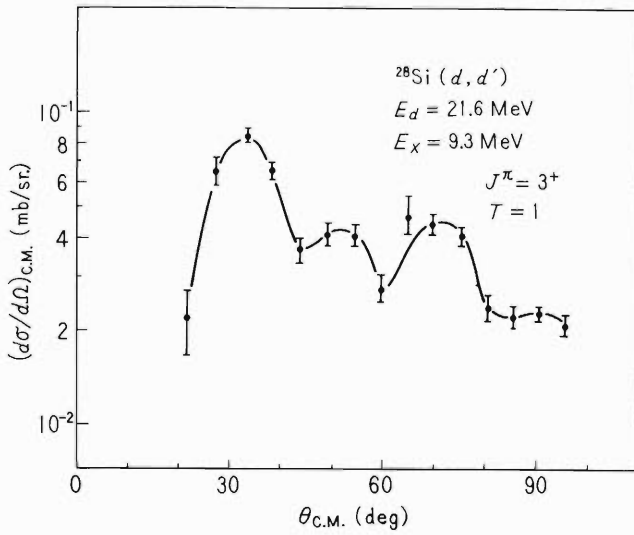


Fig. 2. Deuteron angular distribution for the 9.314 MeV level of ^{28}Si from the $^{28}\text{Si}(d,d')$ reaction.

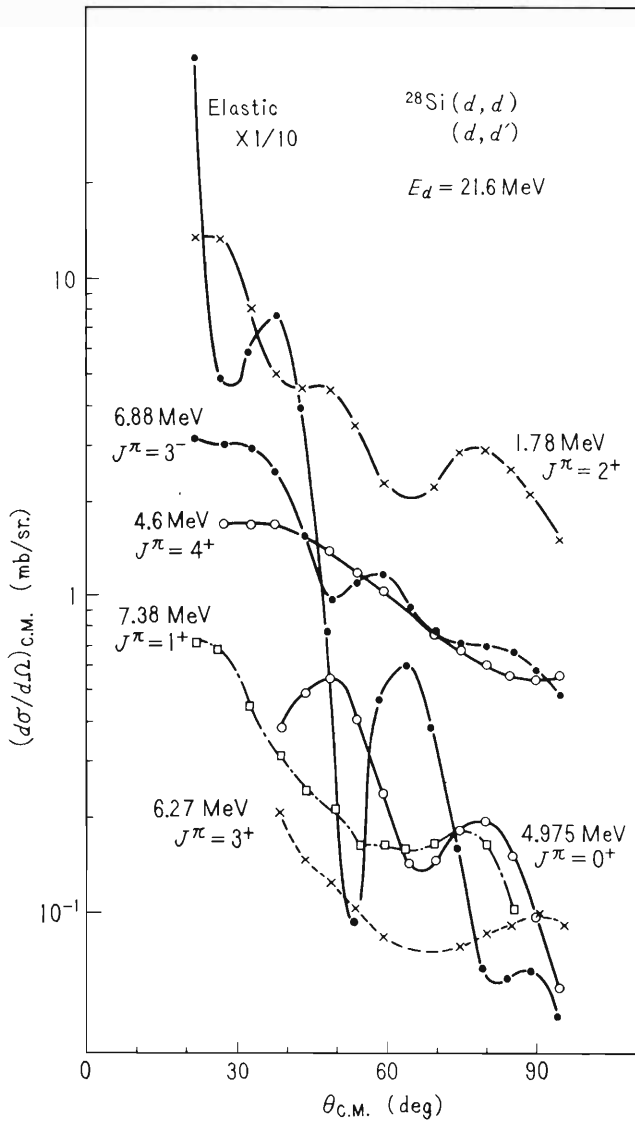


Fig. 3. Deuteron angular distributions for the $^{28}\text{Si}(d,d)$ and (d,d') reactions.

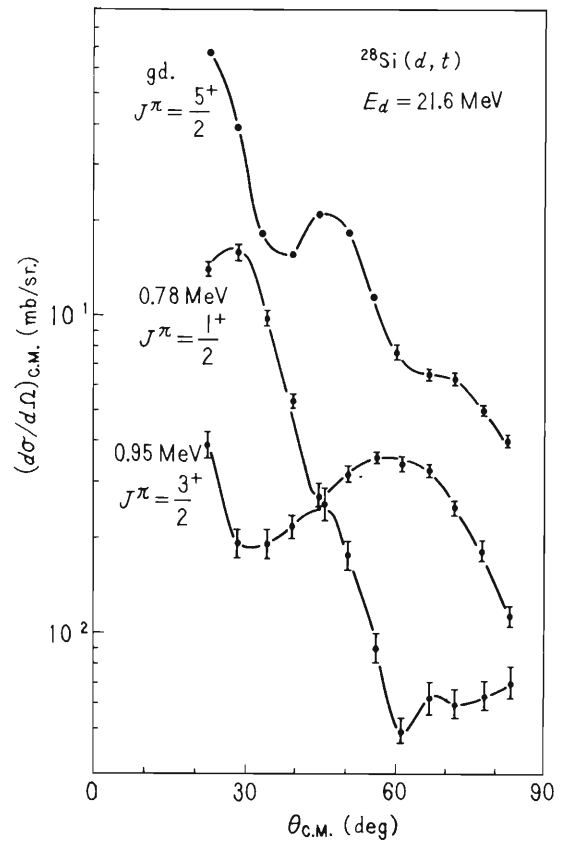


Fig. 4. Triton angular distributions for the $^{28}\text{Si}(d,t)$ reaction.

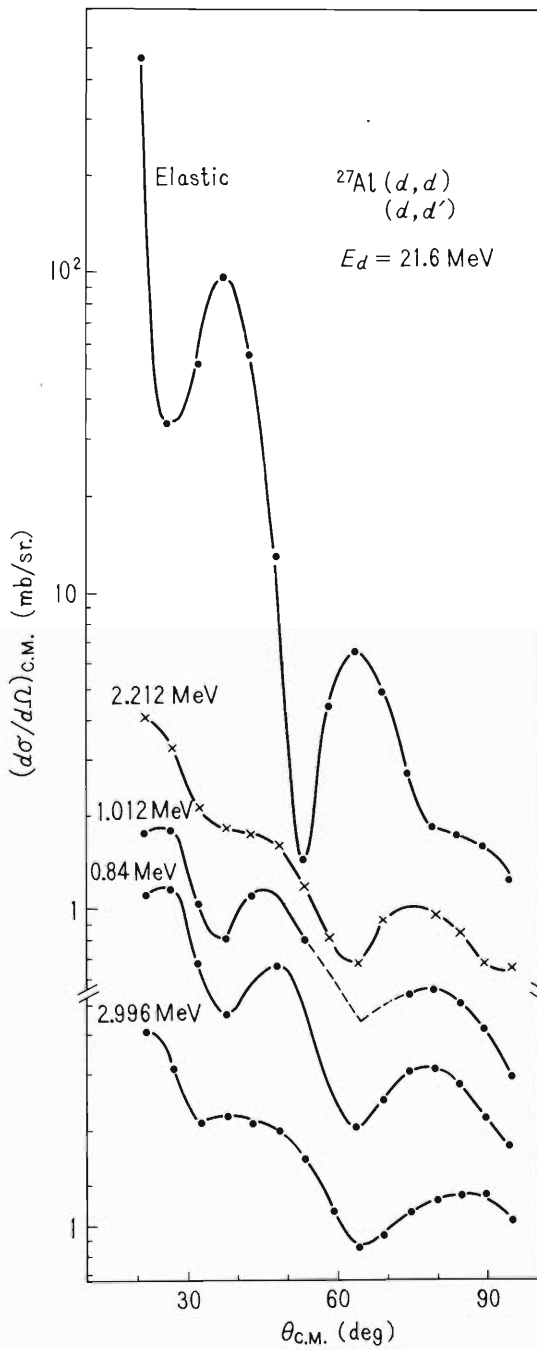


Fig. 5. Deuteron angular distributions for the ^{27}Al (d,d) and (d,d') reactions.

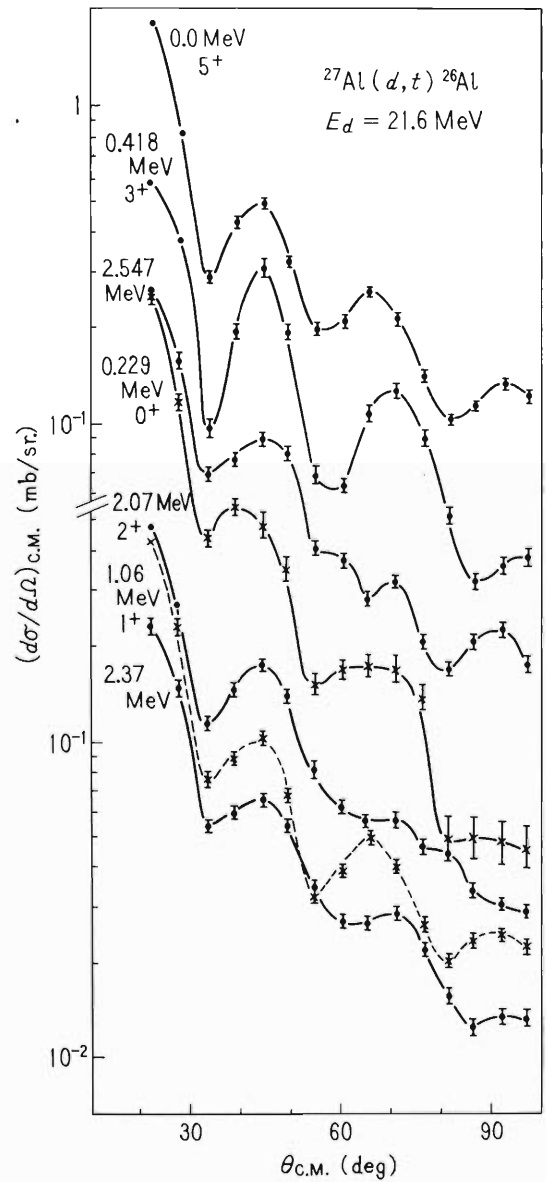


Fig. 6. Triton angular distributions for the ^{27}Al (d,t) ^{26}Al reaction.

References

- 1) G. Ripka: Intern. Nucl. Phys. Conf., Gatlinburg, Tenn., Sept. (1966).
- 2) L.W. Swenson, R.W. Zurmühle, and C.M. Fou: Nucl. Phys., **A90**, 232 (1967).
- 3) M. Odera, I. Kohno, and S. Takeda: This progress report, p. 54.

5-5. Inelastic Scattering of Protons from ^{91}Zr

Y. Awaya, K. Matsuda, N. Nakanishi,
S. Takeda, and T. Wada

The inelastic scattering of protons from nucleus is considered to be a powerful tool for investigating the collective states. This process also gives the information about the microscopic description of the states in some cases. This work has been intended to develop on these points of view. The excited states in ^{91}Zr have been studied extensively by one-nucleon transfer reactions of various types,¹⁻⁶⁾ which excite a particle or hole state preferentially. The levels excited by various reactions^{1,6,7,8)} are shown in Fig. 1 in comparison with the results obtained in the present work.

The ^{91}Zr target was a self-supporting metallic foil with a thickness of 0.82 mg/cm² prepared by the ORNL Isotopes Division. The isotopic abundances for the target are as follows: ^{90}Zr , 5.00 %; ^{91}Zr , 90.88 %; ^{92}Zr , 3.29 %; ^{94}Zr , 0.84 %; ^{96}Zr , ≤ 0.2 %. The energy analyzed proton beam was led to a 75 cm scattering chamber where the target was placed with an inclination of 45° with respect to the beam. The energy of the protons was 14.52 MeV at the center of the target. The scattered protons were detected by a surface-barrier silicon detector with a depletion layer of 2 mm. The over-all energy resolution was 50 keV FWHM in the best condition and about 60 keV FWHM on the average. At some angles, a ΔE -E counter telescope was used to check the peaks caused by other reactions. A typical spectrum of the protons is shown in Fig. 2. The measurements were made from 20° to 160° at 5° intervals for the elastic scattering and from 30° to 160° at the same intervals as above.

The angular distribution for the elastic scattering is shown in Fig. 3 with the theoretical curve obtained by the optical model calculations. Optical parameters are the same as those obtained by Matsuda et al.⁹⁾ for the $^{90,92}\text{Zr}(p, p')$ reactions at about 14.5 MeV. The automatic search of the parameters is now in progress. The angular distributions for the inelastic scattering are shown in Figs. 4, 5, and 6. The error bars show the statistical errors only. The DWBA calculations are made for these angular distributions by using the code "INS-DWBA 2". The one phonon excitation process is employed in the calculations and the form factor is the derivative of the real potential of Woods-Saxon type with the Coulomb excitation term. The theoretical curves are shown in Figs. 4 and 5. The excitation energy, ℓ value and deformation parameter β_ℓ are listed in Table 1. The angular distributions for the 1.17, 1.44, and 1.84 MeV states are fit to the theoretical curves for $\ell = 2$. These states are considered to be the same as have been observed in the one-nucleon transfer reactions and assigned to have the spin-parities of $1/2^+$, $5/2^+$, and $7/2^+$, respectively. The calculation of β_2 values for these states is made on the basis of these values. As the spectroscopic factors for the 1.17, 1.44, and 1.84 MeV states obtained in the (d,p) reaction¹⁾ are 0.72, 0.09, and 0.062, respectively, the weak-coupling excited-core model, which means the coupling of $d5/2$ neutron to the quadrupole core excitation in this case, seems not to be a good description for these states when the values of β_2 and of spectroscopic factors are taken into consideration. The experimental values for the 1.84 MeV state at 35° and 40° are much larger than the theoretical ones. At these angles the 1.84 MeV peak becomes broad and this may be caused by the excitation of 1.78 MeV state of ^{28}Si in the detector. The angular distributions for the 2.00, 2.12, 2.52, 2.64, 2.77, and 2.98 MeV states are fit to the theoretical curves for $\ell = 3$. As the peaks at 2.64, 2.70, 2.77, and 2.89 and at 2.98

and 3.06 MeV are not completely resolved, the intensity of each peak is estimated by using the automatic search code on the assumption that each peak shows a Gaussian distribution with the same width as the elastic peak. The 2.00, 2.12, 2.52, 2.64, 2.77, and 2.98 MeV states are considered to be the members of the sextet which are caused by the coupling of $d_{5/2}$ neutron to the octupole core excitation. They are different from the even-parity states excited in the one-nucleon transfer reactions. It is expected, of course, that a small portion of the differential cross sections for these states are due to the excitation of the states assigned by one-nucleon transfer reactions. When the weak-coupling excited-core model is adopted for these levels, the sum of their cross sections should reproduce the angular distribution of the 3^- states in ^{90}Zr obtained in the $^{90}\text{Zr}(p,p')$ reaction⁹⁾ and this condition seems to be satisfied.

The angular distributions for the 2.30, 2.87, 3.06, 3.22, 3.42, 3.62, and 3.85 MeV states are shown in Fig. 6. The analysis for these states are not made yet. The 2.30, 3.22, 3.42, 3.62, and 3.85 MeV peaks are unresolved.

The analysis is under way and all the results presented here are preliminary ones.

Table 1. Excited states in ^{91}Zr .

Excit. energy (MeV)	ℓ	β_ℓ
1.17	2	0.17
1.44	2	0.12
1.84	2	0.12
2.00	3	
2.12	3	
2.30*		
2.52	3	
2.64	3	
(2.70)		
2.77	3	
2.87		
2.98	3	
3.06		
3.22*		
3.42*		
3.62*		
3.85*		

Asterisk indicates a group of unresolved levels.

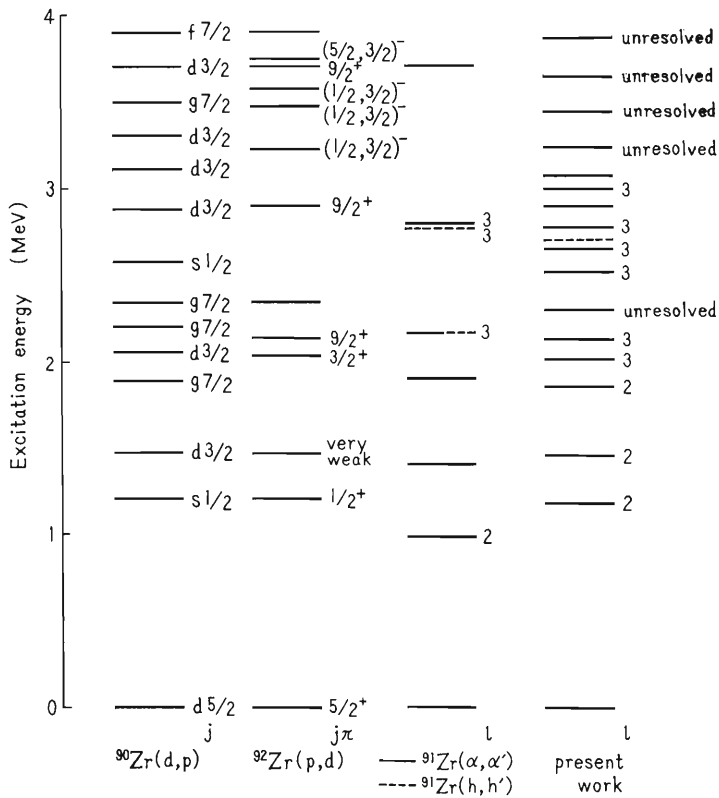


Fig. 1. The excited states in ^{91}Zr obtained by various reactions and the results of the present work. Data of previous works are taken from Refs. 1, 3, 6, 7, and 8.

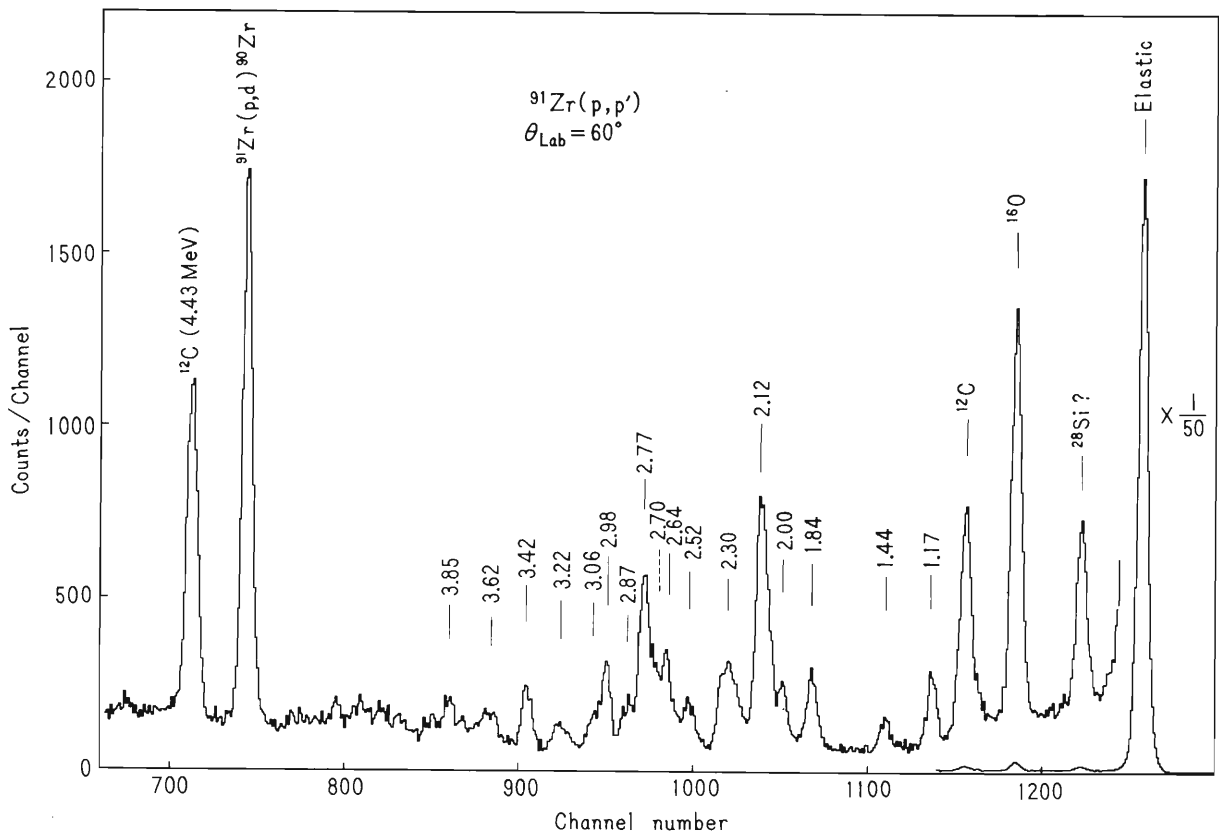


Fig. 2. The typical spectrum of protons obtained at $\theta_{\text{Lab.}} = 60^\circ$. The excitation energies are given in MeV.

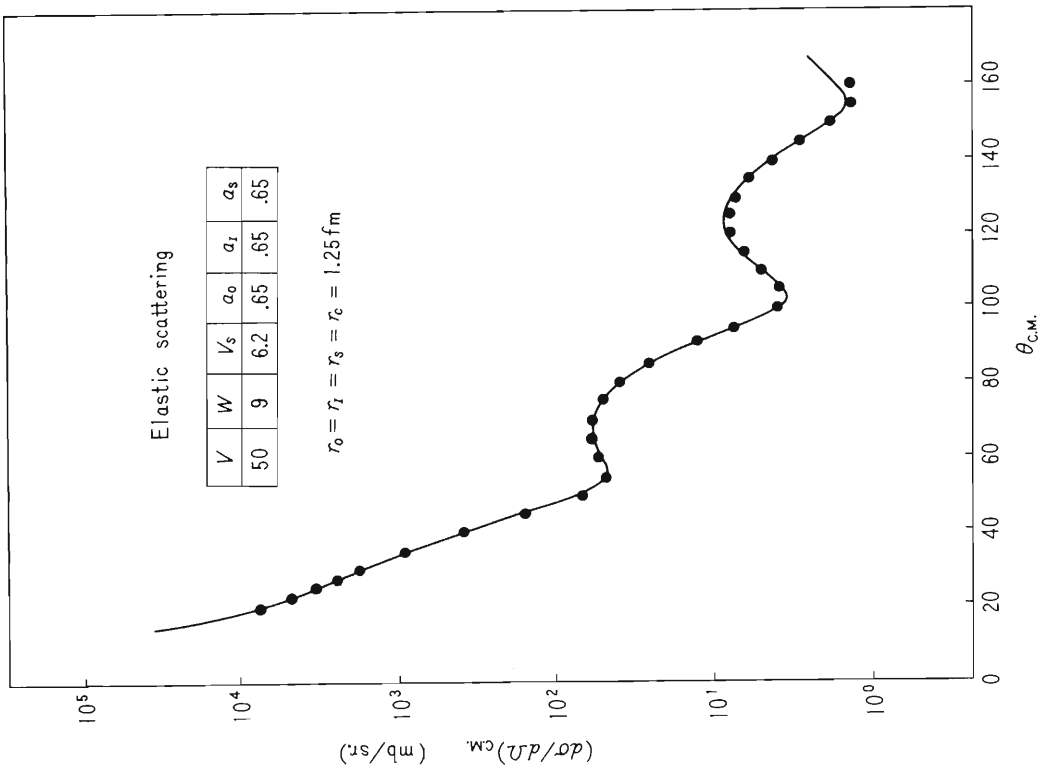


Fig. 3. The angular distribution for the elastic scattering. The curve is obtained from the optical model calculation and the parameters are also shown. The form of the optical potential is $-Vf(r, r_0, a_0) + 4ia_1 W \frac{d}{dr} f(r, r_1, a_1) + 2 \left(\frac{\hbar}{m\pi c}\right)^2 V_s \frac{1}{r} \frac{d}{dr} f(r, r_s, a_s) \times (\mathcal{L} \cdot \mathbf{s}) + V_{\text{coulomb}}, f(r, r_0, a_0) = \{1 + \exp\{(r - r_0 A^{1/3})/a_0\}\}^{-1}$. The theoretical curve is multiplied by the factor 0.98.

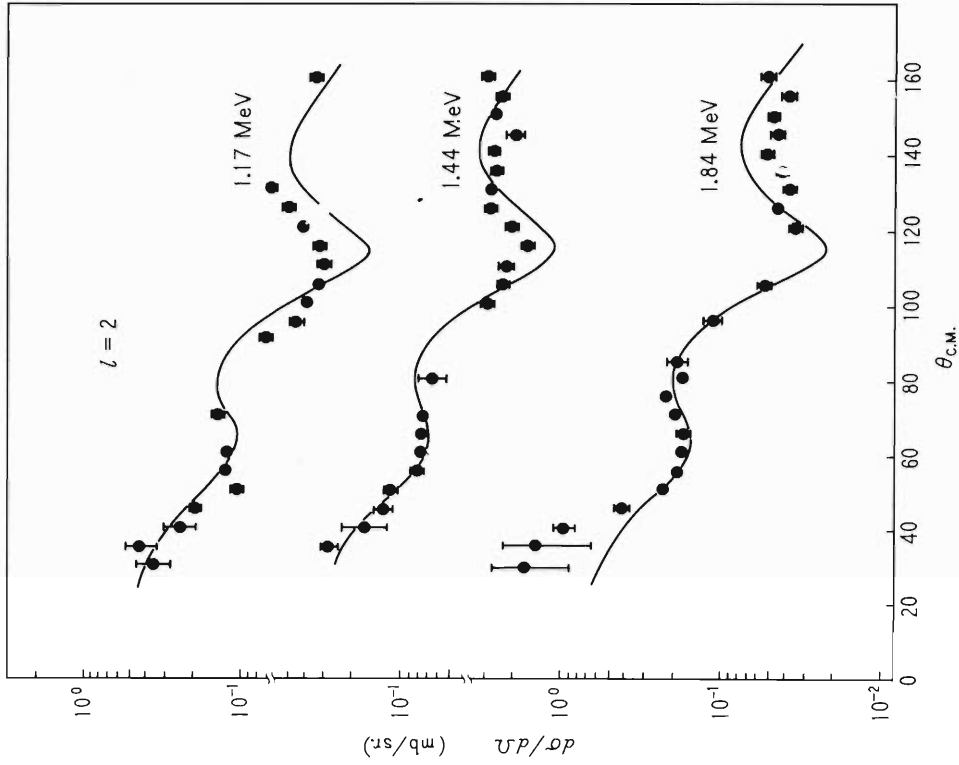


Fig. 4. The angular distributions for the 1.17, 1.44, and 1.84 MeV states. The curves are obtained by the DWBA calculation with the 22-pole one-phonon excitation.

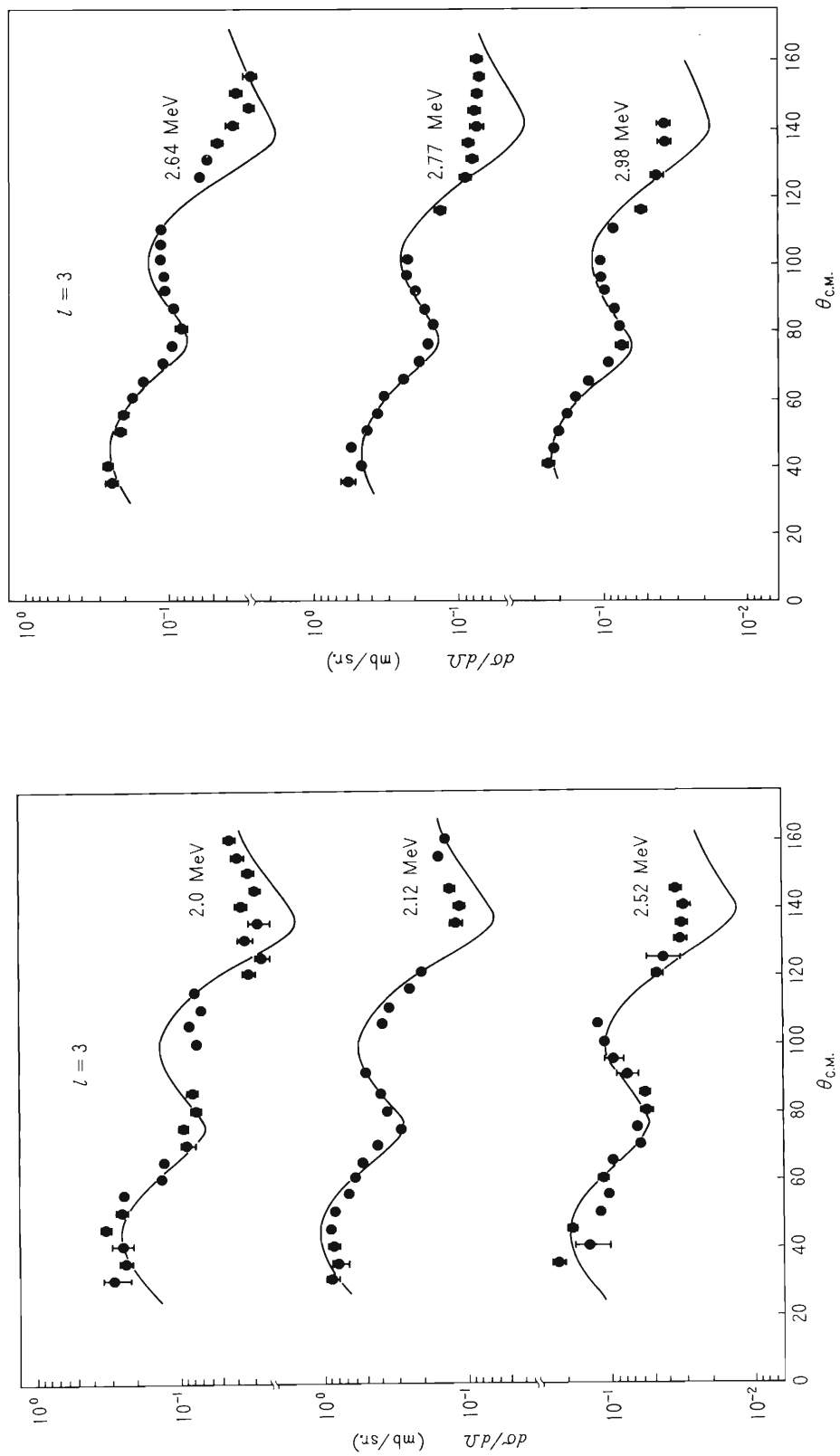


Fig. 5. The angular distributions for the 2.00, 2.12, 2.52, 2.64, 2.77, and 2.98 MeV states. Theoretical curves calculated for $\ell = 3$ are also shown.

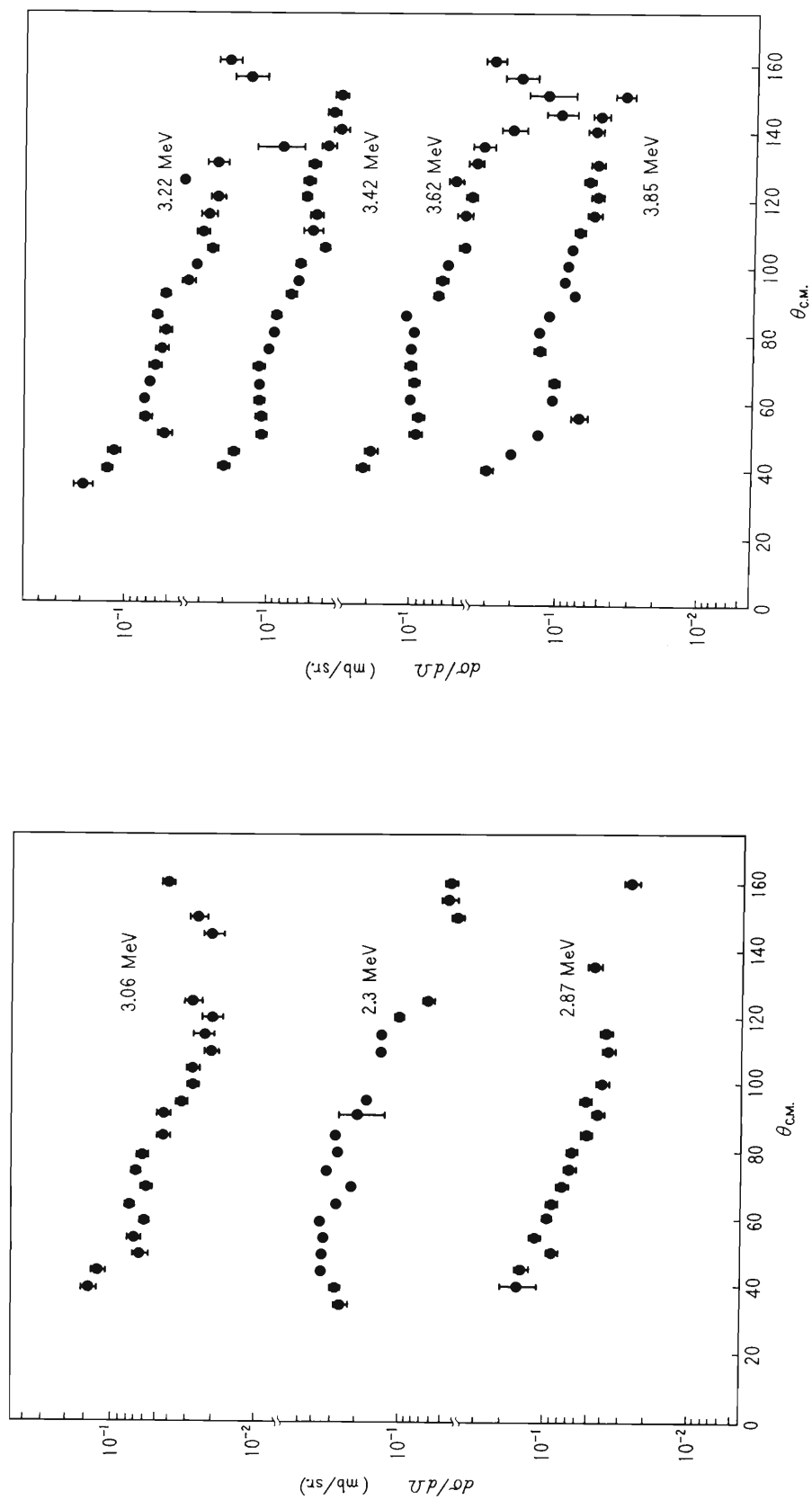


Fig. 6. The angular distributions for the 2.30, 2.87, 3.06, 3.22, 3.42, 3.62, and 3.85 MeV states.

References

- 1) B.L. Cohen and O.V. Chubinsky: *Phys. Rev.*, 131, 2184 (1963).
- 2) J.S. Forster, L.L. Green, N.W. Henderson, J.L. Hutton, G.D. Jones, and J.F. Sharpey-Schafer: *Nucl. Phys.*, A101, 113 (1967).
- 3) C.R. Bingham, M.L. Halbert, and R.H. Bassel: *Phys. Rev.*, 148, 1174 (1966).
- 4) D.E. Rundquist, M.K. Brussel, and A.I. Yavin: *ibid.*, 168, 1296 (1968).
- 5) G. Bassani and J. Picard: "Proceeding of the Symposium on Direct Reactions with ^3He (Sept. 1967)" IRCR Cyclotron Progress Report, Supplement 1, p. 101 (1967).
- 6) J.B. Ball and C.B. Fulmer: *Phys. Rev.*, 172, 1199 (1968).
- 7) H.W. Broek and J.L. Yntema: *ibid.*, 138, B334 (1965).
- 8) D.E. Rundqvist, M.K. Brussel, and A.I. Yavin: *ibid.*, 168, 1287 (1968).
- 9) K. Matsuda, H. Nakamura, I. Nonaka, H. Taketani, T. Wada, Y. Awaya, and M. Koike: *J. Phys. Soc. Japan*, 22, 1311 (1967).

5-6. The $^{12}\text{C}(^3\text{He}, p)^{14}\text{N}$ and $^{27}\text{Al}(^3\text{He}, p)^{29}\text{Si}$ Reactions

N. Nakanishi, S. Takeda, T. Wada,
Y. Awaya, and K. Matsuda

The two-nucleon transfer reaction is now an open problem. The two like-nucleon transfer is especially interested regarding the collective enhancement. The deuteron transfer reaction is also expected as a tool for the nuclear spectroscopic study if the reaction mechanism of the two-nucleon transfer is elucidated. On this point of view, the $^{12}\text{C}(^3\text{He}, p)^{14}\text{N}$ reaction has been taken up at first and the experimental result has already been published,¹⁾ while, a special code for the DWBA analysis is under preparation.²⁾ In the study of $^{12}\text{C}(^3\text{He}, p)^{14}\text{N}$, a particular interest was given to the difference between $(^3\text{He}, p)$ and (α, d) . Of course, the $(^3\text{He}, p)$ reaction transfers not only a $T=0, S=1$ deuteron as the (α, d) reaction, but also a $T=1, S=0$ n-p system. Even for the transfer of a $T=0, S=1$ deuteron, the individual level is excited differently by the $(^3\text{He}, p)$ and by the (α, d) .¹⁾

As the next target, we have taken up the $^{27}\text{Al}(^3\text{He}, p)^{29}\text{Si}$ reaction in order to investigate the mechanisms of deuteron-transfer reactions which go to the residual nucleus ^{29}Si and to test the structure of ^{29}Si . The bombarding energies reported on the reaction^{3,4)} lie in the region where the compound nucleus formation process is not negligible.

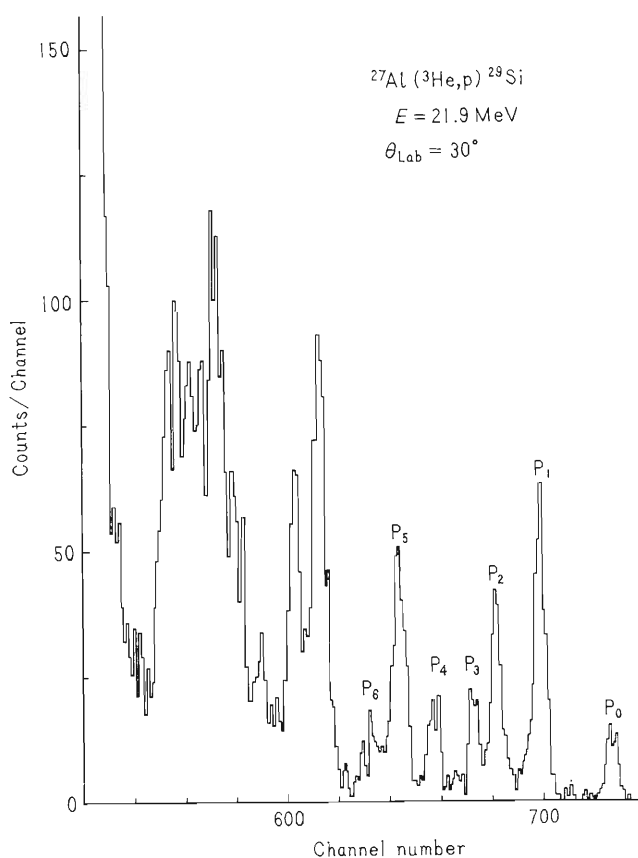


Fig. 1. Proton spectrum of the $^{27}\text{Al}(^3\text{He}, p)^{29}\text{Si}$ reaction at $E_{\text{h}} = 21.9 \text{ MeV}$ and $\theta_{\text{L}} = 30^\circ$.

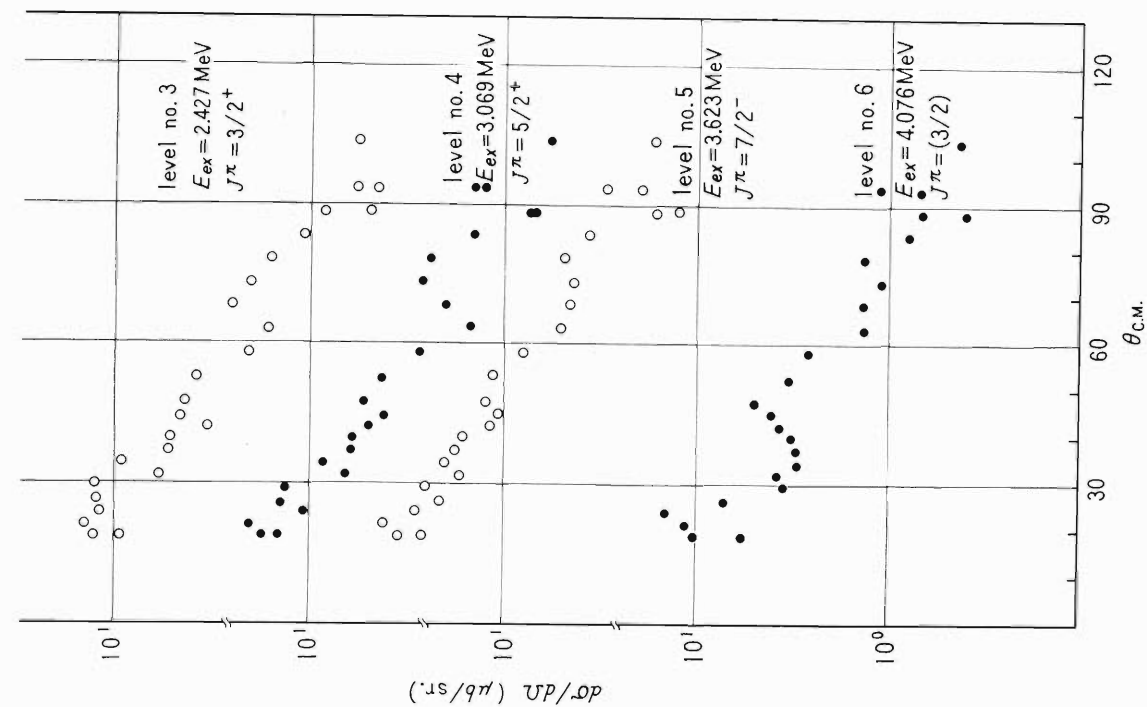


Fig. 2 (b). Angular distributions of the $^{27}\text{Al}(^3\text{He}, p)^{29}\text{Si}$ reaction for the low-lying states.

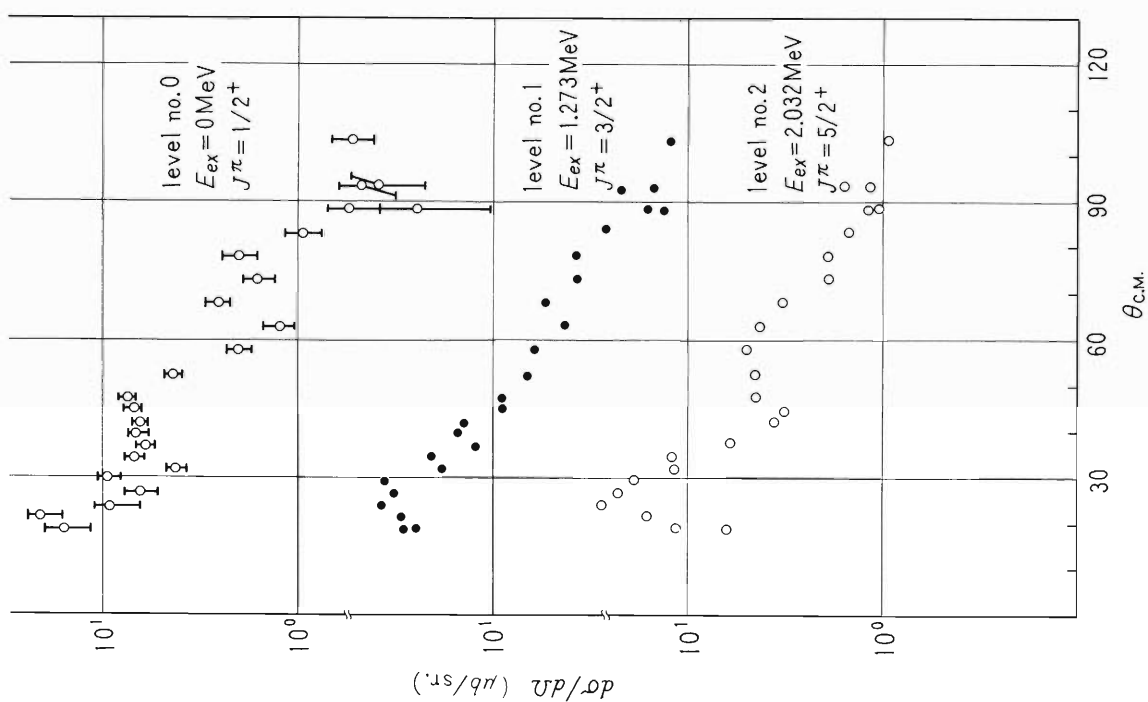


Fig. 2 (a). Angular distributions of the $^{27}\text{Al}(^3\text{He}, p)^{29}\text{Si}$ reaction for the low-lying states.

The residual nucleus ^{29}Si through the deuteron-transfer reactions has some advantages as well as disadvantages. On the favorable side, ^{27}Al and ^{31}P which are targets in the cases of deuteron stripping and pick up reactions respectively, are monoisotopic elements. Moreover, low-lying levels of ^{29}Si is relatively separated and the unified model is also considered to be applicable. On the disadvantageous side, the ground state spin $5/2^+$ of ^{27}Al makes the angular momentum transfer complicated, while the isospin of $T=1/2$ makes the reaction interesting.

A self-supporting target with thickness of about $600 \mu\text{g}/\text{cm}^2$ was bombarded with 21.89 MeV $^3\text{He}^{++}$ beam from the IPCR cyclotron. Emitted protons were detected by a ΔE -E solid state counter telescope, which was composed of a $300 \mu\text{m}$ totally depleted silicon surface barrier detector (ΔE -counter) and two $3000 \mu\text{m}$ totally depleted Li-drifted detectors (E-counter), and discriminated using a Goulding-Landis particle identifier. Overall energy resolution was about 100 keV.

Fig. 1 shows a proton spectrum at the scattering angle (Lab.) of 30 deg. Figs. 2 (a) and 2(b) show preliminary results of angular distributions with excitation energies, spins and parities corresponding to the ground state and first six excited states of the residual nucleus ^{29}Si . Each of differential cross sections observed includes a considerably large statistical error.

Many more levels were excited at higher excitation energies, whose analyses are now in progress.

References

- 1) K. Matsuda, N. Nakanishi, S. Takeda, and T. Wada: J. Phys. Soc. Japan, 25, 1207 (1968).
- 2) S. Yamaji: This progress report, p. 83 .
- 3) S. Gorodetzky, G. Bassompierre, et A. Gallmann: Nucl. Phys., 62, 575 (1965).
- 4) R.L. McGrath: *ibid.*, 85, 161 (1966).

5-7. Double Scattering of ^3He from Carbon

T. Fujisawa, H. Kamitsubo, S. Motonaga,
K. Matsuda, H. Sakaguchi,* and K. Masui*

The measurement of ^3He polarization is important for the determination of the spin-orbit term in the optical model potential as shown in Section 5-1 about the elastic scattering of ^3He from nuclei. Experiments of the ^3He double scattering from carbon have been carried out at Birmingham¹⁾ and Colorado.²⁾

Their results gave some discrepancies and different values of the spin-orbit depth.

We now report a new experiment on the double scattering of ^3He by ^{12}C at energy of 34 MeV. The measurement have been carried out using silicon semiconductor detectors and a particle identification system to discriminate other particles. Figs. 1 and 2 show the geometrical condition of the experiment and the particle identification system. The double scattering experiment was at first carried out with the first tantalum target and the second carbon target and then the first target was replaced by carbon. Then the first target was replaced again by tantalum, as the carbon result was sandwiched between the tantalum result. The measurement was repeated in the same way at the opposite angle and the results were averaged. Thus the asymmetry of the beam position and the analyzer would be eliminated since the asymmetry due to polarization by tantalum was expected to be small. Fig. 3 shows the result.

The tendency of angular distribution does not agree with the former result by Birmingham group. So we calculated polarizations and differential scattering cross sections at the incident energy of 34 MeV by some optical model potentials³⁻⁵⁾ listed in Table 1. The results are shown in Fig. 4. We can see not only discrepancies of calculated polarizations but also those of predicted differential scattering cross sections. The type of the imaginary part of optical potential affects the tendency of the polarization. Namely, the polarization calculated with the potential of Seattle is similar to that calculated with Colorado potential. Their imaginary parts are surface types. On the other hand, the polarization with Birmingham potential is similar to that with Riken potential, by using the volume type imaginary potentials.

At this stage, we should have suitable optical potentials, so we measured elastic scatterings of ^3He from carbon at energies of 25, 30, 35, and 40 MeV. Fig. 5 shows the results but the analysis has not been carried out.

We wish to thank Mr. J. Fujita for his help in electronics and data taking.

* On leave from the University of Tokyo.

Table 1.

Group	Birmingham	Colorado	Riken	Seattle
V_0	76.64	127.1	171.0	172.015
r_0	1.057	1.93	0.899	1.225
a_0	0.881	0.87	0.817	0.7249
W_1 (Volume)	16.6	2.34	7.8	
r_0'	1.77	1.38	2.25	
a_0'	0.744	0.85	0.638	
W_2 (Surface)		11.5		9.7
r_0''		1.38		1.482
a_0''		0.85		0.9601
V_{LS}	3.0	3.0	3.0	3.0
r_{LS}	1.0	1.0 (1.14)	1.0	1.0
a_{LS}	0.7	0.7 (0.69)	0.7	0.70

Units of V_0 , W_1 , W_2 , and V_{LS} are MeV and units of r_0 and a_0 are Fm. Coulomb radii are 1.4 Fm.

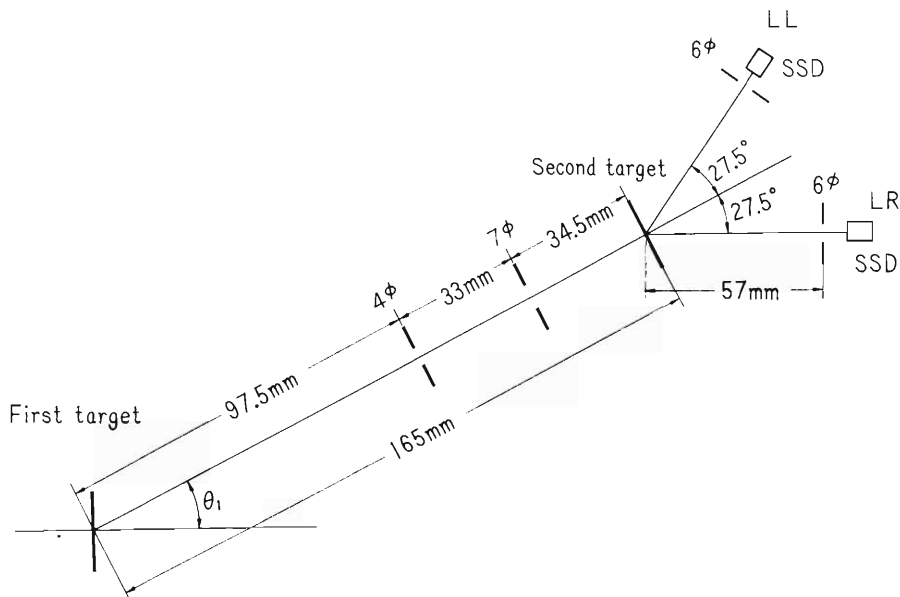
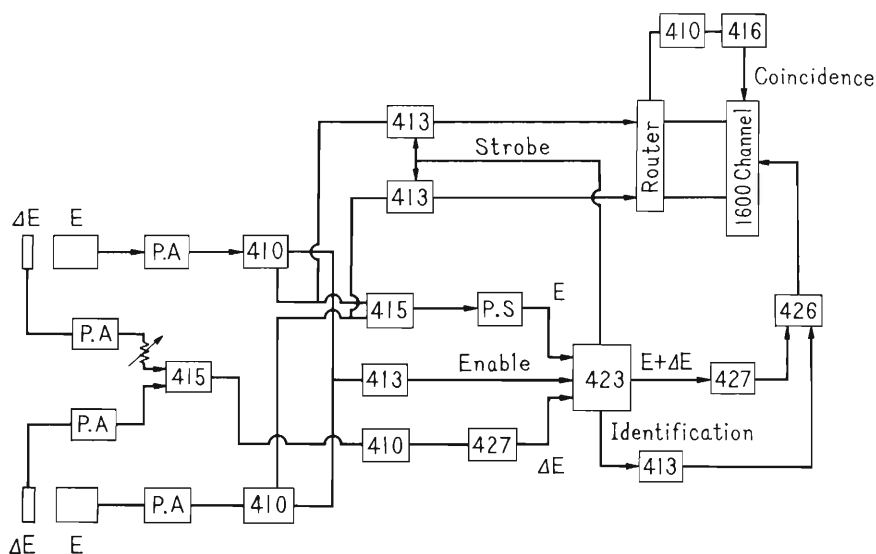


Fig. 1. Geometrical arrangement for the double scattering of $^{12}\text{C}(^3\text{He}, ^3\text{He})^{12}\text{C}$.



P.A : Pre. amp., 410: Linear amp.,
 413 : Single channel analyzer, 415 : Summing
 circuit 416 : Gate and delay generator, P.S.: Pulse
 stretcher, 427 : Delay amp., 423 : Particle
 identifier.

Fig. 2. Electronics for the double scattering. Numbers indicate ORTEC series.

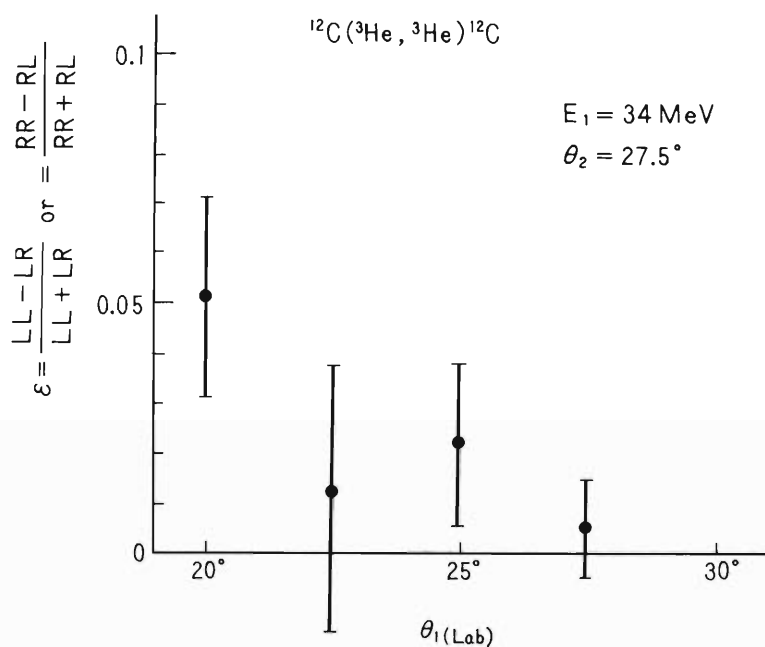


Fig. 3. Results of the polarization experiment for the elastic scattering of ${}^3\text{He}$ from carbon.

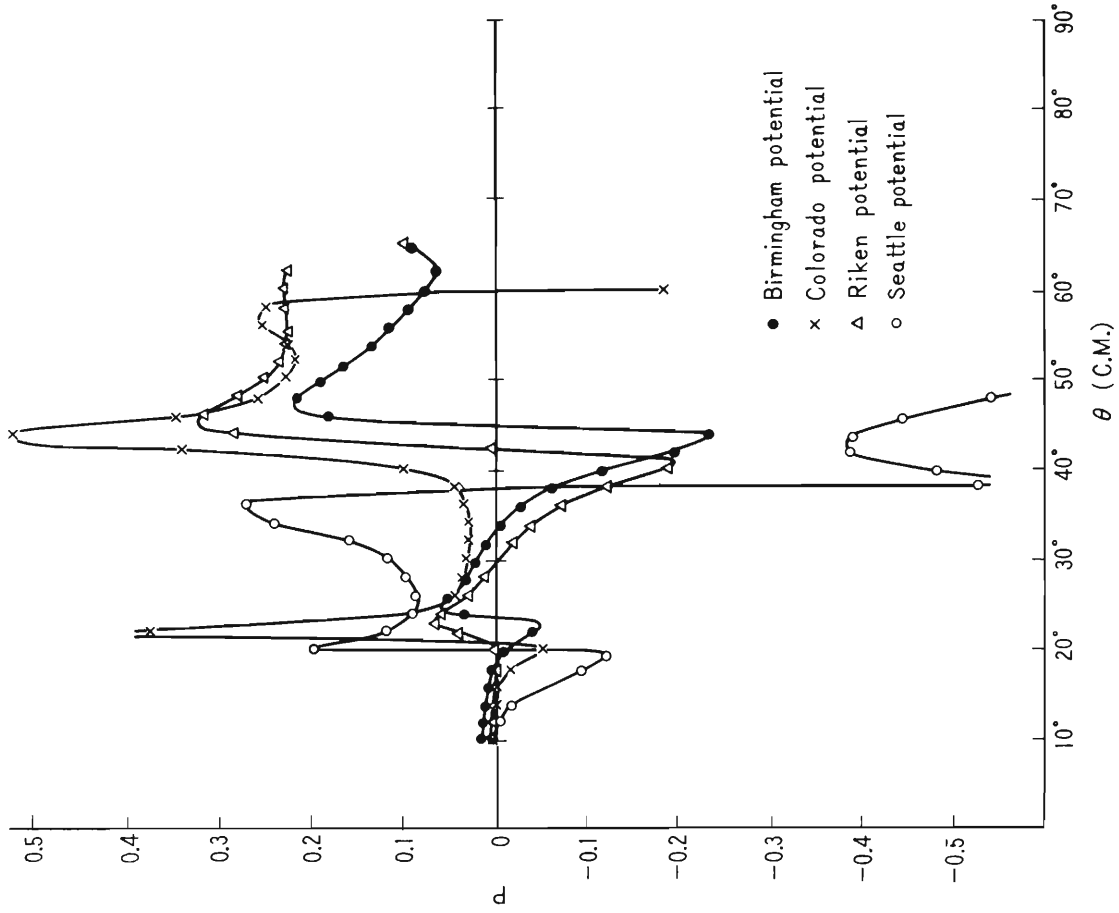


Fig. 4(b). The optical model predictions for polarizations at $E_h = 34$ MeV using potential parameters listed in Table 1.

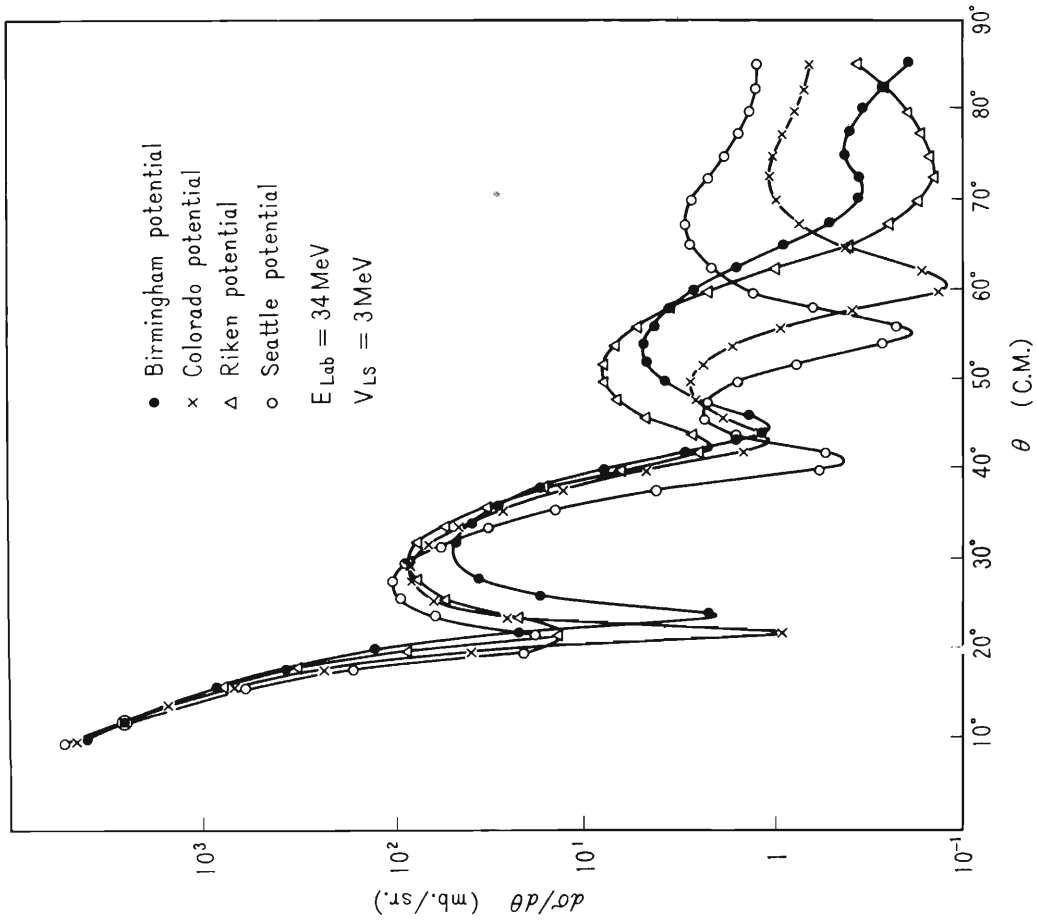


Fig. 4(a). The optical model predictions for differential cross sections at $E_h = 34$ MeV using potential parameters listed in Table 1.

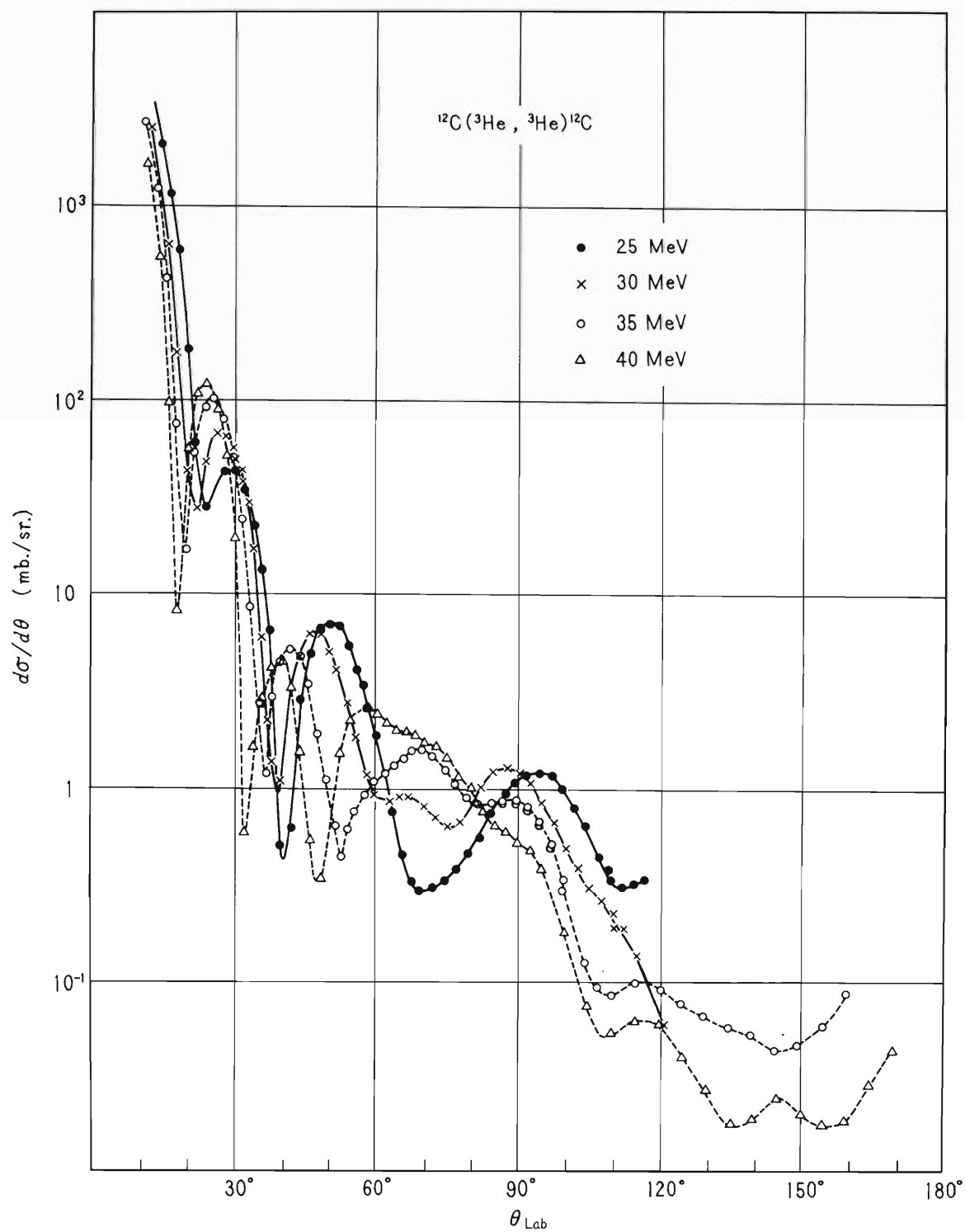


Fig. 5. Differential cross sections of the elastic scattering of ^3He from carbon.

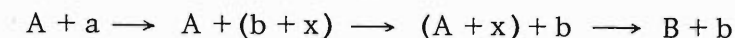
References

- 1) W.E. Burcham, J.B.A. England, J.E. Evans, A. Garcia, R.G. Harris, and C. Wilne: Compt. Rend. Congr. Intern. Phys. Nucl., Paris, p. 877 (1964).
- 2) R.L. Hutson et al.: Phys. Letters, 27B, 153 (1968).
- 3) D.J. Baugh et al.: Nucl. Phys., A95, 155 (1967).
- 4) K. Matsuda et al.: J. Phys. Soc. Japan, 25, 1207 (1968).
- 5) The IPCR Cyclotron Progress Report, Vol. 1 (1967).

5-8. Two-Nucleon Transfer Reaction Code

S. Yamaji*

The cross section of the stripping reaction



is expressed in the following form:

$$\sigma(\theta) = \frac{\mu_a \mu_b}{(2\pi\hbar^2)^2} \frac{k_b}{k_a} \frac{2J_B + 1}{(2J_A + 1)(2s_a + 1)} \sum_{\ell s j m} \left| \frac{1}{i^\ell \sqrt{2\ell + 1}} \int d\vec{r}_a \int d\vec{r}_b \chi_b^{(-)*}(\vec{k}_b, \vec{r}_b) f_{\ell m}(\vec{r}_b, \vec{r}_a) \chi_a^{(+)}(\vec{k}_a, \vec{r}_a) \right|^2,$$

where θ is the angle between the momentum of the incident particle \vec{k}_a and that of the outgoing particle \vec{k}_b . J_A is the total angular momentum of the particle A, s_a the spin angular momentum of the particle a, ℓ , s , and j are the transferred orbital, spin, and total angular momentum respectively. μ_a and μ_b are the reduced masses of particles a and b. $\chi_a^{(+)}$ and $\chi_b^{(-)}$ are the outgoing and incoming distorted waves respectively. $f_{\ell m}(\vec{r}_b, \vec{r}_a)$ is called the form factor, which involves the information of the reaction mechanism and of the spectroscopy. We derived the expression for the form factor of the two-nucleon transfer reaction and are making the computing code.

The form factor $f_{\ell m}(\vec{r}_b, \vec{r}_a)$ is written as $f_{\ell m}(\vec{r}_b, \vec{r}_a) = \sum_{N(n)} D^{(n)}(r_{bx}) A^{(n,N)}_{\ell s j} R_{N\ell}(r_{xA}) (i^\ell Y_{\ell m}(\hat{r}_{xA}))^*$, where $R_{N\ell}(r_{xA})$ is the radial part of the harmonic oscillator wave function and $Y_{\ell m}(\hat{r}_{xA})$ the spherical harmonics. The spectroscopic amplitude $A^{(n,N)}_{\ell s j}$ is expressed as follows:

$$\begin{aligned} A^{(n,N)}_{\ell s j} &= i^{\ell+2b} J U_0 \sqrt{2s_a + 1} \\ &\times \left\{ \binom{a}{2}^{1/2} (t_a m_{ta} \ T_X M_{TX} \mid t_a m_{ta}) D(s) \frac{1}{\sqrt{2s+1}} \right\} \\ &\times \sum_{x_1 x_2} \binom{B}{2}^{1/2} (T_A M_{TA} \ T_X M_{TX} \mid T_B M_{TB}) S(x) g(x_1, x_2) \\ &\times \langle (\ell_{x1} \ 1/2) j_{x1} (\ell_{x2} \ 1/2) j_{x2}; j \mid (\ell_{x1} \ \ell_{x2}) \ell(1/2 \ 1/2) s; j \rangle \\ &\times \sum_{n_{x1} n_{x2}} (N_{x1} \ \ell_{x1} \ K_1 \mid n_{x1} \ \ell_{x1} \ \nu) (N_{x2} \ \ell_{x2} \ K_2 \mid n_{x2} \ \ell_{x2} \ \nu) \\ &\times Cn(n_{x1} \ \ell_{x1} \ n_{x1} \ \ell_{x2}; \ell \mid 1:1 \mid N \ \ell \ n \ 0; \ell). \end{aligned}$$

$$J = \begin{cases} 1 & \text{for "zero-range"} \\ \left(\frac{aB}{x(A+a)} \right)^3 & \text{for "finite-range",} \end{cases}$$

where a, B are the numbers of nucleons of the particle a, B, respectively.

$$g(x_1 x_2) = \begin{cases} 1 & \text{for } x_1 = x_2 \\ \sqrt{2} & \text{for } x_1 \neq x_2. \end{cases}$$

* This work is done in collaboration with Drs. C.L. Lin and H. Yoshida.

where x_1 and x_2 represent the all quantum numbers of the states of the nucleons x_1 and x_2 , respectively.

$$\Omega_b = \begin{cases} 1 & \text{for } a=3 \\ \left[\frac{2\delta\eta}{\delta^2 + \eta^2} \right]^{3/2} & \text{for } a=4 \text{ and "cluster"} \\ \left[\frac{2\delta\eta}{\delta^2 + \eta^2 + \frac{1}{8}\beta^2} \right]^{3/2} & \text{for } a=4 \text{ and "micro",} \end{cases}$$

where we take the expression $N_{\text{exp}} \{-\delta^2 \sum_{ij} r_{ij}^2\}$ for the intrinsic wave function of the particle b, $N_{\text{exp}} \{-\eta^2 \sum_{ij} r_{ij}^2\}$ for the intrinsic wave function of the particle a and $U_0 \exp(-\beta^2 r_{ij}^2) (W + BP^\sigma - HP^\tau - MP^\sigma P^\tau)$ for the interaction between nucleons i and j. N is a normalization constant. P^σ and P^τ are spin and iso-spin projection operators. $D(s)$ is the spin and iso-spin matrix element expressed as follows:

$$D(s) = \begin{cases} -1 + 1.5(B+H) & \text{for } s=1 \\ 1 - 0.5(B+H) & \text{for } s=0. \end{cases}$$

$S(x)$ is a spectroscopic factor.

$\langle (\ell_{x1} \ 1/2) j_{x1} (\ell_{x2} \ 1/2) j_{x2}; j \mid (\ell_{x1} \ell_{x2}) \ell (1/2 \ 1/2) s; j \rangle$ is a nine-j coefficient, $(N_{x1} \ell_{x1} K_1 \mid n_{x1} \ell_{x1} \nu)$ the overlap-integral over the state solved in the Woods-Saxon potential and the harmonic oscillator wave function, and $(n_{x1} \ell_{x1} n_{x2} \ell_{x2}; \ell \mid 1 : 1 \mid N \ell n o ; \ell)$ a Talmi coefficient.

"Micro"¹⁾ means that we treat the interaction between the composite particles b and x as a sum of two-body interactions $\exp(-\beta^2 r_{ij}^2)$, where i is one nucleon in the particle b, j in the particle x. "Cluster"²⁾ means that we approximate the interaction between composite particles b and x to be the interaction between the center-of-masses of both particles. C_n in the expression of the spectroscopic amplitude is written as

$$C_n = \begin{cases} \frac{\{(2n+1)!\}^{1/2}}{2^n n!} \left(\frac{a\nu\eta^2}{2C'} \right)^{3/4} \left(1 - \frac{\nu}{2C'} \right)^n & \text{for "finite-range"} \\ \frac{\{(2n+1)!\}^{1/2}}{2^n n!} \left(\frac{2\pi ab\nu\eta^4}{C'2D'} \right)^{3/4} \left(1 - \frac{\nu}{2C'} \right)^n & \text{for "zero-range" and "cluster"} \\ \frac{\{(2n+1)\}^{1/2}}{2^n n!} \left(\frac{2\pi ab\nu\eta^4}{C^2 D^2} \right)^{3/4} \left\{ 1 - \frac{\nu}{2C} \left(1 + \frac{\beta^4}{4CD} \right) \right\}^n & \text{for "zero-range" and "micro",} \end{cases}$$

where $C' = \frac{1}{4} (\nu + 2a\eta^2),$

$D' = \beta^2 + 2b\eta^2.$

$$\left. \begin{aligned} B &= \beta^2, \\ C &= \frac{1}{4} (\nu + 2a\eta^2 + \beta^2), \\ D &= B - \frac{1}{4C} B^2 + 2b\eta^2, \end{aligned} \right\} \text{for } a=3$$

$$\left. \begin{aligned}
 B &= \beta^2 - \frac{\beta^4}{4C_1} \\
 C_1 &= 2\delta^2 + 2\eta^2 + \frac{1}{4}\beta^2, \\
 D &= B - \frac{1}{4C} B^2 + 2b\eta^2, \\
 C &= \frac{1}{4} (\nu + 2a\eta^2 + \beta^2) - \frac{\beta^4}{16C_1}
 \end{aligned} \right\} \text{ for } a = 4$$

"zero-range" is the so-called zero-range approximation in treating the rearrangement collision and we write "finite-range" when we do not use such approximation.

$D^{(n)}(r_{bx})$ in the form factor is given in the following forms:

$$D^{(n)}(r_{bx}) = \left\{ \begin{aligned}
 &\left\{ \frac{bB}{x(a+A)} \right\}^3 \delta(\vec{r}_{bx}) \dots\dots\dots \text{for "zero-range"} \\
 &\exp(-\beta^2 r_{bx}^2) \left(\frac{4b\eta^2}{\pi}\right)^{3/4} \exp(-2b\eta^2 r_{bx}^2) \\
 &\dots\dots\dots \text{for "finite-range" and "cluster"} \\
 &\exp\left\{-B\left(1-\frac{B}{4C}\right)r_{bx}^2\right\} \left(\frac{4b\eta^2}{\pi}\right)^{3/4} \exp(-2b\eta^2 r_{bx}^2) \sum_{k=0}^n \sum_{s=0}^k \\
 &\frac{n!(-\nu)^k}{(n-k)!2^k} \frac{1}{C^s(2k-2s+1)!} \left(\frac{B}{C}\right)^{2(k-s)} r_{bx}^{2(k-s)} \left(1-\frac{\nu}{2C'}\right)^{-n} \\
 &\dots\dots\dots \text{for "finite-range" and "micro"}.
 \end{aligned} \right.$$

Almost all the calculations on the two-nucleon transfer reaction, at present, rely upon a "cluster" and "zero-range" approximation due to the difficulty of the exact numerical calculation. We are now making the code for the numerical calculation both to test the validity of the zero-range approximation and of the cluster approximation and to make the analysis of the experimental results on the two-nucleon transfer reaction such as (³He, p) and (α, d). We show the outline of the computing code in Fig. 1.

The sub-routines in Fig. 1 play the following roles:

- : INPUT : reads all the necessary input data.
- : SPECT : calculates $A_{\ell sj}^{(n,N)} R_{N\ell}(r_{xA})$ and stores them.
- : BOUND : calculates $\sum_{\bar{n},N} A_{\ell sj}^{(n,N)} R_{N\ell}(r_{xA})$ and stores them in the cases of "finite-range" and "cluster" and of "zero-range". But in the case of "finite-range" and "micro", we cannot sum over n because of the n dependence of the $D^{(n)}(r_{bx})$. So it only calculates $R_{N\ell}(r_{xA})$. The summation over n (N) is carried out after each transition amplitude for n (N) is calculated.
- : OVLP (N1, I1, N2, BE) : calculates overlap-integrals $(N_{x1} \ell_{x1} K_1 \mid n_{x1} \ell_{x1} \nu)$.
- : OMEGA (N1) : calculates coefficients C_n .
- : BOUND 1 : solves bound state wave functions in the Woods-Saxon well.
- : TALMI : calculates Talmi coefficients $(n_1 \ell_1 n_2 \ell_2; A \mid \mu_1 : \mu_2 \mid N L n \ell; A)$.
- : HOWFN : calculates harmonic oscillator wave functions.
- : NINEJ : calculates nine-j coefficients

- : RACAR : calculates Racah coefficients.
- : CLEBSH : calculates Clebsh-Gordon coefficients having zero Z-components of the angular momentum.
- : SKIP : is used to write pages and program numbers on the output program sheet.

In the case of "zero-range", we get the form factor $\sum_{n(N)} A_{\ell s j}^{(n,N)} R_{N1}(r_{xA})$ in MAIN.

Then we input it into DWBA 1 or DWBA 2* and obtain the cross section. In the case of "finite-range" and "cluster", we input the form factor into DWBA 3** to obtain the cross section. In the case of "finite-range" and "micro", we modify the code DWBA 3 by adding the sub-routine which calculates the interaction $D^{(n)}(r_{bX})$. We calculate spectroscopic amplitudes $A_{\ell s j}^{(n,N)}$, input them into the modified DWBA 3 and obtain the transition amplitude for each set of (n,N). We finally get the cross section by summing the transition amplitudes over n and N and squaring the result.

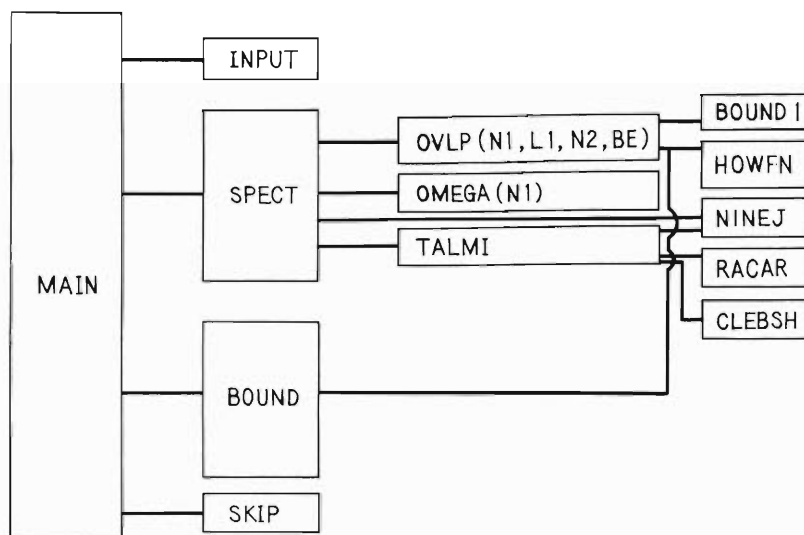


Fig. 1. Form factor calculation.

- * T. Udagawa, H. Yoshida, K. Kubo, and G. Yamaura: Code INS-DWBA 1; M. Kawai, K. Kubo, and G. Yamaura: Code INS-DWBA 2.
- ** T. Une, T. Yamazaki, S. Yamaji, and H. Yoshida: Code INS-DWBA 3.

References

- 1) C.L. Lin and S. Yoshida: Progr. Theor. Phys., 32 885 (1964).
- 2) N.K. Glendenning: Ann. Rev. Nucl. Sci., 13, 191 (1963).

5-9. The Automatic Search Code of the Optical Model

T. Wada

(1) Introduction

A nuclear optical model has been used successfully for the analysis of the elastic scattering of particles by atomic nuclei.¹⁾ This model was first used to analyze the neutron scattering data by Feshbach et al. in 1954,²⁾ but because an extensive computation was needed for accurate calculation, it was not developed until the appearance of fast and big computers.

The following is a brief description of the program SEARCH which is coded to analyze the scattering data of ^3He particles by various target nuclei. These data were obtained using the IPCR cyclotron.³⁾

This program can also be applied to other particles of spin 0 or 1/2, and is being tested for the applicability to the heavy ion scattering.

The optical potential used in SEARCH is the following:

$$V(r) = V_C(r) - V_R(x_R) - i \left\{ W_V f(x_V) + 4 a_S W_S \frac{d}{dr} f(x_S) \right\} \\ - \left(\frac{\hbar}{m\pi c} \right)^2 \left(\frac{\vec{\sigma} \cdot \vec{\ell}}{r} \right) \frac{d}{dr} \left\{ V_{S0} f(x_{R_{S0}}) + i W_{S0} f(x_{I_{S0}}) \right\}$$

Where

$$V_C(r) = \frac{ZZ'e^2}{2R_C} \left(3 - \frac{r^2}{R_C^2} \right) \quad \text{for} \quad r \leq R_C$$

$$\text{and} \quad = \frac{ZZ'C^2}{r} \quad \text{for} \quad r > R_C$$

$$f(x_i) = \frac{1}{1 + \exp\left(\frac{r-R_i}{a_i}\right)}$$

$$R_i = r_i M^{\frac{1}{3}}$$

SEARCH is written in FORTRAN H₂* language of the computer OKITAC-5090H** of IPCR.

(2) Program description

SEARCH is intended not only to calculate the theoretical angular distributions of the cross section and the polarization of scattered particles, but also to search the optical parameters which give the theoretical values best fitted to the experimental data.

As the quantitative measure of the goodness of fit, the usual χ^2 is used.

* The same as usual FORTRAN 2.

** The specifications are as follows:

42 bits/word,	12k words,	10 μ sec cycle time,
floating multiply	250 μ sec,	
floating divide	330 μ sec.	

$$\chi^2 = \sum_{i=1}^N \left\{ \frac{q_t(\theta_i) - q_e(\theta_i)}{\Delta q_e(\theta_i)} \right\}^2$$

where $q_t(\theta_i)$ and $q_e(\theta_i)$ are the theoretical and experimental quantities at scattering angle θ_i respectively, and $\Delta q_e(\theta_i)$ is the associated experimental error.

Fig. 1 shows the configuration of the whole program, and the functions and the core storage of each subprogram are described in the following:

(A) Main program (967 words)

- (a) Initialization of some parameters.
- (b) Input of necessary data and parameters.
- (c) Calculations of k , η , σ_ℓ , $f_c(\theta)$ and other parameters.
- (d) The control of the increase of the optical parameters which are specified to vary stepwise.
- (e) Subprogram SEARCH and DASU are called.

(B) Subprogram SEARCH (668 words)

- (a) The decision of doing automatic parameter search. The following three conditions are necessary; first, there should be experimental data; second, search cut-off time should be greater than zero; third, there should be parameters to be searched.
- (b) Using parabolic approximation,⁴⁾ the parameters which give the minimum χ^2 value are found.
- (c) To test whether the value of each parameter is within the upper and lower limits or not.

(C) Subprogram KEISAN (508 words)

- (a) Determination of r_{\max} by the following equation,

$$r_{\max} = (11 + \log \frac{V^*}{E}) a + R,$$

where V^* is the depth of the Woods-Saxon potential or 4 times the depth of the derivative Woods-Saxon potential. The set of parameters of V^* , a , and R , which gives the maximum r_{\max} is used.

- (b) Calculation of the potential at each mesh point along the radial direction up to r_{\max} in Δr step.
- (c) Subprogram COULFC is called.

(D) Subprogram COULFC⁵⁾ (1111 words)

- (a) Calculation of $G_0(r_A)$ and $G_0(r_A)$ by means of series expansion.

As r_A is a large value, this method is sufficiently accurate. Then $G_0(r_1)$ and $G_0(r_2)$ are calculated by numerical integration of the following equation,

$$\frac{d^2}{d\rho^2} G_0(\rho) + \left(1 - \frac{2\eta}{\rho}\right) G_0(\rho) = 0$$

from r_A to r_{\max} , where $r_1 = r_{\max}$, $r_2 = r_{\max} + \Delta r$, and $\rho = kr$.

- (b) Calculation of $G_\ell(r_1)$, $G_\ell(r_2)$, $F_\ell(r_1)$, and $F_\ell(r_2)$ by means of recurrence formulas.

(E) Subprogram CKEISU (936 words)

- (a) Numerical integration of the Schrödinger equation is done by Noumerov's method.⁴⁾ Then comparing the value of the wave function to the value of the linear combination of Coulomb functions at two points r_1 and r_2 using the following equation,

$$A_\ell \psi_\ell(r) = F_\ell(r) + C_\ell (G_\ell(r) + iF_\ell(r))$$

the coefficients C_ℓ are calculated. By increasing ℓ , when $|C_\ell|$ becomes smaller than 10^{-5} , the value of ℓ is set to be ℓ_{\max} .

- (b) $\sigma(\theta)$ and $p(\theta)$ are calculated and if there are experimental data, χ^2/N is calculated.

(F) Subprogram INCPRM (37 words)

During the parameter search, a procedure to satisfy the following relation is done:

$$\vec{p} = \vec{p}_0 + z \delta \vec{p}$$

where p_0 is the set of parameters at a starting point, $\delta \vec{p}$ is the extension, z is a limitation coefficient and \vec{p} is the next starting point.

(G) Subprogram DASU (810 words)

The results are all printed out.

(H) Subprogram SIMQ (302 words)

General subroutine to solve a simultaneous equation.

(I) Subprogram OFLOW (67 words)

Called at the beginning and the end of each subprogram to test for any overflow conditions.

(J) Common region (3056 words)

The following limitations are set because of the core storage:

- $\ell_{\max} \leq 40$: the angular momentum of partial waves,
- $n_{\max} \leq 200$: the number of mesh points,
- $j_{\max} \leq 70$: the number of scattering angles,
- $p_{\max} \leq 16$: the kinds of optical parameters which can be searched,
- $k_{\max} \leq 8$: the number of optical parameters which can be searched simultaneously,
- $q_{\max} \leq 2$: the number of optical parameters which can be varied stepwise at the same time.

(3) Code test and some examples

(A) Comparison to other codes

Numerical comparison only to the INS codes was made, but graphical comparison to Perey's code⁶⁾ and HUNTER code⁷⁾ was made. Table 1 shows an example of the numerical result of DWBA2⁸⁾ (HITAC version), and SEARCH. The used parameters are listed in Table 2 (A).

Almost all tests were done in case of the scattering of ^3He particles by ^{58}Ni nuclei. In Table 2, the energy of ^3He particle is 27.64 MeV for (A) and 34.14 MeV for (B)~(D).

(B) Effects of varying r_{max} , Δr , and ℓ_{max}

Fig. 2 shows the effects of varying r_{max} , Δr , and ℓ_{max} . The optical parameters are shown in Table 2 (B) and (C) for Fig. 2 (a) and (b) respectively. The error of 5% of experimental data is adopted because relatively more weight is given to the larger angle parts and the above effects are large only at such parts. Then in practice, this effects is less effective. When one of these parameters is varied, the others are fixed to the standard values; $r_{\text{max}} = 14$ fm, $\Delta r = 0.1$ fm, and $\ell_{\text{max}} = 29$. The difference between Figs. 2 (a) and (b) comes from the difference of the wave length in the internal region of the potential.

(C) Effects of varying optical parameters

Figs. 3 (a)~(g) show the variation of the angular distributions when the optical parameters are varied. The variation is 20% for the potential depth and 10 % for the geometrical parameters. The central values are shown in Table 2 (B) and when one of these parameters is varied, the others are fixed to these values. Fig. 3 (h) shows the effect of $V_{\ell S} = 4$ MeV.

(D) Effects of finite width of detector

In an actual case, the particle detectors have finite angle which effects the measured angular distributions. This is expected to be greater at the scattering angles for smaller curvature of angular distribution.

This will be seen in the following approximate calculation.

$$\bar{\sigma}(\theta) \doteq \frac{\sigma(\theta - \Delta\theta) + \sigma(\theta) + \sigma(\theta + \Delta\theta)}{3}$$

$$\Delta\sigma(\theta) = \bar{\sigma}(\theta) - \sigma(\theta)$$

$$= \frac{\sigma(\theta - \Delta\theta) - 2\sigma(\theta) + \sigma(\theta + \Delta\theta)}{3} ,$$

and

$$\frac{d^2}{d\theta^2} \sigma(\theta) \doteq \frac{1}{\Delta\theta} \left\{ \frac{\sigma(\theta + \Delta\theta) - \sigma(\theta)}{\Delta\theta} - \frac{\sigma(\theta) - \sigma(\theta - \Delta\theta)}{\Delta\theta} \right\}$$

$$= 3 \Delta\sigma(\theta) / \Delta\theta^2$$

In Fig. 4, the angular distribution of the cross section and associated $\Delta\sigma(\theta)$ are plotted when $\theta = 1.0^\circ$ and 2.0° . The used optical parameters are (B) of Table 2.

(E) Example of automatic parameter search

Fig. 5 shows the direction of two-parameter search of V and W (volm) with other parameters fixed to the values of Table 2 (D). It can be seen that the terminal point depends on the starting point in case of the χ^2 space with more than one local minima.

(F) Parameter ambiguity

It has been found that there are at least two types of parameter ambiguities in the χ^2 space especially in case of composite particles. The first is the discrete one; more than one local minima appear when the depth of the real potential is increased at about 30 to 50 MeV steps. The second is the continuous one; within one local minimum region, the variations of V and r_R can cancel each other, if they hold the value of $V \cdot r_R^n$ constant.

In Fig. 6 these two types of ambiguities are shown¹⁰⁾.

Table 2. Parameters used for the optical model calculations of elastic scattering of ^3He by ^{58}Ni . $r_C = 1.4$ fm for all sets.

	$V(\text{MeV})$	$r_R(\text{fm})$	$a_R(\text{fm})$	$W(\text{MeV})$	$r_I(\text{fm})$	$a_I(\text{fm})$
A	174.0	1.14	.72	18.5	1.6	.81
B	180.0	1.10091	.77208	20.255	1.62279	.75743
C	130.0	1.11187	.81833	16.32059	1.69025	.72746
D	—	1.14	.72	—	1.60	.81

Table 1. The numerical results of SEARCH and DWBA2.

THETA	DWBA XSECEL(TH)	SEARCH CR (MB/SR)
5.00	1.604214E+06	_____
7.50	3.411088E+05	_____
10.00	1.048207E+05	.104829E+06
12.50	4.178968E+04	.417862E+05
15.00	1.833760E+04	.183045E+05
17.50	8.103836E+03	.807761E+04
20.00	3.872250E+03	.386418E+04
22.50	2.162448E+03	.216251E+04
25.00	1.318544E+03	.131787E+04
27.50	7.843430E+02	.781709E+03
30.00	4.440416E+02	.441591E+03
32.50	2.583484E+02	.257287E+03
35.00	1.701480E+02	.170043E+03
37.50	1.237289E+02	.123729E+03
40.00	8.874895E+01	.885059E+02
42.50	5.884972E+01	.585156E+02
45.00	3.707966E+01	.368985E+02
47.50	2.471996E+01	.247479E+02
50.00	1.892648E+01	.190412E+02
52.50	1.559506E+01	.156490E+02
55.00	1.224471E+01	.121846E+02
57.50	8.595861E+00	.847224E+01
60.00	5.456204E+00	.535454E+01
62.50	3.459609E+00	.342893E+01
65.00	2.565712E+00	.259725E+01
67.50	2.279855E+00	.233201E+01
70.00	2.098038E+00	.213329E+01
72.50	1.776754E+00	.178149E+01
75.00	1.333372E+00	.131556E+01
77.50	8.988636E-01	.874822E+00
80.00	5.784684E-01	.561172E+00
82.50	3.969320E-01	.391214E+00
85.00	3.173258E-01	.321191E+00
87.50	2.856261E-01	.294023E+00
90.00	2.627082E-01	.270826E+00
92.50	2.325470E-01	.237503E+00

REACTION X-SEC = 1.58292E+03 (DWBA)
1589.378641 (SEARCH)

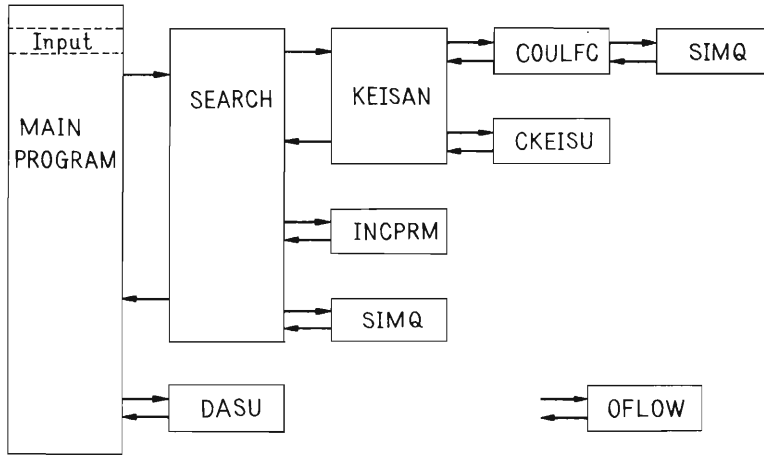


Fig. 1. The whole configuration of SEARCH.

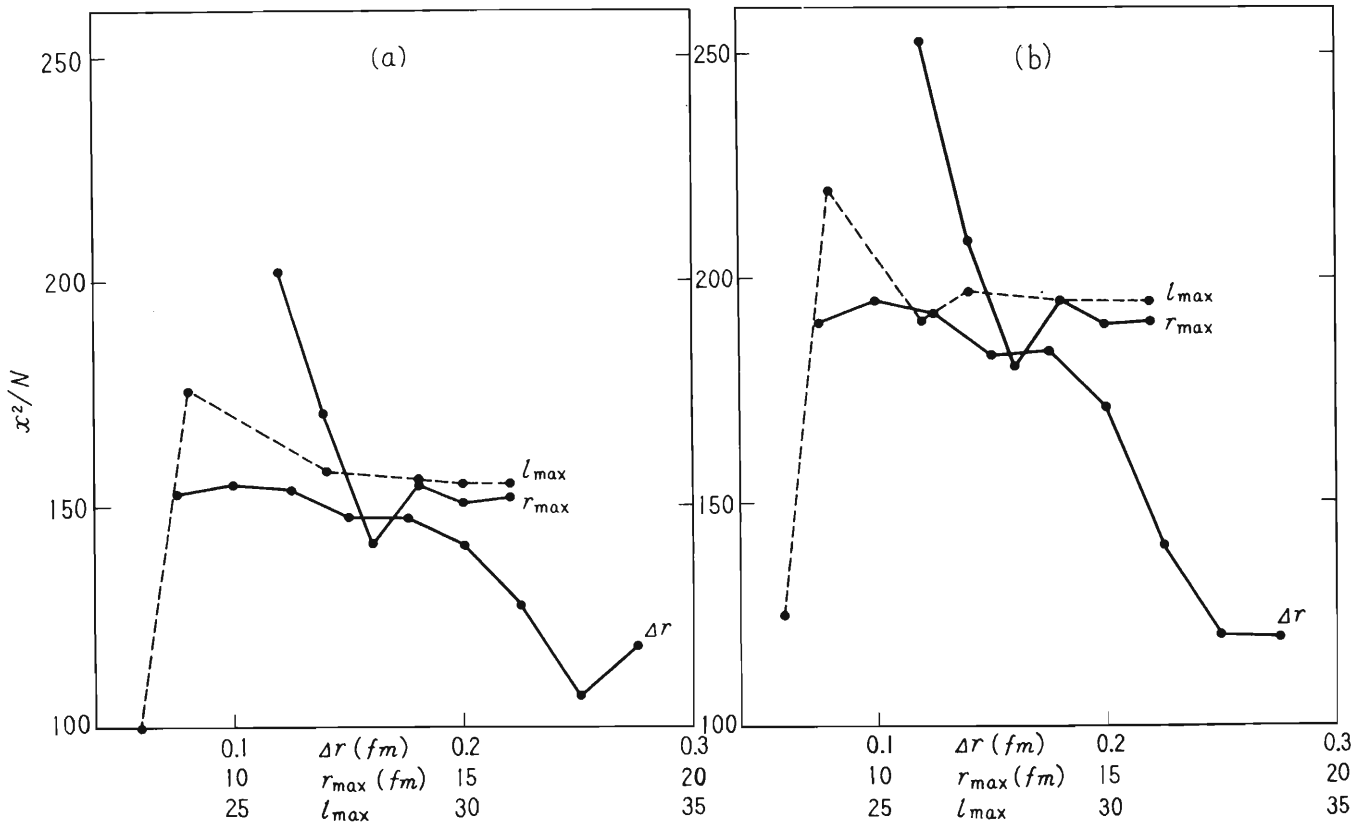
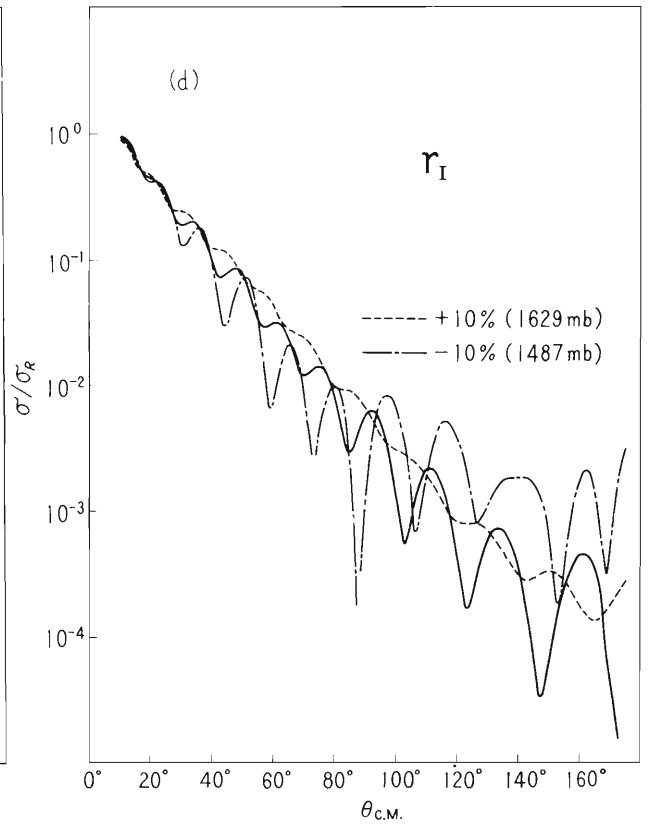
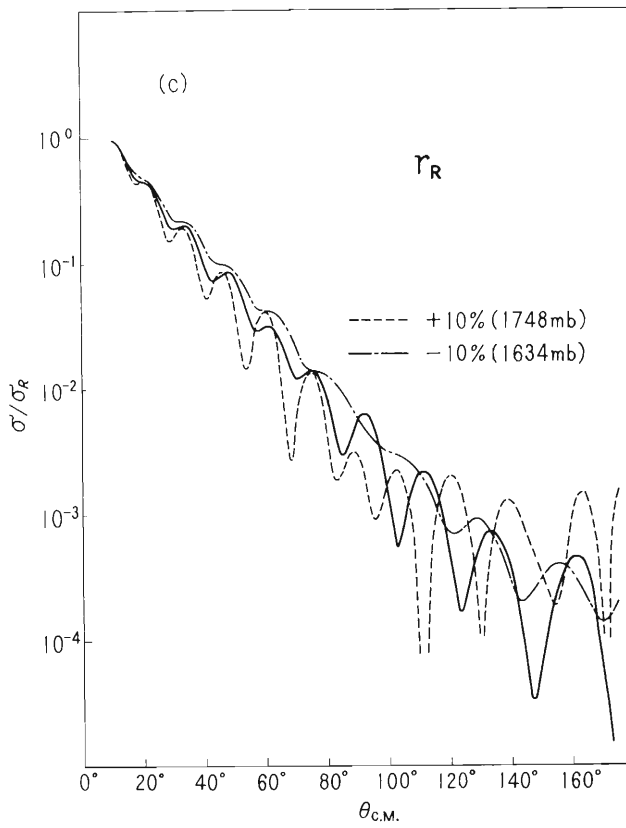
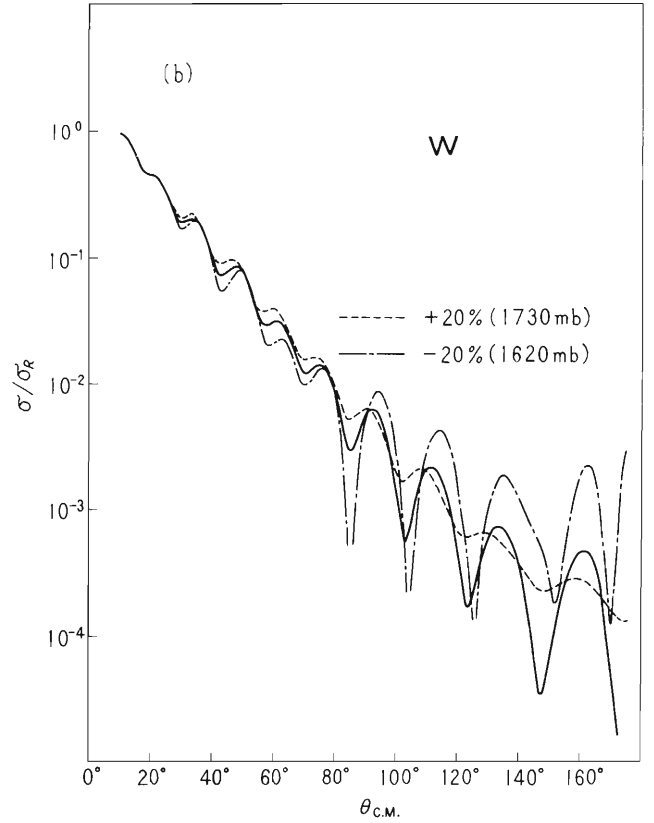
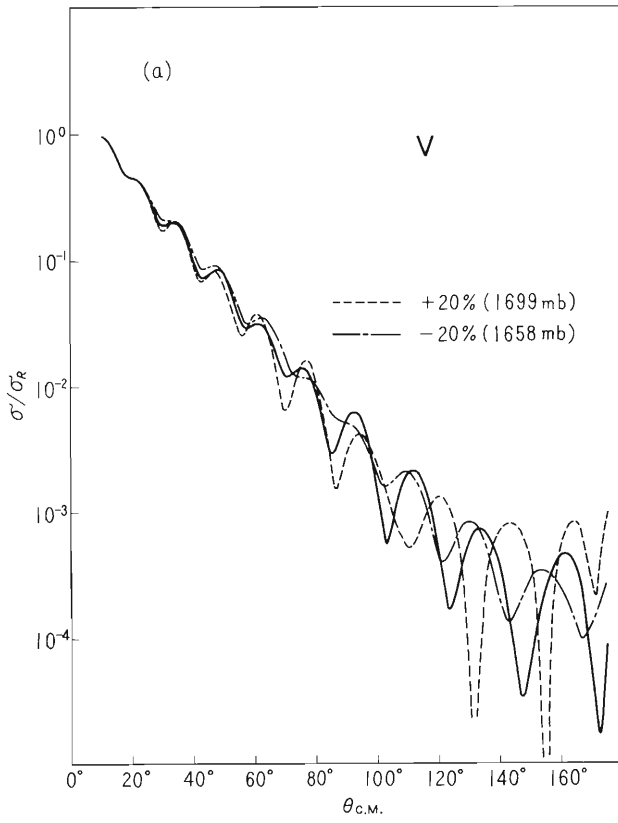


Fig. 2. The effect of varying r_{\max} , Δr , l_{\max} on χ^2 .



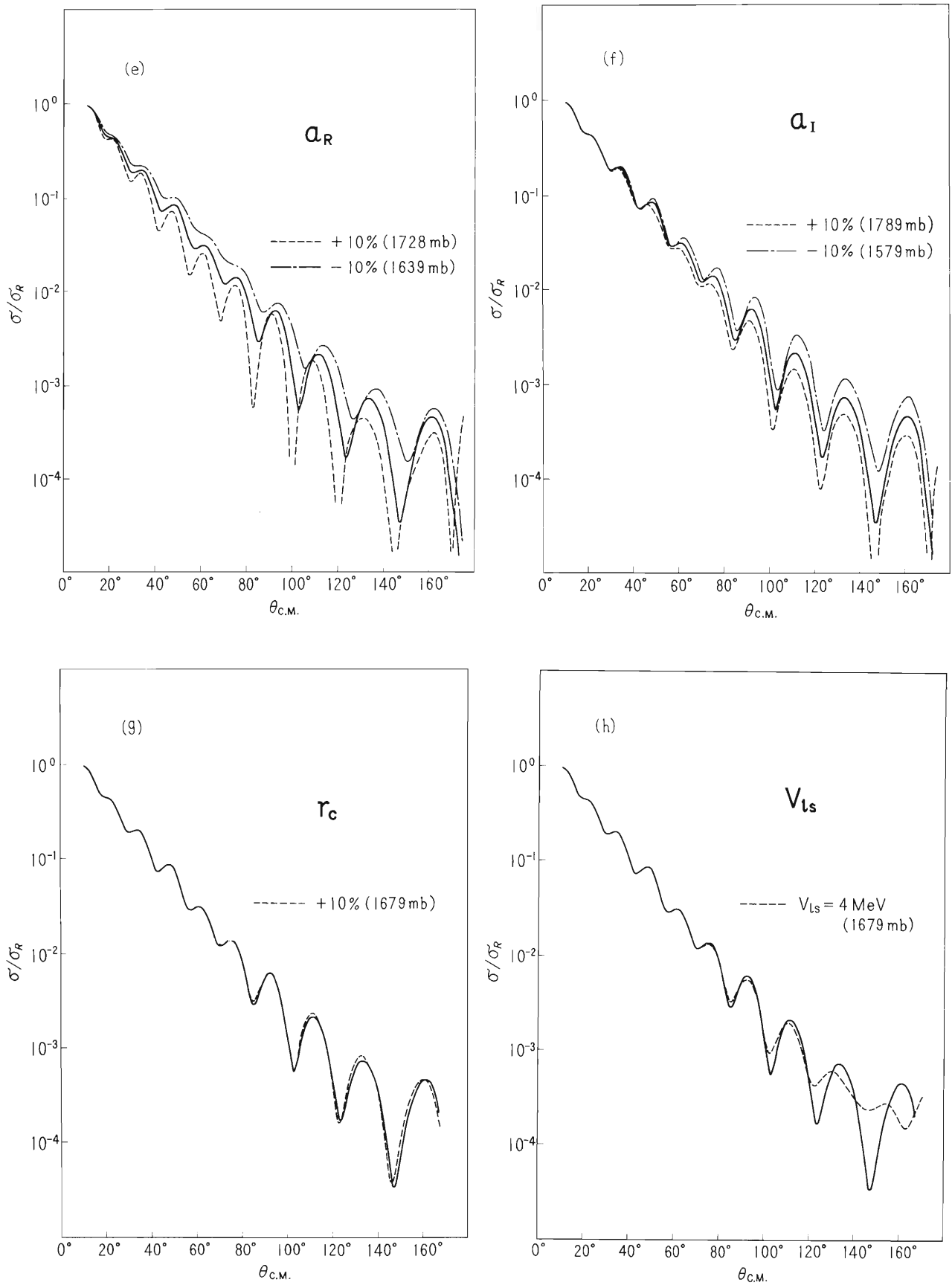


Fig. 3. The effect of varying each optical parameter with others being fixed. The numbers in parenthesis are total reaction cross sections.

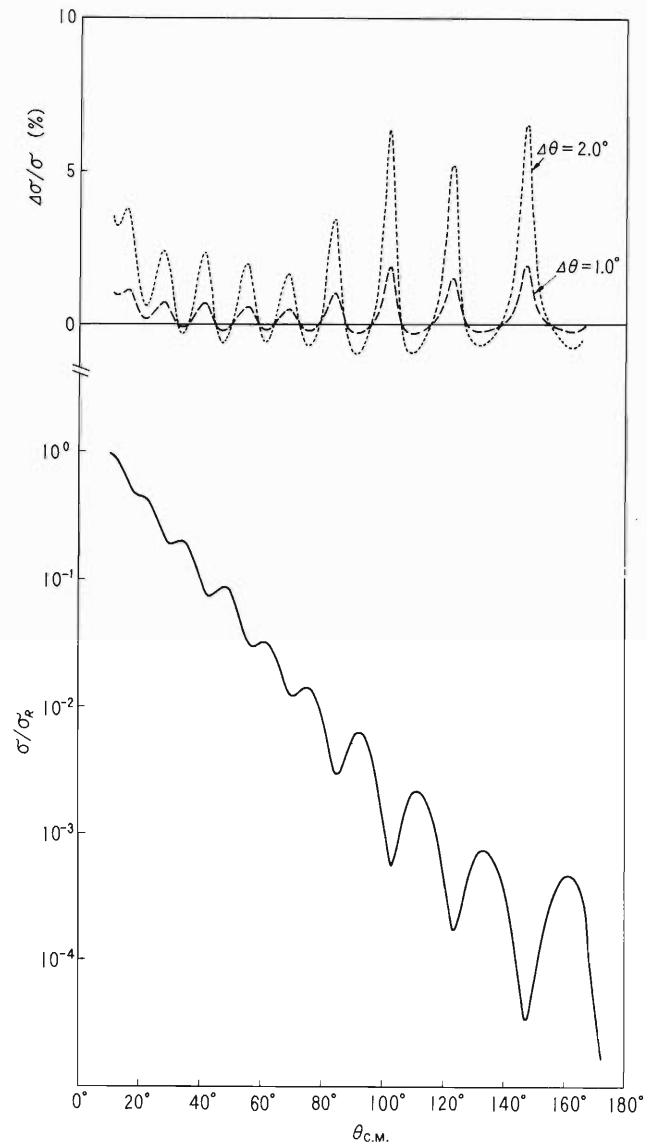


Fig. 4. The deviation of angular distribution by finite angle of particle detectors.

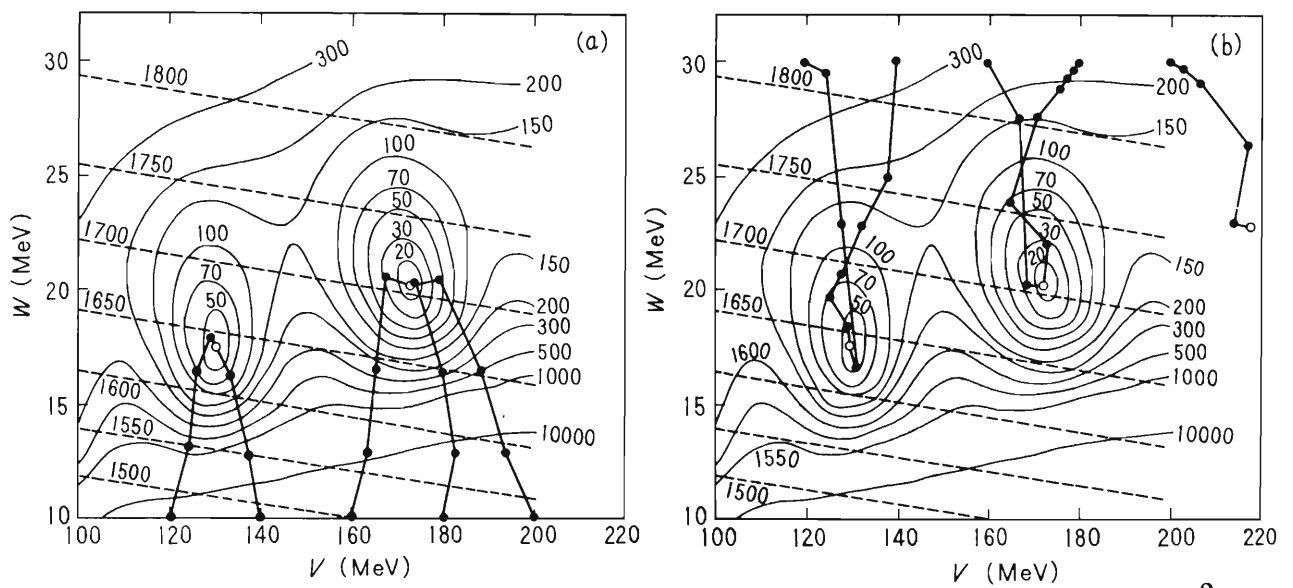


Fig. 5. The direction of automatic parameter search to local minimum χ^2 .

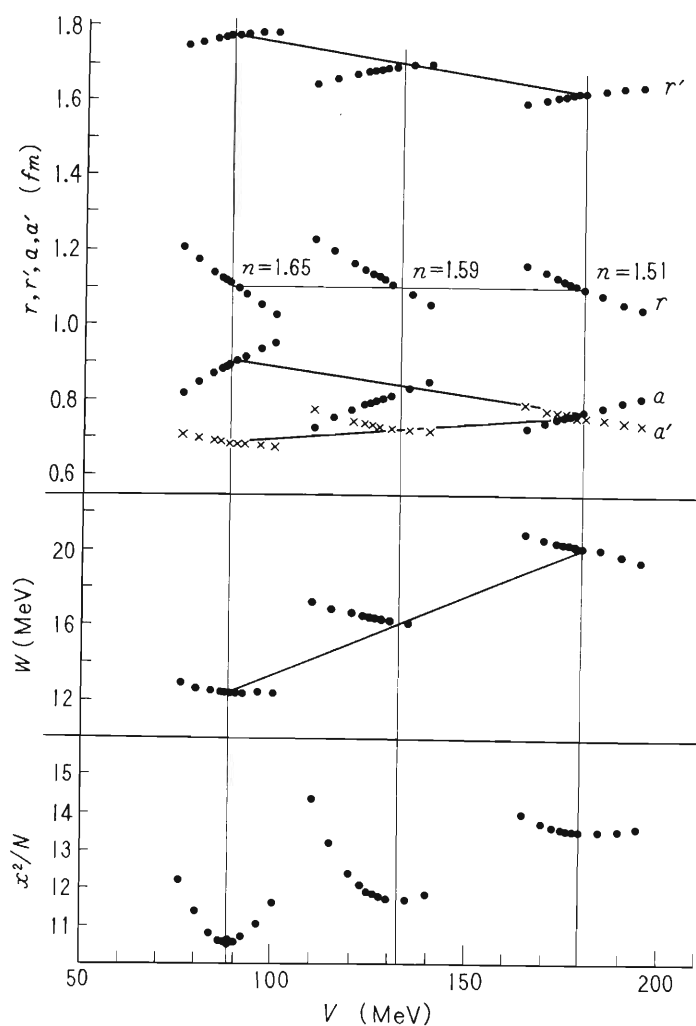


Fig. 6. Two types of parameter ambiguities. n is a constant in $V \cdot r_R^n = \text{const.}$

References

- 1) P.E. Hodgson: "The Optical Model of Elastic Scattering", Oxford University Press, (1963).
- 2) H. Feshbach, C.E. Porter, and V.F. Weisskopf: Phys. Rev., 96, 448 (1954).
- 3) Edited by K. Matsuda, T. Nozaki, and Y.G. Tanaka: IPCR Cyclotron Progress Report, Vol. 1 (1967).
- 4) M.A. Melkanoff, T. Sawada, and J. Raynal: "Methods in Computational Physics", Academic Press, N.Y. and London, Vol. 6 (1963).
- 5) Japanese Nuclear Data Committee: JAERI-1096 (1965).
- 6) F.G. Perey: Phys. Rev., 131, 745 (1963).
- 7) E.F. Gibson, B.W. Ridley, J.J. Kraushaar, M.E. Rickey, and R.H. Bassel: Phys. Rev., 155, 1194 (1966).
- 8) M. Kawai, K. Kubo, and H. Yamaura: INS Report PT-9 (1965).
- 9) T. Fujisawa: J. Phys. Soc. Japan, (to be published).

6. NUCLEAR PHYSICS

Nuclear Spectroscopy and its Applications

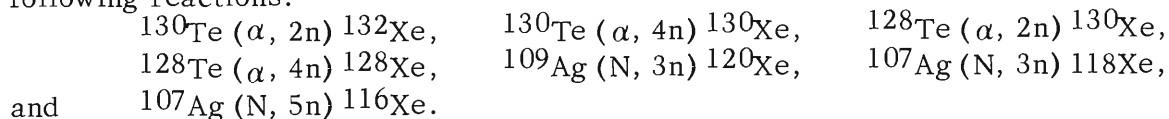
6-1. The Excited States in Xe Isotopes Studied by (H. I., xn γ) and (α , xn γ) Reactions

A. Hashizume, T. Inamura, T. Kato, Y. Tendow,
H. Kamitsubo, T. Yamazaki, T. Nomura

In the region where both neutron and proton numbers lie between 50 to 82, several experiments¹⁾ have shown that there exist the systematics of energies of the excited levels in nuclei with spin 0^+ , 2^+ , 4^+ , 6^+ , etc.

The so-called In Beam Spectroscopy is one of the most suitable techniques to study such energy systematics, because after the formation of compound nucleus and the evaporation of a few neutrons, the nucleus de-excites mainly through γ -ray emission. Especially if we use heavy ions as incident particles, the compound nucleus has very large angular momentum. And if the energy for particle evaporation is no more available, the nucleus is de-excited by γ -rays. And after a few γ -rays are emitted, the most excited nucleus is de-excited through the levels which have the highest angular momentum at the energy (yrast levels).²⁾ Many γ -rays emitted in this final process are of quadrupole type and more intense than other ones. Therefore we can observe easily the photopeaks corresponding to these γ -rays. So it is interesting, on the one hand, to extend the systematics toward the neutron deficient nuclei using heavy ion reaction, and on the other hand a point of interest lies in measuring the life-times of the isomers taking advantage of the bunched character of the accelerated ions by the cyclotron.³⁾

First of all we examined the excited states of Xe isotopes. We have used the following reactions:



Observing the de-exciting γ -rays with a Ge (Li) detector, we could construct the level sequences of 0^+ , 2^+ , 4^+ , 6^+ , and some times 8^+ in the above nuclei. The assignment of the γ -rays mainly consisted of taking the excitation function by varying the energies of the incident particles, and taking the relative intensity rules of the γ -rays. In taking the excitation function by using nitrogen ions, we have changed the energies every 5 MeV from 58 MeV to 86.5 MeV. In the case of α -particles the relative intensities of the γ -rays become weaker for $0^+ \rightarrow 2^+$, $2^+ \rightarrow 4^+$, $6^+ \rightarrow 4^+$ transitions and we could hardly observe the γ -rays emitted in the process $8^+ \rightarrow 6^+$. If nitrogen ions were used, the intensities were nearly the same from $0^+ \rightarrow 2^+$ to $6^+ \rightarrow 4^+$ transitions and we could also observe the γ -rays emitted in the $8^+ \rightarrow 6^+$ transition but hardly in the $10^+ \rightarrow 8^+$.

From our experimental results, we propose the excited levels in ${}^{118}\text{Xe}$ and ${}^{116}\text{Xe}$, the most neutron deficient isotopes in Xe (Fig. 1).

In the course of the survey of the isomers having life-times more than 10 ns by bombarding the target with α -particles, we found that for the isomer in ${}^{132}\text{Xe}$ the intensity of the 538 keV γ -ray is very weak in comparison with other delayed γ -rays (Fig. 2, Table 1).

Table 1. $^{130}\text{Te}(\alpha, 2n)^{132}\text{Xe}$ $E_\alpha = 25$ MeV

Energy	Relative γ -ray intensities		
	0 ~ 28 ns	28 ~ 65 ns	65 ~ 95 ns
174 keV	2.03 ± 0.09	2.25 ± 0.05	1.85 ± 0.04
538	0.79 ± 0.17	0.88 ± 0.09	0.82 ± 0.08
601	7.94 ± 0.28	2.61 ± 0.11	2.14 ± 0.11
669	13.6 ± 0.35	2.49 ± 0.12	2.29 ± 0.11
774	8.85 ± 0.32	2.00 ± 0.10	1.74 ± 0.10

The errors quoted are statistical ones. The errors of the efficiencies of the detector are estimated 10 %.

If the 8.4 ms isomer lies at 2.754 MeV and decays by the γ -ray sequence of 174, 538, 600, 773, and 668 keV to the ground state as proposed by Brinckman et al.,⁴⁾ the γ -ray intensities of the delayed spectrum must be the same. To explain consistently the intensities, there should be the γ -ray sequence of 174, 600, 773, and 668 keV, de-exciting from an isomer at 2.215 MeV. Concerning the delayed 538 keV γ -ray, there are two possibilities; one is that the 2.754 keV state in ^{132}Xe may correspond another isomer

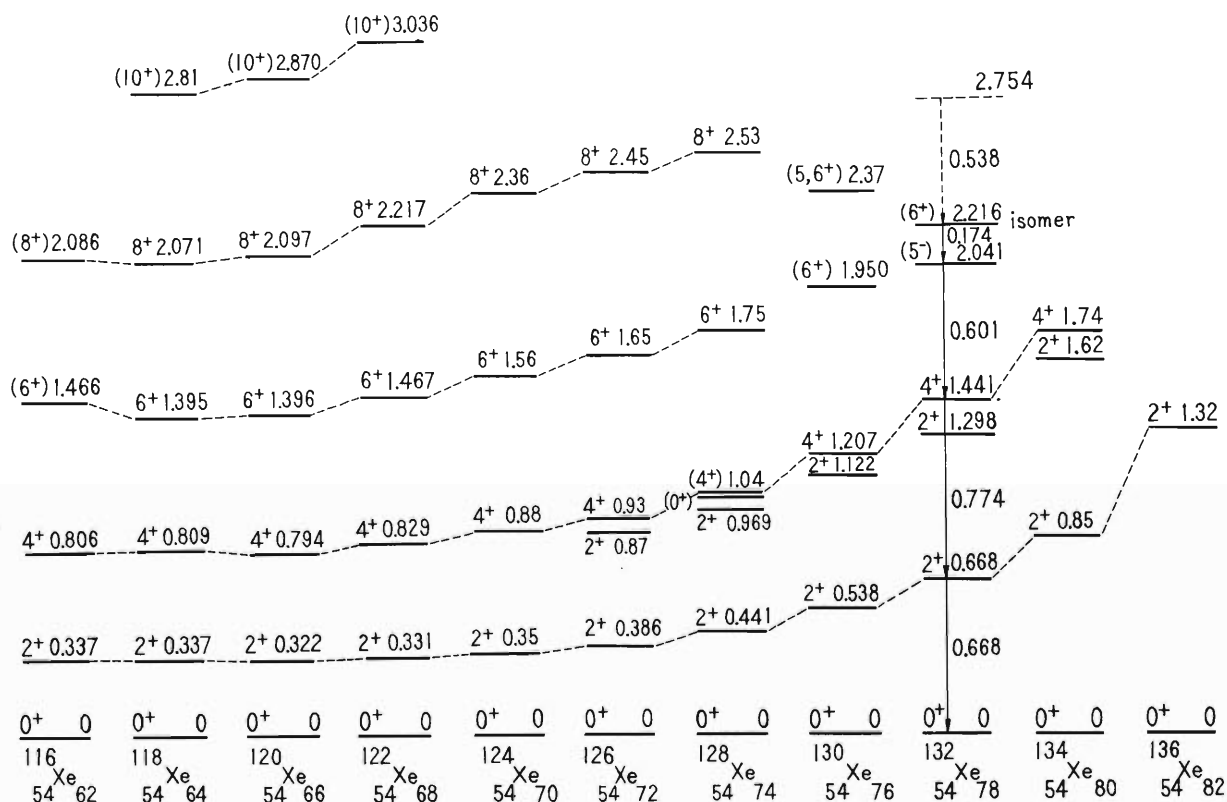


Fig. 1. Energy level systematics of Xe isotopes.

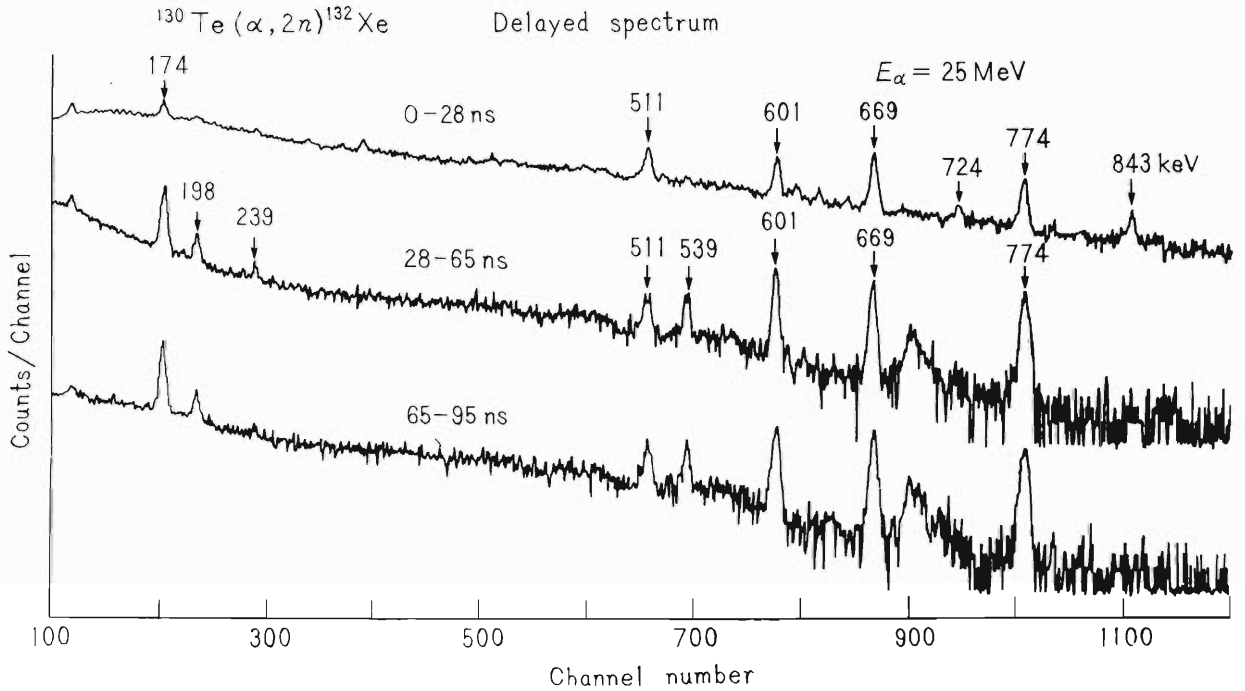


Fig. 2.

and decays to 2.215 MeV state, the other is that the 538 keV γ -ray could be originated from other nuclide. The higher energy part of an excitation curve obtained by detecting 538 keV γ -ray was accidentally contaminated by γ -ray of the same energy emitted from the first excited state of ^{128}Te . But the curve resembles those taken from the $^{130}\text{Te}(\alpha, 2n)$ reaction.

References

- 1) H. Morinaga and P.E. Gugelot: Nucl. Phys., 46, 210 (1963);
J.E. Clarkson, R.M. Diamond, F.S. Stephens, and I. Perlman: *ibid.*, A93, 272 (1967).
- 2) J.R. Grover and J. Gilat: Phys. Rev., 157, 814 (1967).
- 3) T. Yamazaki and G.T. Ewan: Nucl. Instr. Methods. (to be published).
- 4) H.F. Brickmann, C. Heiser, and W.D. Fromm: Nucl. Phys., 96, 318 (1967).

6-2. Decay of ^{171}Lu

Y. Tendow, Y. Awaya, T. Kato, and A. Hashizume

Decay properties of strongly deformed odd nucleus ^{171}Lu (8.3d) are being investigated by use of β and γ -spectroscopic techniques. The properties of odd A nuclei of this region are of interest in connection with the comparison between experimental interband transition probabilities and theoretical predictions under some specific assumptions.

The electron and γ -ray sources of ^{171}Lu were produced by the reaction $^{169}\text{Tm}(\alpha, 2n)^{171}\text{Lu}$ using the alpha beam of 30 MeV energy from the IPCR cyclotron. Natural Tm_2O_3 was embedded in a groove on an aluminum plate attached on a water-cooled radioisotope production probe and bombarded with an alpha beam current of about 30 μA . Because of the target thickness the (α, n) reaction might have took place and therefore ^{172}Lu had mixed in the sources. The carrier-free Lu was separated from the bombarded target by ion-exchange columns. Sources for conversion electron measurements were made with the electrodeposition method in an ammonium lactate solution.

Conversion electron measurements were performed with an iron-free beta-ray spectrometer ($r_0=50$ cm). At present, overall scanings with comparatively low resolution have been completed. Detected conversion electron lines are summerized in Table 1. An example of low energy part of the conversion electron spectrum is illustrated in Figs. 1(a) and (b). Because of complicated weak lines, energy and subshell assignments are a little ambiguous.

The gamma-ray spectra were measured with Ge(Li) detectors of 23 cm^3 coaxial and 4 cm^3 planer type. The 23 cm^3 detector was put in an annular type NaI(Tl) scintillator for the purpose of Compton scattering rejection. The large volume detector and the anti-Compton arrangement unveiled many previously unobserved weak γ -ray peaks. Some of them are caused from the ^{172}Lu contamination. The remainders have no corresponding γ -rays in ^{172}Yb and are supposed to be new transitions in ^{171}Yb . The fact was confirmed by measurements of γ -rays of ^{172}Lu produced by the $^{169}\text{Tm}(\alpha, n)^{172}\text{Lu}$ reaction. Some coincidence works and life-time measurements of isomeric states are hereafter intended. Anti-Compton gated γ -ray spectra measured with 23 cm^3 Ge (Li) detector are indicated in Figs. 2(a), (b), and (c).

Table 1.

Energy (keV)	Subshell						
55.7		L _I			M _I		
66.7		L _I	L _{II}	L _{III}	M _I	M _{II}	M _{III}
72.4		L _I	L _{II}	L _{III}	M _I	M _{II}	M _{III}
75.9		L _I	L _{II}	L _{III}	M _I	M _{II}	M _{III} N
90.6		L _I	L _{II}	L _{III}	M _I	M _{II}	M _{III} N
109.2	K	L _I	L _{II}	L _{III}	M		
163.8	K						
194.8	K						
667.3	K						
689.3	K						
712.7	K						
739.8	K	L					
767.6	K						
780.7	K						
840.0	K	L					
853.1	K						

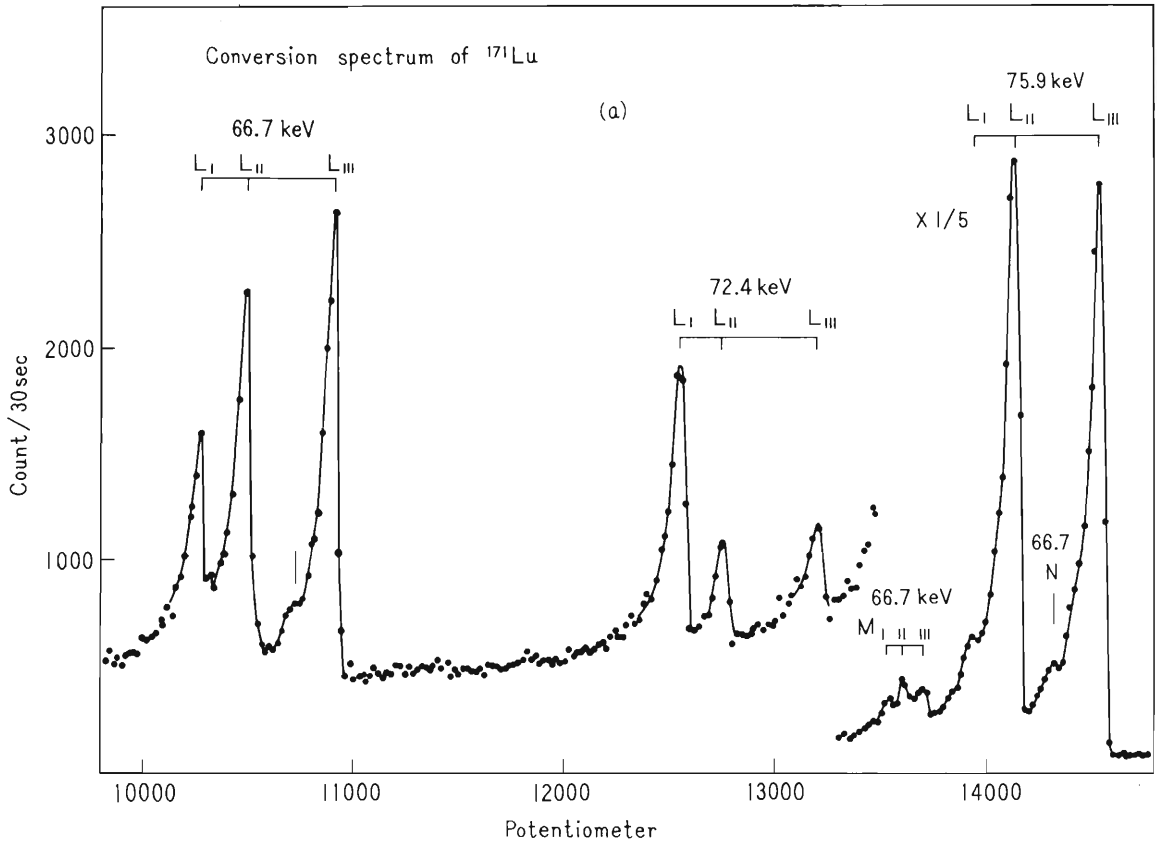


Fig. 1(a).

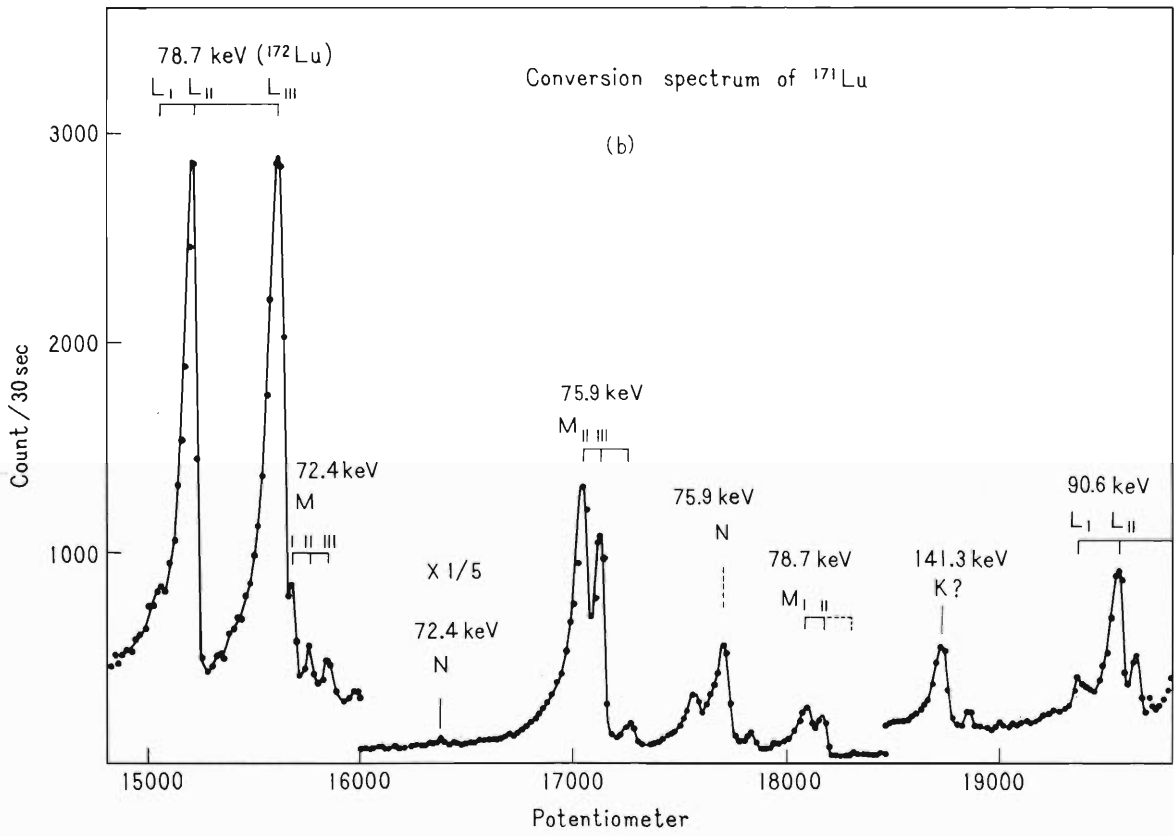


Fig. 1(b)

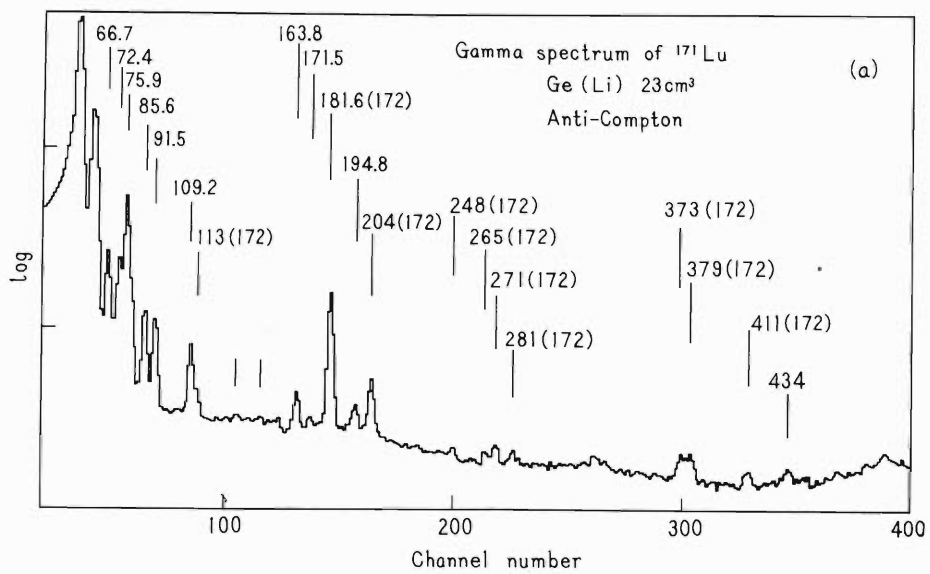


Fig. 2(a).

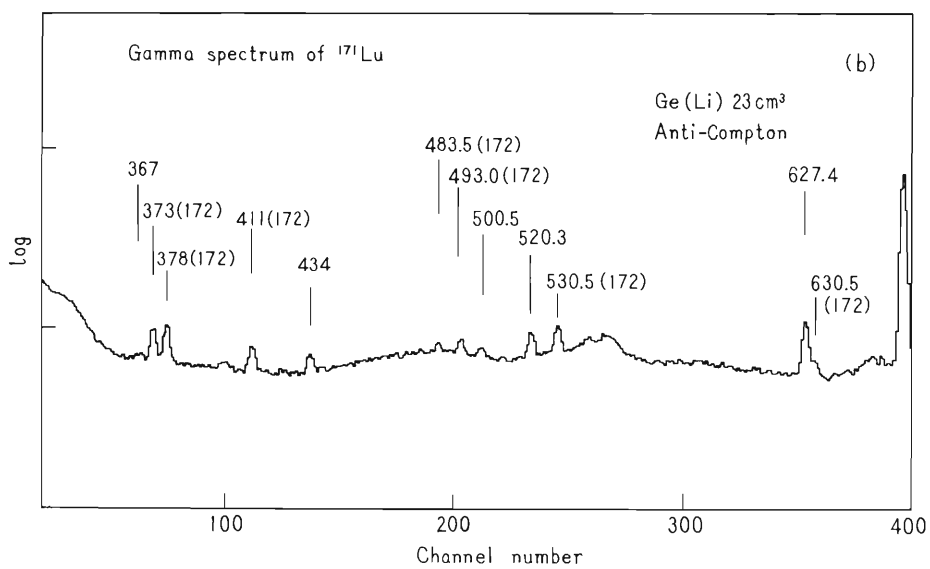


Fig. 2(b).

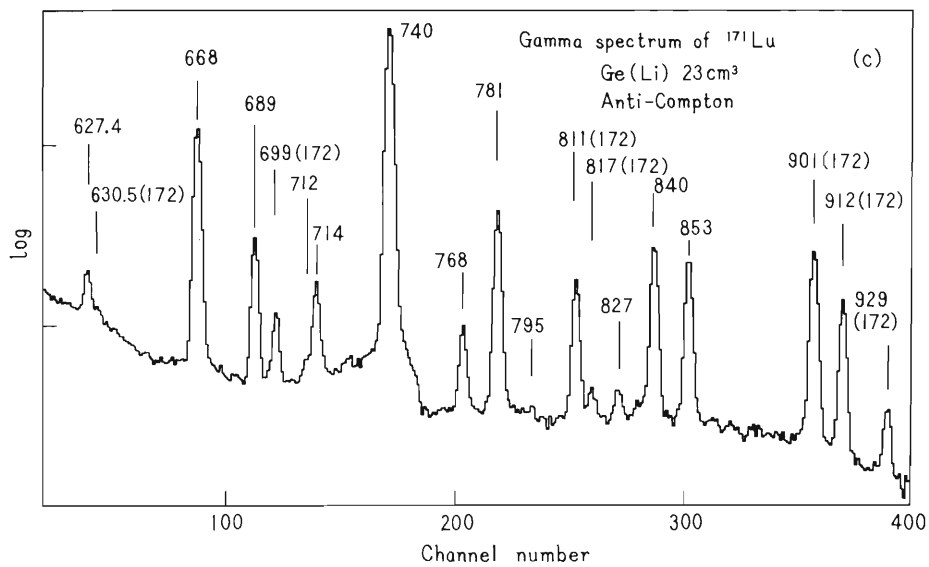


Fig. 2(c).

6-3. Study of Internal Conversion Electrons from ^{151}Eu

A. Hashizume

For the study of mixing ratios of the transitions in odd nuclei near the transition region of mass number 150, the conversion electron spectra from ^{151}Eu in the decay of ^{151}Gd ($T_{1/2} = 120$ days) have been measured by a high resolution air core β -ray spectrometer.

The enriched ^{149}Sm isotope in the chemical form of Sm_2O_3 was bombarded by 30 MeV alpha particles and ^{151}Gd was produced by $(\alpha, 2n)$ reaction. The gadolinium produced was chemically extracted from the target material by the ion-exchange method. A column of 12 mm in diameter and 50 cm in height was used. The flow rate of elute which consisted of 20 % NH_4B and 80 % HB (alpha-hydroxy-isobutyrate) by volume was kept at 20 ml/h

The fraction of gadolinium was then quantitatively eluted in a volume of 5 to 10 ml with the 0.25 M citrate buffer solution by the concentration process. And after the final purification process, the carrier free ^{151}Gd activity was obtained, and then electro-deposited on a thin nickel foil. A typical size of the source was 0.8 mm in width and 20 mm in height.

The over-all internal conversion electron spectra are shown in Figs. 1 and 2. In addition to the known 154, 175, 244, and 308 keV transitions, four new transitions, 197, 240, 262, and 287 keV, were found. These new transitions were also confirmed with a high resolution $23\text{ cm}^3\text{ Ge (Li)}$ γ -ray detector, except 240 keV which could not be resolved from the intense 244 keV peak. For the 154 and 175 keV transitions, L_{I} , L_{II} , and L_{III} electrons were resolved (Figs. 3 and 4) and L-subshell ratios were determined. The decay scheme and the mixing ratios of the transitions are now under investigation.

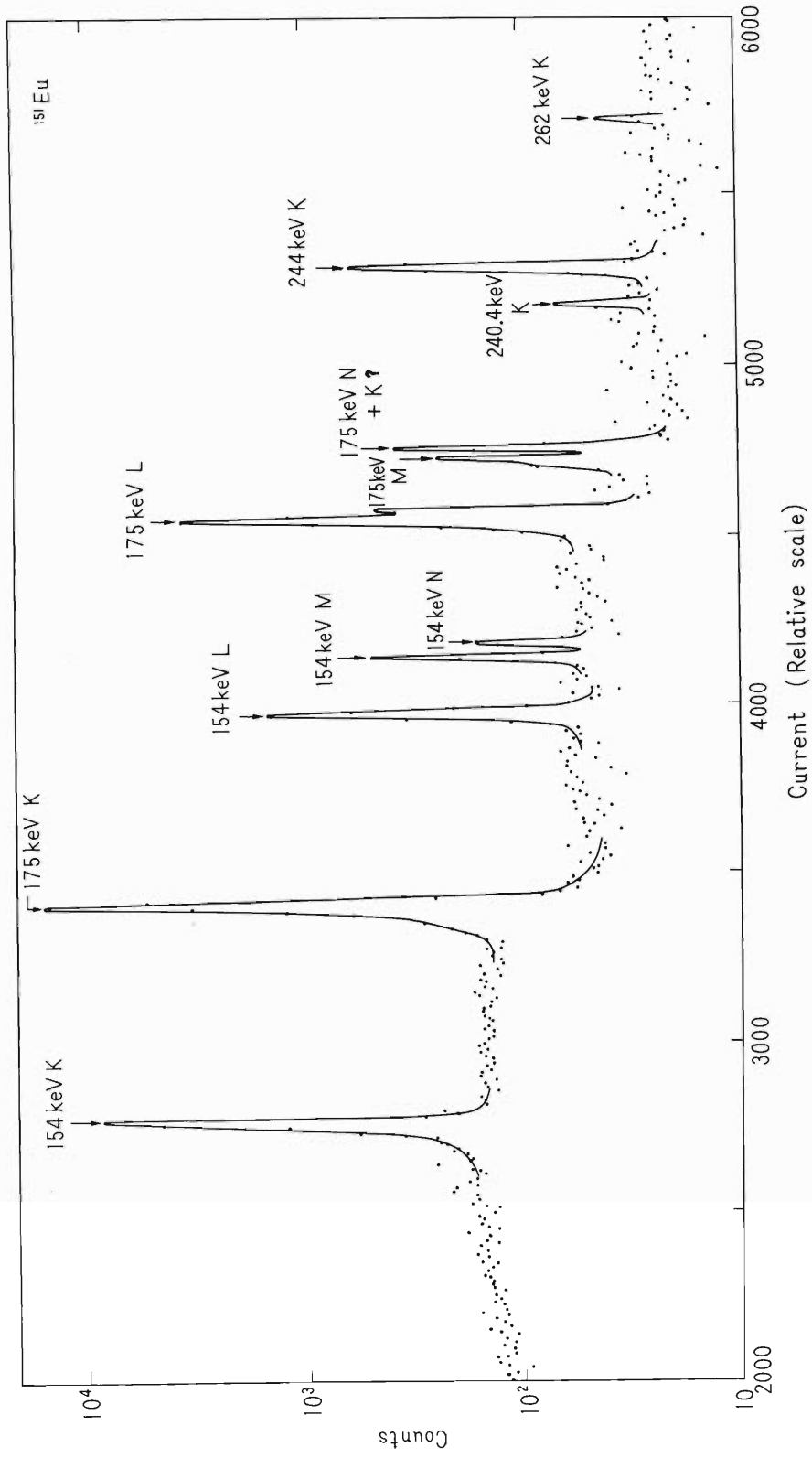


Fig. 1. The internal conversion electron spectrum in the momentum range 1000 ~1700 gauss-cm.

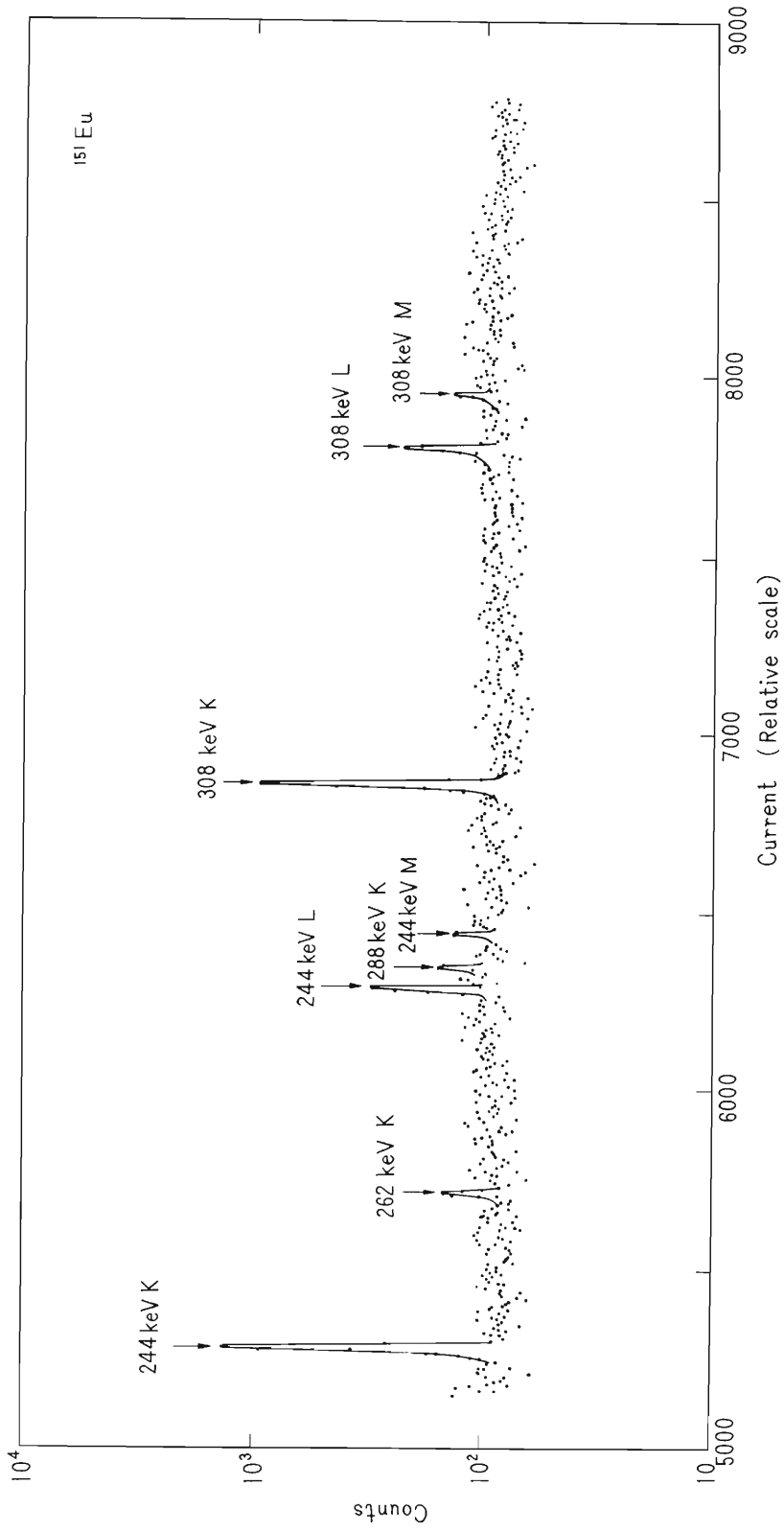


Fig. 2. The internal conversion electron spectrum in the momentum range 1600 ~ 2300 gause -cm.

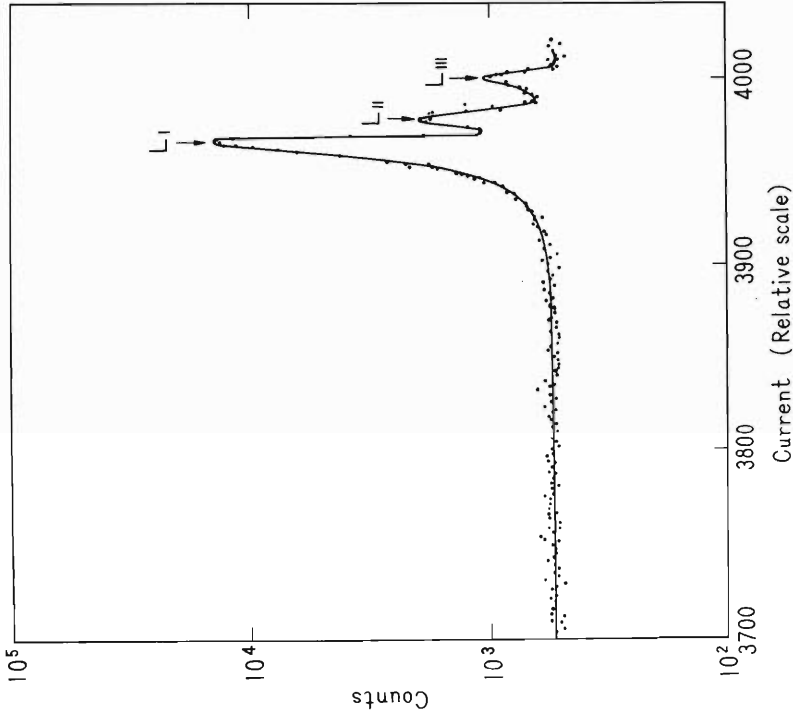


Fig. 4. L - internal conversion electron spectrum from 154 keV transition.

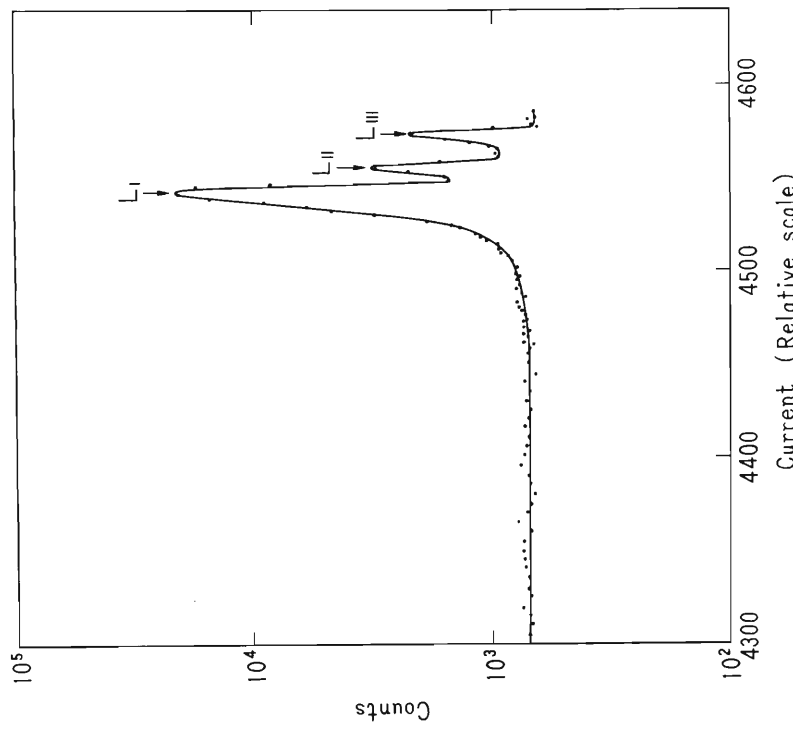


Fig. 3. L - internal conversion electron spectrum from 175 keV transition.

6-4. Decay of ^{87}Zr

Y. Awaya, Y. Tendow, T. Kato,
and A. Hashizume

The decay of ^{87}Zr has been investigated to study the nuclear structure of ^{87}Y . The ^{87}Zr isotope was produced by the $^{86}\text{Sr} (^3\text{He}, 2n)$ and $^{86}\text{Sr} (\alpha, 3n)$ reactions. The isotopically separated $^{86}\text{Sr} (\text{NO}_3)_2$ was used as the target. The zirconium isotopes were separated by using the anion exchange resin.

The gamma-ray spectra and the positron spectra were measured by 4 cc Ge (Li) detector and air-core beta-spectrometer, respectively. In addition to the 1.2 and 2.2 MeV gamma-rays observed in a previous work,¹⁾ several gamma-rays were newly found. The energies of observed gamma-rays which follow the decay of ^{87}Zr are 0.51 (annihilation gamma-ray), 0.765, 0.790, 1.140, 1.175, 1.200, 1.44, 1.56, 2.22, and 2.62 MeV. The gamma-ray spectrum is shown in Fig. 1. The study is in progress.

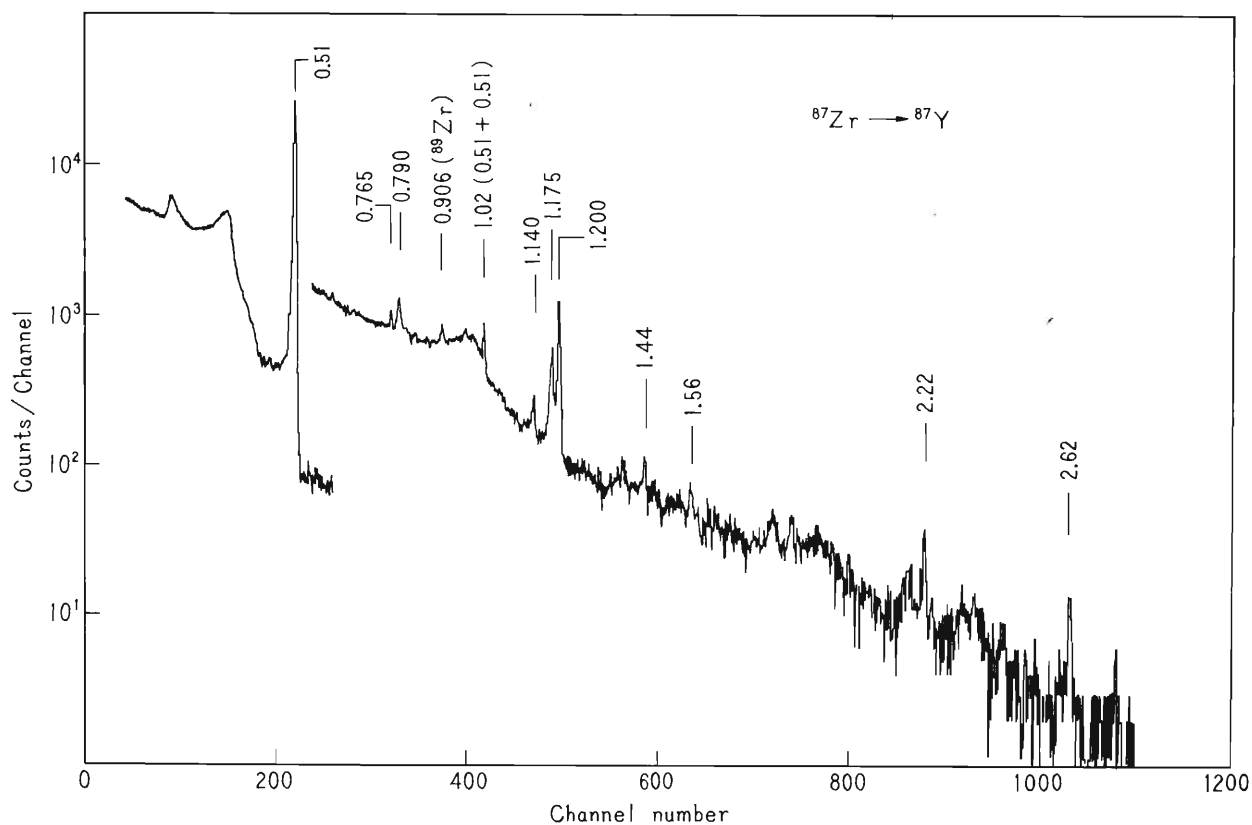


Fig. 1. The gamma-ray spectrum of ^{87}Zr . The energy values are in MeV.

Reference

- 1) Y. Awaya and Y. Tendow: J. Phys. Soc. Japan, 19, 606 (1964).

6-5. Nuclide Analysis Using Nuclear Reactions

M. Okano, A. Hashizume, Y. Awaya,
Y. Tendow, T. Kato, and T. Hamada

Two types of NaI (Tl) scintillation detectors were used so far for the gamma-ray spectroscopy in the study of nuclide analysis.¹⁾ They were recently replaced by a detection system using a lithium-drifted germanium detector because of its high energy resolution.

The primary detector is a 23.1 cc coaxial Ge (Li) detector* surrounded by an annular NaI (Tl) scintillator of 6 in O.D. \times 2 - 9/16 in I.D. \times 6 in, longitudinally split by halves.** Thus, the system works as a pair spectrometer which is advantageous for high-energy gamma-ray spectroscopy, while it works as an anti-Compton spectrometer being suitable for low-energy gamma-ray spectroscopy. Its construction and a block diagram of electronic circuits are shown in Figs. 1 and 2, respectively.

The gamma-ray spectrometer has been proved to be very effective not only in the activation analyses, but also in prompt gamma-ray energy measurements in (p,p') reactions, the latter seems to be useful for the elementary analyses of C, O, and N in organic compounds. In Fig. 3 a typical gamma-ray spectrum for urea, $\text{CO}(\text{NH}_2)_2$, bombarded by 8 MeV protons is shown.

* ORTEC, System Model No. 8001-20P.

** HARSHAW Chem. Comp. Type 24 M6BW 24/1 1/2 - X.

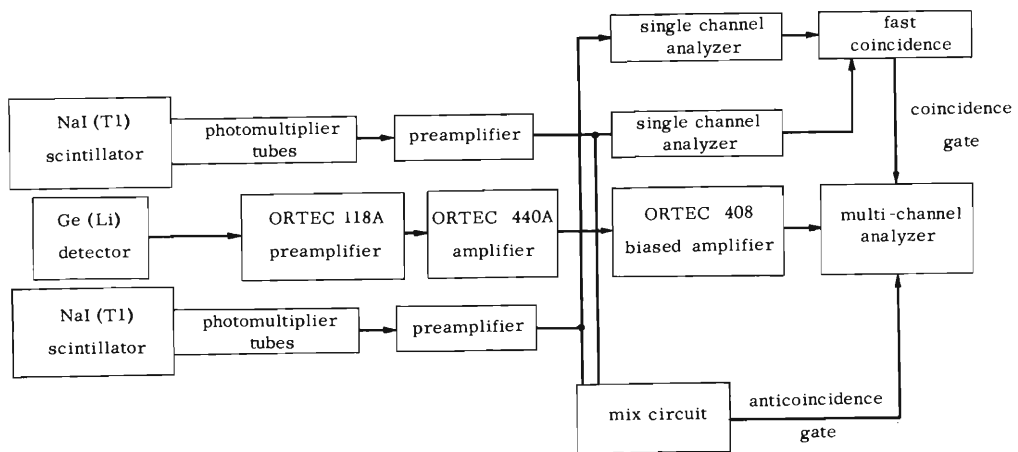


Fig. 2. Block diagram of electronic circuits.

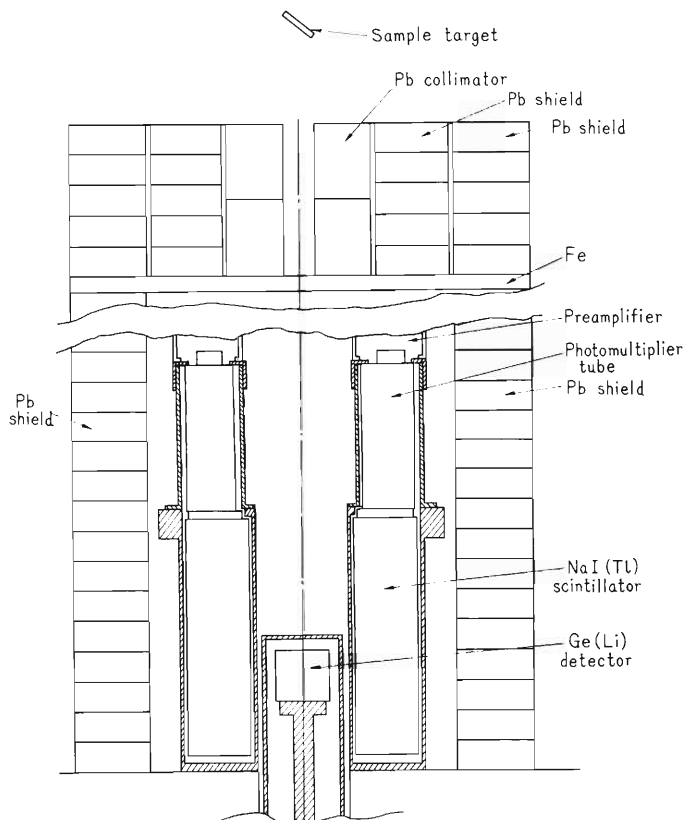


Fig. 1. Cross-sectional schematic drawing of the split annular NaI(Tl) scintillator with the Ge(Li) detector in position.

The lead collimator shown in the figure is for discrimination of stray radiations when the system is used for prompt gamma-ray energy measurements.

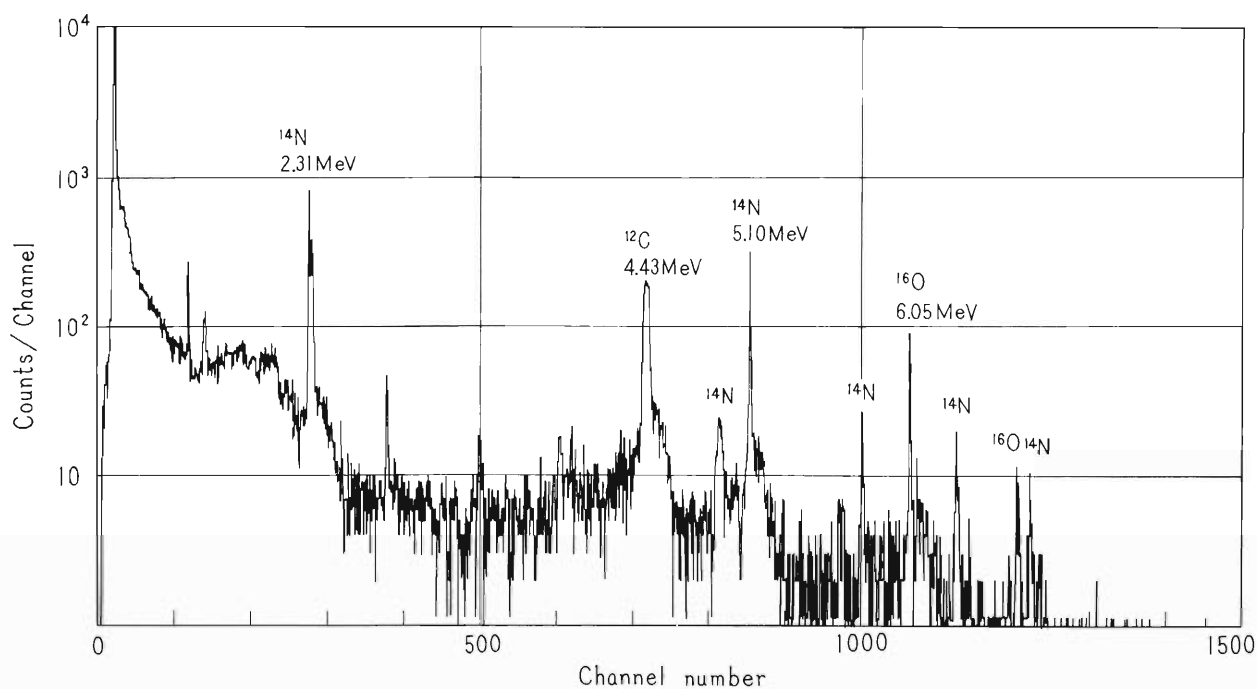


Fig. 3. Gamma-ray spectrum of urea bombarded by 8 MeV protons, obtained by the pair spectrometer.

Reference

- 1) T. Hamada, et al.: IPCR Cyclotron Progress Report, 1, 53 (1967).

7. NUCLEAR INSTRUMENTATION AND TECHNIQUES

7-1. The Polarized Ion Source

S. Motonaga, H. Kamitsubo, T. Fujisawa, and M. Hemmi

A polarized ion source which will be installed for IPCR Cyclotron is described. It is designed basically in the same way as the sources of Birmingham and Auckland. The main characteristics are as follows:

- a) Dissociation of H_2 by RF discharge at a low pressure of 0.4 mmHg.
- b) Collimation of H atoms through a multichannel pyrex nozzle.
- c) Separation of atomic states in a 40 cm long sextupole magnet with magnetic field of 7.5 kG.

Fig. 1 shows a schematic diagram of the complete set of the polarized ion source.

At present, the vacuum system, the dissociator, and the sextupole magnet are completed and their properties have been measured.

(1) Vacuum system

The vacuum system consists of three stainless steel chambers, the first contains the nozzle of discharge tube, the second the sextupole magnet, and the third a space for the anticipated RF transition system and the ionizer. The first chamber is pumped by an oil diffusion pump of 1500 ℓ /sec for air, the second by two pumps of 1500 ℓ /sec and 800 ℓ /sec for air and the ionizer by an oil diffusion pump of 800 ℓ /sec and an ion pump of 125 ℓ /sec.

(2) Dissociator and collimeter

Atoms are produced by dissociation of molecules in an electrodeless discharge. The discharge tube consists of a cylindrical pyrex tube, 3.5 cm in diameter and 20 cm long, located inside the coil of a resonant circuit which is coupled to a 20 Mc/sec RF oscillator. At gas pressure of 0.4 mmHg, about 300 W are dissipated in the discharge tube. The tube is cooled by an air blast. The power dissipated in the discharge tube has been measured by an insertion type RF powermeter. The dissociator and RF system are shown diagrammatically in Fig. 2, and Fig. 3 shows typical results of measurement on the dissipated power against the gas pressure. Measurement of atomic beam intensity is not made regularly. In order to obtain a high dissociation degree the tube will be treated in various ways.

Atoms diffuse out of the dissociator tube and come into the vacuum system through a multichannel nozzle which consists of about 1,000 capillary tubes each 2 mm long and 0.15 ~ 0.2 mm inside diameter. The collimators which have been made so far have a transparency of 65 %. Normal pressures in the dissociator are within the range from 0.2 to 0.4 mmHg, the flow rate of H_2 is 0.3 $m\ell$ /sec.

(3) Sextupole magnet

The separation of the electron spin components is done by a sextupole electromagnet. The poles are of normal soft steel, 40 cm long, and the pole tip radius is 4 mm throughout. Each pole piece is wound with 8 turns of 6 mm water-cooled copper tube and the insulation is made by teflon tape and spacers. The six coils are excited in series by a 10 V, 150 A power supply, and water-cooled in three branches separately.

Measurement of the magnetic field strength was made with a calibrated Hall probe. This measurement indicated that the sextupole properties are achieved in a region with a radius of 4 mm as shown in Fig. 4. The measured field gradient was 32 kG/cm and maximum field strength at the pole tip was 7.5 kG.

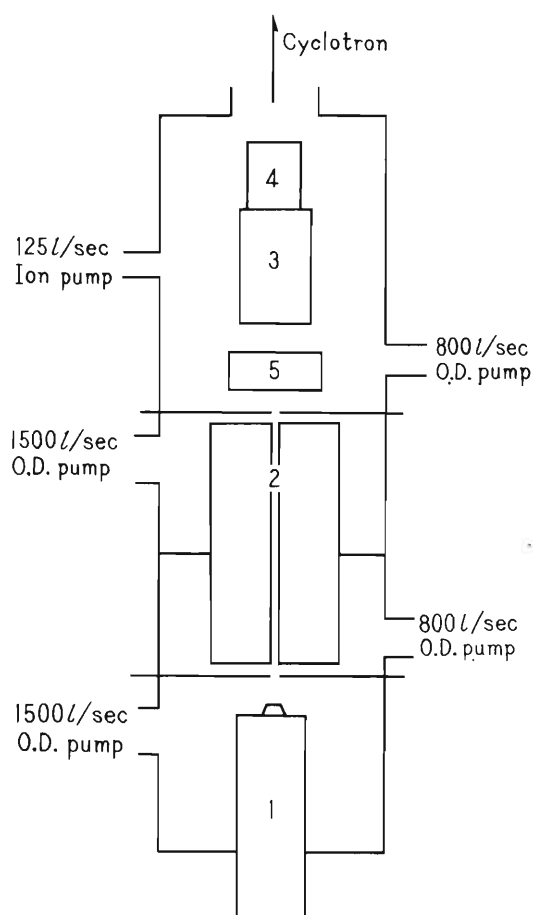


Fig. 1. Schematic design of the polarized ion source for IPCR cyclotron. 1. Dissociator, 2. Sextupole magnet, 3. Ionizer, 4. Extractor and 1st Einzel lens, 5. RF transition unit.

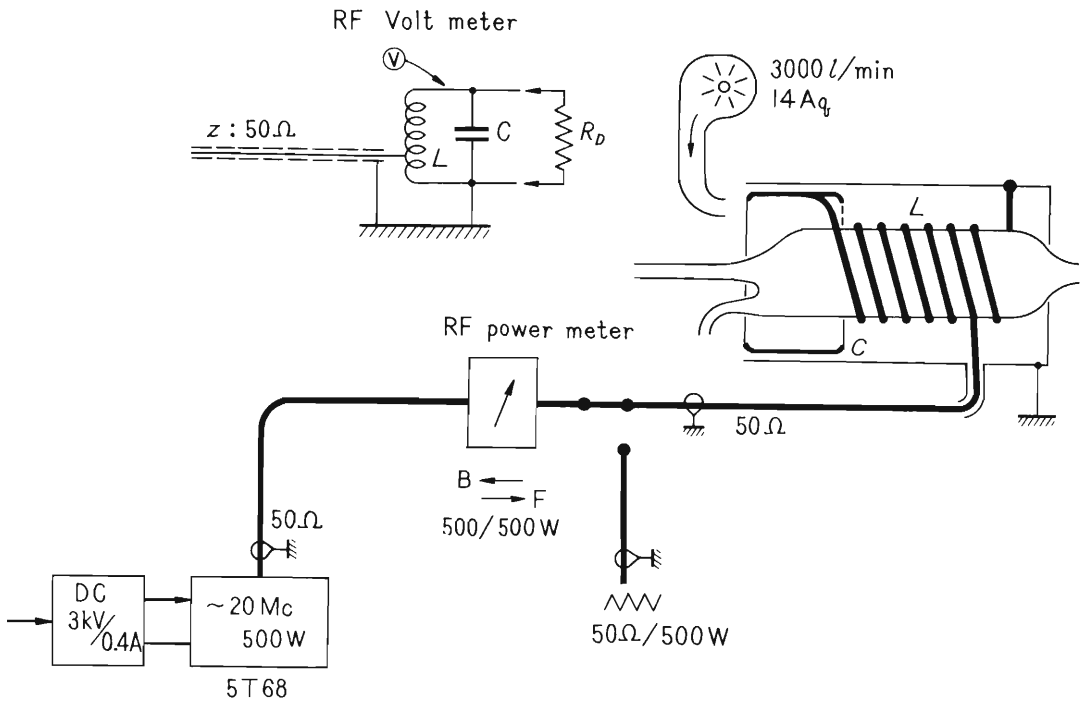


Fig. 2. Diagram of dissociator and RF system of the polarized ion source.

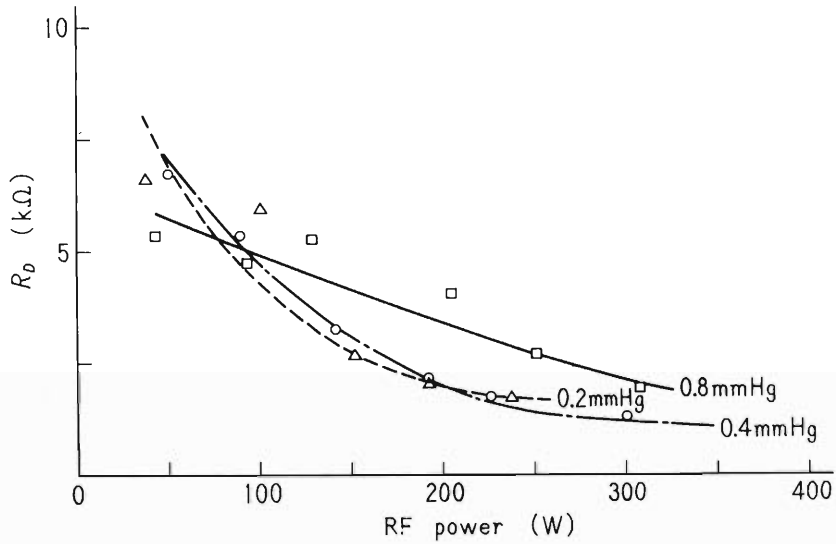


Fig. 3. Typical results of measurement on the dissipated power in the discharge tube. R_D is sluent impedance of discharge on a resonant circuit.

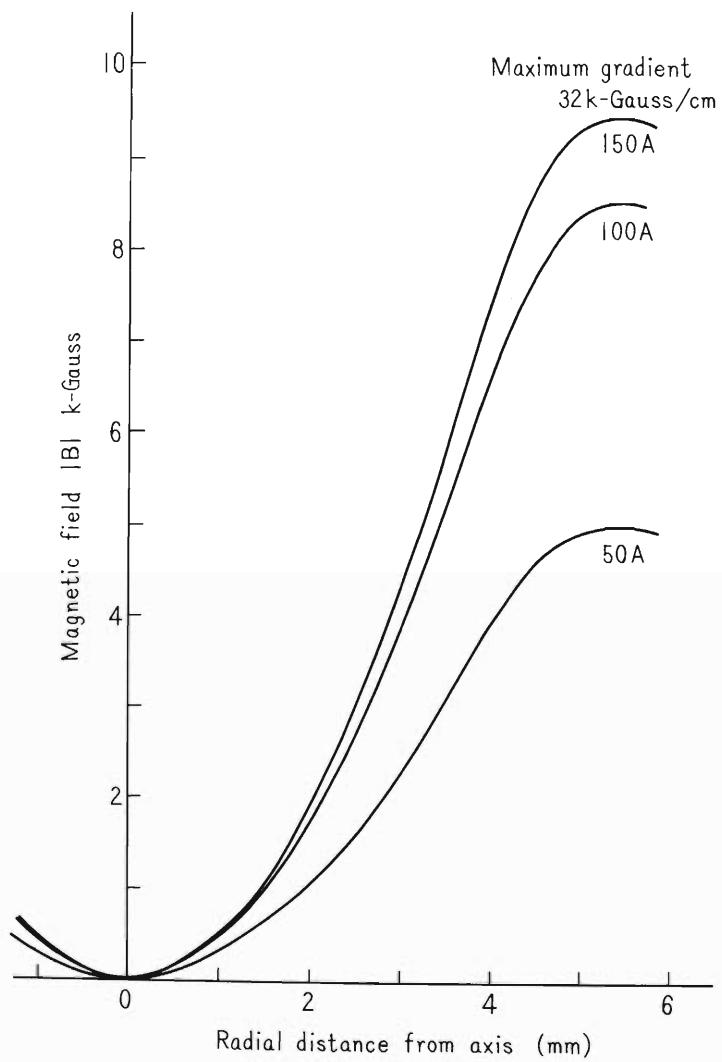


Fig. 4. Field measurement of the sextupole magnet.

7-2. The Electrically Detecting and Recording System Used for Broad-Range Magnetic Spectrometer

S. Takeda, J. Fujita, and T. Inoue

As one of the detection methods of charged particles analyzed by a broad-range magnetic spectrometer,¹⁾ an electronic system using an array of solid-state detectors,²⁾ each detector being of a transmission type, has been introduced in our laboratory. The array is used in place of a conventional nuclear emulsion in the focal plane of the spectrometer. This is a preliminary report about the electronically detecting and recording system, most of which have been developed in our laboratory. A good performance has been obtained by the experimental tests using a pulse generator.

The signals from each detector are amplified independently by the separate charge-sensitive amplifiers which are transistorized for compactness (Fig. 1). The outputs of the amplifiers are connected to a diode-matrix circuit and linear 8 channel-signal-adders as shown in Fig. 2. The diode-matrix initiated by Schmitt circuits converts the signals to the binary code or the address pulses adapted for the ND-2200-memory-driver.³⁾ The 8 channel-adders are used because of the following merits:

- a) Easy discrimination of high-counting rate-channels which interrupt the other channels in actual measurements.
- b) To meet easily the needs of particle identification with the transmission-detectors.
- c) The maintenance of the circuits becomes simple.

The mixed signals from all of the channels (total signal) are used for the gate-trigger of the following interface circuit and the particle identification. Fig. 3 shows the arrangement of the circuits schematically. The interface is put between the diode-matrix and the ND-2200-memory-driver in order to meet the electrical and timing requirements of the driver.* A block diagram of the interface is shown in Fig. 4. Fig. 5 is its timing chart. The particle identification is performed with discrimination between different pulse-heights corresponding to the types of particles using the transmission-detector. 4 channel-PHA has been developed for this purpose (Fig. 6).

* Instruction Manual of ND-2200-series.

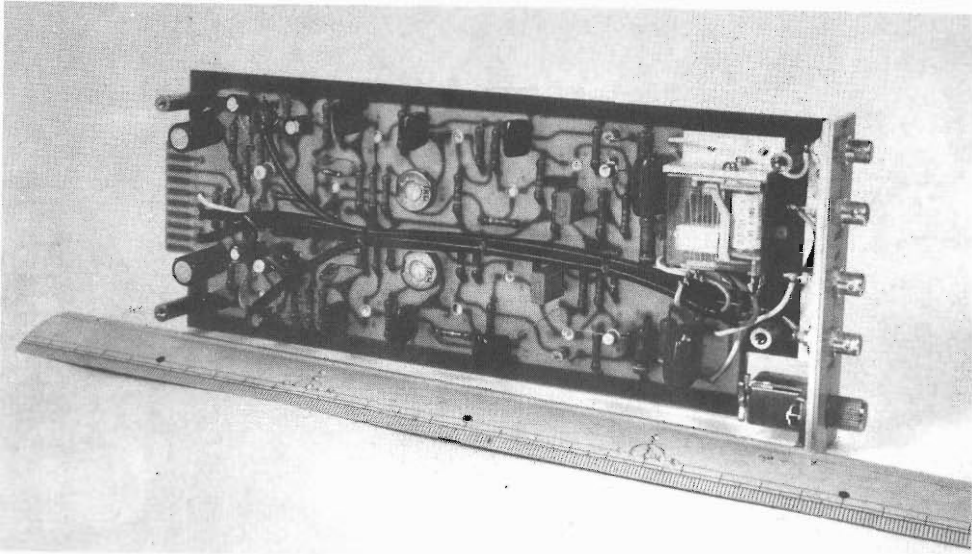


Fig. 1. Charge-sensitive preamplifier for SSD-array.

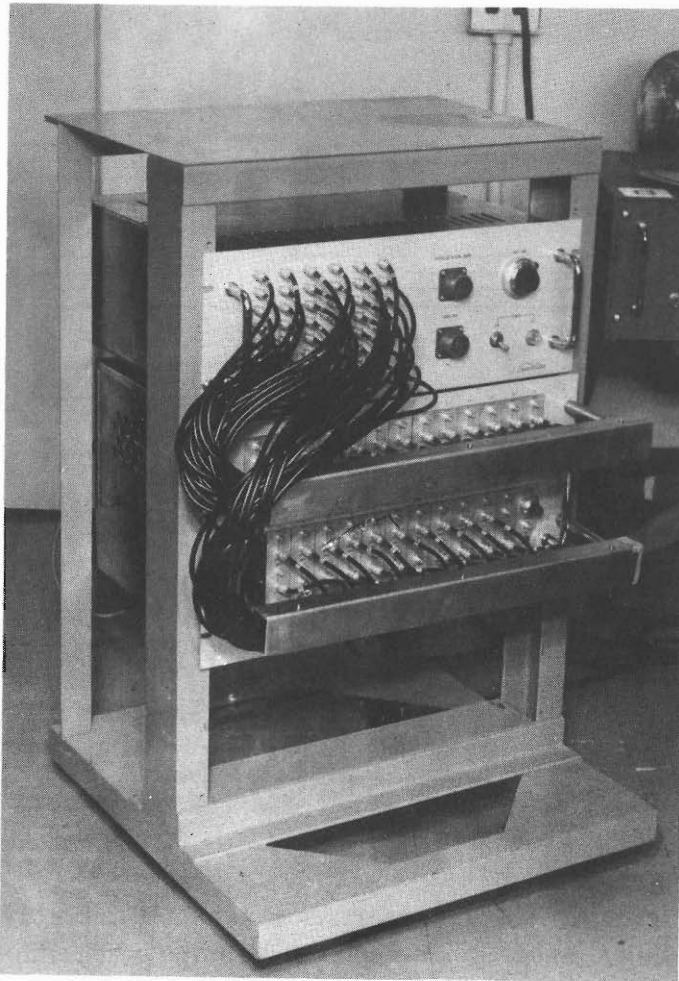


Fig. 2. Diode-matrix and linear signal-adder for data handling.

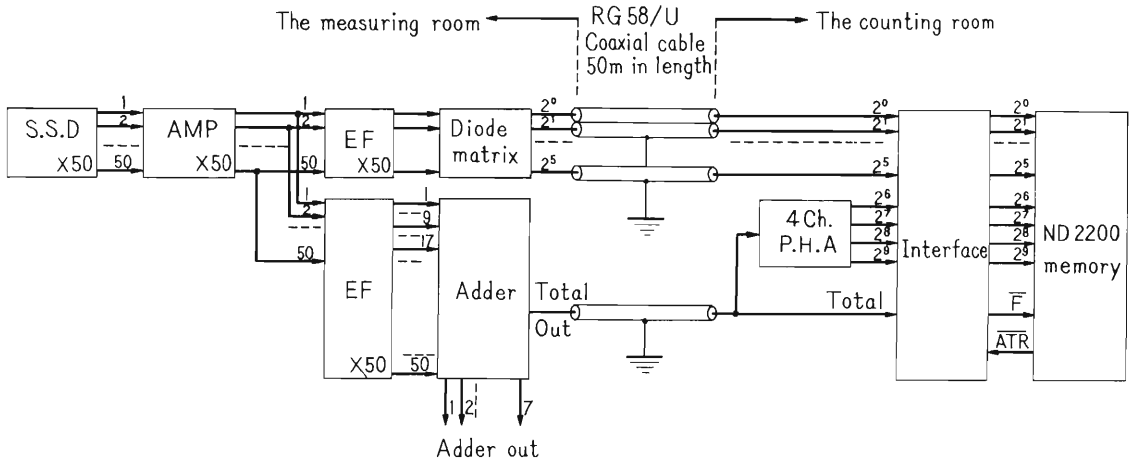


Fig. 3. Schematic diagram of the circuit arrangement for a 50-unit array of SSD.

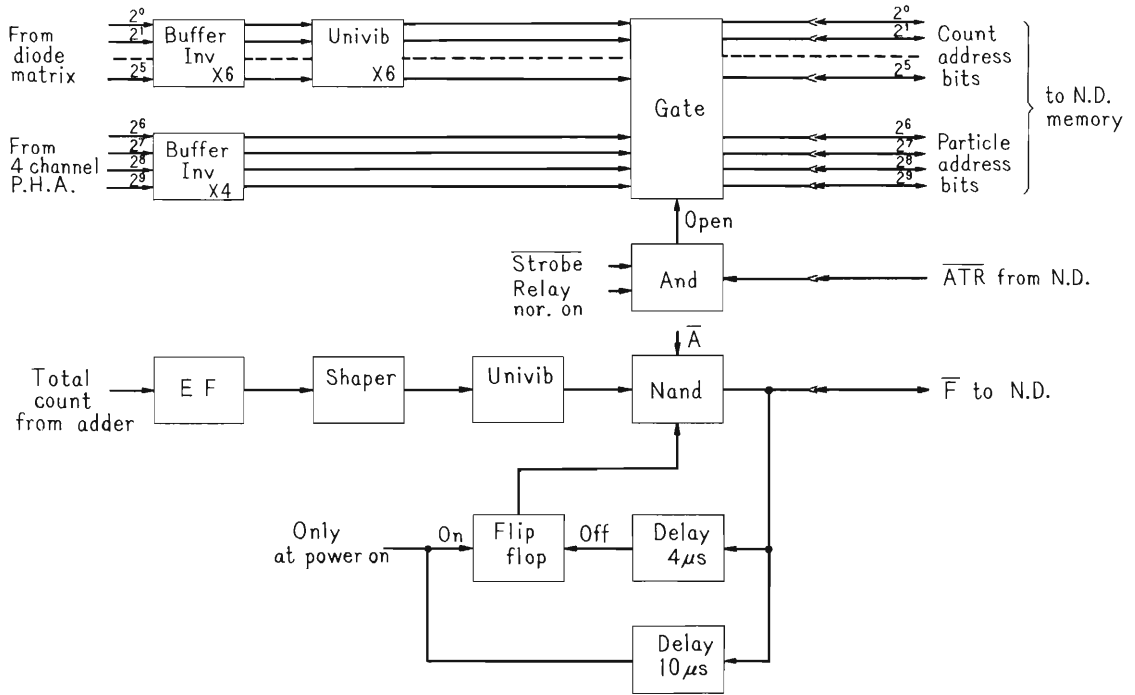


Fig. 4. Block diagram of the interface circuit. The circuit was developed around one diode-transistor-logic-element (the Nand gate).

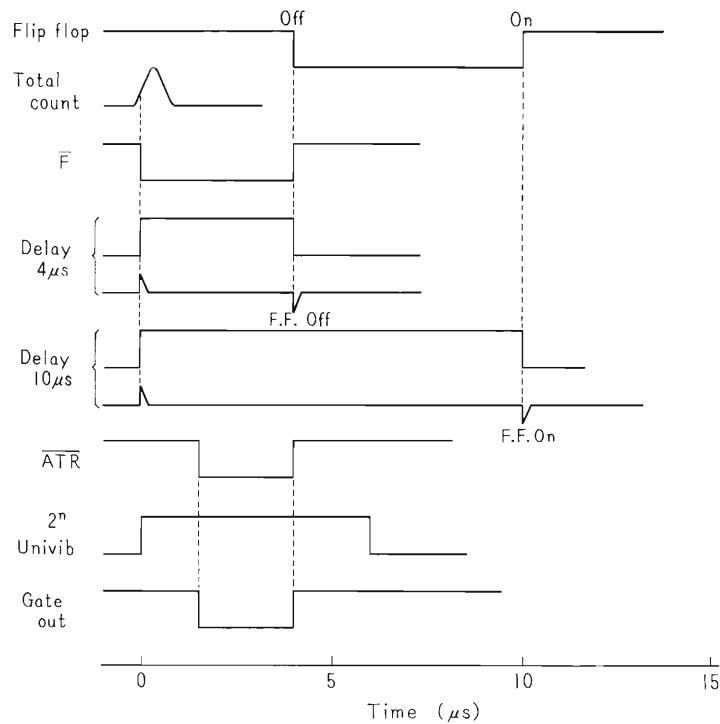


Fig. 5. Timing chart of the interface.

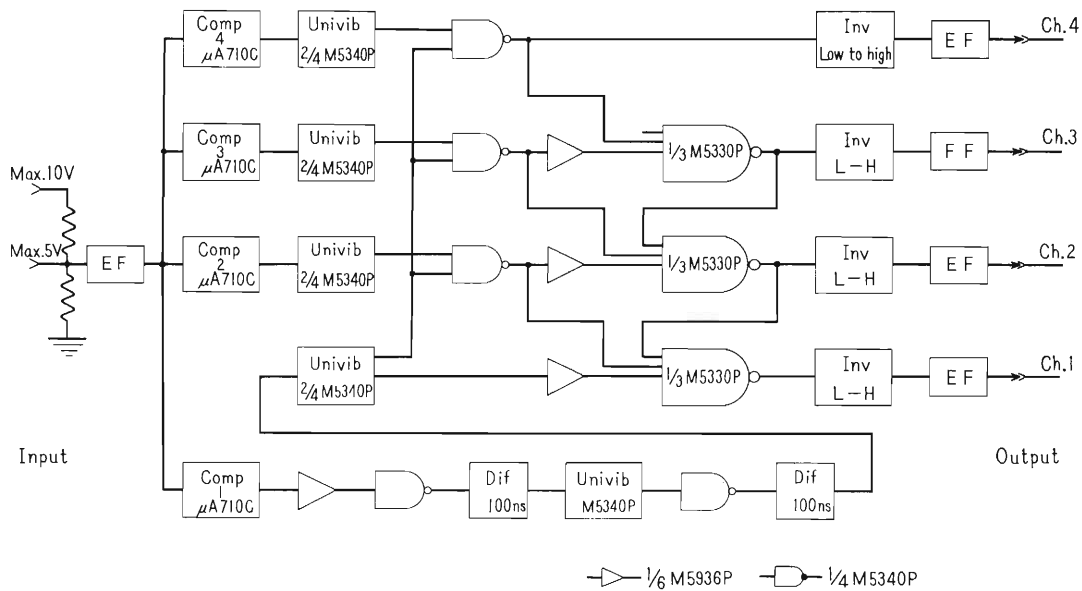


Fig. 6. 4 channel-PHA for particle identification. Almost all of the circuit elements are ready-made integrated circuits.

References

- 1) N. Nakanishi and K. Matsuda: Nucl. Instr. Methods, 57, 245 (1967)
- 2) K. Matsuda, I. Nonaka, K. Omata, K. Yagi, and M. Koike: *ibid.*, 53, 82 (1967).

7-3. A Charge Spectrometer

M. Aratani and N. Saito

The apparatus¹⁾ was outlined in the previous progress report.²⁾ The source volume and the ion-detection system using the pulse counting technique are the technical features of the spectrometer. The latter consists of a detector, a pulse amplifier, and a scaler. In 1968 some preliminary experiments were carried out with a variety of non-radioactive gaseous samples, such as Kr, Ar, He, and hydrocarbons. The ions of the samples were produced by electron bombardment. The ion current, of the order of 10^{-17} A, was measured either by pulse counting with a 400-channel pulse-height analyzer or by DC recording. The detector used in the experiments was a HTV* Cu-Be 10-stage particle multiplier. The results of the experiments have demonstrated that the gain of the particle multiplier varies strongly with the kind of ion being studied. For monoatomic ions the gain increases with a decreasing mass of the ion. In other words, the heavier the monoatomic ion, the lower the secondary electron emission ratio at the first dynode of the multiplier. In the case of the hydrocarbon ions, the gain increases with the number of atoms per ion. It has also been found that the secondary electron emission ratio at the first dynode to incident Kr^{2+} ions is of the same order as to Kr^+ ions. The gain of the particle multiplier was found to be a decisively important factor for the one-by-one pulse counting of the low-intensity beam of low-energy positive ions. The experiment has shown that a gain of at least 6×10^4 is needed for the pulse counting. Below this value noises and signals can not be distinguished from each other. A particle multiplier with a gain higher than 6×10^4 and with an operation voltage lower than 3000 eV seems to be desirable for the present purpose. A 16-stage multiplier is now being developed.

In another experiment, non-radioactive Kr ions formed by electron bombardment outside the source volume were injected into it. The energy of the ions ranged from 10 to 200 eV. The pressure in the source volume varied between 10^{-7} and 10^{-4} Torr at a dynamic equilibrium of the gas flow. A strong differential pumping system was installed between the source volume and the analyzer tube, where the pressure was kept at 10^{-7} Torr. Ion beams were detected by DC recording. When the energy of the ion was over 125 eV, the ion current of secondary krypton ions produced by ion-molecule reactions was negligibly small compared with that of primary ions at the pressure of 5×10^{-6} Torr. The ion current of the secondary ions increased with increasing pressure in the source volume. The current of the secondary ions exceeded that of the primary ions at the pressure of 7×10^{-5} Torr. At a constant pressure of 5×10^{-6} Torr, the doubly-charged ions increased from 8 to 20 % as the energy of the incident ion increased from 10 to 200 eV.

* Hamamatsu TV Co., Ltd., Hamamatsu Japan.

References

- 1) N. Saito and M. Aratani: Reports I.P.C.R. (in Japanese), 43, 153 (1967).
- 2) N. Saito and M. Aratani: IPCR Cyclotron Progress Report, 1, 65 (1967).

8. RADIOCHEMISTRY

8-1. Charged Particle Activation Analysis for Carbon, Nitrogen, and Oxygen in Semiconductor Silicon

T. Nozaki, Y. Yatsurugi, and N. Akiyama

This work has been in progress since last year; most of the results were reported at the "1968 International Conference on Modern Trends in Activation Analysis (October 7 ~ 11, 1968, N. B. S. Gaithersburg, Maryland, U. S. A.)".

Table 1 shows the reactions used and the possible interference reactions, with their threshold energies. It also gives the convenient incident particle energies, which have been selected with regard to the excitation curves or the threshold energies for all of the reactions concerned. The conditions of the bombardment, the surface-contamination removal, and the activity measurement in the analysis for carbon have been described in the "IPCR Cyclotron Progress Report, 1967", along with the technique of the chemical separation of the ^{11}C in a bombarded sample, (A higher beam flux ($3 \sim 8 \mu\text{A}$) is now available.) The ^{18}F was separated as follows: (a) the bombarded sample, after the surface contamination had been removed, was pulverized and dissolved in a NaOH solution containing NaF as a carrier, (b) HClO_4 was added to the resultant solution, and the fluorine was steam-distilled, and (c) it was precipitated as PbFCl and collected by filtration for the activity measurements. As to the activation standards, disks of graphite, nylon, and silica were used for carbon, nitrogen, and oxygen, respectively.

Among the interference reactions, the fissions of the matrix silicon itself should be considered most carefully. Fig. 1 shows the measured excitation curve for the $\text{Si}(\text{natural}) + {}^3\text{He} \rightarrow {}^{11}\text{C}$ reaction. A similar curve was observed for the $\text{Si}(\text{natural}) + {}^3\text{He} \rightarrow {}^{18}\text{F}$ reaction. Table 2 shows the possible reactions for the formation of the ^{11}C , along with their Q values, threshold energies, and Coulomb barriers. Comparing these values with the excitation curve in Fig. 1, we find that a considerable activity of ^{11}C is created by the tunnelling effect. The tunnelling probability or the penetrability through the Coulomb barrier was calculated for the ${}^{31}\text{Si}^* \rightarrow {}^{11}\text{C} + {}^{20}\text{Ne}$ reaction; it is also shown in Fig. 1, ${}^{31}\text{Si}^*$ being the compound nucleus formed from ${}^{28}\text{Si}$ and ${}^3\text{He}$. The penetrability formula described in textbooks treating the α -disintegration theory was used for the calculations. These fission reactions interfere seriously with the determination of the light elements; hence, the bombardment energy should be lowered until the fission reactions are no longer observable. An impurity concentration of 0.1 ppb is slightly beyond our detection limits. Thus, we propose, for general cases, such a selection of the incident particle energy that the tunnelling probability for any of the possible interference fissions of the matrix element does not exceed 10^{-10} .

Table 3 summarizes our analytical results. In order to ascertain the segregation of carbon in silicon in detail, we carried out the following experiments. We painted an aqueous suspension of carbon uniformly on a silicon rod and passed a molten zone through it. In the course of the zone-melting, a third phase, which is carborundum, appeared as a visible powder. Since the three phases, solid silicon, liquid silicon, and carborundum, then coexisted in equilibrium, the carbon concentration in the solid silicon is the solubility of carbon in solid silicon at its melting point. It was found to be about 2.3 p.p.m. From

this value, we can also obtain the equilibrium distribution coefficient of carbon, which can be expressed as its solubility in the solid silicon divided by its solubility in the liquid silicon. The latter was studied by several workers and found to be about 25 p.p.m. at the melting point. Therefore, the equilibrium distribution coefficient is about 0.09. Also using a silicon rod uniformly doped with carbon, we passed a molten zone through its several parts at different velocities. We then determined the resultant carbon distribution and obtained the effective distribution coefficients shown in Fig. 2. By extrapolating the curve of the effective distribution coefficient vs. zone velocities to zero velocity, as is shown in Fig. 3, we find the equilibrium distribution coefficient to be 0.06; this is in fairly good agreement with the above value.

Table 4 shows the oxygen contents of silicons made single-crystalline by various techniques. The oxygen content always increased in the CZ process using a quartz crucible and usually decreased in the FZ process. The FZ in vacuum was found to be very effective in removing the oxygen. When it was repeated, the oxygen content still decreased, but it tended to reach a value determined by the conditions and apparatus used, as was also observed in case of the carbon. When the samples after the FZ in vacuum were zone-melted in argon, their oxygen contents increased. This was surely due to the impurity oxygen in the argon. It was thus found that, in the course of the zone-melting, the oxygen content in silicon maintains an equilibrium with the environmental oxygen concentration.

Table 1. Activation reactions.

Element	Carbon	Nitrogen	Oxygen
Reaction adopted	$^{12}\text{C}(^3\text{He}, \alpha)^{11}\text{C}$	$^{14}\text{N}(p, \alpha)^{11}\text{C}$	$^{16}\text{O}(^3\text{He}, p)^{18}\text{F}$ $^{16}\text{O}(^3\text{He}, n)^{18}\text{Ne} \rightarrow ^{18}\text{F}$
	$^9\text{Be}(^3\text{He}, p)^{11}\text{C}$ {Exoth}	$^{11}\text{B}(p, n)^{11}\text{C}$ {3.1}	$^{19}\text{F}(^3\text{He}, \alpha)^{18}\text{F}$ {Exoth}
Interference reactions	$^{10}\text{B}(^3\text{He}, d)^{11}\text{C}$ {Exoth}	$^{12}\text{C}(p, d)^{11}\text{C}$ {18.0}	$^{20}\text{Ne}(^3\text{He}, \alpha p)^{18}\text{F}$ {3.1}
	$^{14}\text{N}(^3\text{He}, \alpha d)^{11}\text{C}$ {10.2}		$^{20}\text{Ne}(^3\text{He}, \alpha n)^{18}\text{Ne} \rightarrow ^{18}\text{F}$ {9.1}
	$^{16}\text{O}(^3\text{He}, 2\alpha)^{11}\text{C}$ {6.3}		$^{23}\text{Na}(^3\text{He}, 2\alpha)^{18}\text{F}$ {0.4}
	$^{28}\text{Si}(^3\text{He}, ^{20}\text{Ne})^{11}\text{C}$ {11.3}		$^{27}\text{Al}(^3\text{He}, 3\alpha)^{18}\text{F}$ {11.6}
			$^{29}\text{Si}(^3\text{He}, ^{14}\text{N})^{18}\text{F}$ {11.8}
Selected energy of bombardment	15 MeV	12 MeV	15 MeV

Note: Bracket indicate threshold energy in MeV.

Table 2. Possible reactions in $\text{Si} + {}^3\text{He} \rightarrow {}^{11}\text{C}$.

Target	Reaction	$-Q$ (MeV)	E_{th} (MeV)	V_{out} (MeV)	$(-Q) + V_{\text{out}}$
Si-28 (92.18 %)	$({}^3\text{He}, {}^{20}\text{Ne})$	10.2	11.3	12.2	22.4
	$({}^3\text{He}, {}^{16}\text{O } \alpha)$	19.5	21.6	10.1	29.6
	$({}^3\text{He}, {}^{12}\text{C } 2\alpha)$	26.7	29.6	8.0	34.7
	$({}^3\text{He}, 5\alpha)$	34.0	37.6	3.2	37.2
Si-29 (4.71%)	$({}^3\text{He}, {}^{21}\text{Ne})$ etc.	11.9	13.1	12.0	23.9
Si-30 (3.12 %)	$({}^3\text{He}, {}^{22}\text{Ne})$ etc.	12.1	13.3	11.9	24.0

Q: Q-value

E_{th} : Threshold energy

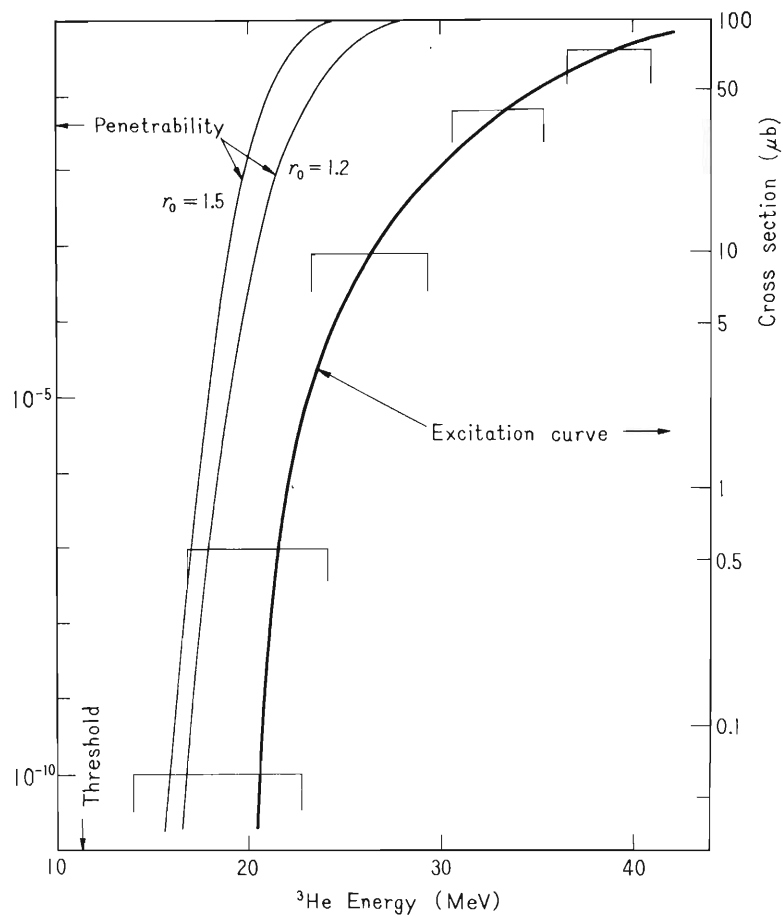
V_{out} : Coulomb barrier for the decomposition of the compound nucleus

Table 3. Summarized results.

Element		C	N	O
Concentration (p.p.b.)	Range	20 ~ 600	< 20	5 ~ 10000
	Most often observed	Around 100	Several	A few hundred
Behavior in zone-melting	Segregation	Significant toward tail	Significant toward tail	Not clear
	Interaction with atmosphere	Escapes into	Escapes into	Either enters from or escapes into

Table 4. Oxygen contents of the single-crystalline silicons.

Method of single-crystal formation	Oxygen content (p.p.b.)	
CZ in argon	5000	
FZ in argon (Single pass)	{ Top	400
	{ Tail	110
FZ in vacuum	{ Single pass	25
	{ Multiple pass	7
Polycrystal (raw material)	100	



r_0 : The nuclear radius constant

Fig. 1. Excitation curve for the $\text{Si} (\text{natural}) + {}^3\text{He} \rightarrow {}^{11}\text{C}$ reaction and penetrability for the ${}^{31}\text{S}^* \rightarrow {}^{11}\text{C} + {}^{20}\text{Ne}$.

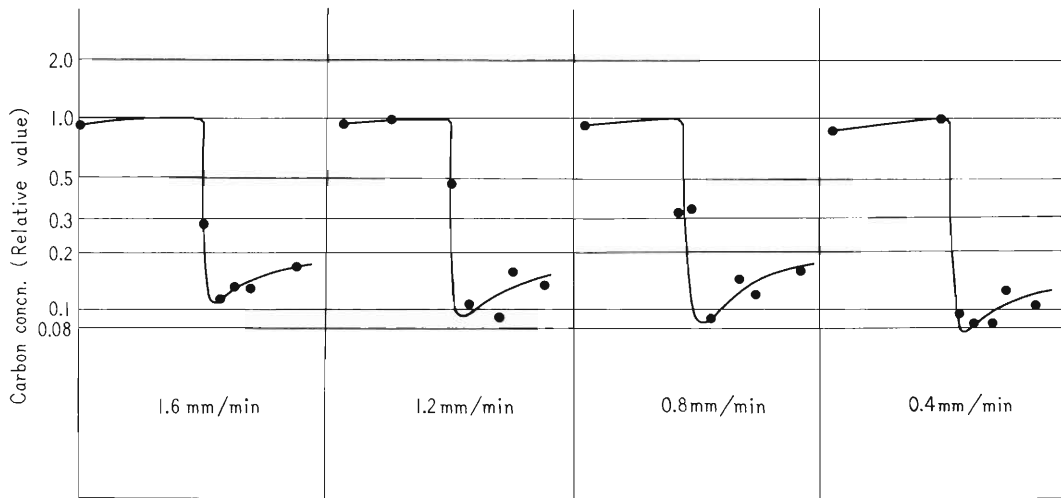


Fig. 2. Segregation of the carbon for zone - meltings with different zone velocities.

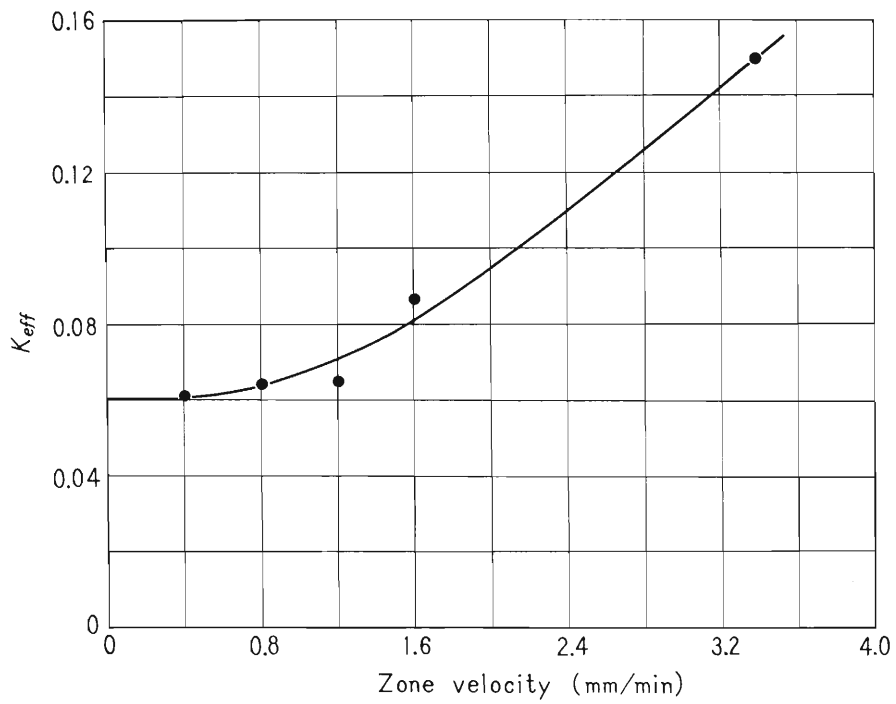


Fig. 3. K_{eff} vs. zone velocity .
(for carbon in silicon)

8-2. Recoil Chemistry of Halates

F. Ambe, S. Ambe, and N. Saito

As a part of a systematic investigation of the chemical effects of nuclear processes in halates,¹⁻⁴ a study was made of the behavior of radioactive recoil iodine atoms arising from the (n,γ) and $(n,2n)$ reactions in solid iodates.

Various iodates were irradiated with slow or fast neutrons obtained by the $^9\text{Be}(d,n)^{10}\text{B}$ reaction. The oxidation states of ^{128}I and ^{126}I , arising from the $^{127}\text{I}(n,\gamma)^{128}\text{I}$ and $^{127}\text{I}(n,2n)^{126}\text{I}$ reactions respectively, were determined by ordinary radiochemical procedures. The details of the experimental procedures were described in the preceding volume of this report, together with some preliminary results.

The results obtained are summarized in Tables 1 and 2. In the tables, the number of water molecules per iodate ion, m/n , is taken as a parameter showing the water content of each salt. From the data in the tables, the following conclusions can be drawn:

(a) The retention is affected by the nature of the salt. For example, in the iodates of heavy alkali metals the retention increases with an increase in the atomic number of the cation. In the case of hydrates with $m/n=1$, the retention of the zinc iodate is considerably higher than that of sodium salt.

(b) Hydrates show a lower retention than the corresponding anhydrous salts for every pair studied.

(c) When the retention of ^{126}I is plotted against that of ^{128}I , the plots lie near a straight line passing through the point of origin, as is shown in Fig. 1. In other words, the retention of radio-iodine depends on two independent factors, the type of nuclear reaction and the nature of the iodates.

(d) There exists no deuterium isotope effect exceeding the limits of experimental error in the case of sodium iodate monohydrate.

Similar work is in progress on chlorates.

Table 1. The Retention of ^{128}I after the $^{127}\text{I}(n, \gamma)$
 ^{128}I Reaction in Iodates, $\text{M}(\text{IO}_3)_n \cdot m\text{H}_2\text{O}$.

M	m/n			
		0	1	2
Li		$61 \pm 1 \%$		
Na		57 ± 1	$37 \pm 1 \%$ $38 \pm 1^*$	
K		57 ± 1		
Rb		63 ± 1		
Cs		66 ± 1		
Mg		56 ± 1		$42 \pm 2 \%$
Zn		57 ± 1	46 ± 2	
NH_4		23 ± 1		

* Deuterohydrate

Table 2. The Retention of ^{126}I after the $^{127}\text{I}(n, 2n)$
 ^{126}I Reaction in Iodates, $\text{M}(\text{IO}_3)_n \cdot m\text{H}_2\text{O}$.

M	m/n			
		0	1	2
Li		$36 \pm 1 \%$		
Na		40 ± 1	$31 \pm 1 \%$ $32 \pm 1^*$	
K		40 ± 2		
Cs		46 ± 2		
Mg		39 ± 1		$34 \pm 2 \%$
Zn		38 ± 2		
NH_4		17 ± 1		

* Deuterohydrate

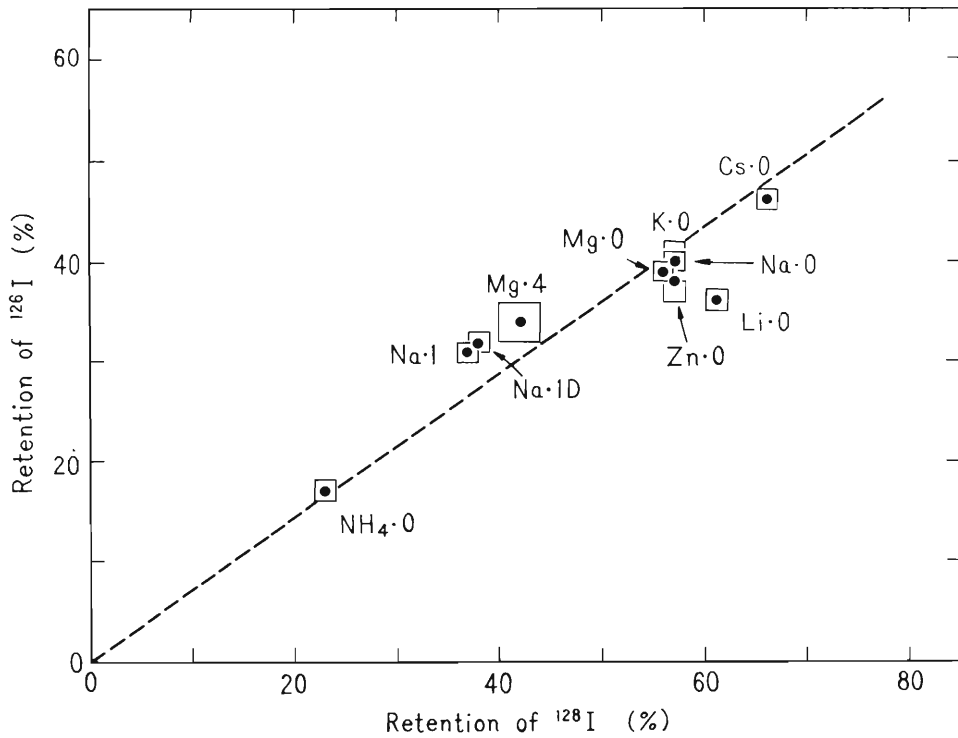


Fig. 1. The correlation of retention between ^{128}I and ^{126}I (the abbreviated symbols M.m stand for $\text{M}(\text{IO}_3)_n \cdot m\text{H}_2\text{O}$, and $\text{Na} \cdot \text{ID}$ for the deuterohydrate of $\text{Na} \cdot \text{I}$).

References

- 1) N. Saito, F. Ambe, and H. Sano: *Nature*, 205, 688 (1965).
- 2) N. Saito, F. Ambe, and H. Sano: *ibid.*, 206, 505 (1965).
- 3) N. Saito, F. Ambe, and H. Sano: *Radiochim. Acta*, 7, 131 (1967).
- 4) F. Ambe, H. Sano, and N. Saito: *ibid.*, 9, 116 (1968).

8-3. Preparation of a ^{61}Cu -Copper Source for the Measurement of the Mössbauer Effect in ^{61}Ni

F. Ambe, S. Ambe, and N. Saito

The Mössbauer effect in the 67.4 keV transition of ^{61}Ni may be expected to give valuable information in the fields of magnetism and coordination chemistry. However, few experiments have been reported since the first observation of the effect on this nuclide by Obenshain and Wegener.¹⁻⁵⁾ This is because the measurement of the effect in ^{61}Ni requires the use of a short-lived radioactive isotope (99 min ^{61}Co or 3.32 h ^{61}Cu) as the source or the use of ^{61}Ni in the 5.2 nsec-excited level produced by Coulomb excitation in an on-line experiment. Moreover, since the target materials used to produce the source nuclides are usually ferromagnets, special care is needed to obtain a single-line source free from magnetic hyperfine splitting. The NBS group used a Ni-Cr solid solution, with a small residual field of 15 kilogauss, as the target to produce ^{61}Co by the $^{62}\text{Ni}(\gamma, p)^{61}\text{Co}$ reaction.^{3,4)} The Oak Ridge group developed a technique to Coulomb-excite ^{61}Ni and, simultaneously, to implant the recoiled nucleus in the 5.2 nsec-excited level into a copper backing.⁴⁾ However, it seems that no radiochemical procedure has yet been reported for preparing a single-line source for the measurement of the effect in ^{61}Ni . We established a procedure to separate radiochemically the ^{61}Cu produced by the $^{58}\text{Ni}(\alpha, p)^{61}\text{Cu}$ and $^{58}\text{Ni}(\alpha, n)^{61}\text{Zn} \xrightarrow[1.48 \text{ min.}]{\beta^+} ^{61}\text{Cu}$ reactions⁶⁾ from the nickel target and to prepare a ^{61}Cu -copper source within several hours; we also measured the Mössbauer spectra of several absorbers by the use of the source.

A nickel foil (100 μ thick) of natural isotopic abundance was irradiated with 20 MeV α -particles accelerated in the IPCR cyclotron. The integrated beam current amounted to 50~100 mC, and 30~60 mCi of ^{61}Cu was obtained at the end of the irradiation. The target was dissolved in hot conc. hydrochloric acid containing hydrogen peroxide. The resulting solution was evaporated almost to dryness with a small amount of a copper carrier. The residue was dissolved in 8 M hydrochloric acid. The solution was passed through a column of an anion exchanger, Diaion SA#100, pretreated with 8 M hydrochloric acid. After the nickel ions had been washed out with a sufficient amount of 8 M hydrochloric acid, cupric ions were stripped from the resin with 2 M hydrochloric acid, whereas radioactive zinc ions produced by the (α, n) and other reactions in the nickel target remained in the resin phase. The effluent containing cupric ions was converted to a 0.5 M sulfuric acid solution free from chloride ions with the aid of a chelating ion exchanger, Dowex A-1. ^{61}Cu was electroplated from the solution onto a copper foil under a controlled potential of 2.2 V at 40°C. The foil with ^{61}Cu was annealed for 30 min. at 850°C in a high vacuum. The net counting rate of 67.4 keV γ -rays at the beginning of the measurement was 2000~3000 cps in the geometry of the spectrometer employed.

The Mössbauer effect was measured with an electromechanical feedback-type spectrometer connected to a Hitachi 400-channel pulse-height analyser. Both the source and the absorber were kept at $79 \pm 1^\circ\text{K}$ in a stainless steel Dewar vessel filled with liquid nitrogen. The 67.4 keV γ -rays were counted with a NaI scintillator 2 mm thick. The S/N ratio was about unity.

A spectrum of ^{61}Ni diffused in copper is shown in Fig. 1 as an example. The application of the technique described here is reported in the Solid State Physics section of this volume.

Measurements of the spectra of various nickel compounds are now in progress.

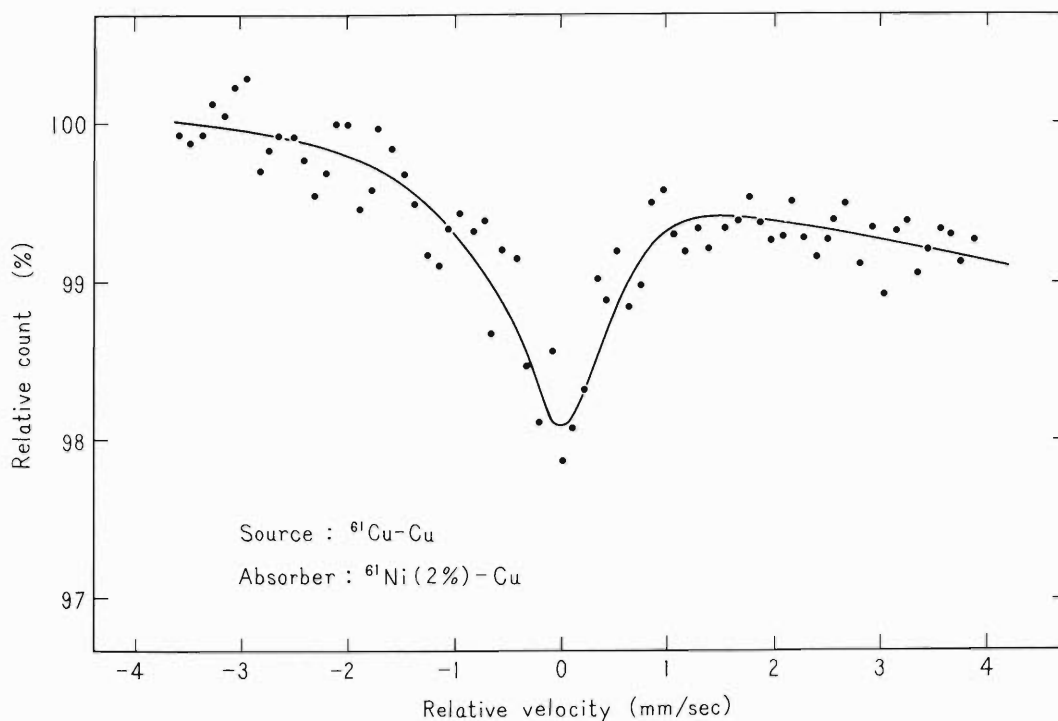


Fig. 1. Mössbauer spectrum of ^{61}Ni diffused in copper (source: ^{61}Cu in copper).

Note : The inclination of base line corresponds to the decay of ^{61}Cu .

References

- 1) F.E. Obenshain and H.H.F. Wegener: Phys. Rev., 121, 1344 (1961).
- 2) D. Seyboth, F.E. Obenshain, and G. Czjzek: Phys. Rev. Letters, 14, 954 (1965).
- 3) J.J. Spijkerman: Symp. Faraday Soc., (No. 1), 134 (1967).
- 4) J.C. Love, G. Czjzek, J.J. Spijkerman, and D.K. Snediker: "Hyperfine structure and nuclear radiations", North-Holland, Publ. Co., Amsterdam, p. 124 (1968).
- 5) U. Erich and D. Quitmann: "Hyperfine structure and nuclear radiations", *ibid.*, p. 130.
- 6) S. Tanaka: J. Phys. Soc. Japan, 15, 2159 (1960).

8-4. ^{14}C -labeling Reaction with Proton Beam from Cyclotron

Y.G. Tanaka, T. Nozaki, and T. Karasawa

Three methods are applicable to labeling with radioisotopes on organic compounds: biochemical, chemical synthetic, and recoil methods. The recoil reaction has certainly a great advantage of labeling with short life nuclide, because large quantity of nuclide is produced in a short time irradiation. On the contrary, it is less useful for labeling with carbon-14, a typical long life nuclide. The same is true of the twin reasons of necessity of long irradiation time for a production of long half life radioactive nuclide, and a radiation damage of an organic substance during long time bombardment onto a target.

Consequently, recoil labeling technique with carbon-14, using $^{14}\text{N}(n,p)^{14}\text{C}$ reaction, may safely be assumed that it can not rival to chemical synthetic labeling methods. Because, specific activities of recoil labeled products could not reach $1\text{ m}\mu\text{Ci/mg-carbon}$ and those of chemical labeling methods reached $0.1 \sim 1\text{ mCi/mg-C}$. Therefore, new techniques have been required for an investigation of labeling reaction with carbon-14.

From this point of view, the authors have carried out the investigation of a new technique of labeling reaction with carbon-14 by bombardment with accelerated proton particles onto a mixture of carbon-14 and an organic compound.

A pyrex irradiation cell attached with $50\ \mu\text{m}$ thickness aluminum foils on both sides was filled with a methanol solution of urea- ^{14}C ($10\ \mu\text{Ci/ml}$). An irradiation was carried out with a proton beam from the IPCR 160 cm cyclotron after passing a thin aluminum window and an air layer. The methanol solution was chilled by a water cooling jacket, then the temperature was kept from 23° to 25°C and the beam intensity was $2.1 \sim 2.7\ \mu\text{A}$. The input charge in the solution was monitored by reading the current between the copper plate in contact with the aluminum foil and that connected to ground through a current integrator.

(1) Bombardment with constant energy (10.3 MeV) proton

All samples (13 ml each) were irradiated with constant energy (10.3 MeV) proton and total charge input was selected stepwise: 3, 6, 12, 24 millicoulombs. After the irradiation, excess urea- ^{14}C was separated by a frozen vacuum distillation. Byproducts, formaldehyde was removed with sodium borohydride; glycol, by fine distillation; carbondioxide, with caustic soda; and gaseous byproducts, by frozen vacuum distillations. The purified methanol- ^{14}C was identified by a Carry-Loenco radio gas chromatography with a carbowax 20 M column. The activities of methanol- ^{14}C were measured every 10 minutes by a Beckman LS 150 liquid scintillation counter, with scintillator Dolite DPO, POPOP toluene. The activities of methanol- ^{14}C were measured from 132 to 1320 hours after the irradiation, but no decline of the activities was observed in this period. The results are given in Fig. 1.

(2) Bombardment with proton changed energy stepwise

The samples were irradiated with proton which changed its energy stepwise: 1.5, 3.0, 6.16, 7.5, 10.3 MeV and total charge input was 12 millicoulombs each. At 1.5 and 3.0 MeV, neither $^{14}\text{N}(p,\alpha)^{11}\text{C}$ nor $^{16}\text{O}(p,\alpha)^{13}\text{N}$ reaction could occur by all means. After

the irradiation, similar treatments were made on the samples. The results are given in Fig. 2.

In the range of the present investigation.

(a) Methanol was labeled with carbon-14 when a mixture of urea- ^{14}C and methanol was bombarded with accelerated protons.

(b) When the energy of proton was constant, the specific activity and the total activity of methanol- ^{14}C were proportional to the total charge input.

(c) When the total charge input was constant, the specific activity and the total activity of methanol- ^{14}C were proportional to the energy of proton particles.

(d) Labeling reaction occurred with 3.0 MeV proton; it means this reaction proceeds by the action of accelerated proton alone.

Acknowledgment

The authors are indebted to the IPCR cyclotron staff for helpful collaboration and operation of the machine.

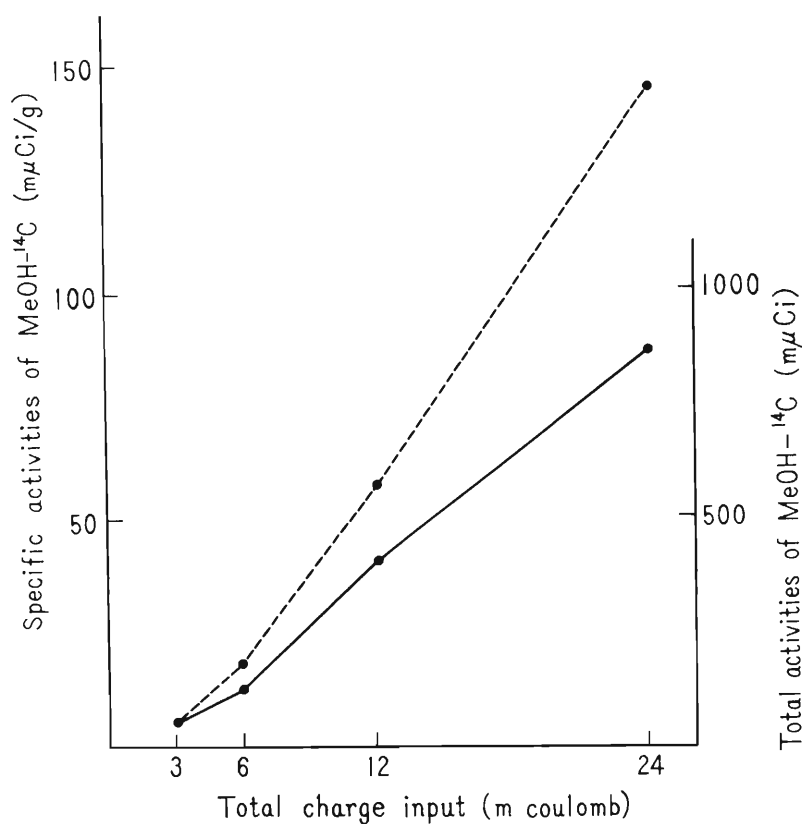


Fig. 1. Specific activities (dotted line) and total activities of methanol- ^{14}C (solid line) vs. total charge input.

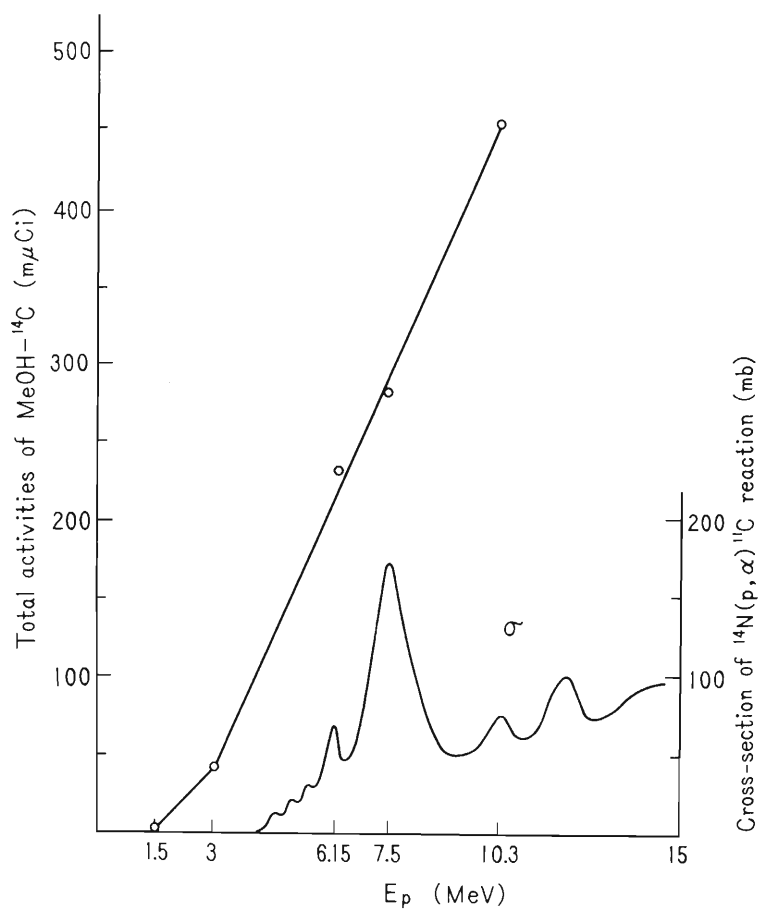


Fig. 2. Total activities of methanol- ^{14}C and cross-section of $^{14}\text{N}(p, \alpha)^{11}\text{C}$ reaction (marked with σ)^{1,2)} vs. energy of proton.

References

- 1) J.P. Blaser, et al.: *Helv. Phys. Acta*, **25**, 442 (1952).
- 2) T. Nozaki, et al.: *Bull. Chem. Soc. Japan*, **39**, 2685 (1966).

9. RADIATION CHEMISTRY AND RADIATION BIOLOGY

9-1. Radiation-Chemical Studies of Fricke Dosimeter with Cyclotron Beams

T. Karasawa, M. Matsui, H. Seki,
and M. Imamura

The yields of chemical reactions induced by ionizing radiation vary with LET (linear energy transfer or stopping power) of the radiation. In order to obtain an accurate yield (represented with G , the number of molecules produced per 100 eV absorbed), an accurate energy absorbed in chemical substance should be determined. Since aqueous ferrous sulfate solution (Fricke dosimeter solution) is advantageously used in radiation chemistry, this solution was utilized for the determination of the dose of cyclotron beams.

Several papers have been published on the oxidation yield of the Fricke dosimeter, $G(\text{Fe}^{3+})$, for various types of radiation.^{1~4)} However, there were some discrepancies among the yields obtained with different radiations with the same LET. According to Schuler and Allen²⁾ α particles give higher yields than those for deuterons of the same LET. This apparent discrepancy has been explained by considering the kinetics of secondary electron production.⁵⁾ On the other hand, Anderson and Hart³⁾ reported that the yields for protons were higher than those for α particles of the same LET. We, therefore, initiated the study to determine $G(\text{Fe}^{3+})$ for several kinds of particles with various LET in the wide range by the same experimental procedure. The variable energy-ordinary type IPCR cyclotron is suitable for this purpose.

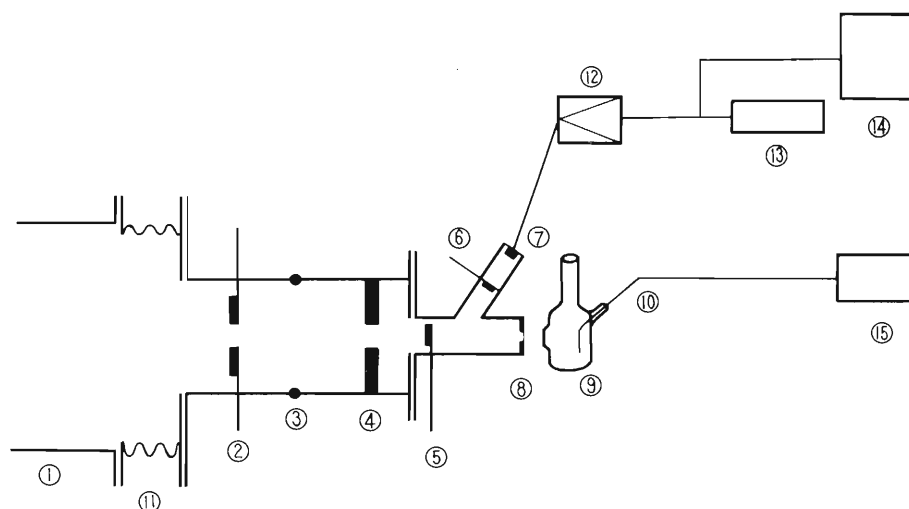
Irradiations were performed at the end of the No. 4 beam course, approximately 10 m from the cyclotron. Irradiation arrangement is schematically illustrated in Fig. 1. A beam spot was about 5 mm in diameter on the window of the irradiation cell. The irradiation cell was made of glass, 100 mm high and 10 mm in O.D., with a aperture 10 mm in diameter. The aperture was covered with a thin quartz or a mica window. Aqueous ferrous sulfate solution was prepared by dissolving $\text{Fe}(\text{NH}_4)_2(\text{SO}_4)_2$ (10^{-2} or 10^{-3} M), NaCl (10^{-3} M), and H_2SO_4 (0.4 M) in aerated triply-distilled water. The volume of the irradiated solution was 5.0 ml. The solution was stirred by a magnetic stirrer during irradiation.

The beam current absorbed in the solution (I_s) through the window was read from a platinum wire immersed in solution and connected to ground through a current integrator. This current was always less than the true current determined with a Faraday cup (I_f) owing to the charge displacement effect at the window. This effect was determined by counting elastically scattered α particles (C) by using a solid state detector (Toshiba M8810B). Scattering foils used were 2μ Au, 3μ Ni, and 1μ Ni for α particles of 40, 20, and 16 MeV, respectively, which were chosen by considering multiple coulombic scattering.

The charge displacement is tentatively expressed as $(C_s/I_s)/(C_f/I_f)$, the variation of which with the beam energy is shown in Fig. 2. The charge displacement increases as the ionization density of the particles increases. At the beam energy in solution of about 1 MeV $(C_s/I_s)/(C_f/I_f)$ reaches 1.7, below which it rises sharply. This value was obtained from that of I_s/C_s at the energy where I_s began to decrease abruptly. The

beam energy was determined with a beam analyzing magnet when an accurate value was desired. Usually it was estimated from a radio frequency of the cyclotron.

The oxidation yields of the Fricke solution were determined for α particles and protons of various energies. The rate of stirring was always maintained well above that at which $G(\text{Fe}^{3+})$ was found to be independent of stirring speed. Irradiations were performed at a current intensity in the range $1 \sim 2 \times 10^{-9}$ A for 30 MeV α particles and $0.5 \sim 1 \times 10^{-9}$ A for 16 MeV α particles, respectively, above which $G(\text{Fe}^{3+})$ decreases depending upon the current intensity and the concentration of ferrous ions in solution as shown in Fig. 3. The yields were calculated from the concentrations of ferric ions produced (determined spectrophotometrically) and the net charge absorbed in solutions with reasonable correction for charge displacement mentioned above. The results are shown in Fig. 4.



(1) beam duct (4" diameter), (2) 1st collimator, (3) device for alignment of collimator, (4) 2nd collimator (4 mm diameter), (5) scattering thin foil, (6) absorber, (7) SSD counter, (8) beam exit foil, (9) irradiation cell, (10) platinum wire, (11) bellow, (12) amplifier, (13) scaler, (14) multi-channel pulse height analyzer, (15) current integrator.

When the ratio of true current to scattered particle was calibrated, the cell 9 was removed and the beam exit 8 was replaced by a Faraday cup. The 1st collimator was 15 cm apart from the 2nd one. The irradiation cell was fixed with an accurately adjustable holder.

Fig. 1. Experimental arrangement for irradiation.

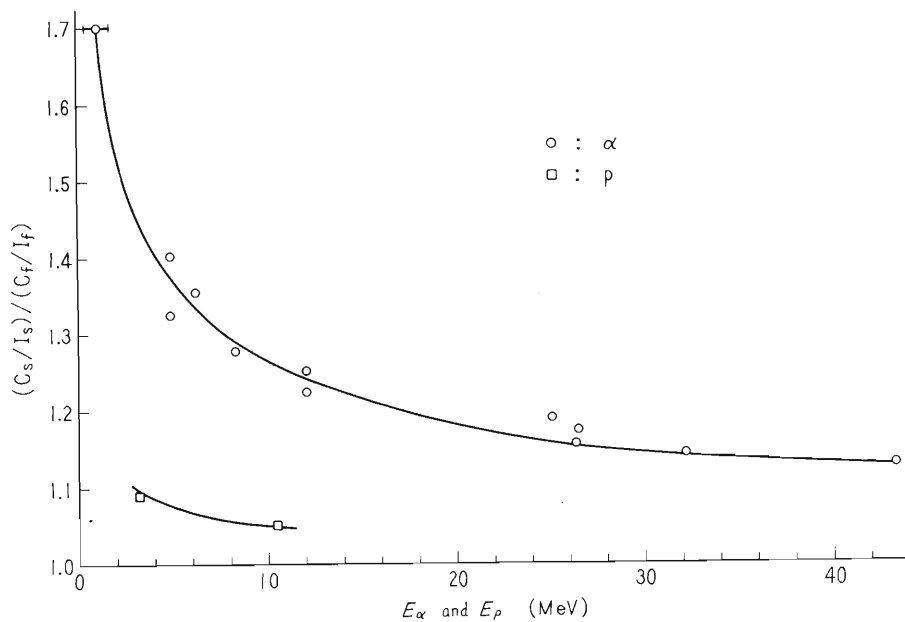


Fig. 2. Charge displacement effect.

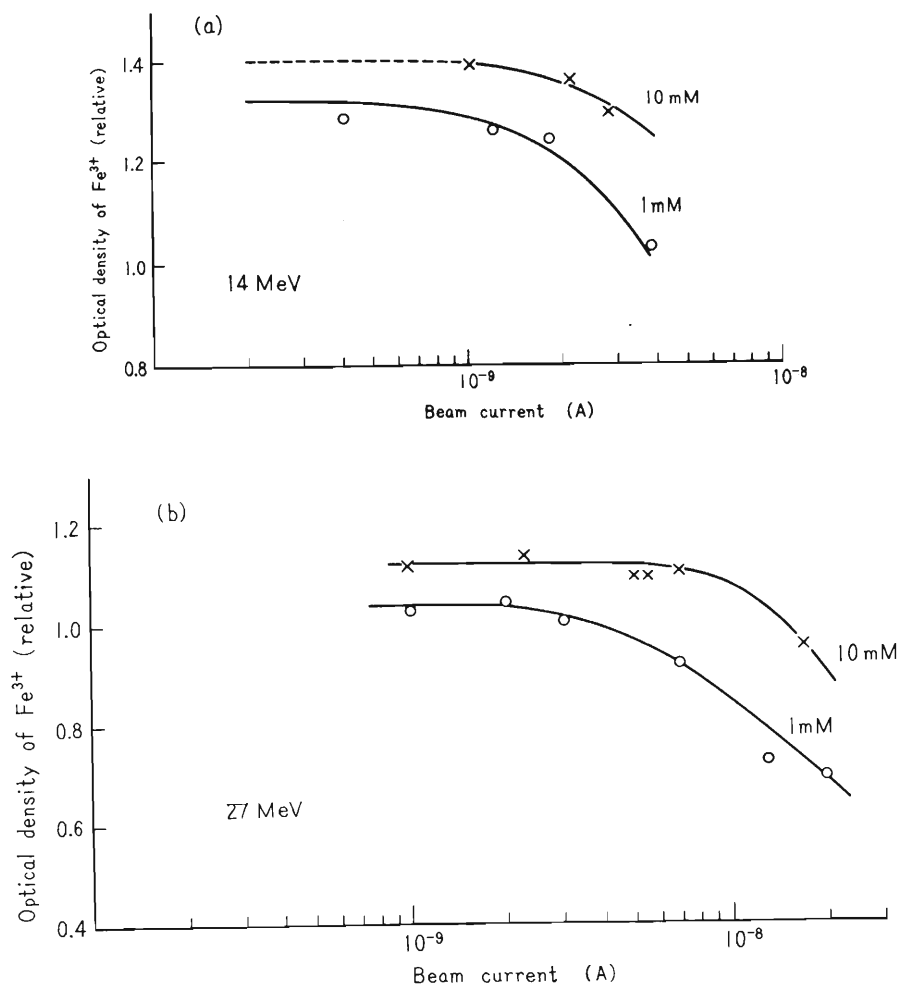


Fig. 3. Dependence of the relative oxidation yield of aerated Fricke solution on beam current.

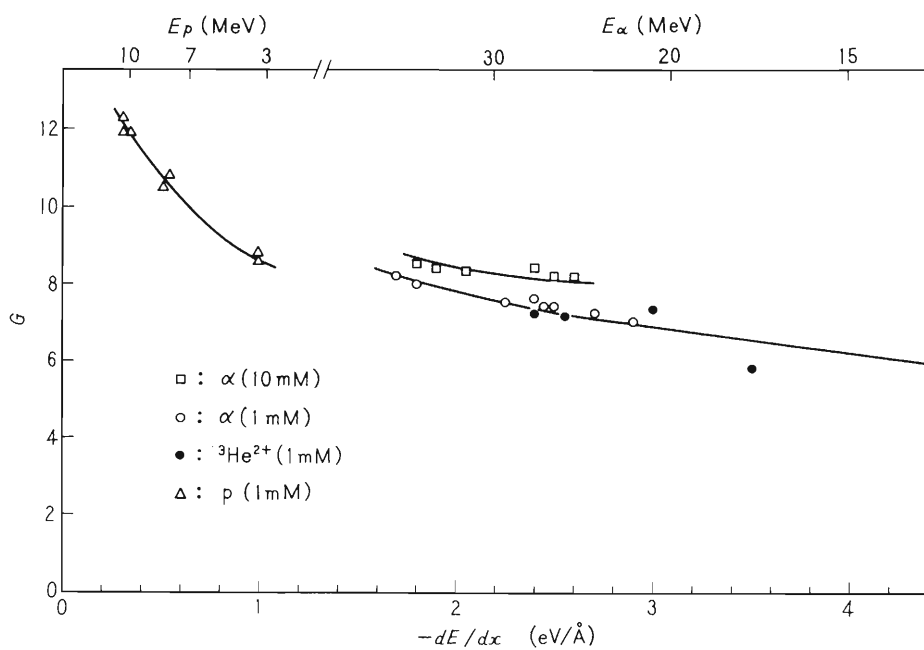


Fig. 4. $G(\text{Fe}^{3+})$ as a function of LET for aerated Fricke solutions of 1 mM and 10 mM.

References

- 1) E.J. Hart, W. J. Ramler, and S. R. Rocklin: *Radiation Res.*, 4, 378 (1956).
- 2) R.H. Schuler and A.O. Allen: *J. Am. Chem. Soc.*, 1565 (1957).
- 3) A.R. Anderson and E.J. Hart: *Radiation Res.*, 14, 689 (1961).
- 4) G.L. Kochanny, Jr., A. Timnick, C. J. Hochanadel, and C.D. Goodman: *ibid.*, 19, 462 (1963).
- 5) R.E. Faw and H.J. Donnert: *Nucl. Instr. Methods*, 58, 307 (1968).

9-2. α -Radiolysis of Methanol and Tetrahydrofuran. LET Effect

M. Matsui, H. Seki, T. Karasawa,
and M. Imamura

(1) Methanol

Hydrogen is the most important product in the radiolysis of methanol and is produced by three processes: molecular, ionic, and radical. Although the total hydrogen yield is not affected greatly by the nature of radiation used, each process and the yields of hydrogen precursors are expected to vary.

One of the hydrogen precursors is solvated electron, the yield of which in the γ - and α , ${}^7\text{Li}$ recoil-radiolysis have been determined to be 2.0¹⁾ and 0.2,²⁾ respectively. The yield of solvated electron in the radiolysis with radiation of an intermediate LET (linear energy transfer or stopping power) was determined by using 30 MeV α -particles. Nitrous oxide was used as a scavenger, which reacts with solvated electron to produce nitrogen:



Concentration of nitrous oxide was in the order of 10^{-2} M. Product gases including hydrogen, methane, and carbon monoxide were subjected to a micro-gas analysis as described previously.³⁾ The results are listed in Table 1 together with those for γ - and recoil-radiolysis.

Table 1. Yields of solvated electron for liquid methanol.

Radiation	LET (eV/A)	G
${}^{60}\text{Co } \gamma$	0.02	2.0
30 MeV α	2	0.7
${}^{10}\text{B}(n, \alpha) {}^7\text{Li}$	20	0.2

These results indicate that the yield of solvated electron escaping ionization spurs decreases with increasing LET of radiation. This fact can be explained by assuming that in the denser ionization spurs or tracks, the more electrons are captured by positive intermediates such as CH_3OH^+ and CH_3OH_2^+ .

Accordingly, the processes of the hydrogen formation should be affected by the nature of radiation. In order to obtain quantitative information on this problem, we determined the isotopic compositions of the hydrogen produced in the radiolysis of CH_3OD (99 %) with 30 MeV α particles. Results are summarized in Table 2.

Similar results for the γ - and the recoil-radiolysis have previously been reported.⁴⁾ The first row gives the isotopic composition for pure CH_3OD . The second and the third ones give those for CH_3OD containing scavengers, FeCl_3 and N_2O , respectively. From FeCl_3 solution hydrogen is produced solely by molecular process and from N_2O solution by both molecular and radical processes. These isotopic compositions vary with LET

Table 2. Isotopic compositions of hydrogen produced in the radiolysis of liquid CH₃OD (99 %) with 30 MeV α -particles.

Solute	Process	H ₂ (%)	HD (%)	D ₂ (%)
none	total	39.9	53.6	6.5
FeCl ₃	molecular	51.5	42.6	5.9
N ₂ O	molecular + radical	43.7	49.4	6.9

of radiation, and the systematic studies of such LET effects would give an important clue to the elucidation of the primary processes of radiation chemistry.

(2) Tetrahydrofuran

The radiolysis of tetrahydrofuran (THF) is more complicated than that of methanol. Some results on the γ -radiolysis of liquid THF have been reported.⁵⁾ Radiolytic products are hydrogen, carbon monoxide, butanol, and several hydrocarbons; hydrogen being a principal product. The mechanistic discussion has also been presented.⁵⁾ In order to obtain further information on the primary processes, we investigated LET effect on the yield of hydrogen from liquid THF in the presence and absence of nitrous oxide by comparing the results obtained with γ - and 30 MeV α -irradiation.*

Figures 1 and 2 represent $G(\text{H}_2)$ and $G(\text{N}_2)$ as a function of nitrous oxide concentration in γ - and α -radiolysis, respectively. In both radiolyses, $G(\text{H}_2)$ decreases with increasing concentration of nitrous oxide and reaches a constant value. The difference $\Delta G(\text{H}_2)$ indicates the yield of the hydrogen precursor which is affected by the presence of nitrous oxide, i.e., solvated electron. Thus we obtain $\Delta G(\text{H}_2) = G(e_{\text{solv}}^-) = 0.80$ for the γ -radiolysis and 0.20 for the α -radiolysis. The decrease in $G(e_{\text{solv}}^-)$ for the α -radiolysis compared with that for the γ -radiolysis is similar to the fact observed for methanol. The lower $G(e_{\text{solv}}^-)$ in the α -radiolysis may suggest the increasing importance of the formation of excited molecules by electron capture and the reactions of excited molecules in the denser ionization tracks.

On the other hand, $G(\text{N}_2)$ increases steadily with increasing concentration of nitrous oxide and does not reach a constant value in the concentration range where $G(\text{H}_2)$ does. The excess yield of nitrogen other than that produced by the reaction of nitrous oxide may be explained by assuming reactions of nitrous oxide with O^- and/or other transient anions which are not precursors of hydrogen.

(3) Experimental procedure

Deaerated samples were sealed in cylindrical quartz cells with thin quartz or mica windows of known thickness, size, and shape which was essentially the same as described in the previous section. Solution was stirred with a magnetic stirrer during irradiation. Alpha-particle beam was focused (3~ 5 mm in diameter) on the window. Radiation

* M. Matsui, T. Karasawa, H. Seki, and M. Imamura: The 11th Conference on Radiation Chemistry, September, Tokyo (1968).

doses were determined and corrected for secondary electrons in the fashion as described in the previous section.

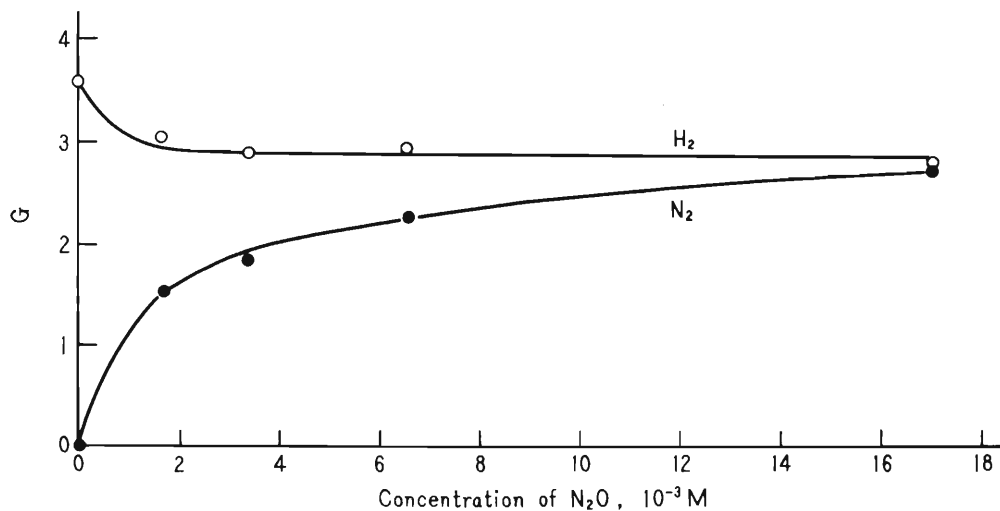


Fig. 1. Effect of nitrous oxide on the γ -radiolysis of liquid tetrahydrofuran.

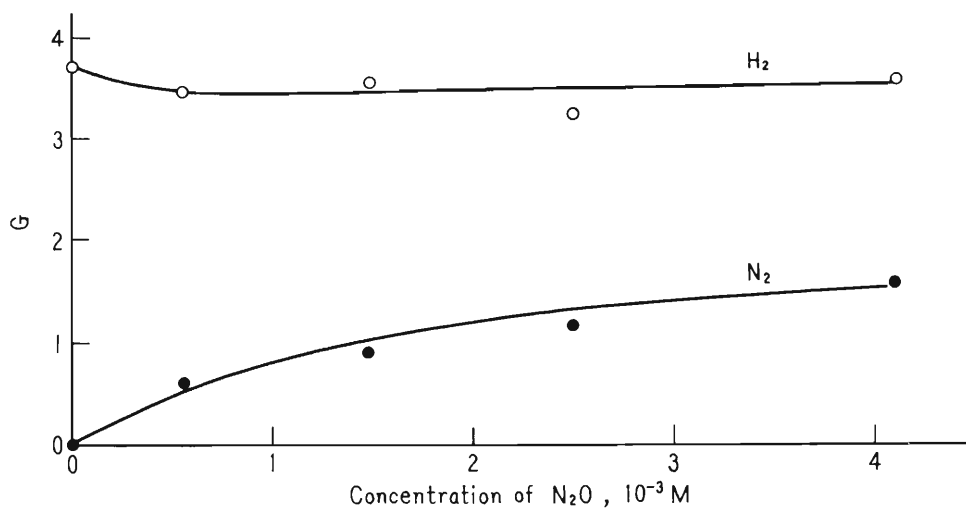


Fig. 2. Effect of nitrous oxide on the α -radiolysis of liquid tetrahydrofuran.

References

- 1) H. Seki and M. Imamura: *Bull. Chem. Soc. Japan*, 38, 1229 (1965); *J. Phys. Chem.*, 71, 870 (1967).
- 2) M. Imamura and H. Seki: *Bull. Chem. Soc. Japan*, 40, 1116 (1967).
- 3) M. Imamura, S.U. Choi, and N.N. Lichtin: *J. Am. Chem. Soc.*, 85, 3565 (1963).
- 4) H. Seki and M. Imamura: *J. Chem. Phys.*, 48, 1866 (1968).
- 5) M. Matsui: *Bull. Chem. Soc. Japan*, 39, 1640 (1966).

9-3. The LET Effects on Biological Cells

A. Matsuyama, S. Kitayama, and T. Karasawa

Log-phase cells of Micrococcus radiodurans R₁, Escherichia coli B/r and Escherichia coli B_{S-1} suspended in 0.067M phosphate buffer were exposed to α -particles from the cyclotron, and the results obtained were compared with the case of ⁶⁰Co γ -ray irradiation. A 3.5-ml aliquot of the cell suspension ($10^7 \sim 10^8$ cells/ml) in a quartz vessel was bubbled with air through capillary tube at a constant rate of 45 ml/min. α -Particles used here had an incident energy of 30 MeV and reduced their energy to 26 MeV when they passed through a thin quartz window of the irradiation vessel (~ 52 μ in thickness). The beam current absorbed in the suspension was read from a platinum wire sealed into the suspension and connected to ground through a current integrator. In the preliminary experiments, no effect of cell concentration at the time of irradiation was found on radiosensitivities of these bacteria in this study. In contrast, remarkable influences of different rates of aeration were observed. Subsequently, irradiation was carried out using the same irradiation vessel at a constant rate of aeration as mentioned above.

(1) Effect of beam current in liquid phase

When bacterial cells suspended in the phosphate buffer were irradiated with α -particles, only a relatively small fraction of the bacterial population was subjected to the bombardment because of the very short range of α -particles in an aqueous system. The effective volume for α -bombardment just behind the window of the irradiation vessel was estimated to be ~ 0.001 ml, corresponding to $\sim 1/3500$ of the sample volume. Therefore, the stirring and beam current should influence seriously upon the radiation effect in the irradiation system of the liquid phase. The effect of beam current on radiation killing was examined under the constant rate of air bubbling. The result obtained with M. radiodurans is shown in Fig. 1. Curves for E. coli B/r and B_{S-1} are now in determination. The survival curves of these three strains for α -rays were exponential over the whole range of the beam intensities examined. When a beam current was sufficiently small, the identical surviving fraction was given with the same dose, independently of the intensity of beam current. However, above a definite beam current which varied with different bacterial strains, the surviving fraction at a given dose was increased with increasing beam current. In the latter range of beam current, surviving fraction may be determined not only by the radiosensitivity of bacterial cells, but also by the efficiency of stirring.

The values of the D₃₇ (a dose required for $1/e = 37\%$ survival) in the liquid phase obtained in this study were 329 krads for M. radiodurans, 9 ± 2 krads for E. coli B/r, and 3.3 ± 1 krads for E. coli B_{S-1}, respectively. The estimates of the D₃₇ calculated from the data of Munson et al.¹⁾ by the integration over the whole range of the energy of α -particles, 0~26 (incident) MeV are 5.5 krads for E. coli B/r and 2.0 krads for E. coli B_{S-1}, respectively. The discrepancy between experimental and calculated values of the D₃₇ in the liquid phase can not be explained at present, but the ratios of the D₃₇ of E. coli B/r to that of E. coli B_{S-1} are in good agreement between both phases. Comparative study on the liquid- and solid-phase irradiations using ionizing particles of different LETs is in progress.

In respect of the kinetics for radiation killing in the range of beam current where the

radiation effect depends upon the efficiency of stirring as well as the radiosensitivity of bacterial cells, the following equation was proposed for 26 MeV α -particles:

$$S = e^{-\frac{It}{q_0} \left(1 - e^{-k \frac{q_0}{I}} \right)}$$

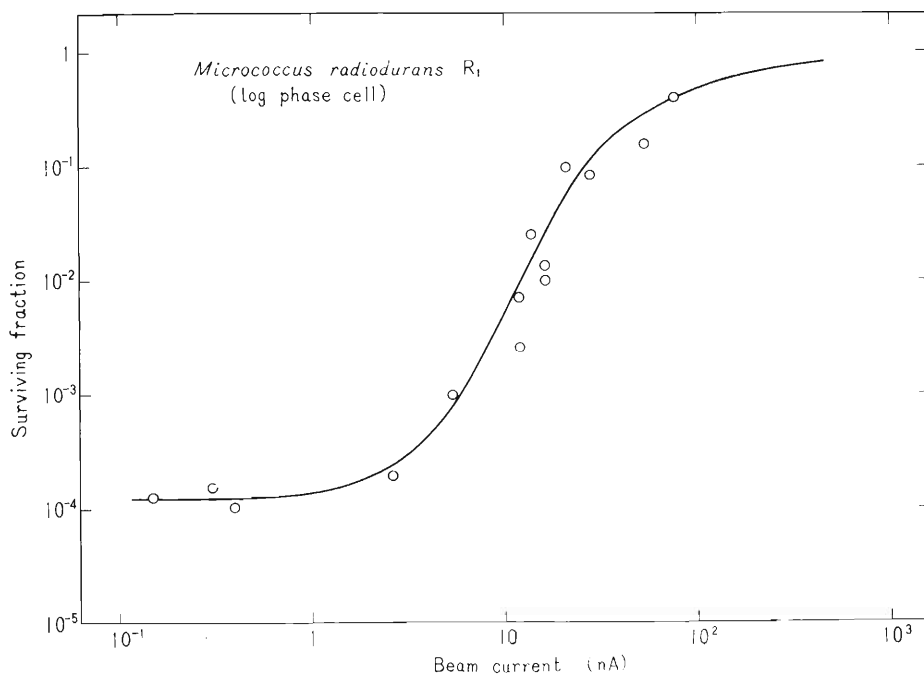
where S is surviving fraction, q_0 is D_{37} in nC, t is irradiation time in sec., I is beam current in nA and k is a constant having a dimension of sec^{-1} and depending upon the rate of aeration and the size of effective volume. The value k is 0.009 for M. radiodurans, 0.005 ~ 0.017 for E. coli B/r, and 0.016 (except the range of lower beam current) for E. coli B_{S-1}, respectively. When I becomes sufficiently small, the equation tends to

$$S = e^{-\frac{It}{q_0}}$$

Irradiation by α -particles of different energies and by other types of particles are now undertaken.

(2) α -Irradiation of M. radiodurans, a radioresistant bacterium

Exponential survival curves were obtained with different beam intensities of α -particles in contrast to the result of γ -irradiation which gave sigmoidal curves. In addition, the difference in radiosensitivity between log- and stationary-phase cells were smaller for α -rays than for γ -rays. The data obtained are partly illustrated in Fig. 2. It should be noteworthy that the results of α -irradiation of M. radiodurans were different from those of γ -irradiation in terms of the shape of survival curves and the effect of the dose rate. In order to accumulate more informations on the mechanism for cell death in M. radiodurans, an extremely radioresistant bacterium, the sedimentation analysis of DNA was performed with α -irradiated cells. Log-phase cells tritiated with ^3H -thymidine were lysed on neutral sucrose gradients (5 ~ 20 %) after exposure to α -bombardment with 3000 nC at a beam current of 10 nA (~10 % colony survival) and centrifuged in a Hitachi RPS40 swinging-bucket rotor (30000 rev/min, 5°C). The sedimentation patterns are shown in Fig. 3. During the course of post-irradiation incubation, the decreased sedimentation rate of DNA caused by α -irradiation was found to restore. Such changes in sedimentation patterns on neutral gradients are interpreted in terms of the reflection of double-strand scissions and their repair which take place in DNA involved at the time of α -irradiation. It appears unnecessary to reserve this interpretation for the consideration of the possibility that the experimental procedure during the sedimentation analysis might produce some secondary double-strand scissions at the sites of single-strand scissions in DNA caused by radiation. The discussion on this point will be presented elsewhere.²⁾ Such results of the sedimentation analysis after α -irradiation may emphasize the capacity of M. radiodurans for the repair of double-strand scissions in DNA, which has been considered from the analysis after γ -irradiation.³⁾ However, questions arise on the view that DNA may be the primary site for radiation kill also in this radioresistant bacterium. Tetrad cells of M. radiodurans in which four separated nuclear materials were observed on electron micrographs, gave the one-hit type of the survival curve for α -rays. In the sedimentation analysis, the restored fraction of the damaged DNA was found to exceed the colony survival. Thus, it appears that cell death caused by radiation in M. radiodurans can not be attributable only to the DNA damage per se. Further investigations are now being undertaken for elucidating the fundamental mechanism for cell death in radioresistant bacteria using ionizing particles of different LETs.



Incident energy, 26 MeV; 8000nC

Fig. 1. Relationship between beam current and surviving fraction at a constant dose of α -rays.

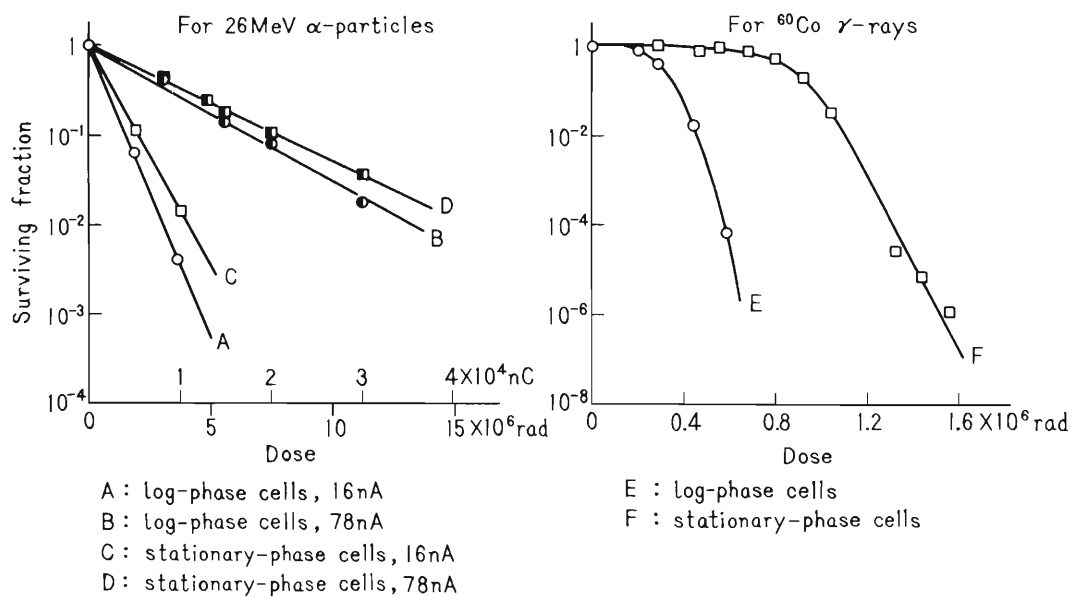
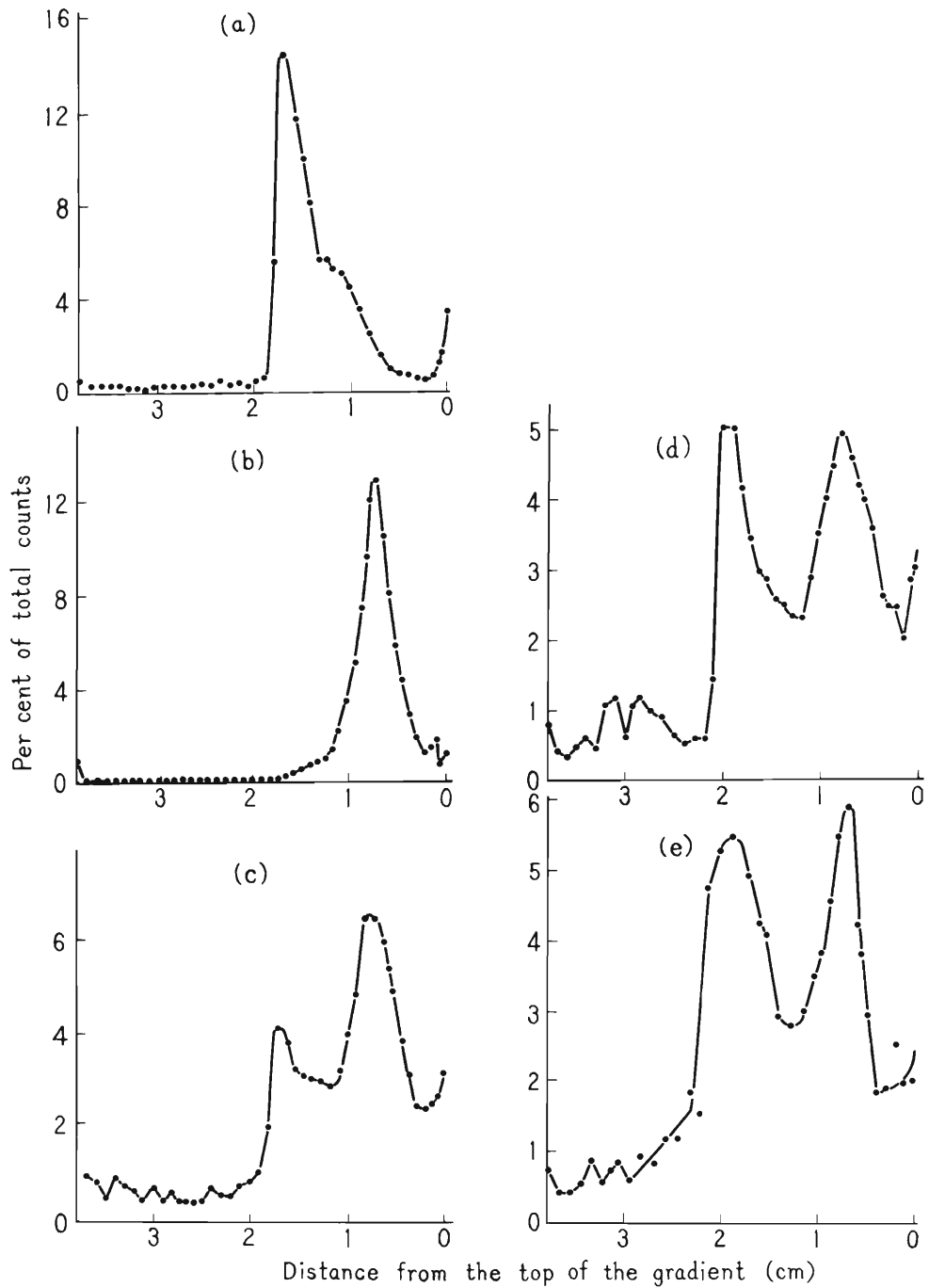


Fig. 2. Survival curves of *Micrococcus radiodurans* R₁.



(a) unirradiated control, (b) irradiated with 1.1 Mrads of α -rays,
 (c) after 3 h of postincubation, (d) after 5 h of postincubation,
 (e) after 7 h of postincubation.

Fig. 3. Sedimentation patterns of tritiated materials in *M. reidiourans* of neutral sucrose gradient centrifugation.

References

- 1) R. J. Munson, G.J. Neary, B.A. Bridges, and R.J. Preston: Intern. J. Radiation Biol., 13, 205 (1967).
- 2) T. Karasawa and A. Matsuyama: in preparation.
- 3) S. Kitayama and A. Matsuyama: Biochem. Biophys. Res. Commun., 33, 418 (1968).

10. SOLID STATE PHYSICS

10-1. Behavior of Helium Bubbles in Stainless Steel

Ryukiti R. Hasiguti, Hideo Sakairi,
Eiichi Yagi, Takashi Karasawa, Yoshitsugu Mishima,*
Shiori Ishino,* and Hiroshi Teranishi*

(1) Introduction

Stainless steel is widely used in nuclear reactors as fuel cladding and structural materials. It has been shown that the helium which is produced by (n, α) reactions is responsible for the embrittlement of stainless steel at elevated temperatures. In reactor irradiation experiments, however, detailed experimental analyses of materials are obstructed by residual radioactivity. We make simulative experiments with α -particle irradiation and observe helium bubbles by a transmission electron microscope.

(2) Experimental

The specimens used are AISI, 316 stainless steel foils which are subjected to one of the following three heat treatments, i. e.,

- A: annealing for one hour at 1050°C and furnace cooling,
- B: annealing for one hour at 1050°C followed by straining to 10% in tension,
- C: cold rolling to 94%.

Helium is injected by irradiating the stacks of the foils with 23 MeV alpha particles from a cyclotron at IPCR. Irradiation dose is 1500 ~ 2000 μ coulomb/cm² ($4.5 \sim 6.0 \times 10^{15}$ particles/cm²).

The specimens are then annealed for one hour at various temperatures from room temperature up to 800°C. Observations are made by a JEM-150 electron microscope.

(3) Results

Sample A

No bubbles are observed in the specimens annealed below 500°C. However, in those which are annealed at 500°C, a large number of helium bubbles with a size of about 1000 Å in diameter are widely spread within the matrix as well as on the grain boundaries and on dislocations, as shown in Fig. 1.

In samples annealed at 600°C, the bubble size increases by a factor of two as compared with the samples annealed at 500°C, but the number of bubbles decreases by an order of magnitude (Fig. 2). The shape of the bubbles after annealing at these

* Faculty of Engineering, University of Tokyo.

temperatures is spherical in the matrix and lemon-like on the grain boundaries. After annealing at even higher temperatures, at 700 °C and 800 °C, the size and the number of bubbles remain unaltered but the shape changes from spherical to polyhedral as shown in Fig. 3.

Samples B and C

No bubbles are observed in samples (B and C) annealed below 700 °C. Bubbles first appear in both samples after annealing at 700 °C. In sample B, the bubbles are attracted to either dislocation lines or to grain boundaries, whereas in sample C, most of them are attracted to precipitates, probably of $M_{23}C_6$ -type, or to grain boundaries. In sample B after annealing at 800 °C (Fig. 4) the bubbles grow in size with the decrease in their number. However, in sample C the size and the number of bubbles are almost unchanged (Fig. 5).

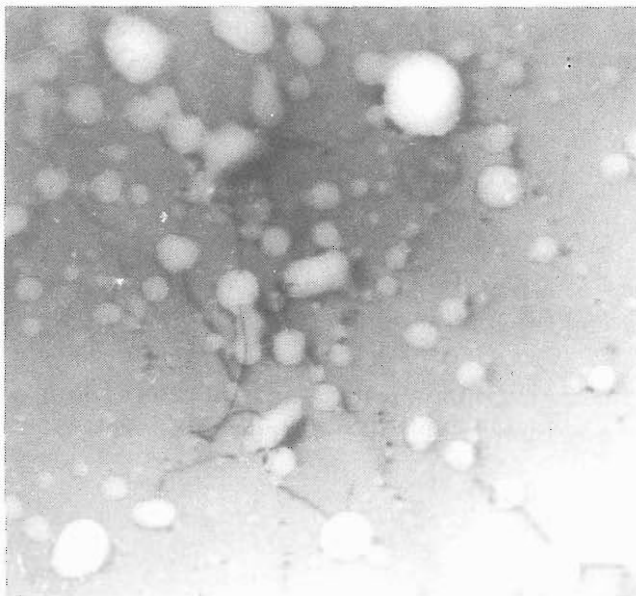
(4) Summary of behavior of bubbles

(a) Bubbles often appear preferentially on dislocations, grain boundaries, and precipitates.

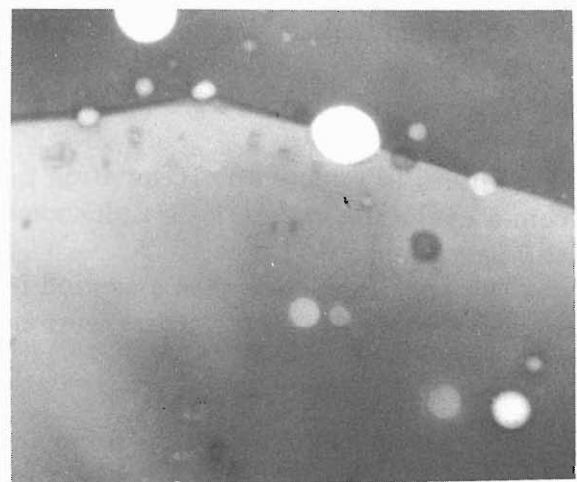
(b) At lower temperatures the growth of bubbles occurs by the migration and coalescence of bubbles. But at higher temperatures the bubble growth takes place by a vacancy flow into bubbles.

(c) When bubbles appear on precipitates, the bubble growth is very much suppressed.

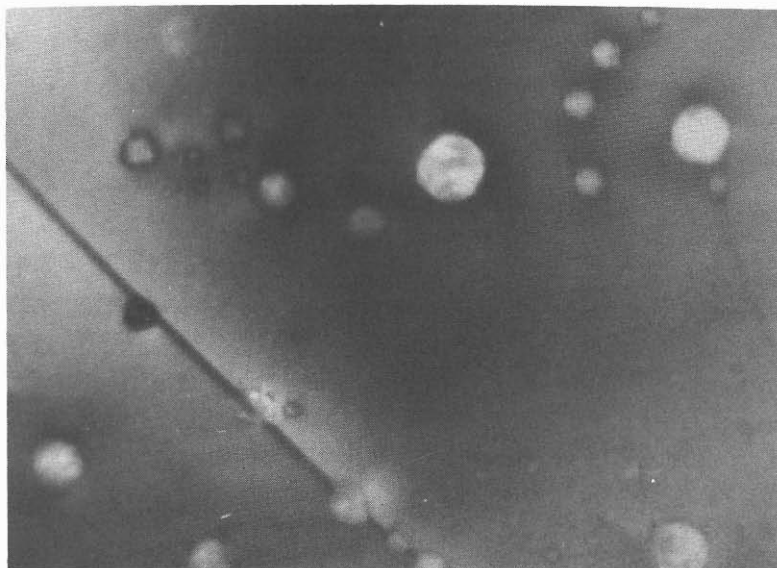
(d) The surroundings of spherical bubbles are strained, while those of polyhedral ones are not. A controlling mechanism of strain relaxation is a vacancy diffusion.



× 34000
Fig. 1. Sample A annealed for 1 h at 500 °C. Bubbles lie on dislocations. Note that bubble coalescence occurs.



× 10000
Fig. 2. Sample A annealed for 1 h at 600 °C. Bubbles lie on a grain boundary. Note the difference between the bubble shape lying on the grain boundary and that in the matrix.



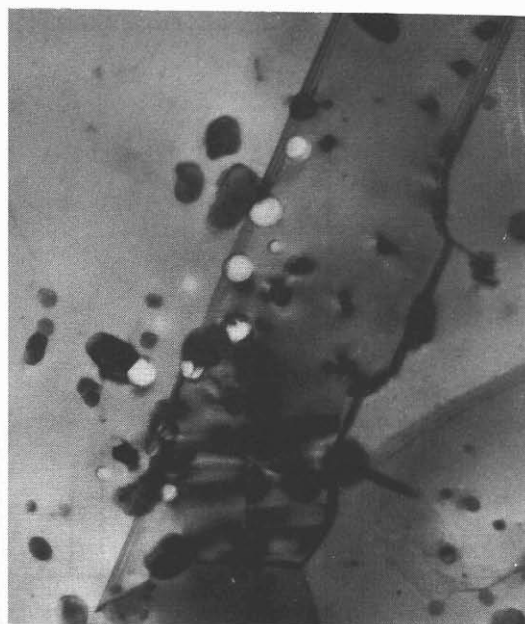
× 30000

Fig. 3. Sample A annealed for 1 h at 800 °C. Bubble shape is polyhedral.



× 31000

Fig. 4. Sample B annealed for 1 h at 800 °C. All bubbles are attached to dislocation lines.



× 31000

Fig. 5. Sample C annealed for 1 h at 800 °C. Bubbles are attached to precipitates and lie upon grain boundaries.

10-2. Mössbauer Effect of ^{61}Ni in Magnetic Materials

H. Sekizawa, T. Okada, and F. Ambe

The Mössbauer effect is utilized very widely as a research tool in the study of solid state physics. But it is concentrated mainly on ^{57}Fe nuclide and studies using other nuclides are rather scarce because of various experimental difficulties. Studies on magnetic properties of iron group transition metals and alloys with Mössbauer effect of ^{61}Ni employing ^{61}Cu source¹⁾ prepared by IPCR cyclotron is now under way.

As a Mössbauer nuclide, ^{61}Ni has many drawbacks compared with ^{57}Fe : the wide line width of the order of 0.8 mm/sec, low fraction of recoilless absorption, the short life time of the parent nuclide, the low natural abundance, etc. On the other hand, it has several merits. Besides the fact that ^{61}Ni is the only available Mössbauer nuclide in the iron group elements except for iron, nickel atoms in alloys accommodate themselves well to the host metal, whereas iron atoms are comparatively insensitive to their environments. Thus, nickel atoms may be considered as a good probe to study magnetism in iron group alloys.

The source driving system is a commercial one composed of a sawtooth waveform generator and a loud-speaker type transducer with a coaxial sensing coil. A scintillation counter and a multichannel pulse height analyzer in time mode are used to count the 67.4 keV γ -ray radiation from the metastable ^{61}Ni source. The preparation of the source is described in the section of radiochemistry in this volume. Because of the rather high energy (for the Mössbauer experiment) and the resulting low fraction of recoilless absorption of the γ -ray, the source is to be kept at liquid nitrogen temperature.

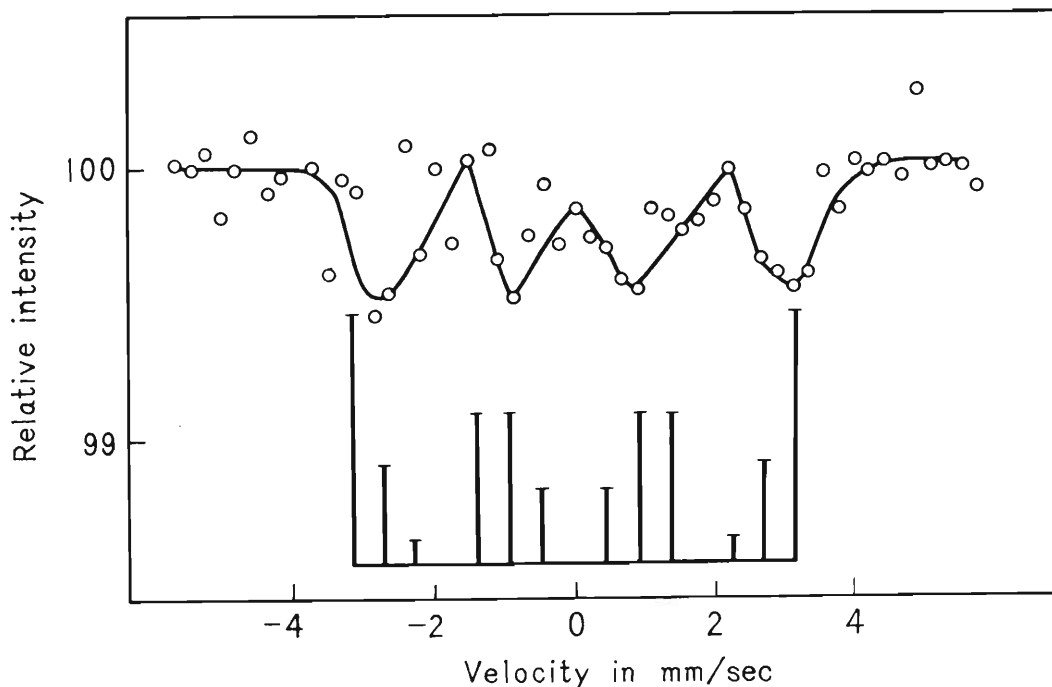


Fig. 1. Mössbauer spectrum recorded at 80°K with a $\text{Fe}_{0.25}\text{Ni}_{0.75}$ absorber and a source of ^{61}Cu in Cu.

Preliminary runs are made at liquid nitrogen temperature for pure nickel metal and Fe_{0.25} Ni_{0.75} alloy (Fig. 1). Rough estimation of the hyperfine field at the Ni nucleus was made and gave values approximately 90 kOe and 180 kOe, respectively.^{2),3)} Computer fitting to the data with appropriate theoretically expected absorption spectrum is in progress.

References

- 1) F.E. Obenshain and H.F. Wegener: *Phys. Rev.*, 121, 1344 (1961).
- 2) J.C. Love, G. Czeck, J.J. Spijkerman and D.K. Snediker: "Mössbauer Effect with Nickel-61", *Hyperfine Structure and Nuclear Radiation* (1968).
- 3) U. Erich and D. Quitman: "Hyperfine Structure of the 67.4 keV Transition in ⁶¹Ni", *ibid.*

10-3. γ -Ray Goniometer for Positron Annihilation Experiment

M. Saito, T. Okada, N. Shiotani,
H. Sekizawa, and T. Karasawa

The system, shown schematically in Fig. 1, is designed to study the angular correlation of two γ -rays arising from the annihilation of polarized positrons with electrons in ferromagnetization, to detect changes in the correlation. Since the shape of correlation curve is related to the distribution in momentum of the electrons, the change in the correlation curve may be associated with that in the electron momenta. Thus study of the angular correlation of two-quantum radiation provides information on the electronic structure of ferromagnetic materials.¹⁾ Details of the system is described in the following.

The whole system (Fig. 1) is composed of following units:

- (a) Source chamber and specimen chamber (Fig. 2)
- (b) Movable detector driving unit (Fig. 3)
- (c) Fixed detector unit
- (d) Horizontal and vertical slits
- (e) Detector and its shielding
- (f) Electromagnet
- (g) Source carrying cart

(1) Source chamber and specimen chamber

The specimen chamber and the source chamber are placed in the 5 cm gap between the pole pieces of an electromagnet. Both chambers are made of brass. The specimen chamber is vacuum tight up to 10^{-5} mmHg. The temperature can be changed by a heating coil and is measured by a thermocouple attached to the specimen. The positrons from the source come into the specimen chamber through a 5 μ thick stainless steel window. The γ -rays resulted from annihilation of positrons in the specimen come out through thin quartz windows on both sides of the specimen chamber. For the adjustment of the position of the specimen, the chamber is rotatable to $\pm 2^\circ$ around the vertical axis and movable to ± 0.5 cm along the axis. A rod, with the source on its end, is dropped in the source chamber from above, then adjusted to the final position by a rack and pinion. The distance between the specimen and the source is 0.5 cm. Both chambers and the pole pieces are covered with lead block with 0.7 cm wide vertical slit for the annihilation γ -rays on each side.

(2) Movable detector driving unit

This unit is designed to make the detector-slit assembly to move on a guide rail (3) in Fig. 3 along a circular arc with a radius of 400 cm centered at the specimen. This keeps the detector-slit assembly aligned accurately to the specimen independent of the position of it on the guide rail. The upper bench board (2) with the detector-slit assembly on it is displaced by a motor driven feed screw rod (10) and a feed nut (5). The above-mentioned alignment of (2) is realized by a guide rail with an accurate curvature and a guide pulley (6). The travel of the bench (2) on the rail is ± 12 cm and the position of

the bench is read from the graduation on a disc (18) or from an electronic register (23) and (24). The guide rail should be machined and fixed to an accuracy of 2.5μ .

(3) Fixed detector unit

This is similar to but simpler than the movable detector unit. The driving mechanism here is only to make manual adjustment of the alignment of the detector-slit assembly.

(4) Horizontal and vertical slits

The geometrical angular resolution is determined by the vertical slit. The values of the slit width and the corresponding angular resolutions are listed in Table 1. Vertical, horizontal and angular fine adjustment mechanisms are provided also in this unit.

Table 1.

Angular resolutions of slits	Slit width
$(2 \pm 0.1) \times 10^{-4}$ rad.	0.8 ± 0.04 mm
(4 ± 0.2) "	1.6 ± 0.08 "
(6 ± 0.3) "	2.4 ± 0.12 "
(8 ± 0.4) "	3.2 ± 0.16 "

(5) Detector and its shielding

The detector is a usual NaI-Tl scintillator, 2" in diameter and 4" in length, with a photo-electron multiplier and a preamplifier. Both movable and fixed detectors are covered with 3 cm thick lead shielding. The detector is placed just behind the vertical slit.

(6) Electromagnet

The magnetic field necessary to study ferromagnetic materials is provided by the electromagnet. The same field is also used in focusing the positron beam from the source on the specimen. The maximum attainable field strength is 15 kOe in 5 cm gap.

(7) Source carrying cart

This is essentially a lead block with a vertical hole for the source at its center placed on a base board with casters.

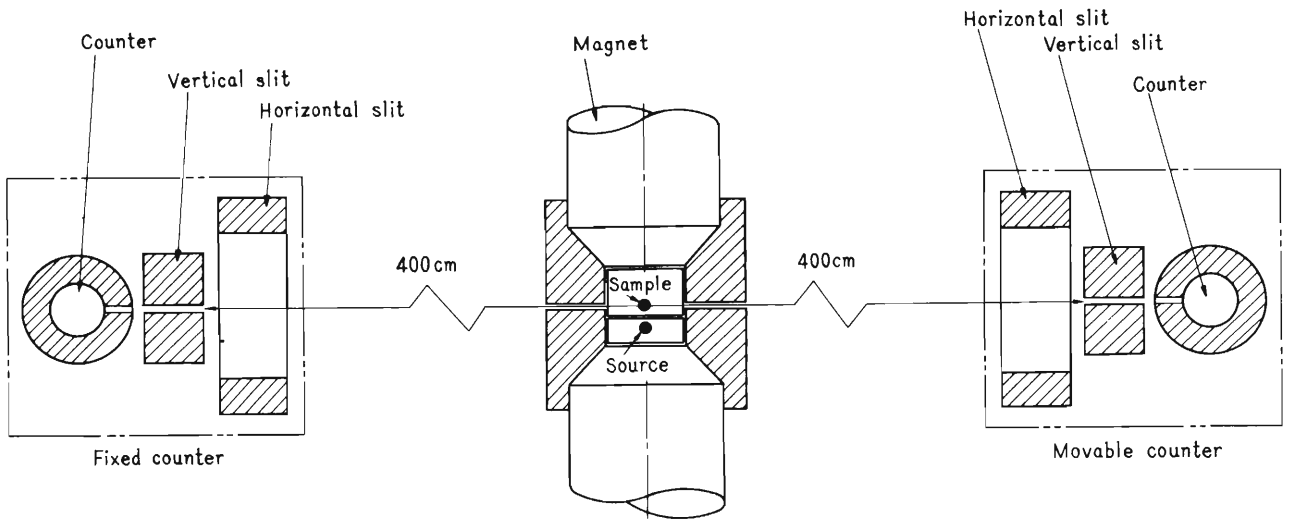


Fig. 1. Schematic diagram of the whole system.

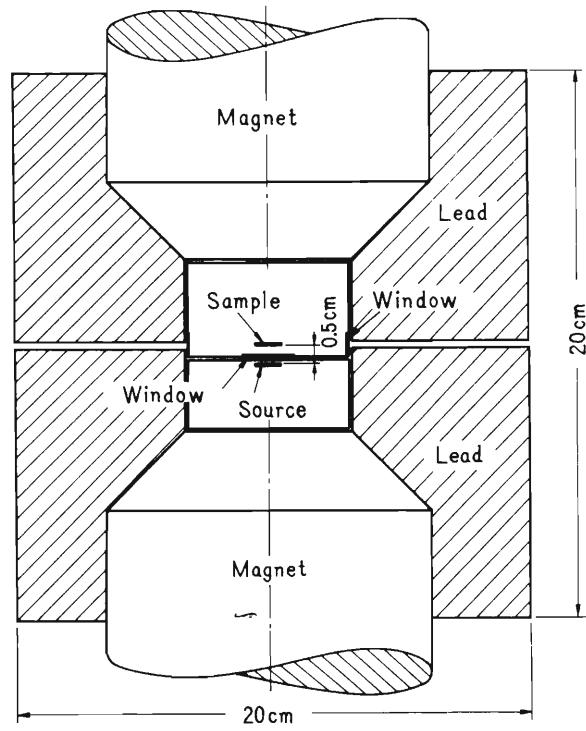
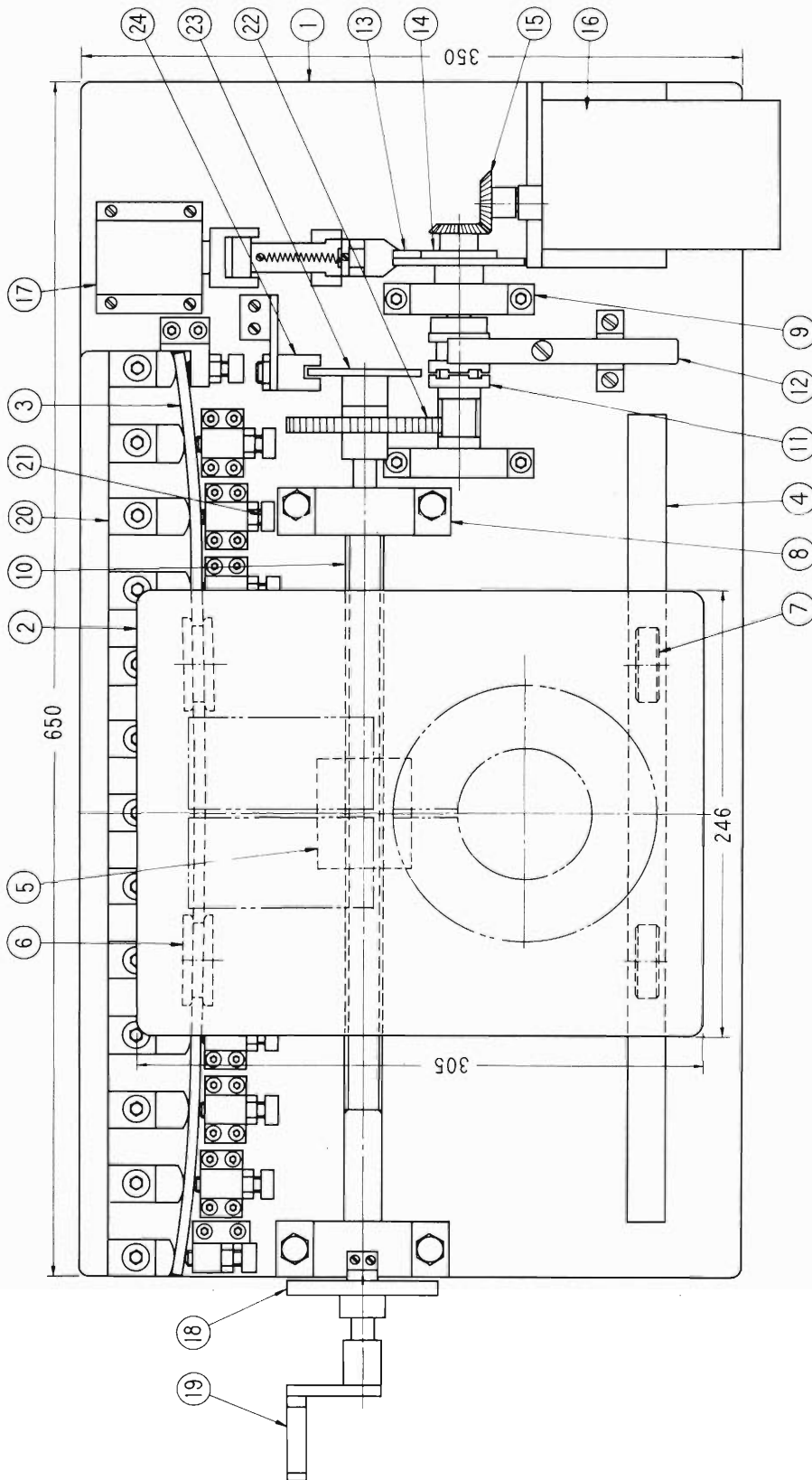


Fig. 2. Source chamber and specimen chamber .



(1) Bench board, (2) Bench board, (3) Curvature guide rail, (4) Guide rail, (5) Feed screw nut, (6) Guide pulley, (7) Pulley, (8) Bearing stand, (9) Bearing stand, (10) Feed screw rod, (11) Clutch, (12) Clutch lever, (13) Click, (14) Ratchet wheel, (15) Bevel-gear, (16) Motor, (17) Solenoid, (18) Calibration disk, (19) Manual handle, (20) Rail holder, (21) Screw bolt, (22) Spurgear, (23) Switch lever, (24) Switch.

Fig. 3. Movable detector driving unit.

Reference

- 1) A.T. Stewart and L.O. Roellig (Ed.): "Positron Annihilation", Academic Press, London & N.Y. (1967).

10-4. Preparation of Positron Sources for Positron Annihilation Experiment

N. Shiotani, S. Ambe, T. Okada,
H. Sekizawa, and T. Karasawa

The study of the annihilation of positron has provided valuable information concerning the properties of matter. In recent years, the development of fast and stable electronic apparatus and availability of strong positron sources have made positron annihilation, especially the angular correlation of two annihilation photons, to be one of the most important experimental techniques in the study of metals and alloys.

Cyclotron-made ^{22}Na and ^{58}Co and reactor-made ^{64}Cu are the only three positron sources used in angular correlation experiments.¹⁾ Where a cyclotron is available to produce radioisotopes locally at the laboratory, other shorter-lived radioisotopes than ^{22}Na or ^{58}Co can be used as positron sources. Cyclotron-produced radioisotopes are ordinarily of different chemical elements from the target. Hence they can be separated with high specific activity and prepared in desired form, for instance thin foil by electroplating on a suitable substrate.

We produced ^{57}Ni and ^{55}Co by IPCR cyclotron as the positron sources for our angular correlation experiments on ferro magnetic metals and alloys. These are chosen by the following reasons:

- (a) β^+ decay is over 50 % of disintegration.
- (b) Half-life is suitable for bombarding time.
- (c) Maximum energy of β^+ is high.
- (d) Target element is metallic and its natural abundance is high.

(1) Bombardments

The thick Fe target was used for the $^{56}\text{Fe} (^3\text{He}, 2n) ^{57}\text{Ni}$ reaction induced with 40 MeV ^3He ions. The total current was 537 μ coulomb. The stacked thin foil Ni target was used for the $^{58}\text{Ni} (p, \alpha) ^{55}\text{Co}$ reaction induced with 15 MeV protons. The total current was 2634 μ coulomb.

(2) Chemical separation of ^{57}Ni

The irradiated iron target was dissolved in hot concentrated hydrochloric acid by the addition of fuming nitric acid. The iron (III) ions in 7 M hydrochloric acid were extracted with 0.5 M xylene solution of tri-n-octylamine. ^{57}Co , ^{58}Co , and ^{56}Co as by-products were removed simultaneously by the solvent extraction procedure. Further purification was carried out using anion exchange resin.

Electrodeposition ^{57}Ni in 0.2 M of ammonia and 0.5 M of ammonium sulphate solution was electroplated on a nickel foil cathode at 50°C. The cell potential applied was 12 V and the electrolytic current was about 400 mA. 90 % of ^{57}Ni was electroplated after 60 min.

(3) Chemical separation of ^{55}Co

The irradiated nickel target was dissolved in hot concentrated hydrochloric acid by the addition of fuming nitric acid. Nickel and cobalt were separated using anion exchange resin.

The ^{55}Co was electroplated onto a copper foil according to the procedure described by Stephen.²⁾ During the electrodeposition nitrogen gas was bubbled through the solution to avoid the oxidation of cobalt (II) ion. The cell potential applied was 2.6 V. 90% of ^{55}Co was electroplated within 2 h.

(4) Results

The roughly estimated yield was $40 \mu\text{Ci}/\mu\text{A}\cdot\text{h}$ for ^{57}Ni and $300 \mu\text{Ci}/\mu\text{A}\cdot\text{h}$ for ^{55}Co . Absence of significant radiochemical impurity was confirmed by γ -ray spectrometry. Hazan reported the excitation function of the $^{56}\text{Fe} (^3\text{He}, 2n) ^{57}\text{Ni}$ reaction for the ^3He kinetic energy up to 30 MeV.³⁾ In order to calculate the thick target yield, the excitation function should be extrapolated for the ^3He kinetic energy up to 40 MeV. The calculated yield was $80 \mu\text{Ci}/\mu\text{A}\cdot\text{h}$. This is twice as large as our experimental value. The discrepancy is mainly due to careless losses in the separation processes. (Thus if the chemical separation is carried out carefully the calculated yield may be expected.) The excitation function of the $^{58}\text{Ni} (p, \alpha) ^{55}\text{Co}$ is not known. To obtain ^{55}Co , we may use the $^{56}\text{Fe} (p, 2n) ^{55}\text{Co}$ reaction. The thick target yield for 21 MeV proton of the reaction was estimated as $11000 \mu\text{Ci}/\mu\text{A}\cdot\text{h}$.⁴⁾ This value is about forty times as large as our experimental yield — $300 \mu\text{Ci}/\mu\text{A}\cdot\text{h}$ — of the $^{58}\text{Ni} (p, \alpha) ^{55}\text{Co}$ reaction. We may conclude that the cross section of the $^{56}\text{Fe} (p, 2n) ^{55}\text{Co}$ reaction is much larger than that of the $^{58}\text{Ni} (p, \alpha) ^{55}\text{Co}$ reaction and the former reaction is better for the production of ^{55}Co than the latter.

References

- 1) A.T. Stewart and L.O. Roellig (Ed.): "Positron Annihilation", Academic Press, London & N.Y. (1967).
- 2) J. Stephen: Nucl. Methods, 26, 269 (1964).
- 3) J. Hazan and M. Blann: Phys. Rev., 137, B1202 (1965).
- 4) J. Martin, R. Livingston, R. Murray, and M. Rankin: Nucleonics, 13, March, 28 (1955).

11. RI PRODUCTION AND ITS APPLICATIONS

11-1. Preparation of ^{18}F -labelled Compounds by the Bombardment of an Oxygen Stream

T. Nozaki, A. Shimamura, and T. Karasawa

We have previously described an efficient method of producing anhydrous H^{18}F using the cyclotron bombardment of an oxygen gas stream (Intern. J. Appl. Radiation Isotopes, 19, 27 (1968)). A similar technique has proved useful for the labelling of acetyl fluoride (CH_3COF , b.p. 20°C) and propionyl fluoride ($\text{CH}_3\text{CH}_2\text{COF}$, b.p. 43°C). In these cases, however, the bombardment should be stopped in the course of the elution; otherwise, the acyl fluorides are partly radiolyzed. These labelled acyl fluorides are very useful as intermediates for many ^{18}F -labelled compounds; the isotopic exchange of fluorine between an acyl fluoride and an inorganic fluorinating agent proceeds rapidly, and a dry acyl fluoride can be handled in a glass vessel.

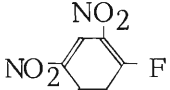
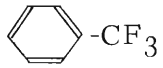
In general, the following three methods are useful for the preparation of ^{18}F -labelled compounds: (1) the elution of the adsorbed ^{18}F , often with a simultaneous isotopic exchange; (2) the halogen-interchange reaction, and (3) the Schiemann reaction. Table 1 shows examples of the preparation of ^{18}F -labelled compounds which we have actually synthesized or tried to obtain.

A dilute aqueous solution of $\text{Sn } ^{18}\text{F}_2$ is useful in dental research, but it is very sensitive to oxidation. This compound can be obtained by the elution of the ^{18}F adsorbed in the bombardment box after sweeping it with nitrogen.

In the use of the halogen-interchange reaction, the following alternative processes are usually useful: (1) the inside of the bombardment box is coated with an inorganic fluorinating agent, which is taken off after the bombardment and then made to react with the organic chloro-, bromo-, or iodo- compound; and (2) the adsorbed ^{18}F is taken out as a small quantity of CH_3COF or $\text{CH}_3\text{CH}_2\text{COF}$, and the halogen-interchange reaction is made to proceed in its presence. In both cases, since the ^{18}F is situated only on or near the surface of grains of the inorganic fluorinating agents, most of the ^{18}F is incorporated in a small quantity of the product ^{18}F -labelled compound formed at the initial stage of the reaction, even when large quantities of the reactants are used. Thus, the product can be obtained with a high specific activity, with ease, and within a relatively short time. This is exemplified by the preparation of $\text{CH}_2\text{FCO}_2\text{Et}$ shown in Fig. 1.

Labelled aryl fluorides are prepared by the Schiemann decomposition of the diazonium fluoroborates- ^{18}F , which we obtain as precipitates by shaking acetonitrile solution of them in the bombardment box and by adding ether.

Table 1. Examples of the preparation of ^{18}F -labelled compounds.

Product compound	Inside of the bombardment box	Fluorinating agent	^{18}F -yield ^{a)}	Synthetic reaction
Carrier-free HF aq.	Polyethylene or noble metal		75 ~ 80	Elution
SnF_2 aq.	ibid.		80	} Isotopic exchange
HBF_4 , H_2SiF_6	ibid.		80 ~ 85	
CH_3COF , $\text{CH}_3\text{CH}_2\text{COF}$	Glass		90	
$\text{CH}_2\text{FCO}_2\text{Et}$	KF-coated or glass(CH_3COF) ^{b)}	KF	30	} Halogen interchange
	ibid.	KF	30	
	SbF_3 -coated or glass(CH_3COF) ^{b)}	SbF_3	50	
Cholesteryl fluoride	Glass(CH_3COF) ^{b)}	AgF	15	
$\text{CH}_3\text{CO}_2\text{CH}_2\text{CH}_2\text{F}$	Noble metal (HF) ^{c)}	HF + HgO		
Aryl fluorides	Glass or NaBF_4 -coated	BF_4^-	10 ^{d)}	the Shiemann reaction

a) The ^{18}F -yield is defined as:

$$100 \times \frac{[\text{dps of the product just as obtained}]}{[\text{dps of the total } ^{18}\text{F} \text{ at the end of the bombardment}]}$$

b) Glass (CH_3COF) means that the ^{18}F is taken out from a glass bombardment box as CH_3COF or $\text{CH}_3\text{CH}_2\text{COF}$.

c) Noble Metal (HF) means that the ^{18}F is taken out as anhydrous HF from a bombardment box with a noble metal inside.

d) This value is for aryl fluorides for which the Shiemann reaction yields are relatively high.

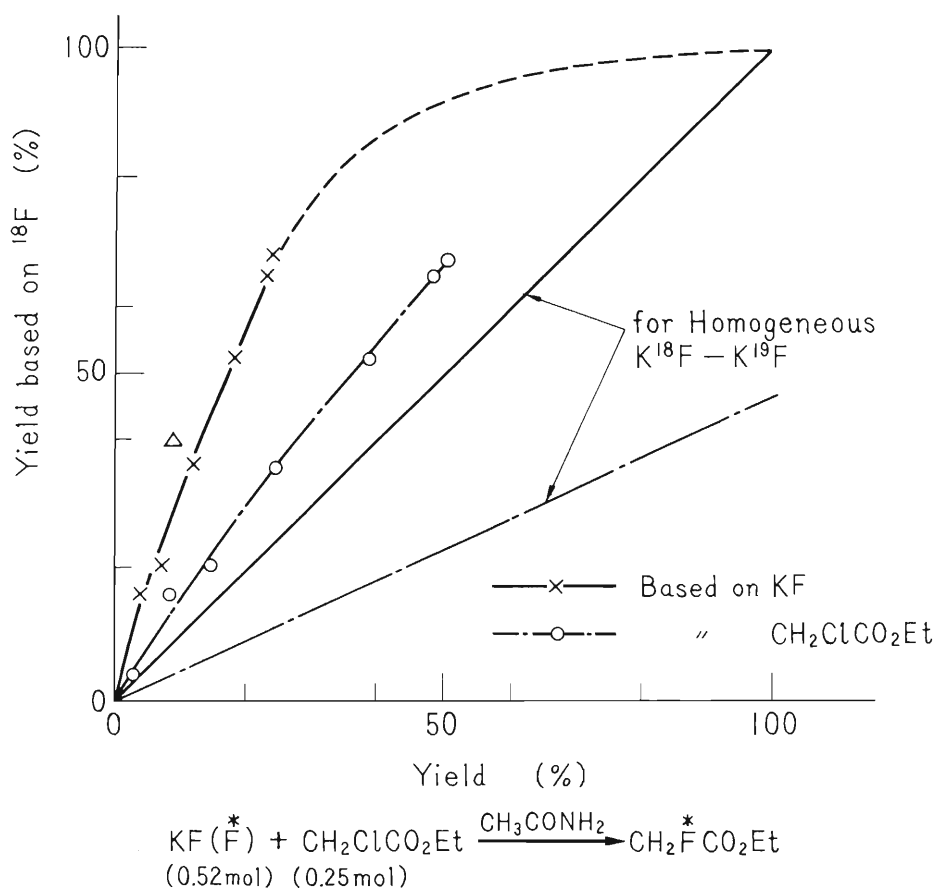


Fig. 1. ^{18}F -Yield vs. chemical yield.

11-2. Preparation of ^{52}Fe

T. Nozaki

^{52}Fe , an RI important as a tracer for medical studies, has been prepared by the $^{50}\text{Cr}(\alpha, 2n)^{52}\text{Fe}$ reaction. Using chromium targets of the natural isotopic composition, we compared the ^{52}Fe yield for the α -bombardment with that for the ^3He -bombardment.

Chromium plates (15 to 40 mg/cm^2 thick) were prepared by electroplating on pure copper, which was then dissolved away. The plates were stacked and bombarded with an α - or ^3He - beam (the integrated beam current being a few milli-Coulombs). Each of the plates was dissolved in a small quantity of conc. HCl containing manganese and vanadium as hold-back carriers, and then Br_2 (a few drops) and 8N HCl (10 ml) were added to the solution. The ^{52}Fe in the resultant solution was extracted into isopropyl ether, which was then washed with 8N HCl, and back-extracted into water. The radio-chemical purity of the separated ^{52}Fe was found to be satisfactory from both its γ -ray spectrum and its decay curve. The loss of the Fe in this chemical process was measured by the use of an ^{59}Fe tracer; it proved to be under 10 %.

The measured excitation curves for the formation of ^{52}Fe and some by-products are shown in Figs. 1 and 2. This study is as yet in its preliminary stages, and so the absolute cross sections in Figs. 1 and 2 involve some uncertainty. It is clear, however, that the ^3He -bombardment gives an ^{52}Fe yield higher by a factor of about 3 than does the α -bombardment of a natural chromium target.

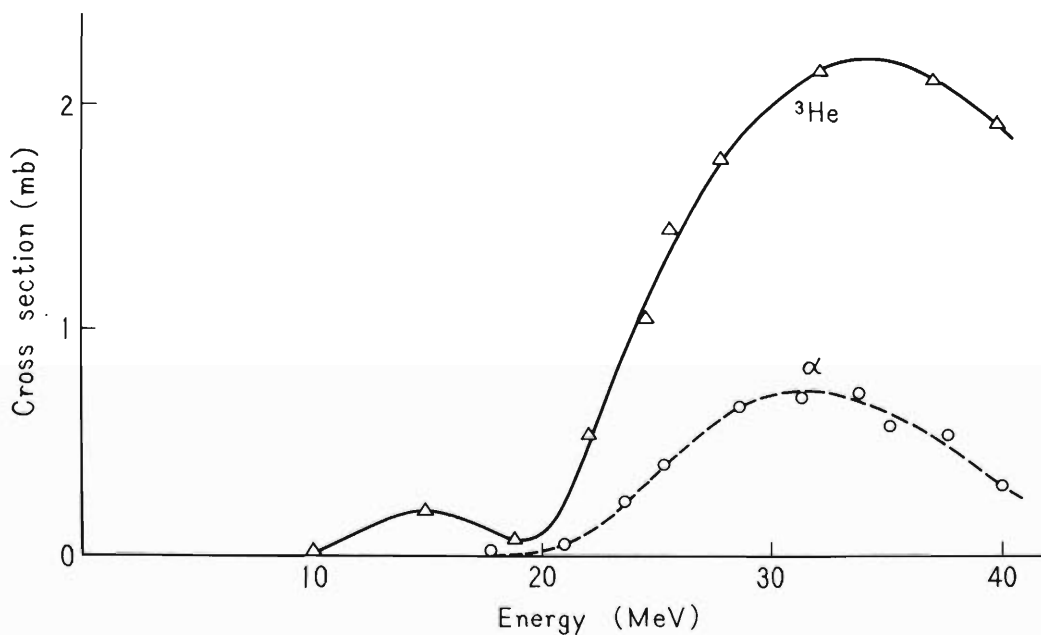


Fig. 1. Excitation curves for $\text{Cr} + ^3\text{He} \rightarrow ^{52}\text{Fe}$ and $\text{Cr} + \alpha \rightarrow ^{52}\text{Fe}$.

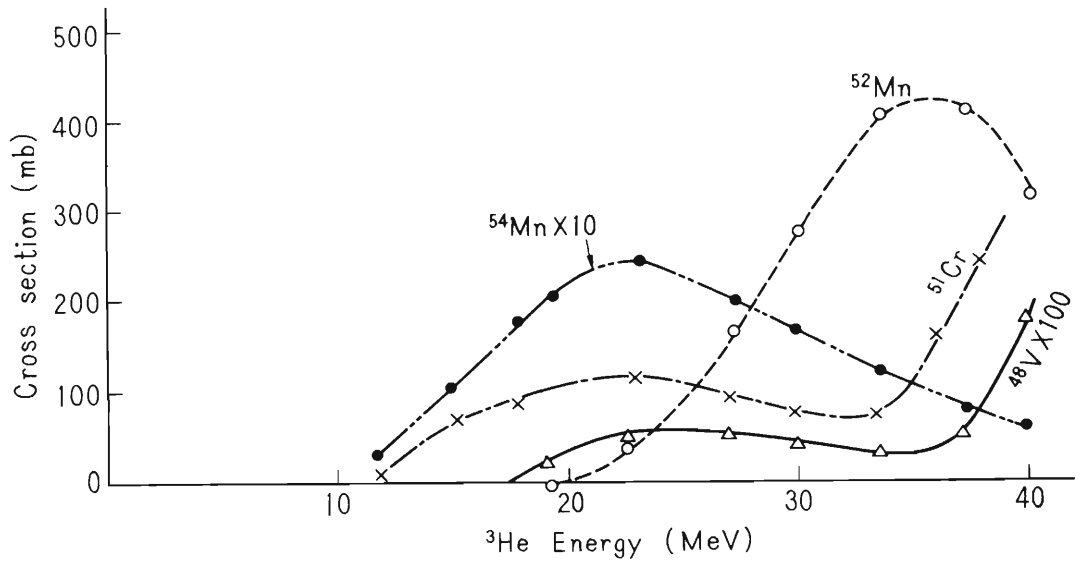


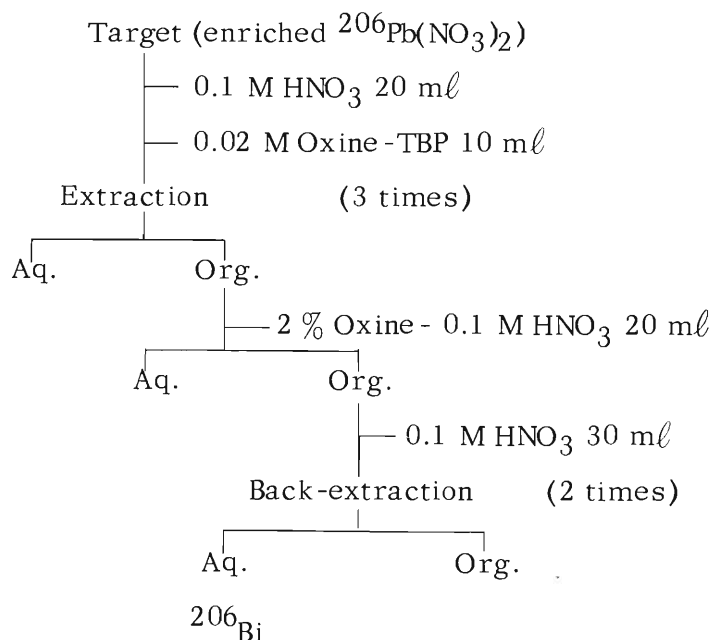
Fig. 2. Excitation curves for some products in ^3He -bombardment of chromium.

11-3. Separation of Carrier-free ^{206}Bi from ^{206}Pb

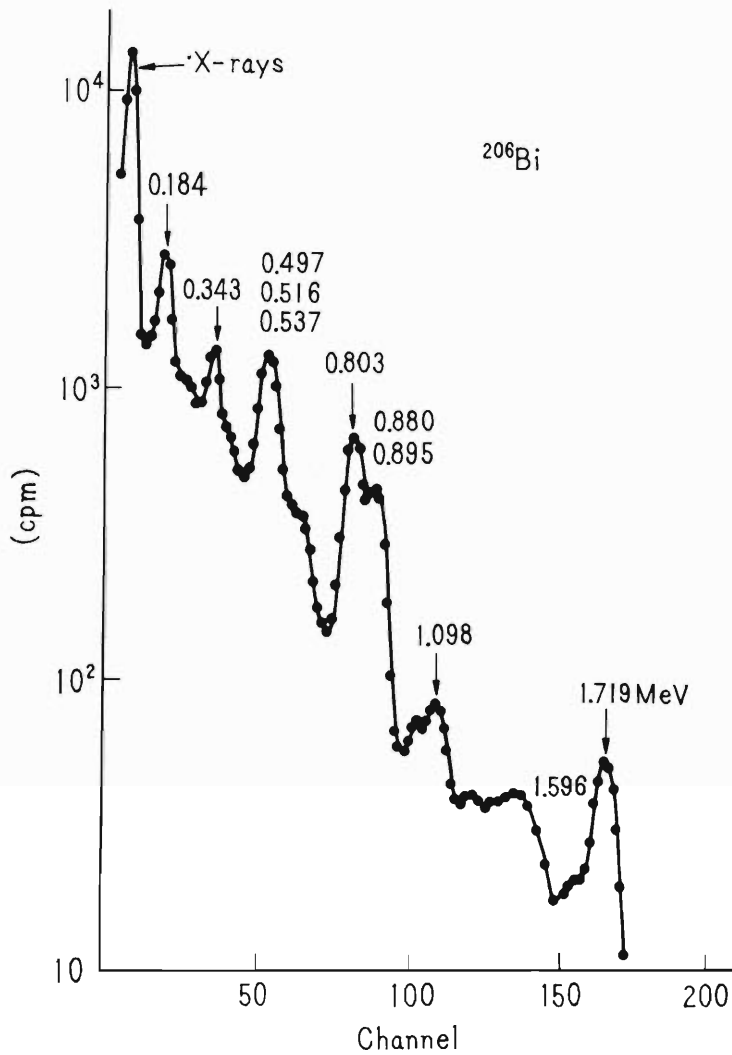
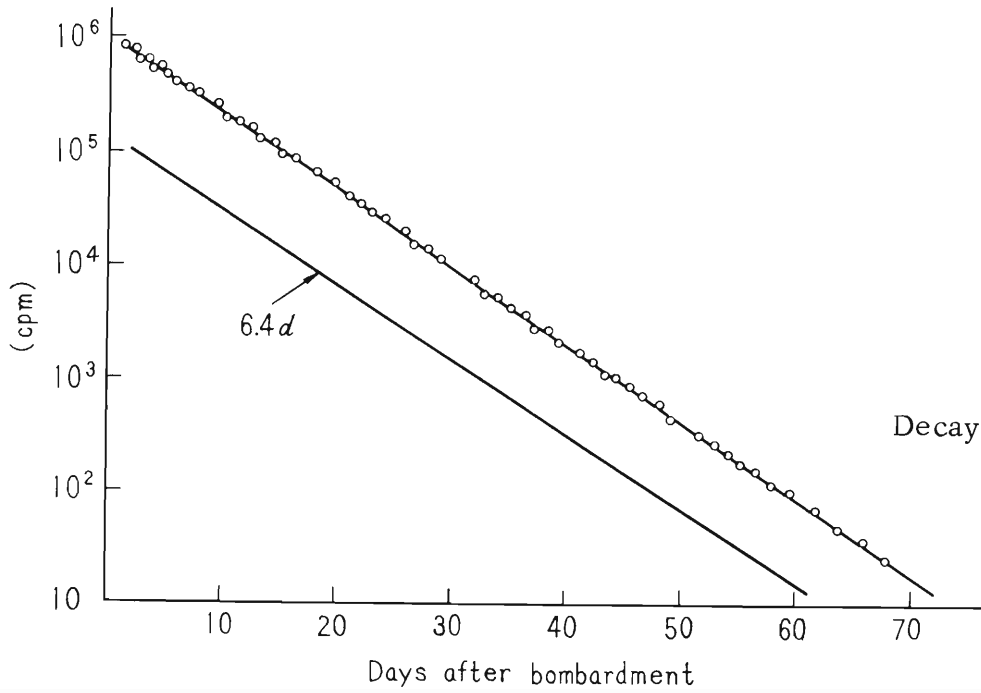
M. Inarida

The deuteron bombardment of lead produces $^{204,206}\text{Bi}$ by the following nuclear reactions: 1,2) $^{204}\text{Pb}(d,2n)^{204}\text{Bi}$ and $^{206}\text{Pb}(d,2n)^{206}\text{Bi}$. This report describes the radiochemical isolation of carrier-free ^{206}Bi from the ^{206}Pb target bombarded with 19 MeV deuteron-particles.

The enriched $^{206}\text{Pb}(\text{NO}_3)_2$ target was wrapped in 8μ -thick aluminum foil and clamped to a water-cooled aluminum target holder attached to the IPCR cyclotron. The target was bombarded with 19 MeV deuterons for 90 min at a beam intensity of $0.2 \sim 1.1\mu\text{A}$ through a window of 50μ -thick aluminum foil. After the bombardment, 160 mg of the target was dissolved in 20 ml of 0.1 M HNO_3 . The method of separating carrier-free ^{206}Bi from ^{206}Pb is shown schematically below:



The activity in the carrier-free bismuth fraction was identified by its half-life (6.4 days) and by means of γ -ray spectrometry. The data obtained are shown in Figs. 1 and 2.



References

- 1) D.H. Templeton, J.J. Howland, and I. Perlman: Phys. Rev., 72, 766 (1947).
- 2) J.D. Gile, W.M. Garrison, and J.G. Hamilton: J. Chem. Phys., 19, 256 (1951).

12. RADIATION MONITORING

12-1. Neutron Monitoring with a Large Neutron Counter

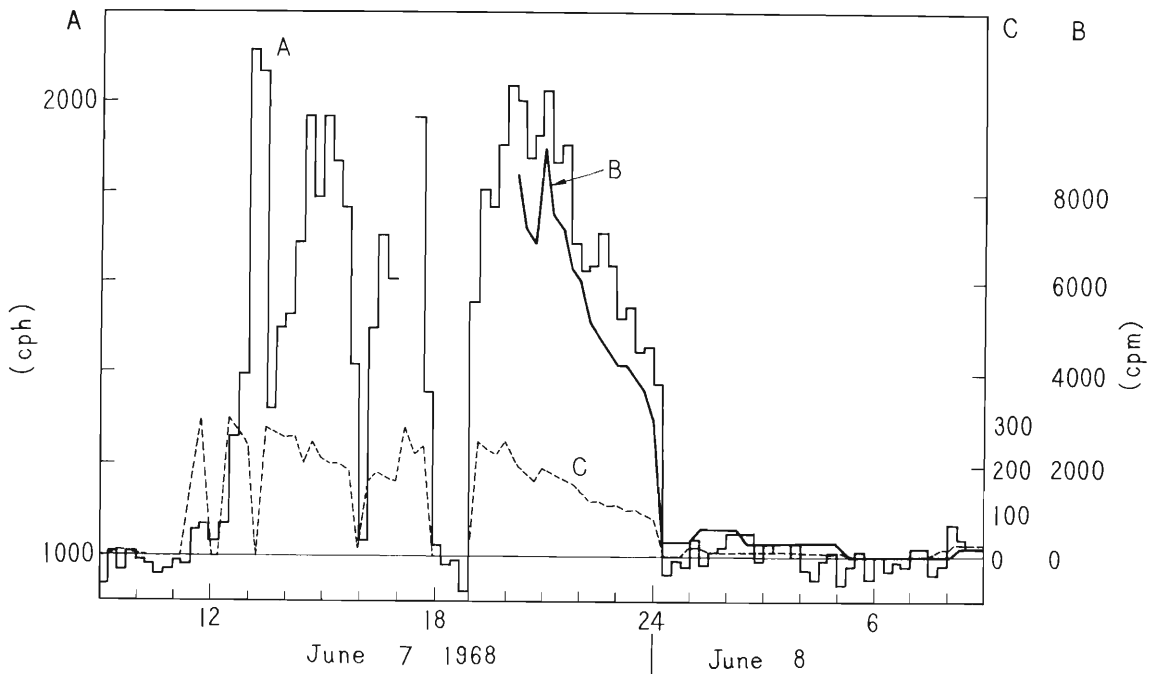
M. Wada, M. Okano, I. Sakamoto, and T. Hamada

A large neutron counter has been operated since April 1968 at the Radiation Monitoring Station¹⁾ at about 85 m apart from the IPCR cyclotron.

The counter²⁾ has effective dimensions of 148 mm dia. \times 1910 mm and is filled with enriched BF_3 gas at 185 mmHg, covered with 20 mm polyethylene. The counting efficiency is given by a slowly decreasing function with increase in energy. The efficiency of 10 keV neutrons is three times greater than that of 10 MeV neutrons.³⁾

Fig. 1 shows an example of the intensity increase when deuterons are accelerated. The parallelism among the variations detected inside and outside the experimental area is clearly seen.

The daily average counts are plotted in Fig. 2. Cosmic-ray neutron intensity varies with barometric pressure as seen during August when the cyclotron was not operated. Superposed on the variation as above, the leakage fluxes are detected, which result in the average increment of several percent of the cosmic-ray level.



A: The large neutron counter at 85 m apart, B: The small counter in the small experimental area,⁴⁾ C: The small counter in the underground passage from the control room to the small experimental area.

Fig. 1. Comparison of time variations of neutron intensity detected by counters at different positions.

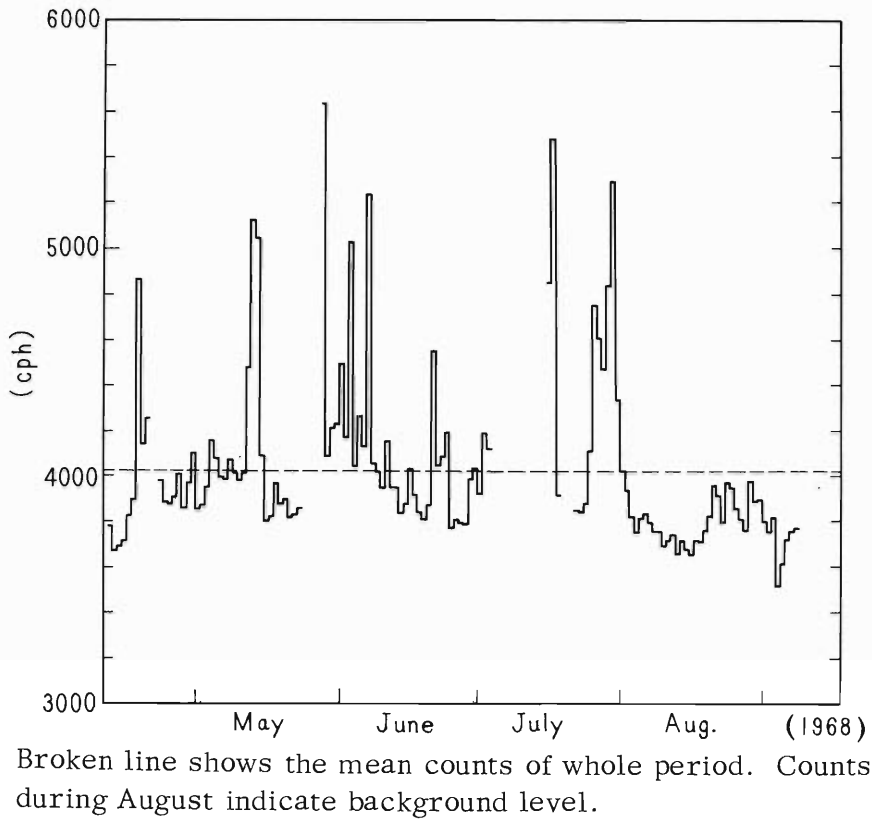
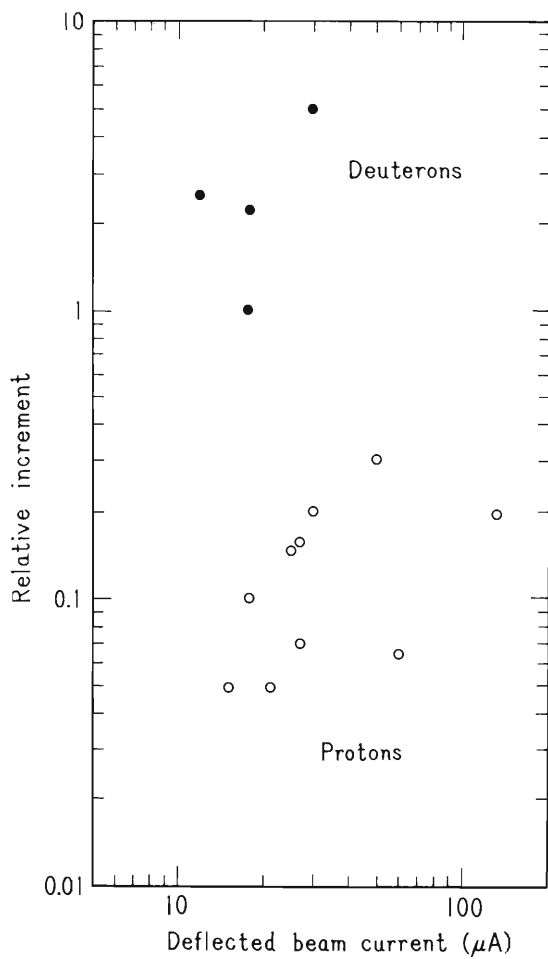


Fig. 2. Daily average counts.

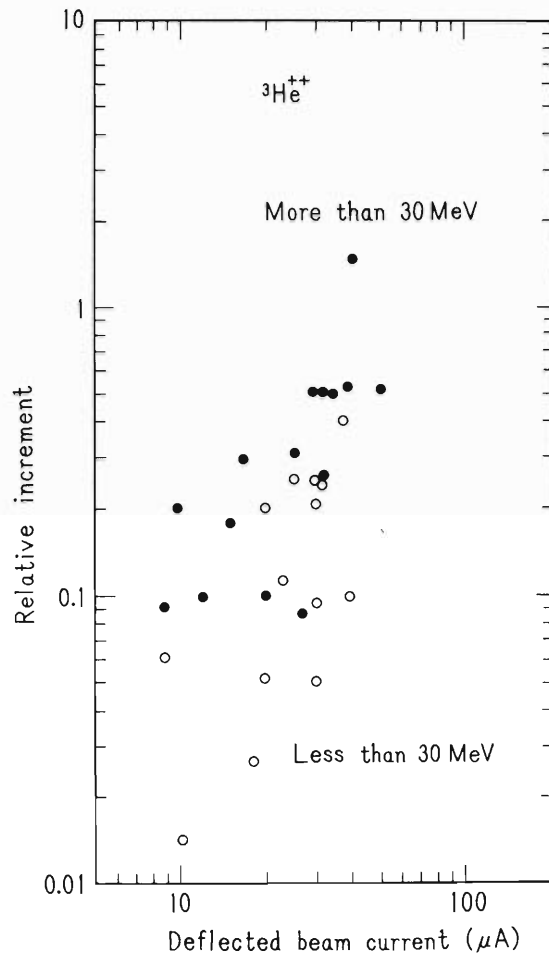


Black dots are for deuterons and open circles are for protons.

Fig. 3.

Peak intensity of neutrons at 85 m as a function of the deflected beam current.

Peak intensities of neutrons detected as 85 m are plotted in Figs. 3 and 4 as a function of the deflected beam current in μA . Amount of neutrons in the case of α acceleration is a bit less than that of ${}^3\text{He}$.



Black dots are for ${}^3\text{He}$ of energies more than 30 MeV and open circles for those less than 30 MeV.

Fig. 4. Peak intensity of neutrons at 85 m as a function of the deflected beam current.

References

- 1) IPCR Cyclotron Progress Report, 1, 81 (1967).
- 2) C.J. Hatton and H. Carmichael: *Can. J. Phys.* 42, 2443 (1964).
- 3) W.N. Hess, et al.: *Phys. Rev.*, 116, 445 (1959).

K. Koda, I. Sakamoto, and I. Usuba

The protection of cyclotron workers from induced activities, caused by the leakage radiation and/or residual activities, is one of the most important problems of health physics. The leakage radiation affects the cyclotron operating persons as a cause of external exposure. In the case of leakage neutron, the biological effect varies with its energy spectrum. The residual activities affect the persons not only as a cause of external exposure after machine shutdown, but also as a cause of contamination and internal exposure. In this paper, the results of measurements made during April 1967 to March 1968 on the intensities of leakage neutrons in the controlled area, the characters of nuclides of the residual activities, as well as the internal and external exposures to the workers are reported.

(1) Leakage radiation

A large quantity of neutrons was produced when the beryllium target was bombarded with alpha, helium-3, deuteron or proton ions. The beryllium target was placed in the course No. 1 where a great influence was observed in the underground passage. In the case of deuteron ions a higher rate of dose equivalent was observed as shown in Table 1.* It shows that the points Nos. 1,3,4, and 7 of the underground passage are almost covered with thermal neutrons and classified as C in the neutron spectrum number. On the other hand, in the point No. 2 the leakage gamma-rays show nearly equal distribution as the leakage neutrons and its contribution was about 100 mR/h.

(2) Residual activities

A dose map of the controlled area measured 20 min after machine shutdown (the cyclotron had been operated 5 h with deuteron ions accelerated to 17 MeV) is shown in Fig. 1. The cyclotron is mainly composed of stainless steel and copper, and brass, graphite, and tungsten as parts. The surface dose rate of the cyclotron was 100 mR/h, falling to 10 mR/h after 2 h. Such high level and short life nuclides imply that ^{11}C , ^{13}N , and ^{15}O are perhaps induced from the vapor of pump oil and the air existing in the vacuum line, but have not been identified. From the samples taken from the inner surface of the cyclotron chamber, ^7Be , ^{64}Cu , and ^{65}Zn are identified by gamma-ray spectroscopy and chemical treatments. They are positively induced from graphite and copper. Especially, ^{65}Zn ($T_{1/2} = 245\text{d}$) and ^7Be ($T_{1/2} = 53\text{d}$) cause the contamination in their long half-life.

(3) Contamination

"Dusting-off" of loose surface contamination has been observed on the floor of the cyclotron room as $10^{-5} \mu\text{Ci}/\text{cm}^2$ (beta-gamma). ^{65}Zn and ^7Be are identified in the dust

* Measured by H. Tatsuta and H. Ryufuku, Japan Atomic Energy Institute.

and air as in the cyclotron chamber itself. It is estimated that the sources of the contamination are released when the cyclotron chamber is opened for overhaul. The contamination ($10^{-5} \mu\text{Ci}/\text{cm}^2$) has been kept for whole year constantly, during which we tried wipe off the induced radio-nuclides on the inner surface of the cyclotron chamber when it was opened.

(4) Personnel monitoring

Concerning the external exposure in the yearlong measurement, the values of total dose of all personnel issued with the film badge are shown in Table 2. Average dose per

Table 2. Accumulated dose distribution of the staffs.
From Apr. 1967 to Mar. 1968

Rank of accumulated dose (mrem)	Undetectable	10~100	101~300	301~1000	1000~
No. of staffs	1	5	9	9	1

Average dose per person : 28.5 mrem

Maximum dose : 1260 mrem

person per month is 28.5 mR that is twice the value in the previous period, for a large scale overhaul of the cyclotron was carried out in February 1968 and the septum was frequently replaced. The induced radio-nuclides diffuse in the air when the cyclotron chamber is opened. The workers breathe the contaminated air and are exposed to the radio-nuclides at their lungs as internal exposure. For 10 persons was measured the internal exposure by the whole body counter* and all of them had clearly ^{65}Zn and ^7Be patterns. The internal exposure amounts at most 5 mR/year (39 nCi as ^{65}Zn) as derived by the method described in ICRP Publication, and is equivalent to 1/200 of external exposure of the persons. ^{65}Zn (from trace to 35 pCi/l) and ^7Be (from trace to 18.6 pCi/l) were also identified in their urine.**

* Measured by Dr. Y. Yoshizawa and E. Konishi: Tokyo University.

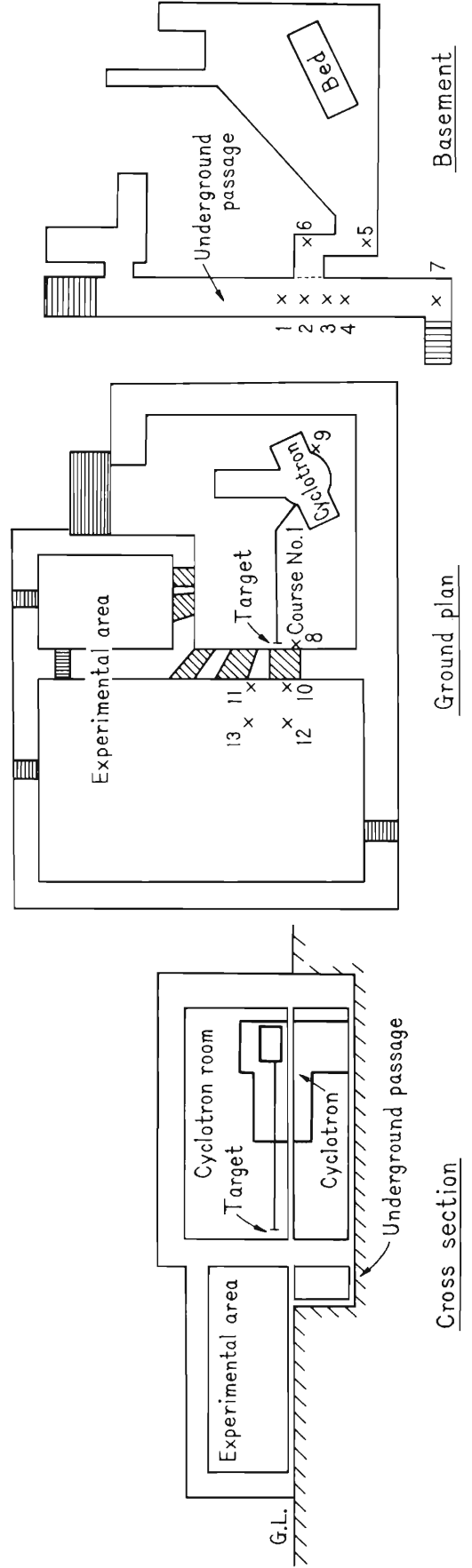
** Measured by S. Ohno: Institute National Radiological Science.

Table 1. Dose equivalent rates and neutron spectra at various points in the cyclotron building.

Unit: mrem/h

Particle	Point of observation*		1	2	3	4	5	6	7	8	9	10	11	12	13	
	Energy (current)															
α	35 MeV (8 μ A)		1.0	20	1.3	0.4				1×10^6						
^3He	27 MeV (17 μ A)		0.9	26	1.7	0.3	260	63	< 0.02	1.1×10^6	Undetectable	140	130			
P	11 MeV (15 μ A)			38						1.7×10^6						
d	23 MeV (10 μ A)		20	630	24	7.0	5200 7800	1300	0.2	2×10^7		360	420	35	32	
Neutron spectrum**			C	B	C	C	B	B	C	A	A	A	A	B	B	B

* See the figure shown below, ** A: 20keV 10MeV, B: 0.6eV~20keV, C: <0.6eV.



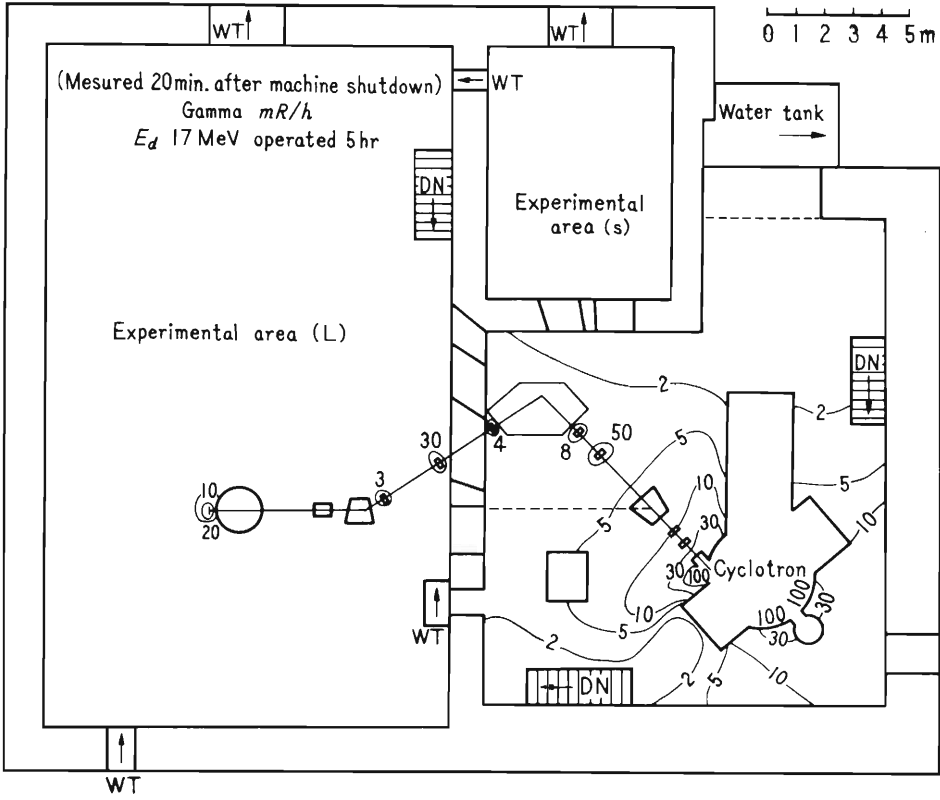


Fig. 1. Residual activity pattern.

13. LIST OF PUBLICATIONS

- 1) N. Nakanishi and K. Matsuda: "Design of Nuclear Reaction Particle Analyzer", Nucl. Instr. Methods, 57, 245 (1967).
- 2) K. Matsuda, N. Nakanishi, S. Takeda, and T. Wada: "Cross Sections of the ^{12}C (^3He , p) ^{14}N Reaction", J. Phys. Soc. Japan, 25, 1207 (1968).
- 3) T. Nozaki, Y. Tanaka, A. Shimamura, and T. Karasawa: "The Preparation of Anhydrous HF^{18} ", Intern. J. Appl. Radiation Isotopes. 19, 27 (1968).
- 4) M. Odera, Y. Miyazawa, T. Tonuma, M. Hemmi, and O. Terajima: "Design and Performance of a Focusing Magnetic Channel for a Variable Energy Multiparticle Cyclotron", Nucl. Instr. Methods. (in press)
- 5) H. Kamitsubo, T. Wada, T. Fujisawa, and M. Igarashi: "Large Angle Scattering of ^3He Particles by ^{58}Ni ", Phys. Letters. (to be published)
- 6) I. Kohno, T. Tonuma, Y. Miyazawa, S. Nakajima, T. Inoue, A. Shimamura, and T. Karasawa: "The Multicharged Heavy Ion Source for the IPCR Cyclotron", Nucl. Instr. Methods. (to be published)

14. LIST OF PERSONNEL

IPCR Cyclotron Administration Committee

熊谷寛夫	Hiroo KUMAGAI (chairman)	浜田達二	Tatsuji HAMADA
橋口隆吉	Ryukiti R. HASIGUTI	今村昌	Masashi IMAMURA
唐沢孝	Takashi KARASAWA	松田一久	Kazuhisa MATSUDA
松山晃	Akira MATSUYAMA	齋藤信房	Nobufusa SAITO
杉本光男	Mitsuo SUGIMOTO	田中穰	Yutaka G. TANAKA

Managers of Users Group

野崎正	Tadashi NOZAKI	小寺正俊	Masatoshi ODERA
-----	----------------	------	-----------------

IPCR Cyclotron Operating Personnel

Management

唐沢孝	Takashi KARASAWA	小寺正俊	Masatoshi ODERA
元永昭七	Shoshichi MOTONAGA	河野功	Isao KOHNO
宮沢佳敏	Yoshitoshi MIYAZAWA		

Operation

藤田新	Shin FUJITA	池上九三男	Kumio IKEGAMI
中島尚雄	Hisao NAKAJIMA	荻原清	Kiyoshi OGIWARA
大沢信道	Nobumichi OSAWA	寺島為	Osamu TERAJIMA
吉田喜作	Kisaku YOSHIDA		

Scientific and Engineering Personnel

Cyclotron Lab.

熊谷寛夫	Hiroo KUMAGAI	千葉好明	Yoshiaki CHIBA
藤沢高志	Takashi FUJISAWA	藤田二郎	Jiro FUJITA
橋本房子	Fusako HASHIMOTO	逸見政武	Masatake HEMMI
稲村卓	Takashi INAMURA	井上敏彦	Toshihiko INOUE
上坪宏道	Hiromichi KAMITSUBO*	唐沢孝	Takashi KARASAWA
河野功	Isao KOHNO	松田一久	Kazuhisa MATSUDA
宮沢佳敏	Yoshitoshi MIYAZAWA	元永昭七	Shoshichi MOTONAGA
中島諄二	Shunji NAKAJIMA	中西紀喜	Noriyoshi NAKANISHI
小寺正俊	Masatoshi ODERA	島村晃	Akira SHIMAMURA
竹田繁	Shigeru TAKEDA	戸沼正雄	Masao TONUMA
和田雄	Takeshi WADA	山路修平	Shuhei YAMAJI

* Now Staying at Saclay

(Visitors)

山崎敏光	Toshimitsu YAMAZAKI (The Univ. of Tokyo)
野村亮	Toru NOMURA (The Univ. of Tokyo)
河合光路	Mitsuji KAWAI (The Tokyo Inst. of Tech.)
坂口治隆	Harutaka SAKAGUCHI (The Univ. of Tokyo)
増井邦明	Kuniaki MASUI (The Unive of Tokyo)

Radiation Lab.

山崎文男	Fumio YAMASAKI	粟屋容子	Yohko AWAYA
浜田達二	Tatsuji HAMADA	橋爪朗	Akira HASHIZUME
岡野真治	Masaharu OKANO	加藤武雄	Takeo KATO
天道芳彦	Yoshihiko TENDOW	太田光子	Mitsuko OTA

Nuclear Analytical Chemistry Lab.

齋藤信房	Nobufusa SAITO	野崎正	Tadashi NOZAKI
荒谷美智	Michi ARATANI	安部文敏	Fumitoshi AMBE
安部静子	Shizuko AMBE	稲荷田万里子	Mariko INARIDA

(Visitors)

八劍吉文	Yoshifumi YATSURUGI (Komatsu Electronic Metals Co., Ltd.)
秋山信之	Nobuyuki AKIYAMA (Komatsu Electronic Metals Co., Ltd.)

Biochemistry I Lab.

田中穰	Yutaka G. TANAKA
-----	------------------

Radiobiology Lab.

松山晃	Akira MATSUYAMA	北山滋	Shigeru KITAYAMA
-----	-----------------	-----	------------------

Radiation Chemistry Lab.

今村昌	Masashi IMAMURA	松井正夫	Masao MATSUI
関博之	Hiroshi SEKI		

Metal Physics Lab.

橋口隆吉	Ryukiti R. HASIGUTI	岩崎邦彦	Kunihiko IWASAKI
坂入英雄	Hideo SAKAIRI	塩谷亘弘	Nobuhiro SHIOTANI
八木栄一	Eiichi YAGI		

(Visitors)

三島良績	Yoshitsugu MISIMA (The Univ. of Tokyo)
寺西洋志	Hiroshi TERANISHI (The Univ. of Tokyo)

Magnetic Materials Lab.

杉本光男	Mitsuo SUGIMOTO	岡田卓也	Takuya OKADA
岡本祥一	Shoichi OKAMOTO	関沢尚	Hisashi SEKIZAWA

Radiation Monitors

甲 田 陸 男 Kugao KODA
薄 葉 勲 Isao USUBA

坂 本 一 郎 Ichiro SAKAMOTO

(Editors of the Progress Report)

松 田 一 久 Kazuhisa MATSUDA
田 中 穰 Yutaka G. TANAKA

野 崎 正 Tadashi NOZAKI

IPCR Cyclotron Progress Report 1968

理化学研究所サイクロトン年次報告 第2巻(1968) 奥付

印刷 昭和44年(1969) 3月25日

発行 昭和44年(1969) 3月30日

発行者 理化学研究所

代表者 赤 堀 四 郎

351 埼玉県北足立郡

大和町大字下新倉4775番地

電話(0484)62-1111

編集者 理化学研究所サイクロトン運営委員会

委員長 熊 谷 寛 夫

印刷所 丸 星 印 刷 社

101 東京都千代田区

神田神保町1丁目42番地

定価 1,500円

理化学研究所

埼玉県 北足立郡 大和町